SIMONE AMOROSO

TUNING OF EVENT GENERATORS TO MEASUREMENTS OF $t\bar{t}$ PRODUCTION AND A GENERAL SEARCH FOR NEW PHYSICS WITH THE ATLAS EXPERIMENT

TUNING OF EVENT GENERATORS TO MEASUREMENTS OF $t\bar{t}$ PRODUCTION AND A GENERAL SEARCH FOR NEW PHYSICS WITH THE ATLAS EXPERIMENT

Dissertation

zur Erlangung des Doktorgrades der
Fakultät für Mathematik und Physik der

Albert Ludwigs Universität Freiburg

Vorgelegt von

SIMONE AMOROSO

ADVISOR: PROF. DR. GREGOR HERTEN

June, 2015

Simone Amoroso: *Tuning of event generators to measurements of* $t\bar{t}$ *production and a general search for new physics with the ATLAS experiment,*
© June, 2015

DATUM DER MUNDLICHEN PRUFUNG: 25.09.2015

DEKAN:	Prof. Dr. Dietmar Kröner
LEITER DER ARBEIT:	Prof. Dr. Gregor Herten
KOREFERENT:	Prof. Dr. Markus Schumacher
PRÜFER:	Prof. Dr. Gregor Herten
	Prof. Dr. Karl Jakobs
	Prof. Dr. Harald Ita

"It is a capital mistake to theorize before one has data. Insensibly one begins to twist facts to suit theories, instead of theories to suit facts..."

— Sherlok Holmes (from "A Study in Scarlet" by Sir A. C. Doyle)

ABSTRACT

The start of the Large Hadron Collider provides an unprecedent opportunity for the exploration of physics at the TeV scale. It is expected to perform precise tests of the structure of the Standard Model and to hint at the structure of the physical laws at a more fundamental level.

The first part of this work describes a tune of the initial- and final-state radiation parameters in the Pythia8 Monte Carlo generator, using ATLAS measurements of $t\bar{t}$ production at $\sqrt{s} = 7$ TeV. The results are compared to previous tunes to the Z boson transverse momentum at the LHC, and to the LEP event shapes in Z boson hadronic decays, testing of the universality of the parton shower model. The tune of Pythia8 to the $t\bar{t}$ measurements is applied to the next-to-leading order generators MadGraph5_aMC@NLO and Powheg, and additional parameters of these generators are tuned to the $t\bar{t}$ data. For the first time in the context of Monte Carlo tuning, the correlation of the experimental uncertainties has been used to constrain the parameters of the Monte Carlo models.

In the second section we report results of a model independent search for new phenomena with data recorded by the ATLAS detector at $\sqrt{s} = 8$ TeV. Event topologies involving isolated electrons, photons, muons, jets, b-jets and missing transverse momentum are investigated. The events are subdivided according to their final states into 697 exclusive analysis channels. For each channel, a search algorithm tests the compatibility of the effective mass distribution in data against the distribution in the Monte Carlo simulated background. No significant deviations between data and the Standard Model expectations have been observed.

ZUSAMMENFASSUNG

Seit der Inbetriebnahme des Large Hadron Colliders stehen uns neue Möglichkeiten offen, die physikalischen Phänomene an der TeV Skala zu erforschen. Präzise Tests des Standardmodells der Teilchenphysik können durchgeführt werden um die zugrunde liegenden physikalischen Gesetze noch besser zu verstehen.

Der erste Teil dieser Arbeit befasst sich mit der Feinabstimmung von Strahlungsparametern des PYTHIA8 Monte Carlo Generators unter Verwendung von ATLAS Daten aus $t\bar{t}$ Produktion bei $\sqrt{s} = 7$ TeV. Die Resultate können mit vorherigen LHC Ergebnissen verglichen werden, die aus der Kalibration des Transversalimpulses des Z Bosons stammen. Ebenso ist ein Vergleich mit Resultaten aus den hadronischen Zerfallsmoden des Z von LEP möglich, was einen Test für die Universalität des Partonmodells darstellt. Diese Feinabstimmung von PYTHIA8 aus den $t\bar{t}$ Ereignissen kann auf Generatoren übertragen werden, die Strahlungskorrekturen höherer Ordnung verwenden, wie MADGRAPH5_aMC@NLO oder POWHEG. Auch können zusätzliche Parameter dieser Generatoren auf die $t\bar{t}$ Ereignisse abgestimmt werden. Im Rahmen dieser Studien wurden zu ersten Mal die Korrelationen experimenteller Unsicherheiten benutzt, um den Parameterraum von Monte Carlo Modellen einzuschränken.

Im zweiten Abschnitt werden die Resultate einer modellunabhängigen Suche nach neuer Physik vorgestellt, die mit ATLAS Daten aus 2012 bei $\sqrt{s} = 8$ TeV durchgeführt wurde. Die Eigenschaften von Kollisionsereignissen mit isolierten Elektronen, Myonen, Photonen, Jets, b-jets und fehlender transversaler Energie werden untersucht. Die Ereignisse können anhand dieser Objekte klassifiziert und in 697 exklusive Analysekanäle eingeteilt werden. Für jeden dieser Kanäle wird ein statistischer Suchalgorithmus angewendet um Abweichungen vom simulierten Untergrund festzustellen. Dabei wurde keine signifikante Abweichung von der Vorhersage des Standardmodells entdeckt.

PUBLICATIONS

The material presented in this thesis is based on work performed within the ATLAS collaboration, thus relying on the contribution of many people. The author's personal contribution is here briefly summarised.

GENERAL SEARCH FOR NEW PHENOMENA

The author has been responsible for introducing and developing general search strategies within ATLAS. General searches have been performed using the datasets collected by ATLAS at 7 and 8 TeV of center of mass energy, respectively [1, 2], for which the author has been editor and main analyzer.

SEARCH FOR SQUARKS AND GLUINOS WITH THE ATLAS DETECTOR IN FINAL STATES WITH JETS AND MISSING TRANSVERSE MOMENTUM USING $\sqrt{s} = 8$ TEV PROTON–PROTON COLLISION DATA [3]

Defined of the trigger strategy for signal and background selection. Validated the jet+E_T^{miss} triggers providing an uncertainty on its efficiency.

SEARCH FOR DIRECT PAIR PRODUCTION OF THE TOP SQUARK IN ALL-HADRONIC FINAL STATES IN PROTON-PROTON COLLISIONS AT $\sqrt{s} = 8$ TEV WITH THE ATLAS DETECTOR[4]

Developed the trigger strategy, and optimized the event selection to be insensitive to pile-up. Computed systematic uncertainties due to the modelling of the top background, dominant in the signal region. Performed studies for constraining nuisance parameters in the global fit to control and signal region.

A STUDY OF THE SENSITIVITY TO THE PYTHIA8 PARTON SHOWER PARAMETERS OF $t\bar{t}$ PRODUCTION MEASUREMENTS IN pp COLLISIONS AT $\sqrt{s} = 7$ TEV WITH THE ATLAS EXPERIMENT AT THE LHC [5]

Responsible for implementing handling of uncertainties correlation in the Professor code. Generated the PYTHIA8 predictions annd tunes. Co-editor of the public note documenting the result.

ACKNOWLEDGMENTS

First of all I would like to thank my advisor, Prof. Gregor Herten, for accepting me into his group, and for the constant support I have been granted. During these four years I have been given the opportunity to participate in many school and conferences, and the rare freedom to pursue some of my own research interests and ideas.

A special thank goes also to Sascha Caron, who has been my supervisor during the first year in Freiburg, with whom I keep collaborating on a number of projects. To him goes the merit of disclosing to me the world of General Searches, and of convincing me of their usefulness and originality,

I am deeply grateful to Anna Sfyrla, for encouraging me to work in the ATLAS trigger, and to Andreas Hoecker and Monica D'Onofrio, who entrusted me with the responsibility of coordinating the trigger strategy of the SUSY group during LS1.

The first part of this thesis originates from work done under an MCnet fellowship. I have to thank Andy Buckley for accepting to supervise me and Stefano Camarda for sharing his deep knowledge of the world of Monte Carlo generators, and for an extremely pleasant collaboration.

I would also like to thank all the people with whom I shared my time in Freiburg. Jan-Erik Sundermann for the constant help on computing matters, my student Fabio and all the other italian PhDs: Manuela, Luisa, Valerio, Manfredi, Francesca and Claudia.

A final thank goes to my family for their support and encouragement in this endeavour.

CONTENTS

INTRODUCTION 1

I THEORY 3

1 THE STANDARD MODEL OF PARTICLE PHYSICS 5
- 1.1 History 5
- 1.2 The matter content 6
- 1.3 The Higgs mechanism and the electroweak sector 8
- 1.4 Fermion masses and mixing 10
- 1.5 The QCD Lagrangian 12

2 THE STRUCTURE OF QCD PROCESSES 17
- 2.1 Infrared Safety 17
- 2.2 Parton Distribution Functions 18
- 2.3 Jets 20
- 2.4 Monte Carlo event generators 23
  - 2.4.1 Hard scattering 23
  - 2.4.2 Parton showers 25
  - 2.4.3 Matching and merging 27
  - 2.4.4 Underlying Event and Multiple Parton Interactions 28
  - 2.4.5 Hadronization 30
  - 2.4.6 Particle decays 32
  - 2.4.7 Tuning 33

3 THEORIES OF NEW PHYSICS 35
- 3.1 Open problems in the Standard Model 35
  - 3.1.1 Dark matter and dark energy 36
  - 3.1.2 Naturalness and fine-tuning 37
  - 3.1.3 Grand Unification 38
- 3.2 Supersymmetry 39
  - 3.2.1 The Supersymmetry algebra 39
  - 3.2.2 The Minimal Supersymmetric Standard Model 40
  - 3.2.3 Supersymmetry breaking 42
  - 3.2.4 A natural spectrum 44
- 3.3 Extra Dimensions 45
  - 3.3.1 Large Extra Dimensions 46
  - 3.3.2 Universal Extra Dimensions 46
  - 3.3.3 Warped extra dimensions 47
- 3.4 Composite Higgs 47
  - 3.4.1 Little Higgs models 48

II EXPERIMENT 49

4 THE ATLAS EXPERIMENT AT THE LARGE HADRON COLLIDER 51
- 4.1 The Large Hadron Collider 51

4.1.1 The accelerator chain 52
4.1.2 Parameters and operations 53
4.2 The ATLAS experiment 55
4.2.1 Coordinate System 56
4.2.2 Magnet system 57
4.2.3 Inner Detector 58
4.2.4 Calorimeter 61
4.2.5 Muon Spectrometer 65
4.2.6 Luminosity and forward detectors 68
4.2.7 Trigger and DAQ 68
5 OBJECT RECONSTRUCTION AND SELECTION 71
5.1 Tracking and vertexing 71
5.2 Jets 73
5.2.1 Clustering 74
5.2.2 Jets reconstruction and calibration 74
5.2.3 Jet energy scale and resolution uncertainties 75
5.3 *b*-jets identification 77
5.4 Muons 80
5.5 Electrons 81
5.6 Photons 84
5.7 Missing Transverse Energy 88
5.8 Overlap Removal 91

iii ANALYSIS 93
6 PYTHIA8 ATTBAR TUNE 95
6.1 Motivation and strategy 95
6.2 Methodology 96
6.3 Sensitivity study 102
6.4 Initial-state radiation 107
6.5 Final-state radiation 109
6.6 Simultaneous tune of ISR and FSR 112
6.7 Tune of the MadGraph5_aMC@NLO generator 117
6.8 Tune of the POWHEG generator 120
6.9 Summary and conclusions 121
7 GENERAL SEARCH FOR NEW PHENOMENA 129
7.1 Searches for new physics at colliders 129
7.2 Model Independent General Searches 130
7.2.1 A history of model-independent searches 131
7.3 Analysis strategy 132
7.4 Data and MC samples 132
7.4.1 Data sample 132
7.4.2 Background Samples 133
7.5 Triggers 136
7.6 Events Classification 137
7.7 Background estimation 139
7.7.1 Estimation of fake lepton background 139

7.7.2 Corrections to the MC prediction 140
7.8 Systematic uncertainties 140
7.8.1 Experimental Uncertainties 141
7.8.2 Uncertainties on the background processes 141
7.9 Classification results 142
7.10 Statistical Interpretation 144
7.11 Search results 146
7.12 Sensitivity to benchmark new physics signals 148
CONCLUSIONS 155

IV APPENDIX 157
APPENDIX01 159
APPENDIX02 169

BIBLIOGRAPHY 171

INTRODUCTION

The Standard Model (SM) of particle physics is a successful theory of fundamental interactions. In the fifthy years of its existence it has explained a wide variety of experimental results, and predicted the existence of several new particles, including the recent discovery of a Higgs-like boson. Several fundamental questions are however left unanswered by the SM, notably an explanation for gravity, the source of matter-antimatter asymmetry and a dark matter candidate. Many extensions have been proposed, including new interactions, new spatial dimensions or new symmetries. In order to avoid the Higgs mass to be driven to very large values by loop corrections we also expect, by naturalness arguments, at least some of the new particles to appear at scales around the TeV, accessible at the Large Hadron Collider (LHC) experiments.

The top quark is the heaviest of all known particles and, due to its short lifetime, the only quark to decay before hadronization. Due to the large Yukawa coupling to the Higgs, the top is believed to play a special role in the mechanism of electroweak symmetry breaking. Precise measurements of its properties thus provide a crucial test of the consistency of the SM and could hint at physics beyond the standard model. At the LHC collider for the first time $t\bar{t}$ processes can be measured with enough accuracy so as to be used for constraining the parameters of the Monte Carlo models. The first part of this work describes a tuning of parameters related to initial- and final-state radiation in the Pythia8 Monte Carlo generator to ATLAS measurements of top pair production at $\sqrt{s} = 7$ TeV. The resulting tunes are compared to previous tunes to the Z boson transverse momentum at the LHC, and to the LEP event shapes in Z boson hadronic decays. Such a comparison provides a strong test of the universality of the parton shower model. The tune is also applied to the next-to-leading order generators MadGraph5_aMC@NLO and Powheg, and additional parameters of these generators are tuned to the $t\bar{t}$ data. For the first time in the context of Monte Carlo tuning, the correlation of the experimental uncertainties has been used to constrain the parameters of the Monte Carlo models.

Despite a wide program of searches, the LHC has yet to find any evidence or indication for the existence of new physics suggesting that, if at all present, it might manifest itself in a more complicated way than predicted. The second part of this work presents a novel model-independent approach to new particle searches, complement-

ing the traditional analyses, usually optimised for specific models. The "General search" is designed to be comprehensive for NP signals appearing at high transverse momenta, and in a small number of final states. All events are partitioned into exclusive classes according to the type and number of high level objects reconstructed (e, μ, γ, jets and b-jets are considered). Subsequently in each of the event classes a statistical search algorithm is used to find the region of largest deviation between data and the SM prediction (mostly obtained from MC simulations) in three variables sensitive to NP effects: the missing transverse energy, the effective mass (sum of the p_T of all objects) and the total visible invariant mass. To quantify the compatibility between the data and the SM prediction, the distribution of the p-values of the observed deviations is compared to an expectation obtained from pseudo-experiments including uncertainties and their correlations between various search classes. No significant excess has been found in the over 697 analyzed event classes, with the distribution of deviations following the expectation from pseudo-experiments.

This thesis is structured as follows. In the first chapter 1 we review the SM of particle physics and the mechanism of electroweak symmetry breaking. The methods used to obtain precise theoretical predictions for the modeling of hadronic interaction are outlined in chapter 2. In chapter 3 the most popular extensions of the SM and their phenomenology are reviewed. A brief overview of the LHC machine and the ATLAS detector is given in chapter 4. In chapter 5 we describe how the complex objects used in physics analysis are reconstructed from basic quantities. In chapter 6 we describe the ATTBAR tune of the Pythia8 Monte Carlo generator to ATLAS measurements of top pair production at 7 TeV, and its application to NLO+PS matched setups. Chapter 7 presents results of a model-independent general search for new physics, obtained with data collected at 8 TeV of center-of-mass energy at the ATLAS detector. In Section 7.12 we summarize the results obtained and provide some prospects for future work.

Part I

THEORY

1 THE STANDARD MODEL OF PARTICLE PHYSICS

Our current understanding of matter at its fundamental level is based on the "Standard Model" (SM) of particle physics. The SM provides a unified description of all the known fundamental particles and interactions (with the exception of gravity), and embodies the outstanding experimental and theoretical achievements carried out over the past sixty years in particle physics. In this chapter we briefly review the structure and development of theory, with an emphasis on the electroweak symmetry breaking mechanism.

1.1 HISTORY

The SM is a renormalizable quantum field theory in which all the interactions between fundamental particles are described by Yang-Mills theories [6]. Inspired by the success of electrodynamics and general relativity, in Yang-Mills theories the existence and dynamics of the gauge fields is determined by imposing invariance under local transformations of a non-Abelian gauge group. They were first introduced in an attempt to describe the strong interactions of vector mesons with a local version of the $SU(2)$ isospin symmetry. The theory predicted however the existence of massless spin-one particles, similar to the photon, but carrying charge. The fact that no such particle was known to exist, together with the general disbelieve that quantum field theories could describe strongly coupled theories, lead to these theories being ignored for many years. The breakthrough came in the late sixties with the discovery that there can be symmetries which cannot be inferred from the particle spectrum of the theory. First studied by Nambu [7, 8] in the context of superconductivity and subsequently by Goldstone [9] such spontaneously broken symmetries are associated by conserved currents but do not leave the ground state of the theory invariant.

In 1961 Glashow [10] used spontaneous symmetry breaking as the basis to unify the electromagnetic and weak interactions. At first the realization that in broken symmetries new massless particles should appear was seen as a serious obstacle. In fact the weak interaction did not seem to involve massless objects, and the theory was set aside until the concept of mass generation through symmetry breaking of a local gauge symmetry was established [11, 12, 13]. This phenomenon, now known as the Higgs mechanism, was incorporated in the Glashow model by Weinberg [14] and Salam [15] and turned out to provide the natural framework for the unification of the weak and

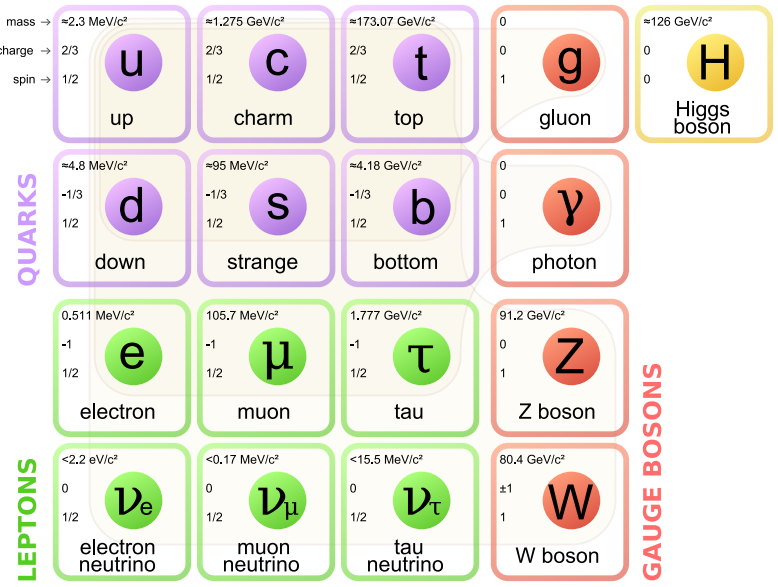

Figure 1: The fundamental fermion fields composing the SM of particle physics as well as the bosons that mediate the gauge interactions. Since July 2012 the Higgs boson, responsible of electroweak symmetry breaking, is an established part of the model [20].

electromagnetic interactions. It was still unclear whether the theory could be consistently used up to high scales. Only after after the proof of renormalizability made by t'Hooft and Veltman [16] The theory became widely accepted by the particle physics community. One of the key predictions of the theory was the existence of a neutral component of the electroweak interactions. The discovery of weak neutral currents in a single neutrino scattering event by the Gargamelle collaboration in 1973 [17] has been the first success for the SM. It took ten more years before the direct observation of the massive electroweak bosons a the SpS $p\bar{p}$ collider at CERN [18, 19]. Since then the SM has been thoroughly tested over many years and by many experiment in all of its sectors. It has made a number of successful predictions (such as the existence of the top quark and the Higgs boson) and is currently the most precisely tested physical theory.

1.2 THE MATTER CONTENT

The SM is a quantum field theory with $SU(3)_C \times SU(2)_L \times U(1)_Y$ as a gauge symmetry group. The subscript C is for the color charge, L for the left-handed weak charge and Y for the hypercharge. The fundamental degrees of freedom in the SM, represented in Figure 1, are the spin one-half quarks and leptons, the spin one gauge bosons and the spin zero Higgs field. Weak interactions at low energy are well described by an effective Lagrangian given by a sum of products of vector and axial vector currents ($V-A$ structure). To respect this struc-

ture we assign the left components of leptons and quarks to $SU(2)_L$ isodoublets, and the right fermions in the singlet representation [1].

$$\text{leptons}: \quad l_L = \begin{pmatrix} l \\ \nu_l \end{pmatrix}_L \quad l_R \tag{1}$$

$$\text{quarks}: \quad Q_L = \begin{pmatrix} u \\ d \end{pmatrix}_L \quad u_R, d_R \tag{2}$$

There is an apparent redundancy in the number of particles; the symmetry multiplets appear in three copies (or *families*), with no fundamental difference observed between them other than their mass hierarchy, that increases going from the first to the third (e, μ, τ for the leptons). The fermion multiplets in the SM and their charge assignment are shown in Table 1.

	$SU(3)_C$	$SU(2)_L$	$U(1)_Y$
Q_f	3	2	1/3
$\bar{u}_f$	$\bar{3}$	1	-4/3
$\bar{d}_f$	$\bar{3}$	1	2/3
L_f	1	2	-1
$\bar{e}_f$	1	1	2

Table 1: Fermion fields in the SM and their representation. The index $f = 1, 2, 3$ denotes the generation or "family".

Ignoring for the moment the colour $SU(3)$, the gauge sector will consists of an $SU(2)$ isotriplet, W^a_μ and an hypercharge singlet B_μ.

$$\mathcal{L}_{gauge} = -\frac{1}{4} B_{\mu\nu} B^{\mu\nu} - \frac{1}{8} \mathrm{Tr}(W^i_{\mu\nu} W^{i\mu\nu}) \tag{3}$$

$$= \frac{1}{4} B_{\mu\nu} B^{\mu\nu} - \frac{1}{4} W^3_{\mu\nu} W^{3\mu\nu} - \frac{1}{4} W^-_{\mu\nu} W^{+\mu\nu} \tag{4}$$

where the $B_{\mu\nu}$ and $W^i_{\mu\nu}$ are the $U(1)_Y$ and $SU(2)_L$ field strengths, respectively, defined as:

$$B_{\mu\nu} = \partial_\mu B_\nu - \partial_\nu B_\mu \tag{5}$$

$$W^a_{\mu\nu} = \partial_\mu W^a_\nu - \partial_\nu W^a_\mu + g\epsilon^{abc} W^b_\mu W^c_\nu \tag{6}$$

$$= \partial_\mu W^3_\nu - \partial_\nu W^3_\mu - ig(W^-_\mu W^+_\nu - W^-_\nu W^+_\mu) \tag{7}$$

with g the coupling strength of the weak interactions and ϵ^{abc} the totally anti-symmetric three index tensor, structure constant of the

1 A right-handed component for the neutrino ν_R is omitted, as not relevant for collider phenomenology

$SU(2)$ group. In the last line of eq. 5 we have introduced the complex combinations:

$$W^+_\mu = \frac{1}{\sqrt{2}}(W^1_\mu - iW^2_\mu) \quad W^-_\mu = \frac{1}{\sqrt{2}}(W^1_\mu + iW^2_\mu) \tag{8}$$

that together with W^3_μ will later become the physical fields.

The interactions between fermions and the gauge bosons come from their kinetic term:

$$\mathcal{L}_F = i\bar{l}_L \not{D} l_L + i\bar{Q}_L \not{D} Q_L + i\bar{l}_R \not{D} l_R + i\bar{u}_R \not{D} u_R + i\bar{d}_R \not{D} d_R \tag{9}$$

Where the covariant derivative is defined as:

$$D_\mu = \partial_\mu - ig' B_\mu Y - igW^a_\mu T^a \tag{10}$$

with g' and Y the coupling strength and value of the $U(1)$ hypercharge. The theory so far describes interaction of massless vector bosons, historically however it was known that the mediator of the weak force had to be massive, both to explain it's short range and describe the low-energy data. While we could insert explicitly a mass term for the gauge bosons of the form $m_V V_\mu V^\mu$ or $m\bar{\psi}\psi = m(\bar{\psi}_L\psi_R + \bar{\psi}_R\psi_L)$ for the fermions they would not be invariant under gauge transformations and can be shown to make the theory non-renormalizable.

1.3 THE HIGGS MECHANISM AND THE ELECTROWEAK SECTOR

While a satisfactory theory of electroweak interactions could be obtained by including by hand mass terms for each particle, this would spoil renormalizability and break gauge invariance. In the Weinberg and Salam electroweak theory the mass of the vector bosons arise from spontaneous symmetry breaking of a gauge symmetry. This is accomplished by introducing a new scalar field:

$$\mathcal{L}_{Higgs} = D_\mu \Phi D^\mu \Phi - V(\Phi^\dagger \Phi) \tag{11}$$

The Higgs field will be singlet under color, to preserve an exact $SU(3)_C$ symmetry (and to maintain massless gluons) while will transform non trivially under $SU(2) \times U(1)$. Since we want to give mass to three intermediate vector bosons we need to introduce at least three scalar fields with charge $0, \pm 1$. The easiest solution is to add a new $SU(2)$ doublet of complex scalar fields:

$$\Phi = \begin{pmatrix} \phi^+ \\ \phi_0 \end{pmatrix} = \frac{1}{\sqrt{2}} \begin{pmatrix} \phi_1 + i\phi_2 \\ \phi_3 + i\phi_4 \end{pmatrix} \tag{12}$$

The most general renormalizable potential we can consider for its self-interactions is:

$$V(\Phi^\dagger \Phi) = -\mu^2(\Phi^\dagger \Phi) + \lambda(\Phi^\dagger \Phi)^2 \tag{13}$$

with μ^2 and λ positive. This potential, shown in Figure 2, has an unstable local maxima at the origin and an infinity of degenerate vacuum-states lying on the circle defined by $\phi_0^2 = v^2/2$, where $v = \sqrt{\frac{\mu^2}{\lambda}}$ is the field vacuum expectation value (vev).

Since we conventionally perform perturbation theory for fields with zero vev, we can reparametrize the field as:

$$\Phi = U(x)\frac{1}{\sqrt{2}}\begin{pmatrix} 0 \\ v + h(x) \end{pmatrix} \tag{14}$$

and exploit an $SU(2)$ gauge transformation to eliminate the $U(x)$ term, reducing Φ to one single degree of freedom. By expanding the potential in the unitary gauge, we obtain:

$$\mathcal{L}_V = -\mu^2 h^2 - \lambda v h^3 - \frac{1}{4}\lambda h^4 \tag{15}$$

And we can identify $h(x)$ as the field of a scalar particle with mass $m_h = \sqrt{2}\mu = \sqrt{2\lambda}v$. After symmetry breaking it is a combination of the weak isospin and the weak hypercharge to be left unbroken. It is the electromagnetic gauge group $U(1)_{EM}$, ensuring that the photon remains massless. The conserved electric charge is defined by the Gell-Mann Nishijima relation as:

$$Q = T_3 + \frac{1}{2}Y \tag{16}$$

an expressions that also ensures a proper normalization of the weak hypercharge, that would otherwise remain arbitrary. After the Higgs acquires a vev the kinetic term of this Lagrangian is diagonal in terms of the physical fields $W^{\pm}$, A, Z. The linear combination $gW_\mu^3 - g'B_\mu$ becomes massive while the orthogonal combination remains massless and can be identified with the photon. Defining the Weinberg angle from the relation $\tan\theta_W = g/g'$ we can write them as a rotation in the (B_μ, W_μ^3) space.

$$Z_\mu = \cos\theta_W W_\mu^3 - \sin\theta_W B_\mu \tag{17}$$

$$A_\mu = \sin\theta_W W_\mu^3 + \cos\theta_W B_\mu \tag{18}$$

The expansion of their kinetic term leads instead to a mass term for the gauge bosons, plus additional interactions involving the Higgs boson.

$$\mathcal{L}_{Kin} = \frac{1}{2}(\partial_\mu h)^2 + \left[m_W^2 W^{\mu+}W_\mu^- + \frac{1}{2}m_Z^2 Z^{\mu+}Z_\mu^-\right]\cdot\left(1 + \frac{h}{v}\right)^2 \tag{19}$$

where $m_Z = M_W/\cos\theta_W$ and $M_W = gv/2$. The Z having a B component results in its coupling to right handed fermions, while the W only mediate purely left-handed interactions. At tree-level a relation holds between the gauge couplings and the boson masses:

$$\rho = \frac{M_W^2}{M_Z^2\cos^2\theta_W} = 1 \tag{20}$$

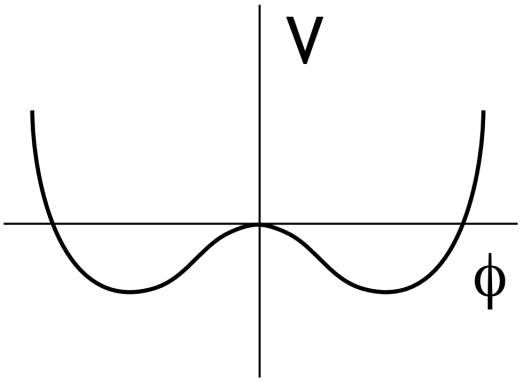

Figure 2: The Higgs boson potential in the Standard Model.

This quantity has been precisely verified with electroweak data, and an agreement with the SM prediction up to values of 10^{-3} is obtained after radiative corrections are included. The prediction of massive vector boson has also been successfully confirmed and their most precise mass measurements to date are:

$$M_W = 80.385 \pm 0.015 \text{ GeV} \quad M_Z = 91.1876 \pm 0.0021 \text{ GeV} \tag{21}$$

The Higgs boson, the last missing particle of the SM model has been finally observed at the ATLAS and CMS experiments at the Large Hadron Collider on the 4th of July 2012 [21, 22]. At the time of this writing it's mass has been measured to be about 125.1 GeV [23] and its couplings are consistent with those predicted by a SM Higgs, although deviations at the level of tenths of percent might still be possible [24]. An excellent level of consistency is found in global fits of precisely measured SM electroweak data, with the uncertainties on the indirect determination of parameters now generally smaller than the uncertainty in the direct measurement [25, 26]. A plot of the determinations of m_W versus m_t, including or not the direct measurements of m_H is shown in Figure 3.

1.4 FERMION MASSES AND MIXING

In the SM, gauge invariant mass terms for the fermions are generated through Yukawa couplings to the Higgs doublet:

$$\mathcal{L}_Y = -y_u \overline{Q}_L \tilde{\Phi} u_R - y_d \overline{Q}_L \Phi d_R - y_l \overline{L}_L \Phi e_r + \text{h.c.} \tag{22}$$

where the y_u, y_d, y_e couplings are arbitrary 3×3 complex matrices and we have introduced the charge conjugate of the Φ field, $\tilde{\Phi} = -i\tau_2 \Phi^*$. When Φ acquires a vev, from eq.22 we obtain mass terms for the quarks of the form:

$$m_u = v \frac{y_u}{\sqrt{2}} \quad m_d = v \frac{y_d}{\sqrt{2}} \tag{23}$$

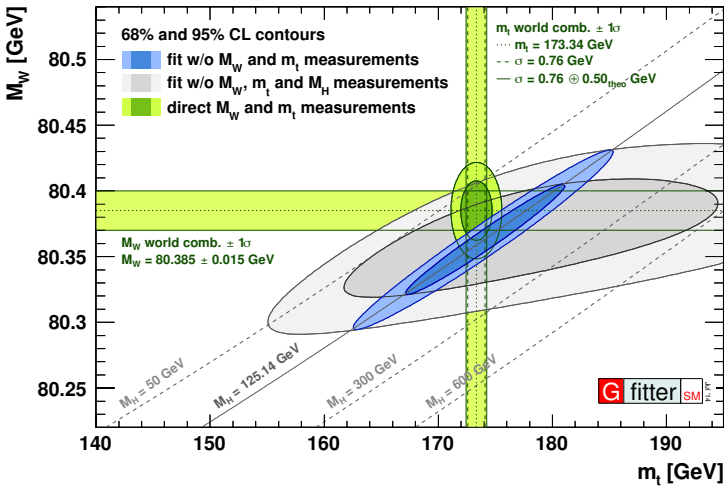

Figure 3: Contours of 68% and 95% confidence level obtained from scans of fits with fixed variable pairs M_W vs. m_t. The narrower blue and larger gray allowed regions are the results of the fit including and excluding the M_H measurements, respectively. The horizontal bands indicate the 1σ regions of the M_W and m_t measurements (world averages) [25].

The Lagrangian of Standard Model is diagonal in the weak eigenstates with a universal coupling constant. Universality is however broken when moving from the interaction basis to the mass basis necessary to obtain Lagrangian mass terms after spontaneous symmetry breaking.

$$V_{dL} m_d V_{dR}^{\dagger} = m_d^{diag} \quad V_{uL} m_u V_{uR}^{\dagger} = m_u^{diag} \tag{24}$$

The charged-current weak interactions are modified by the product of the diagonalizing matrices of the up- and down-type quark mass matrices The CKM matrix[2] is a 3×3 unitary matrix parametrizing the mixing between the three quark families.

$$V_{CKM} = V_{uL}^{\dagger} V_{dL} = \begin{pmatrix} V_{ud} & V_{us} & V_{ub} \\ V_{cd} & V_{cs} & V_{cb} \\ V_{td} & V_{ts} & V_{tb} \end{pmatrix} \tag{25}$$

After reabsorbing arbitrary phases it can be parametrized by three mixing angles and one complex CP violating phase. In the SM this is the only source of CP violation in the quark sector. The CKM elements can be obtained from measurements of semileptonic weak decays. In particular in the past decade specialized e^+e^- colliders, called B-factories, have been built and operated to allow precise measurements of the CKM parameters related to b-quark decays. The

2 First introduced by Cabibbo [27] for the case with only two quark generations and later extended by Kobayashi and Maskawa [28]

neutral-current part of the Lagrangian in the mass eigenstate basis remains unchanged; in the SM there are no flavor-changing neutral currents (FCNC) at tree level. The flavour sector of the SM has been tested in many experiments at the percent level. This puts very stringent constraints on the flavor structure of any theory of new physics.

1.5 THE QCD LAGRANGIAN

Quantum Chromodynamics [29, 30] is a Yang-Mills theory of the $SU(3)$ color charge which describes the strong interactions between quarks and gluons. The classical QCD Lagrangian is composed of a free Dirac term for the six quark fields $\mathcal{L}_{quark}$, and of a kinetic and self-interaction terms for the gluon fields G^a_μ, $\mathcal{L}_{gauge}$, minimally coupled through a gauge covariant derivative.

We first introduce the gluon field G^μ and the covariant derivative D^μ, defined as:

$$D^\mu = \partial^\mu + ig_s G^\mu \quad \text{with} \quad G^\mu = G^\mu_a T^a \tag{26}$$

where we g_S is the strong coupling constant, and the T^a are the eight generators of the $SU(3)$ group. We can now impose local gauge invariance by requiring the G^μ field to transform as:

$$G^\mu \to UG^\mu U^\dagger + \frac{i}{g_S}(\partial^\mu U)U^\dagger \tag{27}$$

And from these considerations we can build the gauge invariant kinetic term for the quark fields:

$$\mathcal{L}_{quark} = \bar{q}_j[i\not{D} - m]_{jk} q_k \tag{28}$$

$$= \bar{q}_j[(i\not{\partial} - m_q)\delta_{jk} - g_S \not{G}_a T^a_{jk}]q_k \tag{29}$$

With j is the color index and a summation over families is implied. At this point the G_μ have only the role of auxiliary fields, but we can provide them with a dynamic by adding the field strength:

$$ig_S G_{\mu\nu} = [D_\mu, D_\nu] = \partial_\mu G^a_\nu - \partial_\nu G^a_\mu - g_S f^{abc} G^b_\mu G^c_\nu \tag{30}$$

which as we can see transforms non trivially under and $SU(3)$ transformation as $G_{\mu\nu} \to UG_{\mu\nu}U^\dagger$. The f^{abc} are the structure constant of the group, which satisfy the relation $[T^a, T^b] = if^{abc}T^c$. A suitable Lorentz and gauge invariant term can now be constructed as:

$$\mathcal{L}_{gauge} = -\frac{1}{2}\mathrm{Tr}(G_{\mu\nu}G^{\mu\nu}) = -\frac{1}{4}G^a_{\mu\nu}G^{a\mu\nu} \tag{31}$$

A peculiar feature of non-Abelian gauge theories like QCD is that the gauge-bosons, the gluons, carry charge and couple to themselves. The gluon self-couplings arise from the non-linear terms in the field-strength, and are responsible for many of the non trivial features of

the theory. This Lagrangian has also important accidental symmetries: it conserves space parity, charge conjugation and the number of quarks for each flavor. Thus QCD immediately explains the fact that the strong interactions respect various symmetries that are not symmetries of all interactions.

The requirement of renormalizability poses strong constraint on the theory and in particular a mass for the gauge bosons would be forbidden. There is however one additional term, with mass dimension four or less, that we could include. By defining the dual field strength tensor:

$$\tilde{G}^a_{\mu\nu} = \frac{1}{2}\epsilon^{\sigma\tau}_{\mu\nu} G^a_{\sigma\tau} \tag{32}$$

where $\epsilon_{\mu\nu\sigma\tau}$ is the totally antisymmetric tensor with four indexes we can construct the so called θ-term:

$$\mathcal{L}_\theta = \theta \frac{g_S^2 T_F}{16\pi^2} G^a_{\mu\nu} \tilde{G}^{a\mu\nu} \tag{33}$$

The inclusion of such term in the Lagrangian would violate P and CP conservation, and in particular would give a contribution to the neutron electric dipole moment (NEDM) d_e. For a value of $\theta \sim 1$ we expect $d_n \sim 10^{-16} e \cdot cm$ [31]. The current experimental bounds [32] can however already put a constrain of $d_n < 2.9 \times 10^{-26}$ e cm, so $|\theta| < 10^{-10}$. In order to explain in a natural way such a small value of θ Peccei and Quinn [33] proposed a model in which θ is promoted to a dynamical field spontaneously relaxing to zero, thereby providing a justification for the non observation of CP violation in QCD. It was later shown [34, 35] that such a model would require the existence of a new light pseudoscalar spinless particle, the *axion*. While the axion in its original formulation has been ruled out by experiments several generalization have been proposed in which the particle coupling to matter is weak enough to have escaped current limits.

Despite it's gauge bosons being massless the strong force has a short range, and is restricted to subatomic distances. This is a consequence of two distinct features of the theory: "Confinement" and "Asymptotic Freedom".

The violations of scale invariance in quantum field theories are associated with the phenomenon of renormalization. The ultraviolet divergences appearing in radiative corrections of quantum field theories can be treated by redefining the parameters of the theory at a given scale and absorbing this way the divergences. By doing so we have introduced an arbitrary scale at which renormalization is performed, μ, and as a consequence the parameters of the theory will acquire a dependence on this scale. Physical quantities are independent on this scale, so their variations must be compensated by an explicit

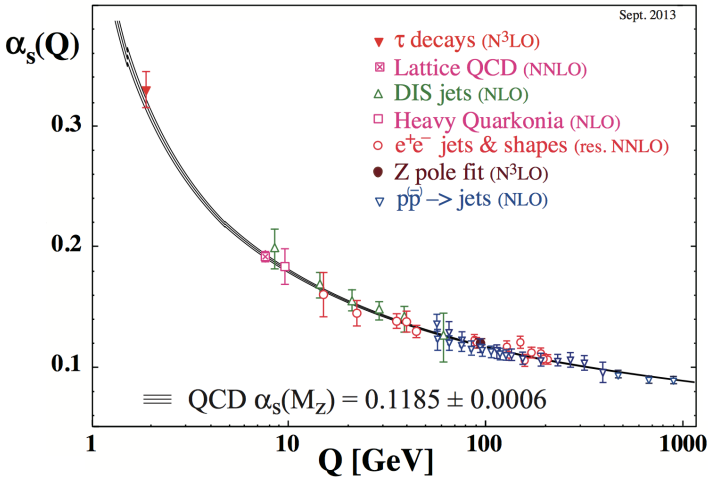

Figure 4: Summary of measurements of α_S as a function of the energy scale Q, obtained at different orders in perturbation theory [36].

dependence of the parameters of the theory on the energy scale. This variation is logarithmic, and described by the renormalization group equations (RGE).

The RGE flow for $\alpha_S = g_S^2/4\pi$ is determined by the *beta-function*:

$$\mu^2 \frac{\partial \alpha}{\partial \mu^2} = \beta(\alpha_S) \tag{34}$$

The beta function can be computed in perturbation theory, and at the 1-loop level we obtain:

$$\beta(\alpha_S(\mu^2)) = -\alpha_S^2(\mu^2)[b_0 + b_1 \alpha_S(\mu^2) + o(\alpha_S^2)] \tag{35}$$

with $b_0 = \frac{33-2n_f}{12\pi}$ and $b_1 = \frac{153-19n_f}{24\pi^2}$, where n_f is the number of active flavors at the scale of interest μ_0^2. For $n_f \leqslant 16$, as is the case in the SM, we see that the beta function has a negative sign, leading to a decreasing value of the strong coupling constant at increasingly high energies. This behavior is opposite to what found for QED, where the coupling is small at low scales and diverges at very high energies. The difference comes from the non-linear contribution of the trilinear and quartic gluon self couplings, which do not appear in the Abelian case. Retaining only the leading-order term we can rewrite eq. 35 as:

$$\alpha_S(\mu^2) = \frac{\alpha_S(\mu_0^2)}{1 + \alpha_S(\mu_0^2) b_1 \ln \frac{\mu^2}{\mu_0^2}} = \frac{1}{b_1 \ln(\mu^2/\Lambda_{QCD}^2)} \tag{36}$$

And we see that the running coupling introduces a dimensional parameter Λ_{QCD}, related to the scale at which the coupling constant becomes large and the physics becomes non-perturbative. Λ_{QCD} is not uniquely defined, as it depends on the renormalisation scheme, the number of active flavors and the order to which the beta function

is computed. At 4 loops, calculated in the $\overline{MS}$ scheme, its value is $\Lambda_{QCD}^{\overline{MS}} = 220\,\text{MeV}$. Various experimental determinations of $\alpha_S(\mu^2)$, at μ^2 values ranging from GeVs to hundreds of TeVs are shown in Figure 4

Given a dimensionless observable $\mathcal{O}$, depending on α_S and a single scale Q. From renormalizability $\mathcal{O}$ can only be a function of Q^2/μ^2 and $\alpha_S(\mu)$. It will then satisfy the RG equation:

$$\left[\mu^2\frac{\partial}{\partial\mu^2} + \beta(\alpha_S)\frac{\partial}{\partial\alpha_S}\right]\mathcal{O}\left(\alpha_S(\mu), \frac{Q^2}{\mu^2}\right) = 0 \tag{37}$$

Which has as formal solution $\mathcal{O} = \mathcal{O}(\alpha_S(Q), 1)$. Hence, any explicit dependence of $\mathcal{O}$ on μ must be canceled by the μ-dependence of α_S. The renormalized results depend on the scale at which renormalization is performed, μ_R. The scale μ_R is arbitrary in the sense that if we could compute the entire perturbative expansion or solve the theory exactly the result would be independent of μ_R. With just terms up to $n = N$, a residual dependence on μ_R will remain, which implies an uncertainty on the prediction of $R(Q)$ due to the arbitrariness of the scale choice. This uncertainty will be $O(\alpha_N + 1)$, i.e. of the same order as the neglected terms.

It is asymptotic freedom that gives QCD much of it's interesting dynamics, and allows to perform perturbative calculations at the high energies of interest at colliders. The effective strong interaction coupling constant becomes so small at short distances that quarks and gluons can be considered as approximately free, and their interactions can be treated in perturbation theory. Vacuum polarization effects occur in QCD, but the coupling is much larger and the consequences are more dramatic. This remarkable feature survives at all orders of perturbation theory.

It was the discovery of asymptotic freedom in non-Abelian gauge theories in 1973 by Grossman, Wilczek [37] and simultaneously Politzer [38] to convince theoretical physicists that QCD could be the correct theory of strong interactions. Their result immediately explained the observations of a puzzling 1968 deep inelastic electron-nucleon scattering experiment at SLAC [39, 40], indicating that strong interactions might get weaker at high energies.

Despite numerous searches, we have no evidence of free quarks or gluons. Since the gluon fields are massless we could expect the strong interactions to be long range, but this appears inconsistent with the observed short range of the color force. QCD exhibits the striking phenomenon of confinement: only colorless states are allowed as physical hadrons. As the theory is strongly coupled at low-momentum transfers the effect of increasing the energy of a quark pair is not to separate the quarks, but to create a new quark-antiquark pair from the vacuum, and thus a new hadron.

If we assign quarks to the fundamental representation $\mathbf{3}$ and antiquarks to the complex conjugate $\bar{\mathbf{3}}$ the simplest color singlet configurations we can define are

- Baryons, $\epsilon^{abc} q_a q_b q_c$ made of three quarks (e.g. one red, one blue, one green)
- Mesons, $q_a \bar{q}^a$ made of one quark and one antiquark of opposite color (e.g. red and anti-red)

Remarkably those combinations are also the only ones observed in nature.

2

THE STRUCTURE OF QCD PROCESSES

The theoretical description of the events produced in hadronic collisions is driven by our understanding of QCD. In this chapter we provide a review of the calculation techniques and phenomenological model used to obtain predictions for hadron collider physics.

2.1 INFRARED SAFETY

After renormalization, higher order QCD contributions will still contain divergences from infrared configurations arising in the real emission of a soft or collinear parton and in soft and collinear configurations of momenta in a virtual loop.

Considering the propagator for a gluon splitting into two quarks:

$$\frac{1}{(q+g)^2 - m_q^2} = \frac{1}{2E_g E_q (1 - \beta_q \cos\theta_{qg})} \tag{38}$$

we can see that eq. 38 has non-integrable divergences both when the angle between the two partons $\theta_{qg} \to 0$ in the massless limit and for the gluon energy $E \to 0$ which are mirrored also in the structure of divergences in loop diagrams. These divergences are important being responsible of the typical structure of QCD events. They induce multiple low energy or small angle emissions with respect to hard partons and determine which observables can be calculated within perturbative QCD.

Infrared and collinear safe observables are a class of quantities sufficiently inclusive not to distinguish between a final state with n and $n+1$ partons in the soft and collinear limit. An observable $\mathcal{O}$ is said to be infrared safe if the energy of subsequent emissions tends to zero and if subsequent emissions are parallel:

$$E_{n+1} \to 0 \qquad \mathcal{O}(p_1, \ldots, p_n, p_{n+1}) \to \mathcal{O}(p_1, \ldots, p_n) \tag{39}$$

$$p_n // p_{n+1} \quad \mathcal{O}(p_1, \ldots, p_n, p_{n+1}) \to \mathcal{O}(p_1, \ldots, p_n + p_{n+1}) \tag{40}$$

For such observables the Kinoshita-Lee-Nauenberg (KLN) theorem [41, 42] guarantees that, order-by-order in perturbation theory, the infrared divergences cancel when summing the real and virtual corrections. An heuristic explanation is that infrared safe observables are dependent primarily on the short distance physics, while long distance effects give only corrections suppressed by powers of the large momentum scale.

2.2 PARTON DISTRIBUTION FUNCTIONS

The basic property that enables the perturbative computation of cross sections for processes with hadrons in the initial state is their factorization into a process dependent hard scattering happening at short distances and a process independent long distance component, the parton distribution functions (PDFs), absorbing the non-perturbative physics. The hard scattering can be computed in perturbation theory, by use of the quark and gluon degrees of freedom of the QCD Lagrangian and is independent of the incoming hadron. The PDFs characterize instead the hadronic bound states and are universal (i.e. do not depend on the specific process). Thanks to universality, one can determine PDFs by using the experimental information on a particular set of processes and then use them to obtain predictions for different processes. The cross section for the production of any final state X in the collision of two hadrons h_1, h_2 can thus be written as:

$$\sigma(h_1 h_2 \to X) = \sum_{i,j} \int dx_1\, dx_2 f_{q_i/h_1}(x_1;\mu_F^2) f_{q_j/h_2}(x_2;\mu_F^2) \hat{\sigma}_{ij\to X}(\hat{s},\mu_F^2) \tag{41}$$

where $\hat{s} = x_1 x_2 s$ is the collision energy, $\hat{\sigma}_{ij\to X}$ the partonic cross section, calculated in perturbative QCD, and the f_i are the parton distribution functions, describing the probability of finding a parton of type i inside the hadron h_i carrying a momentum fraction x_1. The *factorization scale*, μ_F, is introduced to separate the soft from the hard distance physics. As with the renormalization scale, the choice of factorization scale is arbitrary, by including an infinite number of terms in the perturbative series, the μ_F dependence of the coefficient functions and PDFs will compensate each other fully. If the series is truncated at a given order N, a residual $O(\alpha_S^N + 1)$ uncertainty is associated with the ambiguity in the choice of μ_F.

Large logarithms related to gluons emitted collinear with incoming quarks can be absorbed in the definition of the parton densities, giving rise to logarithmic scaling violations which can be described via the DGLAP[1] evolution equations [44, 45, 46]:

$$\mu_F^2 \frac{df_a(x,\mu_F^2)}{d\mu_F^2} = \sum \int_x^1 \frac{dz}{z} \frac{\alpha_S}{2\pi} \hat{P}_{ba}(z) f_b(x/z,\mu_F^2) \tag{42}$$

The kernels $\hat{P}_{ba}(z)$ are the regularized Altarelli-Parisi splitting functions. At LO they have a simple interpretation in terms of the probability for a parton of type b to branch into a parton of type a carrying a fraction of momentum x/z. As for the partonic cross sections, the splitting functions can be computed perturbatively as a power series expansion in α_S. Having determined $f_a(x, Q_0^2)$ at a given input scale

1 Dokshitzer-Gribov-Lipatov-Altarelli-Parisi

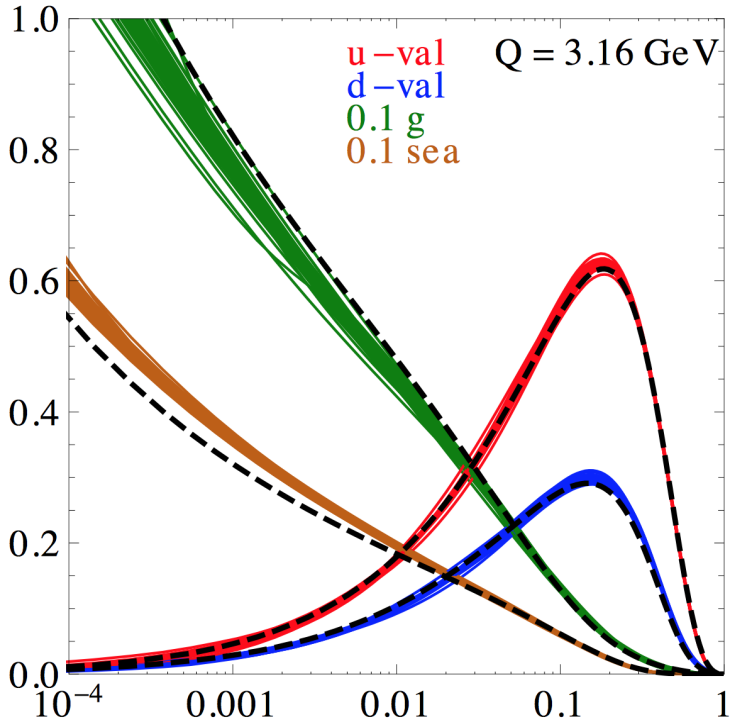

Figure 5: The central value of the parton densities (dashed black line) and their uncertainties (coloured lines) as computed with the NNLO set at $Q = 3.16$ GeV [43].

$\mu = Q_0$, the evolution equation 42 can be used to compute the parton densities at different scales μ and values of x.

At the current stage of knowledge of strong interactions, parton distributions cannot be computed from first principles. They are instead determined by comparing the PDF dependent prediction for one or more physical processes with its actual measured value over a large range of x and Q^2. In order to determine the parton distributions from data, a parametrization is assumed to be valid at some starting value $Q^2 = Q_0^2$. The DGLAP evolution equations 42 are then used to evolve the PDFs to the different Q^2 where the measurements are taken. The predictions are then fitted to the measured datasets, constraining the parameters (typically from 10 to 30) of the functional form.

Different PDF determination exists [47] differing in the choice of datasets included, the functional form used for parametrisation, the value of α_S and the treatment of heavy-quark masses. Typically fits are based on computations at different perturbative orders, both for the evolution equations and for the processes used. Among the most widely used sets are the global analyses provided by the CT [43], MRST [48] and NNPDF [49] collaborations, which make use of a large set of fixed target and collider data (mainly jets production and Drell-Yan production). Other collaborations focus on a more spe-

cific datasets, such as the HERAPDF [50], making use of the precise DIS data from HERA only, attempt to study specific effects like the description of heavy quark effects in ABKM [51] or the dynamical generation of sea quarks and gluon PDF in the JR sets [52, 53]. To obtain uncertainties on the PDF two main methods are used. In the Hessian method the χ^2 function is approximated by a quadratic form near the minimum and its eigenvectors are used as uncertainty variations. A Monte Carlo sampling method is instead used by the NNPDF group which employs neural network to obtain a more flexible data parametrization.

Several features can be observed in all of the fits. For protons, at small Q^2 and large x values above 0.1, the u quarks are the dominant distributions, more than twice as large as the d quarks at high x and much larger than the heavy quarks. At small x the valence quark densities vanish and the gluon density dominates. The sea-quark densities also increase at small x because they are driven by the strong rise of the gluon density and the splitting of gluons in $q\bar{q}$ pairs. It can be seen that the quark densities are not flavour-symmetric either in the valence sector ($u_v \neq d_v$) or in the sea sector ($\bar{u} \neq d$). All densities decrease at large x and the shape of the quark and gluon distributions at high Q^2 changes quickly at very low x.

2.3 JETS

Due to color confinement the partons produced in a hard scattering cannot be directly observed. Each of those partons will be source of additional soft and collinear parton emissions, which further undergoes hadronisation. The result of the hadronisation process is what appear as a bunch of particles, leaving collimated tracks and clusters of energy deposits in the calorimeters: a jet. In order to map the observed hadrons onto a set of jets, one uses a jet algorithm [54]. Jet algorithms cluster partons, particles or calorimeter towers based on their proximity in coordinate space (as in cone algorithms), or proximity in momentum space (k_T algorithms). A good jet definitions should be soft and collinear safe, to be calculable in perturbation theory, and be simple and with a fast implementation, to allow for usage by the experiments.

The first-ever jet algorithm was developed by Sterman and Weinberg in 1977 [55]. It defined an event as containing two jets if all the energy, excluding at most a fraction ϵ of the total, was contained in two cones of opening angle δ.

A common class of jet algorithms are the *cone algorithms* which cluster pair of particles i, j if their distance satisfies $\Delta R_{i,j} < R$, with R the jet radius. This procedure is performed iteratively, until a stable set of jets is found and jets four momenta are finally evaluated by summing the momenta of all particles falling inside the cone. Several

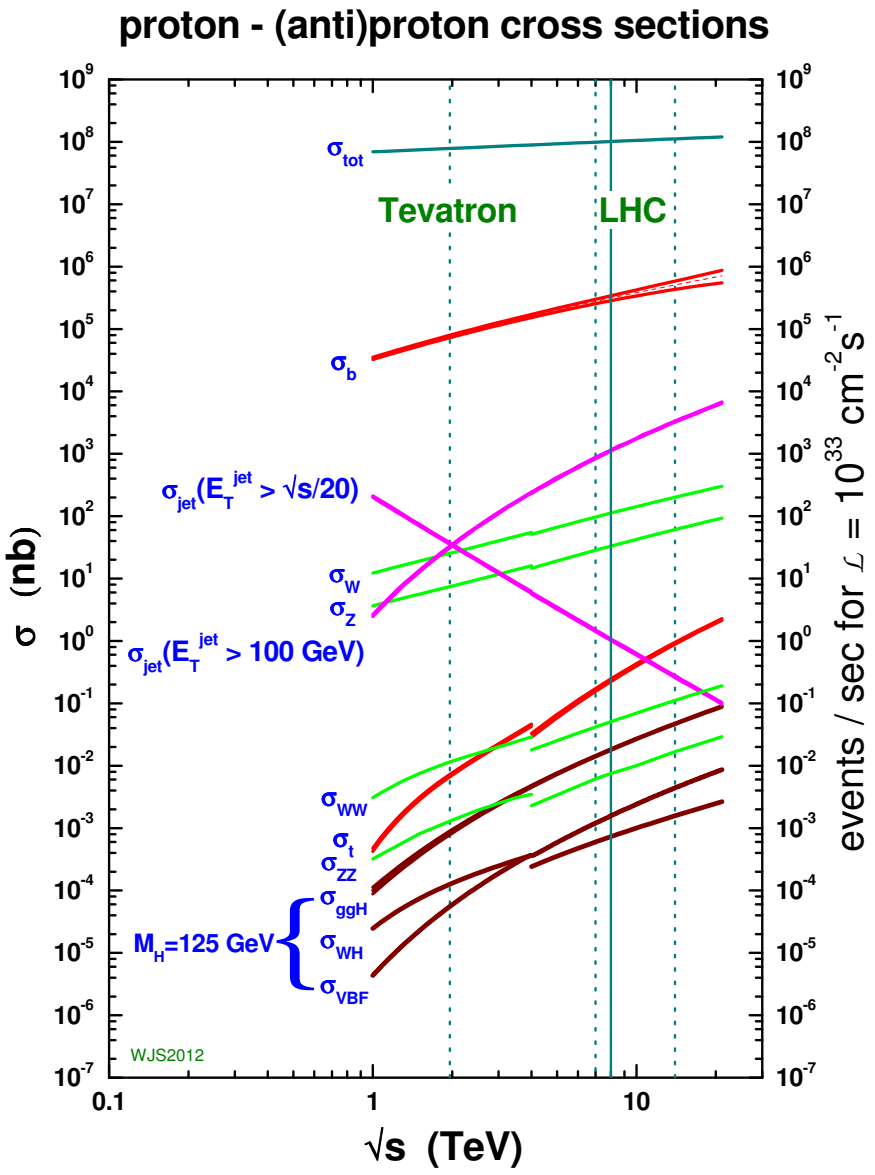

Figure 6: Cross sections for various Standard Model processes and their evolution with the center-of-mass energy. Vertical lines correspond to energies of operation of the Tevatron (1.96 TeV) and LHC (7, 8 and 14 TeV) colliders. The discontinuity in the curves reflects the change from $p\bar{p}$ to pp interactions. The cross section are calculated at next-to-leading order in perturbation theory using the MSTW2008 PDF set [48].

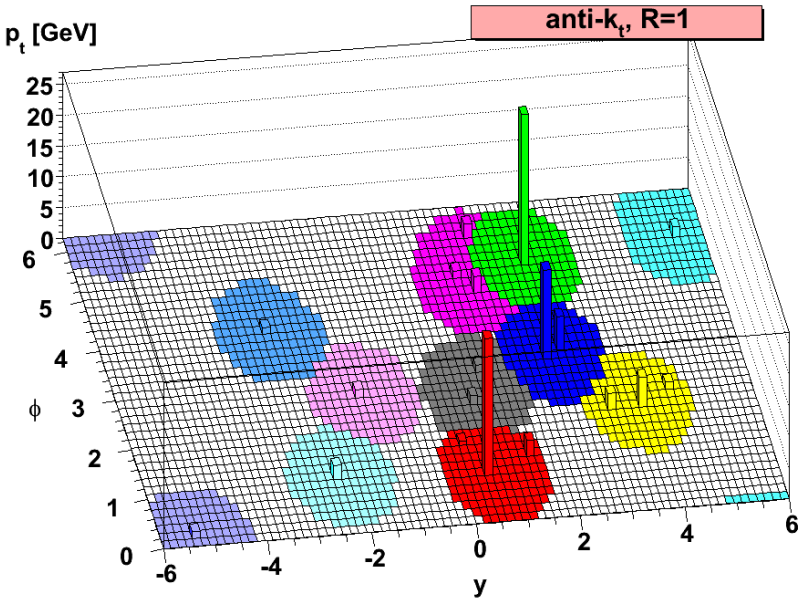

Figure 7: A sample parton-level event generated with Herwig, together with many random soft "ghost" particles, clustered with the anti-k_t jet algorithm, illustrating the catchment areas of the resulting hard jets [56].

variants exists, making use or not of seed particles, and differing in the sharing of energy for overlapping jets. Seeded cone algorithms are known to be infrared unsafe, and while popular in the Tevatron era, they are now fell into disuse.

Sequential recombination algorithms [54] are a second class of jet definitions, that try to reverse the pattern of parton emission in an iterative procedure. In contrast to the cone type algorithms, all sequential recombination algorithms are infrared and collinear safe and have rather simple definitions. They are characterized by a distance $d_{ij} = \min(k_{t,i}^{2p}, k_{t,j}^{2p})\Delta_{ij}^2/R^2$ between all pairs of particles i, j, where Δ_{ij} is their distance in the rapidity-azimuthal plane, $k_{t,i}$ is the transverse momentum with respect to the incoming beams, and R is a free parameter. They also involve a beam distance $d_{iB} = k_{t,i}^{2p}$. One first identifies the smallest of all the d_{ij} and d_{iB}, and, if it is a d_{ij}, then i and t, ij are merged into a new pseudo-particle (with a prescription for the definition of the merged four-momentum). If the smallest distance is a d_{iB}, then i is removed from the list of particles and called a jet. The parameter p determines the kind of algorithm; at the LHC experiment the anti-k_t algorithm [56], corresponding to the choice $p = -1$, has become the standard. It produces cone-like jets and is insensitive to UE and pile-up radiation.

2.4 MONTE CARLO EVENT GENERATORS

Monte Carlo event generators aim to produce simulated datasets at particle level sharing all the properties of events from real collisions [57]. In high energy physics they find widespread use in the design of new experiments, the optimization of data analyses and in estimating the expected contribution from new signals and their background. They are also used to correct for detector and selection effects and in measurements of SM parameters.

The Monte Carlo method makes use of pseudo-random numbers to simulate the event-to-event fluctuations intrinsic to quantum processes. The simulation normally begins with the hard subprocess, in which the parton constituents of the colliding particles interact at a high momentum scale to produce a few outgoing fundamental objects: SM quarks, leptons, gauge or Higgs bosons, or hypothetical particles of some new theory. The partons involved, as well as any other particle carrying colour charge, can radiate virtual gluons by bremsstrahlung, which can themselves emit further gluons or split into quark-antiquark pairs. Similarly photons can also by emitted from charged fermions. Such emissions can be modeled by parton showers algorithms. During parton showering the interaction scale falls and the strong interaction coupling rises, eventually reaching the scale of hadronisation. Phenomenological models are used to bound the partons, connected by color flux tubes, into colourless hadrons. Many of the produced hadrons are unstable, so the final stage of event generation is the simulation of the hadron decays. In hadron-hadron collisions, the other constituent partons of the incoming hadrons can undergo multiple interactions which will contribute the underlying event.

A representation of the structure of an event as produced by a MC event generator is shown in Figure 8.

2.4.1 *Hard scattering*

The decrease of the strong coupling α_S at high momentum transfer allows to compute the parton level hard scattering cross section in perturbation theory as a series expansion in powers of the strong coupling α_S:

$$\hat{\sigma}_{(i,j\to X)} = \sigma_{LO} + \alpha_S \sigma_{NLO} + \alpha_S^2 \sigma_{NNLO} + \mathcal{O}(\alpha_S^3) \tag{43}$$

where the σ coefficients are computed using Feynman diagrams. The leading-order (LO), is the first order at which the observable is not vanishing. LO predictions usually give only a qualitative understanding of the behavior of observables but fail to describe data accurately. Next-to-leading-order (NLO) calculations includes diagrams with one further power of α_S. NLO allows for a reduced depen-

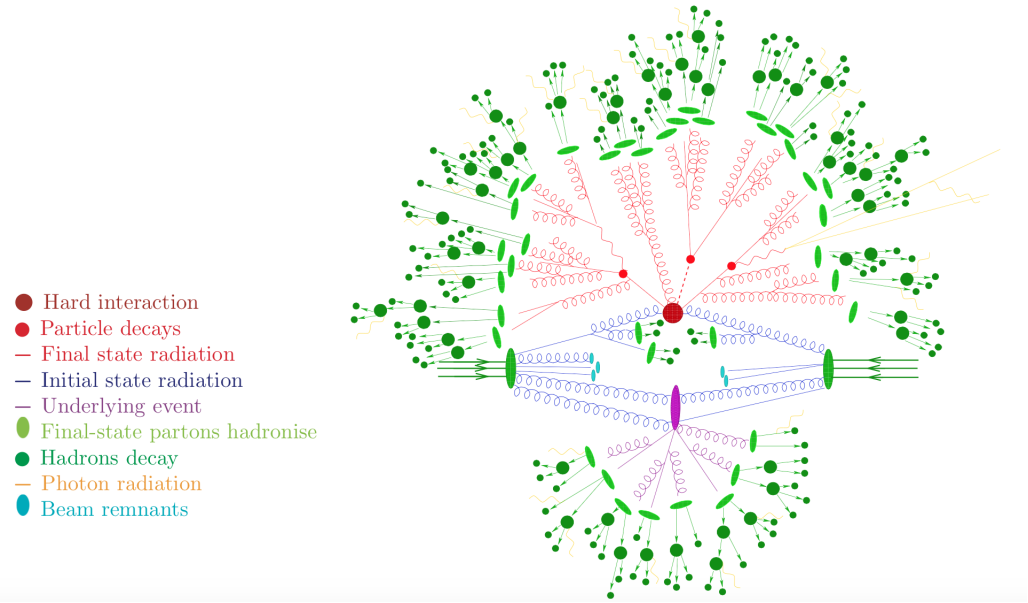

Figure 8: Pictorial representation of a $t\bar{t}h$ event as produced by an event generator [58]. The hard interaction (big red blob) is followed by the decay of both top quarks and the Higgs boson (small red blobs). Additional hard QCD radiation is produced (red) and a secondary interaction takes place (purple blob) before the final-state partons hadronise (light green blobs) and hadrons decay (dark green blobs). Photon radiation occurs at any stage (yellow).

dence on the scale choice and, as it accounts for extra radiation, for a first reliable estimate of the normalization and shape of distributions. NNLO calculations are available only for a small number of $2 \to 1$ inclusive processes (such as $pp \to H$ and $pp \to Z$); it provides a first estimate of the uncertainty, can reach an accuracy for inclusive observables of few percents and strongly reduce the dependence on the scales choice.

At LO the partonic cross-section for a $2 \to n$ process is given by:

$$d\sigma_{LO} = \frac{1}{2\hat{s}} \int d\Phi_n |M_{LO}(\Phi_n; \mu_F, \mu_R)|^2 \tag{44}$$

with $1/2\hat{s}$ the input current, $d\Phi_n$ the n-particle phase space and M_{LO} the squared matrix element (ME) for the process of interest averaged over the polarization, which will depend on the specific choice of scales. The integral is typically performed with MC methods, while many codes exists for the automatic computation of ME at LO accuracy where, depending on the process, up to ten outgoing partons can be considered.

NLO generators are used to compute infrared and collinear safe observables at one loop. They reduce considerably the uncertainty on the prediction due to scale variations. A calculation performed at

NLO is composed of the Born level term, a virtual correction and a real emission.

$$d\sigma_{NLO} = d\Phi_n \left[B(\Phi_n) + V(\Phi_n)\right] + d\Phi_{n+1} R(\Phi_{n+1}) \tag{45}$$

In addition to the ultraviolet divergences, which are treated by renormalization, the computation of an observable at NLO includes divergences in the infrared limit.

The cancellation of soft and collinear singularities in an NLO computation is typically achieved with a subtraction method. An auxiliary term is introduced, which in the soft and collinear limit is required to coincide with the amplitude of the real emission.

$$d\sigma_{NLO} = \int_{d\Phi_n} \left[B(\Phi_n) + V(\Phi_n) + \int_{d\Phi_1} S(\Phi_n)\right] + \int_{d\Phi_{n+1}} \left[R(\Phi_{n+1}) - S(\Phi_{n+1})\right] \tag{46}$$

Different methods to construct a subtraction term exists, such as dipole-factorization [59, 60], FKS [61] and antenna subtraction [62].

While we know that for sufficiently inclusive observables the real and virtual divergences will cancel, for more exclusive quantities only a partial cancellation occurs, and at each order in α_S additional logarithms of the form $L = \ln(Q^2/Q_0^2)$ appears, which can spoil the convergence properties of the perturbative series. In such cases it is convenient to perform a "resummed" calculation, accounting for the logarithmically enhanced terms to all orders in $\alpha_S \cdot L$. The first term in this series will be the leading logarithm approximation (LL), followed by the next to leading logarithm (NLL), and so on.

2.4.2 *Parton showers*

In the limit where the branching is nearly collinear, the matrix element for parton emission factorizes, so that each parton in the event at a given time can be treated as branching independently of other partons and the process that produced it. The parton shower (PS) formalism is a Monte Carlo approach to resum the soft and collinear enhanced terms to leading-log precision and is constructed by a succession of $1 \to 2$ branchings.

For quark and gluon radiation from particles in the final-state (FSR), the probability to radiate a parton in the soft or collinear limit is given by:

$$d\mathcal{P} = \frac{\alpha_S(k_T)}{2\pi} \frac{dQ^2}{Q^2} P(z) dz \frac{\Delta_S(Q^2_{max}, Q^2)}{\Delta_S(Q^2, Q_0^2)} \tag{47}$$

Where the $P(z)$ are the same DGLAP splitting functions encountered in eq.42, z is the momentum fraction of the radiated parton with respect to the emitter and Q^2 the evolution variable of the shower. In

47 $\Delta_S(Q_1^2, Q_2^2)$ is the Sudakov form-factor [63] which represents the probability of a parton evolving from the scale Q_1^2 to Q_2^2 with no resolvable emission.

$$\Delta_S(Q^2_{max}, Q^2) = exp\left\{-\int_{Q^2}^{Q^2_{max}} \frac{dk^2}{k^2}\int_{z_{min}}^{z^{max}} dz \frac{\alpha_S(z,k^2)}{2\pi} P(z)\right\} \quad (48)$$

The ratio of the form-factors represents the probability that the considered emission is exactly the first, and there is no emission between Q^2 and Q^2_{max}, where Q^2_{max} is set by the hard scattering process. Q_0^2 is instead the scale at which the shower evolution is interrupted and hadronisation begins.

The shower cross section can then be formulated in a probabilistic way. The Sudakov form factor $\Delta_S(Q_2^2, Q_1^2)$ is interpreted as the probability for a splitting not to occur, for a parton of type i, starting from a branching vertex at the scale Q_1, down to a scale Q_2. Event generation then proceeds as follows. One first gets a uniform random number $0 \geqslant r \geqslant 1$, and obtains a solution of the equation $r = \Delta_i(t_2, t_1)$ as a function of Q_2. If r is too small and no solution exists, no splitting is generated, and the line is interpreted as a final parton. If a solution Q_2 is found, a parton branching is generated at the scale Q_2. Its z value and the final parton species jk are generated with a probability proportional to $P_{i,jk}(z)$. The azimuthal angle is generated uniformly. This procedure is started with each of the primary process partons, and is applied recursively to all generated partons. It may generate an arbitrary number of partons, and it stops when no final-state partons undergo further splitting. The four-momenta of the final-state partons are reconstructed from the momenta of the initiating ones, and from the whole sequence of splitting variables, subject to overall momentum conservation. Different algorithms differ for the choice of the evolution variable (such as k_T or angle) and employ different strategies to treat recoil effects due to momentum conservation, which may be applied either locally for each parton or dipole splitting, or globally for the entire set of partons (in a procedure called momentum reshuffling).

Initial state radiation

By initial state radiation (ISR), we consider radiation emitted by the incoming partons before entering the hard-scattering process. For ISR it would be particularly inefficient to generate events evolving forwards from an initial set of partons, as the conditions to match the momenta needed in the hard scattering would not be satisfied most of the time. The development of initial state showers is thus done in a backward evolution, starting at the scale of the hard interaction and evolving to the initial partons [64, 65]. The no-splitting probability in this case is no longer given by the Sudakov form factor alone, as

given in eq. 48, but a modification factor given by the ratio of PDFs needs to be included:

$$\Delta'_S(Q_1^2, Q_2^2) = \Delta_S(Q_1^2, Q_2^2)\frac{f(x/z, Q_2^2)}{f(x, Q_1^2)} \tag{49}$$

Each ISR emission generates a finite amount of transverse momentum. Details on how the recoils generated by these transverse kicks are distributed among other partons in the event, in particular the ones involved in the hard process, constitute one of the main areas of difference between existing algorithms.

The partons inside the proton will have a certain Fermi motion, called *primordial* K_T, expected to be of order the inverse hadron radius, or few hundreds MeV. In event generators this is typically added as an additional contribution on top of the emissions generated by the initial-state shower. Tuning of this parameter to data suggests a high value of about 2 GeV, interpreted as representing not only the parton motions but also the sum of all unresolved or non-perturbative motion below the shower cutoff scale, as well as activity not accounted for in the shower model.

2.4.3 *Matching and merging*

Fixed order calculations and parton showers provide complementary descriptions of the structure of an event. Shower algorithms are only accurate in the soft and collinear region, failing to describe hard or large angle radiation. Fixed order calculations can greatly improve the precision for inclusive quantities, but are computationally expensive, are available for only a limited number of external legs and do not provide an exclusive picture of an event. Matching and merging techniques attempt to obtain the best from both approaches by providing a consistent combination of a matrix-elements fixed-order description at high momentum-transfer scales and a parton-shower one at low scales.

The first possibility is the merging of tree-level multijet matrix elements of varying multiplicity with parton showers (ME+PS) [66, 67]. The possible double counting of emissions can be avoided through a slicing of the real-emission phase space in terms of a hardness scale that regulates any infrared singularities and allows to consistently combine exclusive matrix elements of varying parton multiplicity dressed with parton showers into an inclusive sample. Several variants of LO merging techniques exist, such as MLM [68, 69] or CKKW(-L) [70, 71, 72, 73], and are now the standard approach for the simulation of multi-jet final states for LHC analyses.

Alternatively, one can perform an exact matching of an NLO QCD calculation with a parton-shower cascade off the underlying Born process (NLO+PS) [74, 75]. In this case the real-emission correction in the

fixed-order calculation has to be properly modified to account for the overlap with the first, i.e. hardest, shower splitting. Furthermore, the NLO accuracy with respect for inclusive quantities needs to be preserved. Two basic solutions exist to this problem, which are known as MC@NLO [76] and Powheg [77].

Over the last years significant progress has been made in automating these techniques [78, 79, 80] and in the development of hybrid solutions that combine either NLO+PS calculations with LO ME for higher multiplicities [81, 82] or NLO+PS calculations of varying jet multiplicity [83, 84, 85]. While such methods are expected to significantly improve the description of data for high multiplicity final states and complex observables, being still in their infancy they are not yet popular in LHC applications.

2.4.4 *Underlying Event and Multiple Parton Interactions*

In hadron-hadron scattering the "underlying event" (UE) is defined as any hadronic activity additional to what can be attributed to the hadronisation of partons involved in the hardest scatter and its initial and final state QCD radiation [86]. The UE activity is thus due to the hadronisation of partonic constituents that have undergone multiple parton interactions (MPI), as well as to beam-beam remnants[2], concentrated along the beam direction.

Modeling of these soft interactions is important because they impact all other high-p_T measurements. At higher luminosities, for example, minimum bias interactions are a major background, numbering up to 25 interactions on average per bunch crossing at LHC design luminosity. Studying the UE is critical for understanding the evolution of QCD with collision energy, as well as understanding the systematic corrections on many studies such as mass measurements. A proper model of the UE is also important for precise high-p_T measurements, since it can affect the jet E_T resolution, lepton identification and isolation quantities. While it is impossible to unambiguously separate the UE from the hard scattering process on an event-by-event basis,distributions can be measured that are sensitive to the properties of the UE. Measurements typically follow the approach pioneered at the Tevatron of selecting a leading object in each event, then used to subdivide the space in azimuthal angle into a toward, transverse and away region, sensitive to the modeling of UE [87, 88]. Several objects, such as leading track, jet, or a Z-boson events.. The three regions, shown in Figure 9, are defined according to the azimuthal angular difference, $\Delta\phi$ relative to the high-p_T object. The transverse region ($60° < |\Delta\phi| < 120°$) is assumed to be perpendicular to the axis defined by the hard $2 \to 2$ parton process and is therefore most sensi-

2 The beam-beam remnants are what is left over after a parton is knocked out of each of the initial two beam hadrons.

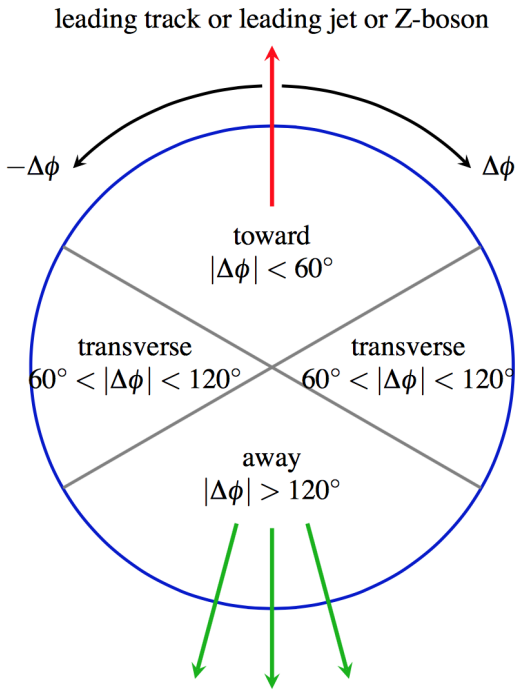

Figure 9: Definition of the toward, transverse and away regions in the azimuthal angle with respect to the leading object, used in measurements of the UE.

tive to activity coming from the UE. The toward region is defined as $|\Delta\phi| < 60°$ and the away region as $|\Delta\phi| > 120°$.

In event generators multiple parton interactions (MPI) is the basic concept driving the modelling of all inelastic non-diffractive events as well as underlying event. The dominant contribution to the QCD $2 \to 2$ process is t-channel gluon exchange which diverges at low momentum transfer, behaving as $d\sigma_{2\to2} \propto dp_T^2/p_T^4$. At LHC energies this parton-parton cross section becomes larger than the total pp cross section at p_T of order 5 GeV, violating unitarity. This can be interpreted assuming that in each pp collision multiple parton interactions can happen [89]. Assuming that all interactions are independent and equivalent the mean number of interactions is given by a Poisson distribution with mean $n(p_{Tmin}) = \sigma_{tot}/\sigma_{2\to2}(p_{Tmin})$. In practice this is described by introducing a regularization scale p_{T0}, of the order of $1.5 - 2$ GeV, removing the divergence for $p_T \to 0$ in the interaction cross section:

$$\frac{d\sigma_{2\to2}}{dp_T^2} \propto \frac{\alpha_S(p_T^2)}{p_T^4} = \frac{\alpha_S(p_T^2 + p_{T0}^2)}{(p_T^2 + p_{T0}^2)^2} \tag{50}$$

Depending on the generator, p_{T0} can be implemented as a smooth (such as in PYTHIA and SHERPA) or steep (as in Herwig++) function. The MPI cross-section in the $p_T \to 0$ limit now tends to a constant, dependent on the effective p_{T0} parameter, the value of $\alpha_S(M_Z)$ and

the PDF set used for the MPI. The MPI cut-off is also assumed to have an energy dependence of the form:

$$p_{T0}(\sqrt{s}) = p_{T0}\left(\frac{\sqrt{s}}{E_0}\right)^b \tag{51}$$

with E_0 a reference scale and b a tunable parameter.

The MPI activity is also dependent on the spatial distribution of partons inside the proton. Depending on their impact parameter b, collisions may vary from central to peripheral. The more central, the larger the overlap between the colliding partons, and the larger the average number of parton interaction per collision. The addition of an impact parameter dependence also leads to a good description of the "Pedestal Effect", where events with a hard scale have a tendency to have more underlying activity. The current models make the assumption that the dependence on the partonic momentum fraction x and on the impact parameter of the collision b factorize. Different hadronic matter distributions in the proton can be considered. A Gaussian distribution is used in the *Pythia* and Herwig [90] programs, and found to give a good description of data, but other choices, like exponential or the double Gaussian used in Sherpa, are possible.

An additional complication in the model is the description of color reconnection [91, 92], the rearrangement of the final state parton connections due to the color structure of the scattering. Such effects, still poorly understood, are typically describes with phenomenological models which rearrange the partonic configurations before hadronisation [93, 94].

2.4.5 *Hadronization*

To complete the simulation of realistic event topologies as observed in experiments, the quarks and gluons from the hard scattering, the parton shower and multiple scattering simulations must be transformed into color-neutral final states. In the context of Monte Carlo event generators this process is called hadronisation or jet fragmentation. This non-perturbative transition takes place at the hadronisation scale Q_{had}, which by construction is identical to the infrared cutoff of the parton shower. In the absence of a first-principles solution to the relevant dynamics, event generators use QCD-inspired phenomenological models to describe this transition. The two hadronisation models in use in today's event generators are the string and cluster models, both based on ideas pioneered in [95].

The cluster model

The cluster model is based on the preconfinement property of QCD [96, 97], the observation that colour-singlet clusters of partons have

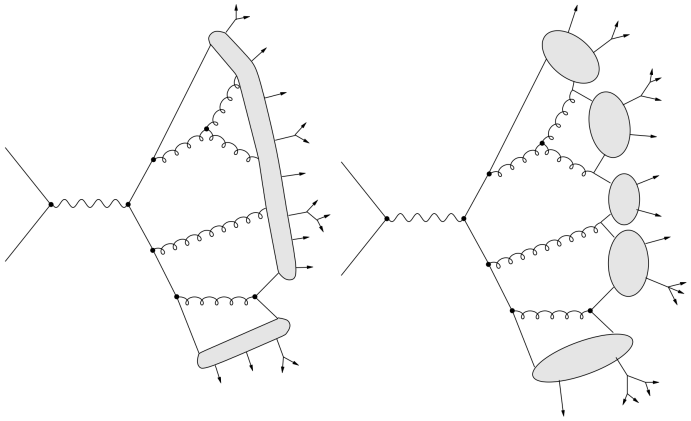

Figure 10: Illustration of the radiation pattern generated by a $q\bar{q}$ pair and the subsequent hadronisation in the string (left) and cluster (right) models.

a universal invariant mass distribution at low scales. Cluster hadronisation starts with non-perturbative splitting of gluons into quark-antiquark (and possibly diquark-antidiquark) pairs. Clusters are then formed from colour-connected pairs. These color-singlet combinations are assumed to form clusters, which mostly undergo simple isotropic decay into pairs of hadrons, chosen according to the density of states with appropriate quantum numbers. This model has few parameters and a natural mechanism for generating transverse momenta and suppressing heavy particle production in hadronisation. However, it has problems in dealing with the decay of very massive clusters, and in adequately suppressing baryon and heavy quark production. The cluster model is currently implemented in both the HERWIG++ [98] and SHERPA [99] generators.

The string model

From result obtained in quenched[3] lattice QCD simulations we know that the potential of the color-dipole field between a charge and an anticharge grows linearly with the separation of the charges, for distances greater than about a femtometer [100]. This property, known as "linear confinement", forms the basis for the string model of hadronisation [101, 102]. Due to linear confinement the potential of a moving $q\bar{q}$ pair can be approximated with a potential of the form $V(r) = kr$, with $k \approx 1$ GeV/fm. This potential is equivalent to a string with tension k.

As the q and $\bar{q}$ move apart, the potential energy stored in the string increases, and the string may break with the creation of a new $q'\bar{q}'$ pair from the vacuum, so that the system splits into two colour singlet systems $q\bar{q}'$ and $q'\bar{q}$. If the invariant mass of either of these

3 In quenched simulations no dynamical quarks can be generated, e.g. no $g \to qq$ splittings are allowed.

string pieces is large enough, further breaks occur until only on-shell hadrons remain, each hadron corresponding to a small piece of string. In general, the different string breaks are causally disconnected. This means that it is possible to describe the breaks in any convenient order, e.g. from the quark end inwards, and also include as constraint that the hadrons produced must have their physical masses. Results, at least not too close to the string endpoints, should be the same if the process is described from the q end or from the $\bar{q}$ one. This left-right symmetry constrains the allowed shape of fragmentation functions, $f(z)$, which describe how energy is shared between the hadrons. In the Lund string model, the form of the fragmentation function is [103]:

$$f(z) \propto \frac{1}{z}(1-z)^a \exp\left(-\frac{bm_T^2}{z}\right) \tag{52}$$

where z is the remaining light-cone momentum fraction of the quark (antiquark) in the $+z$ ($-z$) direction and a and b are free parameter which needs to be determined from data. A slightly modified form is introduced for heavy quarks [104]. The transverse motion of the newly created quarks/antiquarks is parametrized as a quantum mechanical tunneling effect, with probability proportional to:

$$\exp\left(-\frac{\pi m_T^2}{k}\right) = \exp\left(-\frac{\pi m^2}{k}\right) \cdot \exp\left(-\frac{\pi p_T^2}{k}\right) \tag{53}$$

The factorization of mass and transverse momentum dependence leads to a flavour-independent transverse momentum spectrum of the hadrons and to a natural of heavy-flavour hadrons. Gluons produced in the parton shower give rise to "kinks" on the string. The string breaks up into hadrons via qq pair production in its intense color field. Baryon production can also be introduced in the model. The simplest scheme is to allow the production of antidiquark-diquark pairs the field, in a triplet-antitriplet representation. More advanced scenarios for baryon production have also been proposed, in particular the so-called popcorn model [105] with a sequential production of several qq pairs that subsequently combine into hadrons. The string model has extra parameters for the transverse momentum distribution and heavy particle suppression. It has some problems describing baryon production, but less than the cluster model. It is currently implemented in the Pythia event generator [101, 106].

2.4.6 *Particle decays*

Many of the hadrons produced during hadronisation (primary hadrons) have very short lifetimes and they decay before hitting the first detector layer of a typical collider experiment. The last step in a generator program is to let these unstable particles decay.

The information on the decay tables is usually taken from the PDG review [36]. However, for many particles the data can be incomplete or too inaccurate to be used, and specific choices are taken by each generator. In particular it can happen that not all resonances in a given multiplet have been observed, or that the branching fractions of a given particle do not exactly add to 100% More sophisticated simulation of hadronic decays can also be performed using specialized "afterburner" packages that reweigh the generator event record, such as EvtGen [107] for hadron decays and TAUOLA [108, 109] for tau decays.

2.4.7 *Tuning*

Each MC generator comes with a number of free parameters (usually related to the modeling of the soft and non-perturbative physics) which are not constrained by first principle and need to be determined from data, in a process referred to as *tuning*. While the number of parameters in a generator can be large (and more than 30 in some cases), the majority of the physics is determined by only a few, very important ones. These are the value of α_S in the initial- and final-state shower, the properties of the non-perturbative fragmentation functions, and the parameters related to the modeling of the soft-physics and UE.

It is normally assumed that each model controls only a small part of the event generation and that a factorized approach can be used, tuning each subset of the model parameters separately. A tune would typically start from the hadronisation and FSR parameters using the clean LEP measurements, and then use Tevatron and LHC data to constrain the modeling of the ISR and MPI.

Because of the large and varied data sets available, and the high statistics required mounting a proper tuning effort can therefore be quite intensive often involving testing the generator against the measured data for thousands of observables, collider energies, and generator settings.

Traditionally tunes have been performed manually, MC predictions for suitable observables are generated for a set of parameter values and their agreement with data is evaluated by personal judgment. Manual tuning typically requires significant insight in the generator models and, requiring many iterations, is intrinsically slow. In recent years more automated methods have been developed in an attempt to reduce the need in computing power and the overall complexity of performing tunes [110, 111]. The Professor code [110], in particular, has allowed to perform many successful generator tunes and it has been used in most of the tunes performed by the LHC experiments. It allows simultaneous tuning of a large number of parameters by approximating the MC response to the parameters analytically, using a

parametrisation fitted to generator runs at randomly sampled points. The optimal values for the parameters can then be obtained with a numerical minimization of a goodness-of-fit function using MINUIT [112].

The precision measurements made available with the start of the LHC, and the need for a more accurate description of the data have outlined several shortcomings of current tunes.

MC models are expected to be universal, and the same set of parameters, should be able to describe various processes at different energies and collider types. Global tunes are performed with the goal of obtaining a good overall description of the data, but little emphasis is placed on tensions and disagreements in specific distributions. Specific tunes, focused on a limited set of observables, provide a stringent test of the universality of the resulting parameters, and a powerful check of the validity of the underlying physics model.

A tune can be of little usefulness, without proper estimates of the uncertainties on the parameters, which only recently start to be available. The uncertainties can be determined by tuning to different but redundant observables, or different observable ranges, or by allowing a limited deviation from the optimal parameters. Professor allows the creation of deviation tunes, *eigentunes*, obtained by defining the principal directions around the parameters minima and moving out from the best tune point of a given goodness-of-fit distance.

Little explored is also the effect of performing tunes to PS matched setups, either to LO multijet or NLO matrix elements. The hadronisation and MPI parameters are expected to be universal and largely unchanged in the presence of matching. However, QCD higher order corrections affect some of the observables used for the tuning, and, in particular, there are theoretical arguments to expect the value of α_S in the shower to be different in multijet LO matching.

3

THEORIES OF NEW PHYSICS

We review here the main limitations of the Standard Model of particle physics and the most promising theories that have been proposed as its possible extensions, namely Supersymmetry and theories with extra dimensions or composite Higgses.

3.1 OPEN PROBLEMS IN THE STANDARD MODEL

Despite being extremely successful in describing the physics of strong, weak and electromagnetic interactions up to energies of several hundreds GeV, a number of experimental observations and theoretical arguments make us believe that the SM is only a low energy effective approximation of a more complete theory manifesting itself at higher energies.

- The Standard Model completely lacks an explanation for gravity. A massless spin-2 particle, the graviton, could give an effective description of the gravitational interactions, but no theory valid up to high energy exists.
- The established existence of neutrino masses requires at least the addition of an ν_R state in the Lagrangian, if the masses are Dirac, or, more likely, some new physics at a high energy to account for Maiorana type masses.
- Assuming that the universe can be described by an effective quantum field theory up to Planck energies we can compute the value cosmological constant. This determination is larger than what is observed by more than 120 orders of magnitude.
- The SM is completely specified with nineteen input parameters[1] These parameters and their hierarchy are not explained by the theory, suggesting the existence of a deeper structure.
- Matter and antimatter are expected to have been produced in equal amounts during the creation of the universe. The fact that the present day universe is mostly constituted by matter is an unexplained phenomenon. The violation of CP in electroweak interactions is a known source of baryon asymmetry but its amount is insufficient to fully explain baryogenesys.

1 The three charged lepton masses, six quark masses, the gauge couplings strength, three quark-mixing angles and a complex phase, a Higgs mass and quartic coupling and the value of the QCD vacuum angle

- The absence of CP violation in the strong sector, see Section 1.5, is another source of unexplained fine-tuning in the SM that might be clarified in SM extensions.

Of the many unexplained issues three of them play a special role in the development of theories with new states at electroweak energies. These are the gauge coupling unification, the existence of Dark Matter and the hierarchy between the electroweak and gravity scales. Given their relevance they are further discussed in separate sections below.

3.1.1 *Dark matter and dark energy*

There is a strong evidence that most of the matter in our universe is non luminous. The first indications came from measurements of the rotational speeds of galaxies [113] and the orbital velocities of galaxies within galaxy clusters [114]. More recently the existence of dark matter has been inferred from gravitational lensing [115, 116], the analysis of the cosmic microwave background [117, 118], primordial nucleosynthesis [119] and large scale structures in the universe [120].

Among the large number of dark-matter candidates that have been proposed [121, 122] particularly motivated are particles which are heavy, electrically neutral and weak interacting (WIMPs). Assuming thermal equilibrium of DM and SM particles in the very early universe we can use the Boltzmann equation to compute the dark matter density after decoupling, the so called "thermal relic density", from which we can derive the current fraction of energy in the Universe carried by dark matter [123]:

$$\Omega_\chi h^2 = \frac{s_0}{\rho_c/h^2}\left(\frac{45}{\pi g_*}\right)^{1/2}\frac{x_f}{M_{Pl}}\frac{1}{\langle\sigma_{\chi\chi}v\rangle} \tag{54}$$

where s_0 is the current entropy of the Universe, ρ_c the critical density, h the Hubble constant, g_* the effective number of relativistic degrees of freedom at freeze-out, M_{Pl} the Planck mass, $x_f = m/T_f \sim 25$ the inverse freeze-out temperature in units of the WIMP mass and σv the thermal average of the dark matter pair annihilation cross-section multiplied by the relative velocity.

If we require this process to produce the entire observed thermal abundance of dark matter [118] the thermally averaged annihilation cross-section is required to be $\langle\sigma_{\chi\chi}v\rangle \simeq 3\times10^{-26}$ cm^{-3} s^{-1} (0.9 pb). Remarkably this value is very close to the range of cross-sections for particles annihilating through exchange of electroweak gauge or Higgs bosons. In particular from $\langle\sigma_{\chi\chi}v\rangle = \pi\alpha^2/8m^2$ we can infer a mass for the WIMP of order $m_\chi \sim 100$ GeV. We are thus highly motivated to search for dark-matter particles with electroweak interactions and a mass close to the EWSB scale.

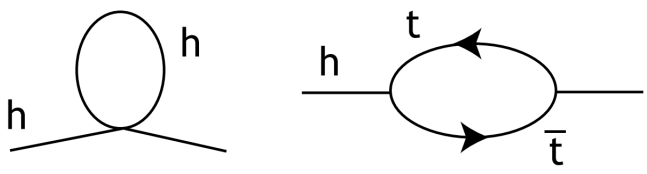

Figure 11: SM diagrams contributing to the radiative corrections to the Higgs boson mass exhibiting quadratic divergences.

3.1.2 *Naturalness and fine-tuning*

The SM is a renormalizable theory, and we expect that even if we extend to infinity the cut-off of virtual momenta running in the higher order corrections we would retain finite results. Electroweak symmetry is spontaneously broken in the SM, by the introduction of the single elementary Higgs boson field. This explanation however has an important shortcoming. The Higgs field potential in the SM is:

$$V = \mu^2|\Phi|^2 + \lambda|\Phi|^4 \tag{55}$$

And the single assumption that $\mu^2 < 0$ is enough for a complete explanation of EWSB. But since μ^2 is a renormalizable coupling of the theory the value of μ cannot be computed from first principles and even its sign cannot be predicted. This model has an even worse feature: the μ^2 parameter receives large additive radiative corrections from loop diagrams. As an example both diagrams shown in Figure 11 (Higgs self renormalization and top loop) exhibit a quadratic divergence in the ultraviolet. If we cut-off the momentum integral in the UV, at a scale Λ^2, their contributions become:

$$\mu^2 = \mu^2_{bare} + \frac{\lambda}{8\pi^2}\Lambda^2 - \frac{3y_t^2}{8\pi^2}\Lambda^2 + \cdots \tag{56}$$

where y_t is the Yukawa top-Higgs coupling. The radiative corrections in eq.56 can easily change the sign of μ^2, and if we insist that the SM is valid up to high scales the corrections quickly become larger than the tree-level result. To obtain the Higgs field vev required for the weak interactions, $|\mu|$ should be of order 100 GeV. The highest energy at which we can expect the SM to work is the Planck scale, $M_{Pl} = 10^{19}$ GeV, where gravitational effects become important. The formula 56 requires then cancellations between the bare value μ and the radiative corrections in the first 36 decimal places. This problem, referred to as the "gauge hierarchy problem" is one of the most compelling reasons to assume some New Physics should appear at a scale $\Lambda << M_{Pl}$.

To prevent the Higgs mass to be pushed to the Planck scale a physical principle should imply $\mu^2 = 0$ at leading order of some expansion.

2 If we view the SM as an effective theory Λ should be considered the largest scale at which the theory is assumed to be valid.

This is the case for fermions and bosons that do not exhibit the same problem, as gauge symmetries can protect them. However there is no such symmetry that protects the Higgs boson in the SM. Three main class of symmetries are considered to avoid large corrections to the Higgs mass term:

$\delta\phi = \epsilon \cdot \phi$ The Higgs field can mix with a fermion field, whose mass is forbidden by a flavor symmetry.

$\delta\phi = \epsilon_\mu A^\mu$ If we relate the Higgs field to a vector (gauge) field, a mass term is forbidden by gauge invariance.

$\delta\phi = \epsilon$ Forbid the Higgs mass term by a shift symmetry.

The first possibility is the basis of Supersymmetry (which introduces scalar tops and fermionic W, Z, h), the second leads to extra spatial dimensions and the last to Higgs as a pseudo Goldstone boson (introducing fermionic tops and scalar W, Z, h).

In all of these theories there are residual contributions to the Higgs mass as the cancellation of the quadratic divergences is not exact. The amount of this "fine-tuning" to be considered acceptable is a subjective matter (there are examples in nature of quantities fine tuned to $o(10^{-1})$). A theory is usually considered "natural" if it has a fine-tuning not below the percent level, i.e. not higher than few TeVs.

3.1.3 *Grand Unification*

Grand Unified Theories (GUT) are a tentative to embed the symmetry groups of the SM into a large symmetry group G. The first approach of this kind has been taken by Georgi and Glashow [124] using the group $SU(5)$, shortly after the SM development. At higher energy scales this symmetry is supposed to be unbroken and all interactions can be described by a local gauge theory with coupling α_G. Combining quarks and leptons into the same representation also allows to explain charge quantization. The model predicts also new interactions mediated by super-heavy X,Y gauge bosons that relate quarks with anti-leptons and anti-quarks. The new interactions are lepton and baryon number violating (but $B - L$ is conserved), and could mediate proton decay [125]. A typical mode is $p \to e^+\pi^0$ with an expected lifetime of:

$$\tau_p \sim \frac{M_X^4}{\alpha^5 m_p^5} \sim 10^{29}\,\mathrm{yr} \tag{57}$$

if we assume $M_X \sim 10^4$ GeV. The current limits from water-cherenkov experiments however rule out this value and so $SU(5)$ GUT. Other symmetry groups, like $SO(10)$ [126] or E_6 could still be compatible with the experiment, but the current consensus is for GUT to be realized in the context of supersymmetric theories [127, 128].

3.2 SUPERSYMMETRY

Among the many proposed theories of New Physics, Supersymmetry, a space-time symmetry between bosons and fermions, has emerged as the leading candidate. SUSY is both strongly motivated on theoretical grounds and provides a rich phenomenology, making it a useful benchmark for experimental searches. Some of the reasons that have made Supersymmetry so popular are:

- It helps stabilizing the mass scale of electroweak symmetry breaking, by cancelling the quadratic divergences to the Higgs boson mass, thus solving the hierarchy problem.
- The lightest supersymmetric particle can, in some SUSY scenarios, be made stable, and being heavy and naturally neutral, is excellent candidates for DM.
- Including SUSY particles in the RGE for the gauge couplings of the SM allows to unify them at high scales (if the SUSY scale is below 10 TeV).
- The observation of a light Higgs boson can be accommodated by the theory.
- Supersymmetry is a highly predictive theory with a various and rich phenomenology, testable at LHC energies.
- It can be a valid theory up to very high energy scales, near the Planck scale, and is not sensitive to new states at higher scales.
- Low energy Supersymmetry is strongly favored in string theory scenarios.

3.2.1 *The Supersymmetry algebra*

A very powerful result from the early days of quantum field theory is the Coleman and Mandula [129] no-go theorem, stating that any further tensor external symmetry to the Lorentz group must be trivial. Shortly after it was however realized that the Coleman-Mandula theorem only considers symmetries involving bosonic generators, and does not apply to conserved charges transforming as spinors. A class of such symmetries are Supersymmetries, that involve transformations changing bosons into fermions. An internal symmetry relating bosonic and fermionic hadrons was first proposed in 1966 in a largely ignored paper by Miyazawa [130] . Supersymmetries were later reintroduced in the context of string theory. In the 70s several groups, both in the US (Gervais and Sakita) [131] and in the Soviet block (Golfand and Likhtman) [132] in 1971 and (Volkov and Akulov) in

1972 [133], all independently introduced the concept of Supersymmetry as a space time symmetry of quantum field theories. In 1974 Wess and Zumino produced the first example of an interacting QFT model in four dimensions including Supersymmetry. Their model [134, 135] used the simplest representation of the algebra, the massless chiral supermultiplet (consisting of a complex scalar ad a spinor fermion).

It was later shown by Haag, Lopuszanski and Sohnius [136] that Supersymmetry is the only possible external symmetry beyond the Lorentz Symmetry for which the scattering amplitudes are not trivial, making it the unique maximal external symmetry possible in nature.

The simplest Supersymmetry version ($N = 1$) involves a single Weyl spinor operator Q_α and its complex conjugate $Q^\dagger_\alpha$. By defining Q_α and $Q^\dagger_\alpha$ the generators of the Supersymmetry transformations we can completely characterize the supersymmetric algebra by adding to the Poincare' algebra the following relations:

$$[P^\mu, Q_\alpha] = 0 \quad [M^{\mu\nu}, Q_\alpha] = -i(\sigma^{\mu\nu})^\beta_\alpha Q_\beta \tag{58}$$

$$\{Q_\alpha, Q_\beta\} = 0 \qquad \{Q_\alpha, Q^\dagger_\beta\} = 2(\sigma^\mu)_{\alpha\beta} P_\mu \tag{59}$$

where P^μ is the four-momentum vector, $\sigma^\mu = (1, \sigma^i)$, $\bar\sigma^\mu = (1, -\sigma^i)$ the Pauli matrices and $\sigma^{\mu\nu} = (\sigma^\mu\bar\sigma^\nu - \sigma^\nu\bar\sigma^\mu)/4$. We can see how the operator Q raises the spin by $1/2$, while $Q^\dagger$ lowers it by $1/2$.

3.2.2 *The Minimal Supersymmetric Standard Model*

In 1981 a first supersymmetric version of the SM [137] was proposed, addressing the hierarchy problem and predicting superpartner masses in the range of 100 GeV to 1 TeV.

In the Minimal Supersymmetric Standard Model (MSSM) all the left-handed fermions and anti-fermions are promoted to chiral super multiplets denoted, as L, Q, e^c, d^c and u^c, with all gauge and family indexes suppressed, which will include their scalar supersymmetric counterparts, squarks and sleptons. Conventionally the right handed fermion fields e^c (and d^c, u^c) are represented through their charge conjugates, which transform as left-handed spinors. The SM gauge fields are assigned to vector super multiplets, whose component expansion contains their fermion partners, the gauginos. In order to avoid a triangle anomaly, the Higgs supermultiplets must appear in pairs with opposite hypercharges, and the minimal possibility is to add a single pair, H^i_u, H^i_d.

$$H_u = \begin{pmatrix} H^0_u \\ H^-_u \end{pmatrix} \quad H_d = \begin{pmatrix} H^+_d \\ H^0_d \end{pmatrix} \tag{60}$$

The minimal super-potential needed to accommodate all the Yukawa couplings and mass terms is:

$$W = \epsilon_{ij}(y_e H_u L e^c + y_d H_u Q d^c + y_u H_d Q u^c + \mu H_u H_d) \tag{61}$$

where the Yukawa couplings y, are dimensionless 3×3 matrices in generation space. The term $\mu H_u H_d$, which is not present in the SM, gives rise to masses for the Higgsinos (Higgs boson superpartners). The physical Higgs spectrum contains five states (while three degrees of freedom are absorbed in EWSB): two charged Higgses $H^{\pm}$, two neutral Higgs scalars h, H, and a pseudo-scalar A.

In the same fashion as in the SM, the charge neutral Higgsinos and charginos (called binos and winos) will mix to form four neutralinos $\tilde{\chi}_1^0, \tilde{\chi}_2^0, \tilde{\chi}_3^0, \tilde{\chi}_4^0$. Similarly the charged higgsinos and winos mix into two charginos $\tilde{\chi}_1^{\pm}, \tilde{\chi}_2^{\pm}$.

There are additional terms that one could add in the super-potential that are analytic, gauge and Lorentz invariant, but lead to baryon and lepton number violation[3].

$$W_R = \frac{1}{2}\lambda \epsilon_{ij} L^i L^j e^c + \lambda' \epsilon_{ij} L^i Q^j d^c + \frac{1}{2}\lambda'' \epsilon_{ij} u^c d^c d^c + \mu' L^i H_d^j \quad (62)$$

the terms proportional to λ, λ' and μ' violate lepton number by one unit, whereas the term proportional to λ'' violates baryon number by one unit.

The lack of observed baryon and lepton number violations means that these terms are either absent or the production coefficients are very small. In particular a non-zero λ' and λ'' would lead to the proton decay process $p \to e^+\pi^0, \mu^+\pi^0, \nu\pi^+, \nu K^+, \ldots$ Given the current limits on proton decay, e.g. [138], the product of λ' and λ'' must be very small, or exactly zero.

To eliminated these unwanted superpotential terms a common (but not unique) solution is to postulate a discrete Z_2 symmetry on the theory called R-parity, which can be represented as:

$$R = (-1)^{3B+L+2s} \quad (63)$$

with B, L and s baryon number, lepton number and spin respectively. With this definition all SM particles have R-parity $+1$, while SUSY particles -1. If R-parity is exactly conserved then all the superpotential terms in 63 must vanish. This has several important phenomenological consequences:

- The interaction of SM particles can produce only pairs of SUSY particles, and heavier SUSY particles can decay only into lighter SUSY particles.
- The lightest supersymmetric particle (LSP) can then only be stable, making it a natural candidate for DM. The DM energy density would be in the right ballpark of cosmological observations if the SUSY scale is around the TeV.
- In collider experiments we expect large missing energy from the LSP escaping the detectors volume undetected.

3 No such term is allowed in the SM, which accidentally conserves B and L to all orders in perturbation theory.

3.2.3 *Supersymmetry breaking*

If SUSY would be an exact symmetry in nature, we expect SM particles and their superpartners to be degenerate in mass. Since no such pair of particles has been observed if Supersymmetry is realized in nature it must be a broken symmetry at low energies.

The mechanism whereby SUSY is broken is unknown and usually phenomenological ansatz are used. Similarly to the SM, in which it is not possible to break EW symmetry from within and we are forced to introduce the Higgs sector, it is also not possible to break supersymmetry in the "visible" sector of SM particles and their superpartners. A separate (so called "hidden") sector is needed in which the breaking happens, and some interaction to transmit the breaking to the visible sector. Gravity, which will affect the particles of both sectors, can always be the messenger of SUSY breaking [139]. Other known mechanisms invoke the SM gauge interactions [140, 141] or anomalous $U(1)$ groups [142, 143].

In particular by promoting Supersymmetry to a local symmetry (SUGRA) we automatically obtain a description of general relativity, which allows to embed SUSY in a unified theory valid up to the Planck scale. The massless gauge field associated with local supersymmetry is a spin 3/2 fermion, the gravitino, in the same supermultiplet we need to include a spin-2 particle, which we can identify with the graviton.

Irrespective on the specific breaking mechanism, the effective Lagrangian at the electroweak scale can be parameterized by a general set of additional terms. As we do not want to spoil the Supersymmetry's solution to the hierarchy problem we only consider operators that do not reintroduce quadratic divergences in the theory, so-called *soft-breaking terms* [144].

Soft SUSY breaking is the source of many new terms and parameters in the MSSM. In particular we can include a soft mass term for the gauginos $M_{\frac{1}{2}}\chi\chi$ and the scalars (squarks and sleptons) $M_0^2\phi\phi^\dagger$, a trilinear couplings $A_{ijk}\phi_i\phi_j\phi_k$ and a bilinear Higgs mass terms $B_{ij}\phi_i\phi_j$.

After breaking we end up with 111 parameters, that can be reduced to 105 independent parameters with the redefinition of some of the fields. These parameters include masses, mixing angles, and phase combinations invariant under reparametrizations.

Gauge coupling unification is found to work extremely well if we ask the GUT theory to satisfy Supersymmetry at low energies. SUSY modifies the RGE above the superpartners mass scale, and the couplings are found to unify at a scale of 10^{16} GeV. A comparison of the couplings evolution in the SM and MSSM is shown in Figure 12. This is in contrast with standard GUT theories 3.1.3, in which the

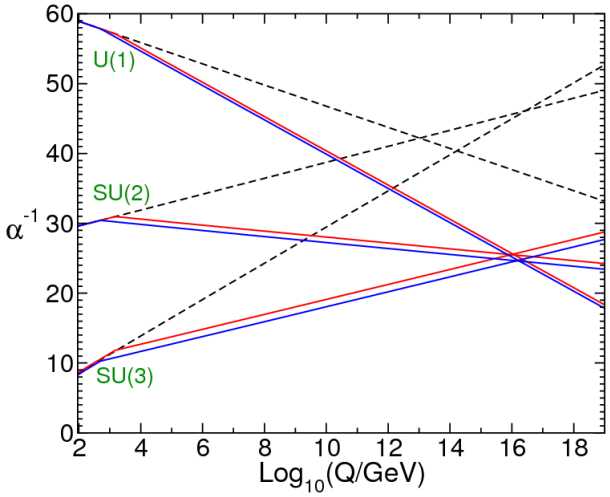

Figure 12: The two loop evolution of the inverse gauge couplings $\alpha_a^{-1}(Q)$ in the SM (dashed lines) and in the MSSM (solid lines). From [145]

couplings miss by 12 sigma, and the addition of new weak states is needed.

The phenomenology of the Higgs sector in the MSSM can be described entirely by two parameters, one Higgs mass that is usually taken to be that of the pseudoscalar A boson M_A and the ratio of the vacuum expectation values of the two doublet fields, $\tan\beta$. From Supersymmetry breaking we can now derive an important prediction on the mass of the lightest Higgs boson. By denoting the vev's of the two Higgs bosons as $< H_u >= v_u$ and $< H_d >= v_d$ we can write:

$$m_h^2 \simeq \frac{1}{4}(g + g'^2)(v_d^2 - v_u^2) \tag{64}$$

Which can be rewritten as $m_h^2 = M_Z^2 \cos\beta$, implying that the tree-level mass of the Higgs boson should be lower than 91 GeV. After including radiative corrections the Higgs mass increases, but is generally expected to stay lower than 150 GeV for generic supersymmetric theories.

To overcome the difficulties of dealing with such a high dimensional parameter space many of the phenomenological analyses of the MSSM assume that the 105 parameters at take on simplified forms at high scales. A very popular model is the Constrained MSSM (CMSSM) [146] where the simplification of the soft parameters is inspired by simple supergravity models.

- All the scalar masses are the same m_0 universal scalar mass parameter. Called *universality* of scalar masses.
- The gaugino masses are all the same $m_{\frac{1}{2}}$ universal gaugino mass parameter, Referred as the *GUT relation* as it's generally true in grand unified theories.

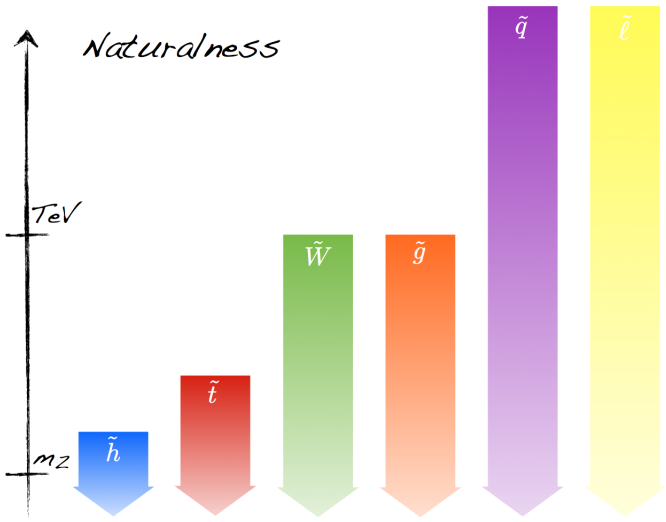

Figure 13: Illustration of the mass scales for various particles in a low fine-tuning supersymmetric scenario, as expected by electroweak naturalness arguments, from [149].

- The assumption of *proportionality*; the soft breaking cubic terms are assumed to be:

$$\mathcal{L}_{tri} = A(H_U Q y_u \bar{u} + H_D Q y_d \bar{d} + H_D L y_l \bar{e}) \tag{65}$$

With those assumptions the SUSY space is reduced to only five parameters. These are the universal scalar (m_0) and fermion ($m_{1/2}$) masses, the universal soft trilinear coupling A_0, $\tan\beta$ and $\mathrm{sign}(\mu)$, the sign of the supersymmetric Higgs parameter relative to A_0. While extremely practical from a phenomenological point of view, the CMSSM assumptions are very restrictive and somewhat arbitrary.

A different, bottom-up approach that recently gained popularity is the phenomenological MSSM (pMSSM) [147, 148], in which by applying only few, experimentally driven conditions, the SUSY space can be reduced to only 19 parameters without having applied much theoretical prejudice.

3.2.4 *A natural spectrum*

The Higgs discovery has important consequences for supersymmetric theories. The rather heavy mass of 125 GeV observed for the SM Higgs boson requires large radiative corrections, nearly as large as the tree-level contribution, mostly coming from the top-stop sector. If we refrain from adding new degrees of freedom to the theory there are only two ways in which the observed Higgs mass can be accommodated in the MSSM. Both suggests that squarks soft masses might not be flavor degenerate.

As the radiative corrections to the Higgs mass are driven by the stop-top loop a simple solution is to require the stop to be heavy, with a mass larger than 4 TeV. This would however completely spoil naturalness, with fine-tuning at the per mill level.

An alternative possibility is to require the quantity $X_t = A_t - \cot\beta$, parametrizing the stop left-right mixing, to be maximal. In this case, which is however also fine-tuned in the A_t parameter, we can reduce the lower bound on the stop mass at about 1 TeV. The typical allowed range for SUSY particle masses in a model with low fine-tuning is shown in Figure 13

3.3 EXTRA DIMENSIONS

A different class of New Physics theories can be obtained assuming the existence of additional space-time dimensions in addition to the four we know about. As these dimensions are not visible they must either be very small, or possess a non trivial topological structure. Theories with extra dimensions arise naturally when attempting to quantize gravity (string theory requires at least a ten dimensional space), can provide a dark matter candidate and, in some models, a solution to the hierarchy problem.

Extra dimensions were introduced in attempts to unify gauge theories with gravity, and the realization that a five dimensional space-time could embed at a classical level both general relativity and electromagnetism was first made by Nordstrom in 1914 [150]. Kaluza and Klein rediscovered this mechanism in 1926 [151, 152], developed the idea of compactification and gave it a quantum interpretation. Their work was largely ignored until the 70s when theories with extra dimensions had a resurgence within supergravity and superstrings.

We can describe theories with compactified extra dimensions as field theories in four dimensions by mean of a Kaluza-Klein (KK) reduction. As an example we consider a complex scalar field and a single new dimension, x_5, with zero curvature that we compactify by assigning periodic boundary conditions around a circle of circumference $2\pi R$. The Klein-Gordon equation in this space is:

$$(\partial_M \partial^M + m^2)\phi = 0 \quad M = 0, 1, 2, 3, 5 \tag{66}$$

And the periodicity condition allows a Fourier decomposition of the field:

$$\phi(x, x_5) = \sum_n \phi_n(x) e^{i k_n x} \quad k_n = n/R \tag{67}$$

If we insert the Fourier expansion back in eq.66 we obtain:

$$(\partial_M \partial^M + k_n^2 + m^2)\phi_n = 0 \tag{68}$$

Which is an infinite set of equation for ordinary Klein-Gordon fields in 4D, having a mass $M = \sqrt{(n/R)^2 + m^2}$. If the original field was

massless the spectrum of a compactified theory consists of a single real massless scalar field, called the *zero-mode* ϕ_0, and an infinite tower of massive complex scalar fields (KK modes) with masses inversely proportional to the compactification radius $M = |n|/R$.

3.3.1 *Large Extra Dimensions*

An important observation by Arkani-Hamed, Dimopoulos and Dvali (ADD) [153] is that the hierarchy problem can be solved in models with large extra dimensions, with sizes up to a millimeter.

In their model we introduce n compactified extra dimensions, and while the particles of the SM live on a 3-dimensional hypersurface (brane), gravity can propagate to all the $4 + n$ dimensions. This introduces a new fundamental scale of gravity in extra dimensions, M_*, which together with the ultraviolet completion scale of the SM is around a few TeV or so, thus eliminating the Higgs mass hierarchy problem; If the compactification volume of the extra dimensions is V_n we can obtain the relation: $\overline{M}_{Pl}^2 = V_n M_*^{n+2}$ And by postulating that the quantum gravity scale $M_* \sim TeV$, the size of the extra dimensions can be estimated to be $L \sim 10^{-17+30/N}$ cm. Because the extra dimensions are so large in the ADD framework, their effects might be measurable even in low-energy table-top experiments. For one extra dimension, $N = 1$, we obtain $L \sim 10^{13}$ cm, implying modifications of gravity over astronomical distances. On the other hand, for $N = 2$ we get $L \sim 10^{-2}$ cm. Searches for deviations from Newton's law of gravitation have been performed in several experiments [154], and the best present limits are of $R < 37$ μm for $N = 2$, corresponding to $M_* > 3.6$ TeV. For larger N, the value of L decreases but, even for $N = 6$, L is very large compared to $1/M_{Pl}$.

The compactification of the extra dimensions results in a KK tower of massive graviton excitations. Furthermore, because the true, higher dimensional gravity is strong at the electroweak scale, it should be possible to produce gravitons in collider experiments. Because the gravitons propagate in the extra dimensions, they can escape detection, leading to a missing energy signature very similar to that from SUSY models. Another striking signatures of this models is the possible production of microscopic black-holes that would evaporate into all possible SM states.

3.3.2 *Universal Extra Dimensions*

In universal extra dimensions (UED) [155] we assume that all fields propagate universally in the extra dimensions. This case does not address the hierarchy problem but can be shown to have other interesting features. From momentum conservation along the extra dimension we would derive that the number of KK particles should

be a conserved quantity. In realistic compactification scenarios what is conserved is only a sub-symmetry, KK-parity, which conserves the KK-even and KK-odd states. The theory has a phenomenology very similar to SUSY, at colliders KK particles can be created in pairs, and decay to the lightest KK particle, which is stable and escaped the detector. The energy scale at which the KK state would appear is directly related to the inverse size ("compactification scale") of the extra dimension, $M_{KK} \propto R^{-1}$, where $R \sim 1$ TeV to escape experimental constraints.

3.3.3 *Warped extra dimensions*

The Randall-Sundrum model of warped extra dimensions [156], with the introduction of only one additional new dimension, provides an attractive solution to the hierarchy problem. In this model, the extra dimension separates two $3+1$ dimensional surfaces (branes) in the full higher-dimensional space. Gravity is concentrated on one brane, while the particles of the SM reside on the other. Gravity can propagate in the bulk region between the two branes, but it is exponentially attenuated. It is this attenuation that makes gravity appear weak, rather than the dilution effect that operates in the ADD model. Any mass parameter m_0 on the visible 3-brane in the fundamental higher-dimensional theory will correspond to a physical mass

$$m = e^{-kr_c\pi} m_0 \tag{69}$$

with r_c the compactification radius and k a constant related to the model. Because of this exponential factor, there is no need for large hierarchies in the fundamental parameters of the theory. By choosing $e^{-kr_c\pi}$ of order 10^{15} we can produce mass scales in the TeV range from fundamental parameters at the Planck scale. As in the case of ADD, the theory predicts a Kaluza-Klein tower of graviton modes, but in this case the decay signature does not involve large missing energy.

3.4 COMPOSITE HIGGS

The breaking of electroweak symmetry, and a solution to the hierarchy problem, can be obtained dynamically from a strongly coupled theory at an energy scale of 1 TeV or below. The Higgs field would then be a composite object, and its potential the result of pair condensations of fermion constituents. This was actually the original Higgs proposal, inspired by superconductivity, as a mechanism to produce his field [11]. Several years later Susskind [157] and Weinberg [158, 159], in analogy with the elegant breaking of chiral symmetries in QCD, provided an explicit model realizing EWSB by new strong interactions, known as "technicolor". Technicolor intro-

duces new massless fermions called technifermions and new force-carrying fields called technigluons. As in the SM, the left-handed components of the technifermions are assigned to electroweak doublets, while the right-handed components form electroweak singlets, and both components carry hypercharge. At $\Lambda_{EW} \sim 1$ TeV the technicolour coupling becomes strong, which, like in QCD, leads to the formation of condensates of technifermions. Because the left-handed technifermions carry electroweak quantum numbers, but the right-handed ones do not, the formation of this technicondensate breaks electroweak symmetry. The scale Λ_{TC} at which technicolour interactions become strong is related to the electroweak scale: $\Lambda_{TC} = f_\pi/\sqrt{N_D}$ where N_D is the number of technifermion doublets. The simplest technicolour models could provide masses for the gauge bosons $W^\pm$ and Z_0, but not to quarks and leptons. More realistic technicolour models allow for fermion masses by introducing new interaction with technifermions, as in "extended technicolour" [160, 161]. These theories predict a large number of relatively light pseudo-Goldstone bosons that have not been observed. Moreover, constraints from flavor-changing neutral currents exclude the possibility of generating large fermion masses. Strong dynamics at the weak scale would generically give sizable contributions to EW observables, disfavored by the global electroweak fit [25]. is also particularly difficult to accommodate in technicolor frameworks.

3.4.1 *Little Higgs models*

An approach which attempts to reconcile the idea of dynamical electroweak symmetry breaking with the existence of a light Higgs is to consider the Higgs as a pseudo Goldstone boson [162, 163, 164]. The basic idea of such "Little Higgs Models" is that there are some new strong interactions, at a scale M, and that these interactions possess an approximate global symmetry which is explicitly broken. One of the Goldstone bosons of this symmetry acts as the Higgs boson. The explicit breaking is said to be "collective". None of the coupling constants in the Little Higgs Lagrangian breaks all the global symmetries required to keep the Higgs massless by itself, it is only their collective effect that results in the Higgs acquiring a mass and non-derivative interactions. All Little Higgs models contain new particles with masses around the 1 TeV scale. The spectrum includes a vector-like quark at the TeV scale, required to cancel the top loop divergence, and new gauge bosons, canceling the W and Z loop divergences. The masses of the new particles are bounded from above by naturalness considerations. While precision electroweak constraints provide strong lower bounds at least part of the spectrum is expected to be observable at the LHC.

Part II

EXPERIMENT

4

THE ATLAS EXPERIMENT AT THE LARGE HADRON COLLIDER

This chapter provides a brief description of the construction, design and operations of the LHC accelerator, and a comprehensive overview of the ATLAS detector and its subsystems.

4.1 THE LARGE HADRON COLLIDER

The Large Hadron Collider [165, 166] is a proton-proton collider and the highest-energy particle accelerator to date. It is hosted at the European Center for Nuclear research (CERN), in Geneva, Switzerland, in a 27 Km long circular tunnel (built in 1985 for the former LEP collider [167]) at a depth ranging from 50 to 75 m underground. It is designed to collide bunches of protons at a luminosity of $10^{34} cm^{-2} s^{-1}$ and at the unprecedent energy of 14 TeV.

The two proton beams travel in opposite directions in separate beam pipes, with common sections only at the four interaction regions where the experimental detectors are located. The peak beam energy depends on the integrated dipole field around the storage ring; which for the nominal energy of 7 TeV amounts to 8.33 T. This field is achieved with 1232 Nb-Ti superconducting magnets, working at a temperature of 1.9 K, below the phase transition of Helium from normal to superfluid state. While proton-proton collisions are the main operation mode the LHC is able to perform lead-lead or proton-lead collisions at an energy of 2.76 TeV per nucleon pair, for the study of QCD at high temperatures and densities.

Four main experiments are located at the interaction points around the accelerator circumference. ATLAS [168] and CMS [169] are general purpose detectors working at the design luminosity. The other two experiments are working at lower peak luminosities: LHCb [170] for the study of B-physics and CP violation and ALICE [171] to investigate the properties of the quark-gluon plasma created in heavy ion collisions. Three smaller experiments make use of detectors placed close to the beamline near the interaction points. TOTEM [172] for measurements of elastic and diffractive scatterings, MoEDAL [173] to search for magnetic monopoles and LHCf [174] to measure particle multiplicities at very high rapidities to constrain the interaction models used to simulate cosmic ray showers at very high energies.

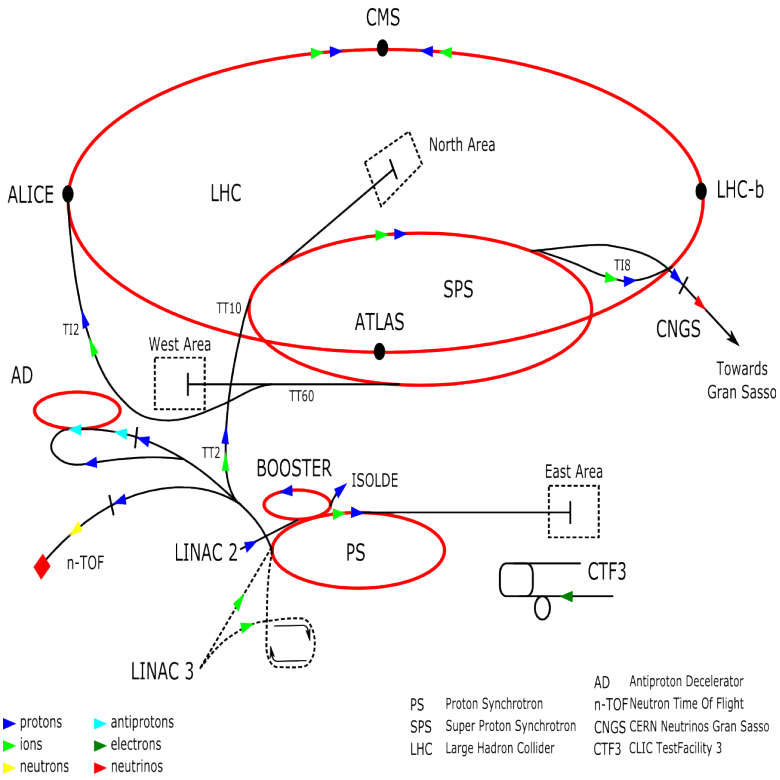

Figure 14: The LHC accelerator complex at CERN.

4.1.1 *The accelerator chain*

Before particles can enter the LHC they go through a succession of different accelerators, shown in Fig. 14, that gradually increase the beam energy and refine the beam parameters. Protons are first extracted from a source of ionized hydrogen atoms, and accelerated up to 50 MeV by the *Linac2*, that then injects them into *Proton Syncrotron Booster* (PSB). Successively they go into the *Proton Syncrotron* (PS), the oldest CERN accelerator still in function, where their energy is increased from 1.4 to 25 GeV. The *Super Proton Syncrotron* (SPS) finally brings the beam energy to 450 GeV, the injection energy of the LHC machine. They are then transferred to the LHC where they are accelerated for 20 minutes to their nominal energy.

The proton beams circulate the ring in bunches. Under nominal operating conditions, each proton beam has 2808 bunches, each containing about 10^{11} protons, and a bunch separation of 25 ns. However, in 2011 and 2012 the LHC has operated with only up to 1380 bunches per beam with a 50 ns separation. These bunches are a few centimeters long and about 16 µm wide when they collide. As a result, multiple pp interactions will be produced in the same bunch crossing (also called *pile-up* interactions).

4.1.2 *Parameters and operations*

The number of events per second generated at a particle collider is given by $N_{events} = \sigma \times L_{Int} = \sigma \times \int \mathcal{L} \cdot dt$ where σ is the cross-section for the production of the events of interest, and $\mathcal{L}$ is the instantaneous machine luminosity. The luminosity is only dependent on the beam parameters, and for beams with a Gaussian profile it can be written as:

$$\mathcal{L} = \frac{N_b^2 n_b f_{rev} \gamma_r}{4\pi\epsilon_n \beta^*} F \tag{70}$$

where N_b is the number of particles per bunch, n_b the number of bunches in each beam, f_{rev} is the revolution frequency, γ_r the relativistic gamma factor, ϵ_n the normalized transverse beam emittance, β^* the beta function at the interaction point and F a reduction factor to the geometric luminosity due to the crossing angle [165]. The term $\epsilon_n \cdot \beta^*$ is a measure of the area of the beam spot at the interaction point.

The LHC started its operations on the 10^{th} September 2008 when the first beams circulated in the accelerator. sSoon after a quench in one of the dipole magnet caused an helium leak that compromised the vacuum in the beampipe and damaged 53 magnets [175]. Following extensive repairs the LHC restarted in November 2009 and the first pp collisions were achieved in November at a reduced beam energy of 450 GeV. Shortly after the energy was increased to 1.18 TeV per beam, setting a new record for man made high energy particle collisions. The early part of 2010 saw the continued ramp-up in beam energies, achieving collisions at 7 TeV of center-of-mass energy, that was later brought to 8 TeV later in 2012. The luminosity also rapidly evolved thorough the successive runs. The peak instantaneous luminosity reached in 2010 is slightly higher than $2 \times 10^{32} cm^{-2} s^{-1}$, increased to $3.65 \times 10^{33} cm^{-2} s^{-1}$ during 2011, delivering a total integrated luminosity of 5.6 fb^{-1}. In 2012 the instantaneous luminosity increased to $7.73 \times 10^{33} cm^{-2} s^{-1}$ for a total of 23.3 fb^{-1} delivered to each of the ATLAS and CMS experiments. The evolution of the peak and integrated luminosity as measured in ATLAS is shown in Figure 15 and 16 respectively. During 2011 the number of interactions produced per bunch crossing increased from 5 to 15, which increased in 2012 from 10 to a peak of 35, as show in in Fig. 17. In 2010 and 2011, two heavy ion runs with lead-lead and p-lead nuclei took place, where a maximum luminosity of $30 \times 10^{24} cm^{-2} s^{-1}$ has been achieved.

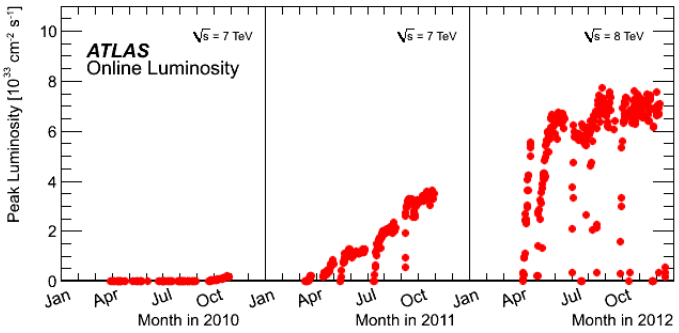

Figure 15: The peak instantaneous luminosity delivered to ATLAS per day versus time during the p-p runs of 2010, 2011 and 2012.

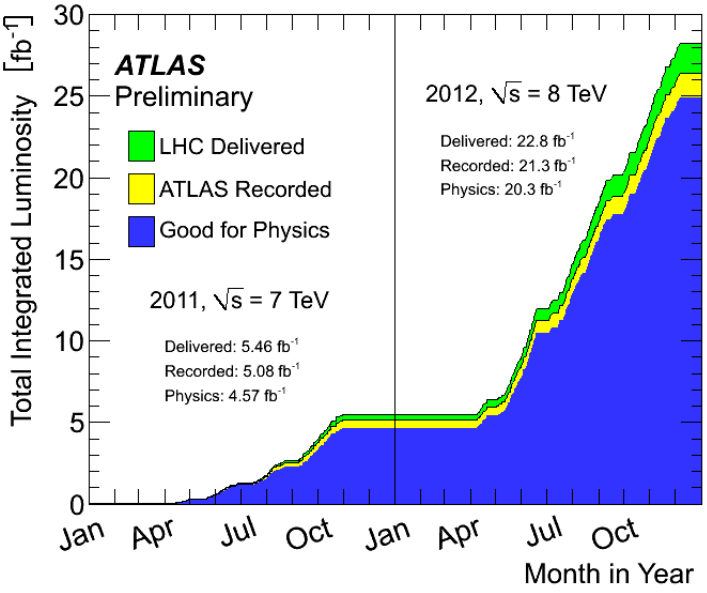

Figure 16: Cumulative luminosity versus time delivered to (green), recorded by ATLAS (yellow), and certified to be good quality data (blue) during stable beams and for pp collisions at 7 TeV centre-of-mass energy in 2011.

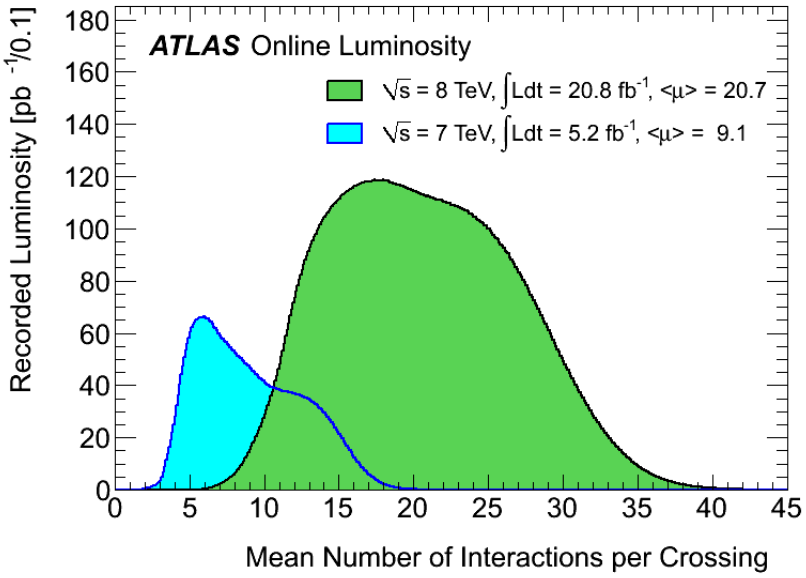

Figure 17: Luminosity-weighted distribution of the mean number of interactions per crossing for the 2011 and 2012 data.

4.2 THE ATLAS EXPERIMENT

ATLAS (**A** **T**oroidal **L**HC **A**pparatu**S**) is a general purpose particle detector located in a large underground cavern at the point 1 interaction point of the LHC.

It is 25 m in diameter and almost 46 m long, for a total weight of approximately 7000 tonnes. It is built around the LHC beam pipe, in a large cavern 300 feet underground.

The design of the ATLAS experiment has been driven by its physics priorities: the investigation of the mechanism of EWSB and the search for a SM Higgs boson, as well as the search for direct evidence for new physics. The production of a SM Higgs boson provides a particularly important benchmark, with a production rate varying widely over the allowed mass range and a large number of possible decay modes. The general requirements followed in the design of the ATLAS detector [176, 177] can be summarised as:

- Excellent electromagnetic calorimetry for electron and photon identification and measurements, complemented by full-coverage hadronic calorimetry for accurate jet and E_T^{miss} measurements;
- High-precision muon momentum reconstruction, with the capability of accurate measurements with the stand-alone muon spectrometer;
- Efficient charged particle tracking at high pile-up for high-p_T lepton, electron and photon identification, τ-lepton and heavy-

flavour identification, and full event reconstruction capability at lower luminosity;

- An hermetic construction in order to reconstruct all particles produced in the interactions and for the accurate computation of missing transverse energy.
- Triggering and measurements of particles at low-p_T thresholds, providing high efficiencies for most physics processes of interest at the LHC.

ATLAS is composed of a series of concentric sub-systems, each sensitive to different types of particles produced in the collisions. The Inner Detector (ID) [178, 179] is the closest to the interaction point and measures the trajectories of charged particles. It is composed of the Pixel Detector [180, 181], the Semiconductor Tracker (SCT) [182, 183, 184], and the Transition Radiation Tracker (TRT) [185, 186, 187], and operates in a 2 Tesla magnetic field provided by the solenoid magnet [188]. Surrounding the ID is the calorimeter system [189], designed to measure the energy of electromagnetic showers produced by electrons and photons and of hadronic showers produced by the fragmentation of hadrons. The calorimeter system consists of the liquid argon electromagnetic calorimeters [190], the Tile hadronic calorimeters [191], the liquid argon hadronic end-cap calorimeters, and the forward calorimeters. The Muon Spectrometer (MS) [192] surrounds the calorimeter system and measures the trajectories of muons leaving the calorimeter. The MS is composed of muon chambers operating in a magnetic field, provided by the toroid magnets [193, 194]. A cutaway view of the ATLAS detector, with the position of each of the sub-detectors is shown in Figure 18.

4.2.1 *Coordinate System*

ATLAS uses a right handed coordinate system with the x-axis pointing towards the center of the LHC tunnel and the y axis pointing upward. The nominal interaction point (IP) is conventionally considered to be at the center of the detector, where $x = y = z = 0$. In cylindrical coordinates the azimuthal angle ϕ is measured with respect to the positive x-axis and the polar angle θ is measured with respect to the positive z-axis. Since θ is not a boost invariant quantity, quantities are instead commonly expressed in terms of the *rapidity*, $y = \frac{1}{2} \ln \left(\frac{E+p_z}{E-p_z} \right)$. For highly relativistic particles, in the limit in which the mass becomes negligible, there is an analogue variable which maintains all the properties of the rapidity but is much easier to compute experimentally, the *pseudo-rapidity*, defined as $\eta = -\ln \tan(\theta/2)$. A Lorentz invariant measure of the angular separation between particles can also be defined as $\Delta R = \sqrt{\Delta\eta^2 + \Delta\phi^2}$. At hadron colliders the longitudinal momentum of the individual colliding partons is unknown

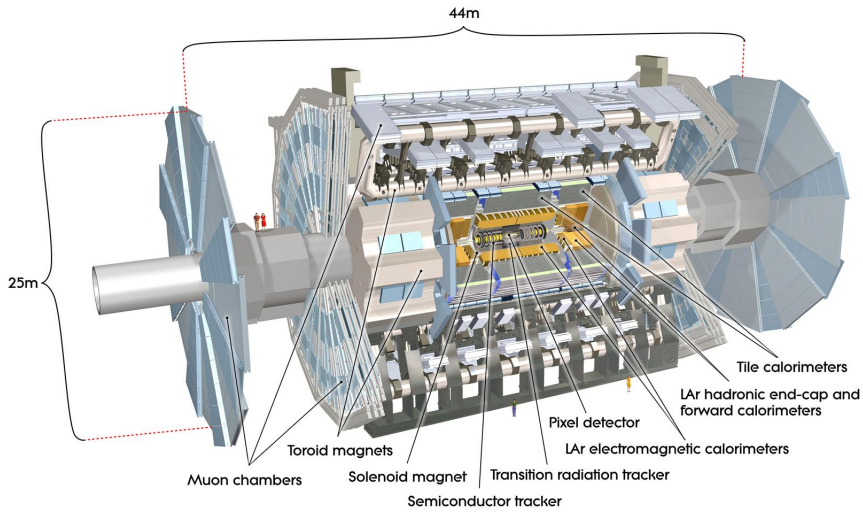

Figure 18: A cut-away view of the ATLAS detector, showing the different subsystems around the beam-axis. The main detector components are indicated.

and due to the difficulty to measure particles very close to the beamline particles energies and momenta are measured in the transverse plane. We define he transverse momentum as the momentum transverse to the z axis, $p_T = \sqrt{p_x^2 + p_y^2}$, and similarly the transverse energy $E_T = \sqrt{E_x^2 + E_y^2}$. Missing transverse energy (E_T^{miss}) is commonly used to infer the presence of non-detectable particles escaping the detector, such as neutrinos or particles predicted in many NP theories. It is defined as the momentum imbalance in the plane transverse to the beam axis, where momentum conservation is expected.

4.2.2 *Magnet system*

To be able to reconstruct charged particles momenta up to energies in the TeV range strong magnetic fields are required. The ATLAS magnet system, shown in Fig.19 consists of a central solenoid and three outer air core toroids (one barrel and two endcaps). It makes use of Nb-Ti superconducting technology and is cooled down to 4.5 K. With a total size of 22 m in diameter and 26 m in length; it covers a volume of over 12000 m^3 and stores up to 89 GJ of energy [195].

The central solenoid measures 5.8 m in length and is arranged around the beampipe, with inner and outer radii of 2,46 and 2,56 m (check), respectively. It provides a 2 T axial magnetic field in the inner detector. To avoid degrading the electromagnetic calorimeter performance it is made of a single layer of Nb-Ti superconductor, allowing

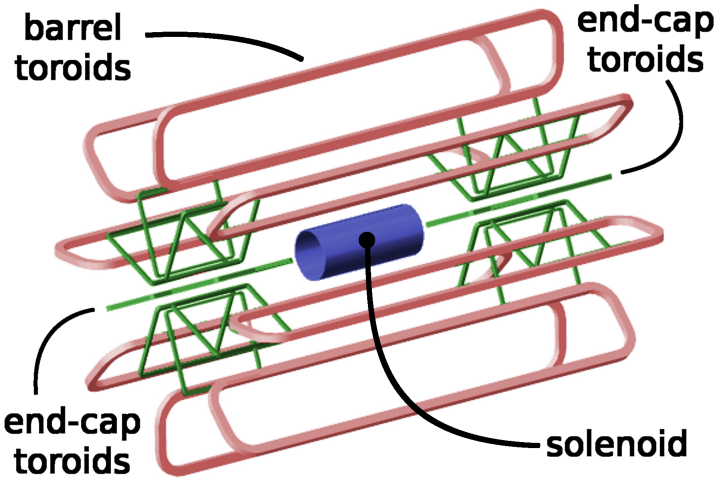

Figure 19: A schematic view of the ATLAS magnet systems.

a reduced thickness of 45 mm and it shares the same vacuum vessel of the LAr calorimeter, for a total material budget of 0.85 X_0[1].

The barrel toroid has a total length of 25.3 m with inner and outer radii of 9,4 m and 20.1 m. Two end-cap toroids are inserted within the barrel toroid, each measuring 5 m in length. Each of these toroids contains eight additional coils, arranged at constant radius with respect to the beam pipe. The toroids provide the muon system with a magnetic field of 0.5 T and 1 T in the barrel and end-caps respectively.

4.2.3 *Inner Detector*

The Inner Detector (ID) is the innermost system of the ATLAS detector, it provides precise track momentum measurements and efficient primary and secondary vertex reconstruction. It is composed of three independent but complementary sub-detectors. Two detectors are based on semiconductor technology: the Pixel Detector and the Semi-Conductor Tracker (SCT), while the Transition Radiation Tracker (TRT) is made of straw-tubes. The ID is 2.1 m in diameter and 6.2 m in length and is immersed in an axial magnetic field of 2 T. It consists of three sections, a central part and one end-cap at each side, covering the pseudorapidity range $|\eta| < 2.5$. The number of precision silicon layers is limited to keep a low cost and material budget before the calorimeters. The ID provides a combined track momentum resolution of $\frac{\sigma_{p_T}}{p_T} = 0.05\% \oplus 1\%$.

1 A radiation length, X_0 is defined as the distance over which a particle energy is reduced by a factor $1/e$ due to radiation losses only.

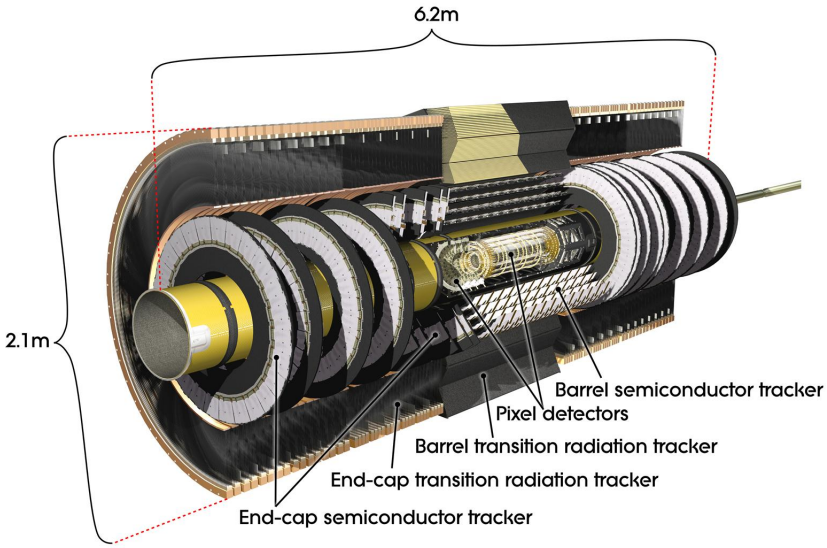

Figure 20: ATLAS inner detector.

Pixel Detector

It is the closest sub-detector to the interaction point, built directly on the beryllium beam pipe. It comprises three cylindrical barrel layers and three forward disks layers on either side, which typically provide three hits per particle. Due to the high occupancy it has the finest granularity providing a position resolution of 10 μm in the R-ϕ direction and 115 μm in the R(z) direction for the barrel disks. The time resolution is less than the 25 ns of the nominal bunch spacing in the LHC. The nominal pixel size is 50 μm in the ϕ direction and 400 μm in R(z) in the barrel and end-caps respectively. The barrel layer closest to the beam, also called B-layer for its importance in secondary vertex reconstruction, is situated at a radius $R_0 = 50.5$ mm . The two outer layers are situated at radii $R_0 = 88.5$ mm and $R_2 = 120.5$ mm and are 800 mm long. The three end-cap disks are perpendicular to the beam axis, with an inner radius of 89 mm and longitudinal positions of $|z_0| = 495$ mm, $|z_0| = 580$ mm and $|z_0| = 650$ mm. Each layer and disk supports a number of pixel modules, composed of silicon sensors bump-bonded to the front-end electronics and control circuitry. Each module has 40,080 pixel electronic channels for a total number of channels in the Pixel Detector of approximately 80 Millions. To suppress electronic noise a cooling system keeps the pixel detector at a temperature of 0°C. After three years of operation the hit detection efficiency is still about 96%.

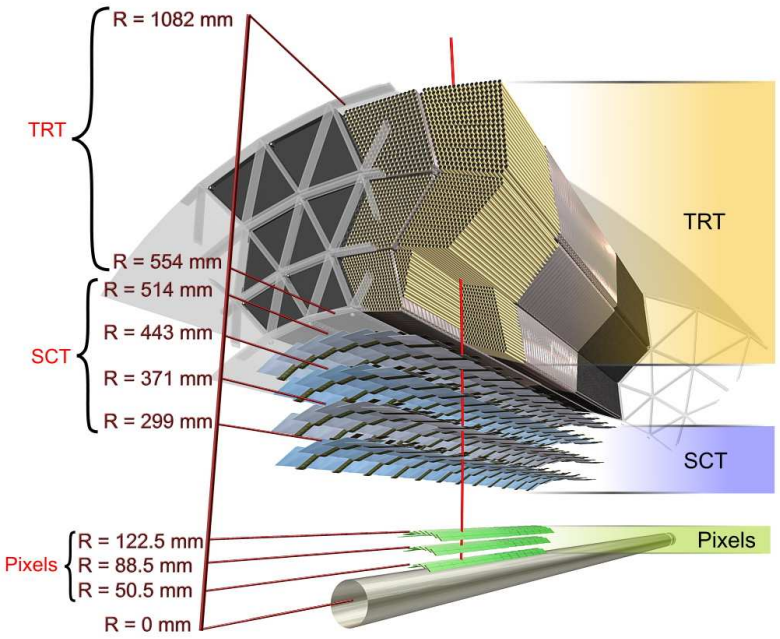

Figure 21: ATLAS inner detector.

SCT

The SCT is the second system of the ID, making use of silicon microstrip technology. It is composed of four layers covering the barrel region in the pseudorapidity range $|\eta| < 1.1 - 1.4$ with radii between 299 mm and 514 mm and a length of 1492 mm. Nine endcap disks are placed on each side at positions from 853.8 mm to 2720.2 mm and radii up to 56 cm, to extend the coverage to $1.1 - 1.4 < |\eta| < 2.5$. The barrel layers consists of 2112 identical rectangular modules while the endcap disks use 1976 wedge shaped modules of three different sizes. To provide a measurement of the second coordinate the modules in the barrel layer are tilted with a 40 mrad stereo angle. The SCT covers a total area of 61 m^2 with a total of 6.3 million of readout channels. The position resolution of the SCT is of 17 μm in the azimuthal direction and 580 μm along the beam. It makes use of single sided p-in-n silicon detectors, operated at a temperature of -7°C to suppress electronic noise, and at a bias voltage of 150 V, which can be increased over the lifetime of the experiment to recover efficiency losses due to radiation damage. The barrel section has a measured hit efficiency of 99.9% over all layers, while for the endcap is of 99.8%.

TRT

The TRT volume covers the radial section from 563 mm to 1066 mm. It consists of over 300.000 drift tubes with a 4 mm diameter made from wound Kapton (straw tubes) reinforced with carbon fibers and filled with a gas mixture of 70% Xe, 27% CO_2 and 3% O_2. In the center

of each tube is a gold-plated tungsten wire with a 31 μm diameter. With the wall kept at a voltage of -1.5 kV and the wire at ground potential the tube acts as a small proportional counter. The barrel region consists of 144 cm long straws parallel to the beam, covering $|\eta| < 1.1$. Wires are electrically split and read-out at both ends. The endcaps have 37 cm straws assembled radially in wheels and read out at their outer length, and extends the coverage to $|\eta| < 2$.

The TRT provides a single hit resolution of about 120 (130) μm in the barrel (end-cap) and complements the track measurement of the silicon sensors with, on average, an additional 30 hits per track at larger lever arm.

The TRT also provides particle identification via the transition radiation photons[2] produced in polymer fibers (barrel) and foils (endcaps) interleaved with the straws. The photons are absorbed by the Xe atoms in the gas, significantly amplifying the ionization signal. The TRT signal is readout with two thresholds. As electrons produce on average many more TRT photons compared to charged hadrons, such as pions, by counting the number of high-threshold photons it is possible to discriminate between particle types.

4.2.4 *Calorimeter*

The goal of the calorimeter system is to measure the energy of particles by total absorption, to provide a crude estimate of their position and to help in their identification. ATLAS uses a non-compensating sampling calorimeter system covering the range $|\eta| < 4.9$. It is subdivided in an electromagnetic calorimeter (EM) and an hadronic (Had) calorimeter. The EM calorimeter uses liquid argon technology (LAr) [196] and is divided into a barrel+endcap calorimeter for $|\eta| < 3.2$ and a forward calorimeter covering $3.2 < |\eta| < 4.9$. The Had calorimeter is an Iron-scintillator sampling calorimeter composed of a central cylinder and two side extensions. The hadronic end-caps use the same LAr technology of the EM calorimeter. The total thickness of the EM calorimeter is of 22 X_0 in the barrel and more than 24 X_0 in the endcap. It can contain EM showers up to a TeV and absorb $2/3$ of the energy of a typical hadronic shower. The total thickness at $\eta = 0$ is of 11 λ_0[3], 1.3 coming from the support material. It can measure the energy of a 100 GeV EM cluster with a resolution of the order of 1% and similarly for a jet of 100 GeV, as well as reduce "punch-through" jets [4].

2 Soft X-rays emitted by a charged particle when transversing the boundary between materials with different dielectric constants.

3 The nuclear interaction length, λ_0, is defined in analogy to X_0.

4 Jets not contained in the calorimeter that can reach the muon system

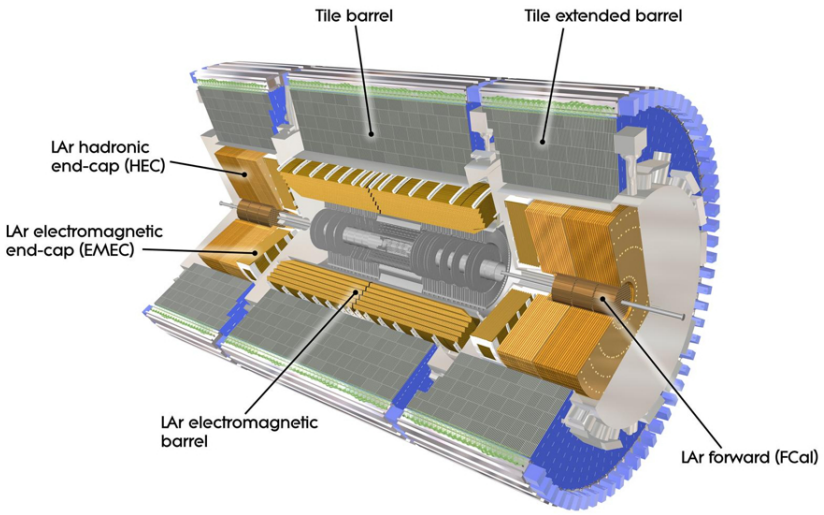

Figure 22: Schematic view of the ATLAS calorimeter system, from [197].

Liquid Argon Calorimeter

The EM calorimeter is a liquid argon (LAr) sampling calorimeter, with lead plates as absorbers. To ensure maximum azimuthal coverage the EM calorimeter uses an accordion geometry; the readout electrodes and the lead absorbers are laid out radially and folded so that particles cannot cross the calorimeter without transversing it. It is divided into a barrel and an endcap region. The barrel calorimeter (EMB) [198] covers $|\eta| < 1.475$ (with a small non instrumented region near $|\eta| = 0$) and consists of two identical half barrels housed in the same cryostat (shared with the central solenoid). Each half-barrel is 3.2 m long and inner and outer radii of 1.4 m and 2 m. The endcap calorimeters (EMEC) [199] is made of two wheels, one on each side of the EMB. Each wheel is 63 cm thick with an inner radius of 0.33 m and an outer radius of 2.1 m. They are contained in two independent endcap cryostats, together with the hadronic endcap and forward calorimeters 4.2.4. The wheels consists of two co-axial wheels, with the outer wheel (OW) covering the region $1.375 < |\eta| < 2.5$ and the inner wheel (IW) covering the region $2.5 < |\eta| < 3.2$.

The EM calorimeter is based on accordion-shaped copper-kapton electrodes positioned between similarly shaped lead absorber plates and kept in position by honeycomb spacers, with the whole system immersed in LAr gas. The electrodes are built out of three copper layers etched on polyamide: two outer conductive layers kept at high voltage and a central layer to collect the signal through capacitive coupling. The inner plate is used as readout using capacitive coupling. When the nominal potential difference of 2000 V between the electrodes and the absorbers is applied, the charges induced by ionisation in the argon drift in 450 ns towards the electrodes.

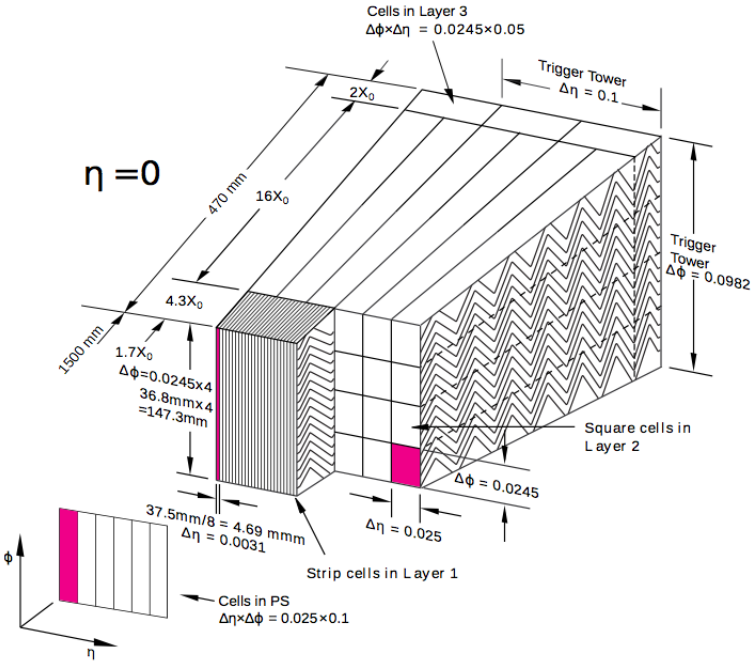

Figure 23: Schematic of a section of the EMB, displaying the different sampling layers and their granularity [168].

In the EMB and EMEC-OW each module is segmented into three longitudinal sections, with different granularities: strips, middle and back. An illustration of a module of the EM calorimeter is shown in Figure 23 The EMEC-IW is segmented in only two longitudinal sections and has a coarser lateral granularity. While the largest fraction of the energy of EM objects is collected in the middle layer, helps in discriminating between prompt γ and photons from $\pi^0 \to \gamma\gamma$ decays. The back section measures the tails of highly energetic showers, helping distinguishing deposits of electromagnetic or hadronic origin.

An additional 11 mm thin LAr presampler covering the region $|\eta| < 1.8$ allows for corrections of the energy losses in material upstream the EM calorimeters. It uses a fine η granularity of 0.2. With its projective geometry the calorimeter is also able to reconstruct the direction of neutral particles, such as photons, for which the ID cannot be used. From drift-time measurements [200] the energy resolution has been measured to be about $\frac{\sigma_E}{E} = \frac{10\%}{\sqrt{E/\text{ GeV}}} \oplus 0.7\%$.

Tile Calorimeter

The Tile calorimeter is a sampling calorimeter using steel as absorber and scintillator plastic tiles as detecting medium. It provides an average resolution for hadronic jets of about $\sigma_E/E = 50\%/\sqrt{E/\text{ GeV}} \oplus 3\%$ in the barrel and endcap and of $\sigma_E/E = 100\%/\sqrt{E/\text{ GeV}} \oplus 10\%$ in the forward section. It is segmented into three barrel structures placed directly outside the EM calorimeter, with an inner radius of 2.2 m

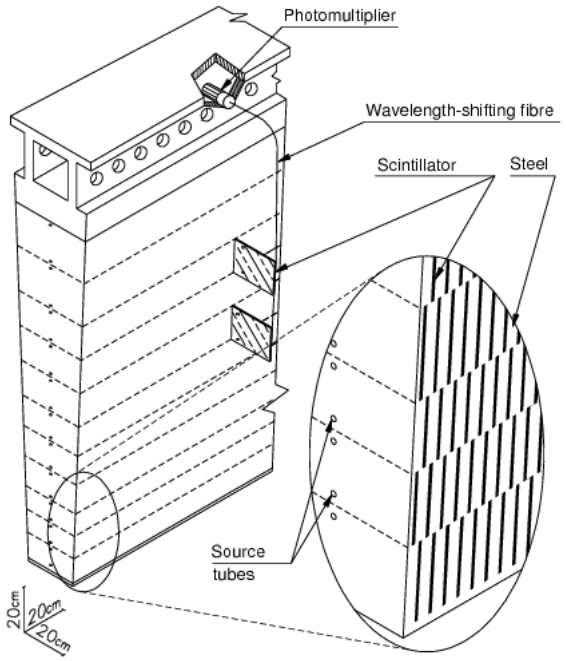

Figure 24: Schematic view of a tile calorimeter module, showing the alternating steel and scintillating material [168].

and an outer radius of 4.25 m. The central barrel is 5.8 m long and extends to $|\eta| < 1.0$, two extended barrels, each 2.6 m long, cover the range $0.8 < |\eta| < 1.7$. Each barrel is made of 64 wedge-shaped modules in ϕ, each covering a sector $\Delta\phi \sim 0.1$. The space between the central and extended barrel calorimeter presents a 60 cm gap where ID service cables and LAr pipes are mounted, thus providing only limited instrumentation.

The scintillating light is read by fibers on either side of the scintillator tile and guided to photomultipliers housed on the outer radius of the module. The fibers are grouped together in readout cells, segmenting the Tile calorimeter in three layers. Cells have dimensions $\Delta\eta \times \Delta\phi = 0.1 \times 0.1$ in the two innermost layers and $\Delta\eta \times \Delta\phi = 0.2 \times 0.1$ in the outer layer.

The Hadronic Endcap (HEC) calorimeter consists of two independent wheels per endcap, located behind the EMEC calorimeters. It covers the region $1.5 < |\eta| < 3.2$, overlapping with both the Tile and Forward calorimeters, with which it shares the cryostats. Each HEC wheel is made of 32 wedge-shaped modules of parallel plate copper/LAr technology. The wheels have an inner radius of 372 mm for the first nine plates and 475 for the rest, and outer radius of 2.03 m. The two wheels combined provide four longitudinal calorimeter layers with a granularity of $\Delta\eta \times \Delta\phi = 0.1 \times 0.1$ for $1.5 < |\eta| < 2.5$ and $\Delta\eta \times \Delta\phi = 0.2 \times 0.2$ for $2.5 < |\eta| < 3.2$.

Forward Calorimeter

The Forward Calorimeter (FCal) covers the region $3.1 < |\eta| < 4.9$ and is also based on LAr technology. To withstand the high particle fluxes in this region it exploits a novel design, using cylindrical electrodes consisting of rods concentrically inside tubes parallel to the beam axis, supported by a metal matrix. It consists of three modules; the first and closer to the interaction point is optimized for EM measurements and uses mainly copper as absorber. The other two are mainly made of tungsten and optimized for hadronic measurements.

4.2.5 *Muon Spectrometer*

The Muon Spectrometer (MS) is the largest of all ATLAS subdetectors, designed to measure particles momenta up to pseudorapidity $|\eta| < 2.7$ and to provide trigger capabilities up to $|\eta| < 2.4$. measure particle momenta from 3 GeV to 1 TeV with a design performance of stand-alone transverse momentum resolution of 10% for 1 TeV muons. It is built in and around the toroid magnets.

Resistive Plate Chambers (RPC) [201] and Thin Gap Chambers (TGC) [202, 203] provide muon trigger information in the barrel and endcap regions respectively, while Monitored Drift Tubes (MDT) [204] and Cathode Strip Chambers (CSC) [205] are used to precisely measure the position in the bending plane (parallel to the beam axis).

For muons with transverse momenta up to 400 GeV the p_T resolution as measured in beam tests [197] is $\frac{\sigma_{p_T}}{p_T} = 0.29\ \text{GeV}/p_T \oplus 0.043 \oplus 4.1 \cdot 10^{-4}\text{GeV}^{-1} \cdot p_T$

Monitored Drift Tubes

MDTs are aluminium tubes of a diameter of 30 mm with a tungsten wire running through the center, immersed in a gas mixture of 93% Ar, 7% CO_2. The passage of a muon ionize the gas, and the electron avalanche is collected by the wires. MDTs are used in both barrel end end-caps to provide precise position and momentum measurements for the full $|\eta| < 2.7$ coverage of the muon system (except in the innermost endcap layer where their coverage is limited to $|\eta| < 2.0$). The size and spacing of the MDTs increases with the distance from the beampipe. A typical chamber will consist of two multi-layers of drift tubes, separated by aluminium spacer bars. In the barrel inner layer each chamber consists of four layers of tubes, while in the middle and outer regions they consist of only three layers. The chambers are operated at an absolute pressure of 3 bar, which achieves an average resolution of 80 μm per tube, or about 35 μm per chamber. On average a muon is expected to leave a hit on 20 individual tubes.

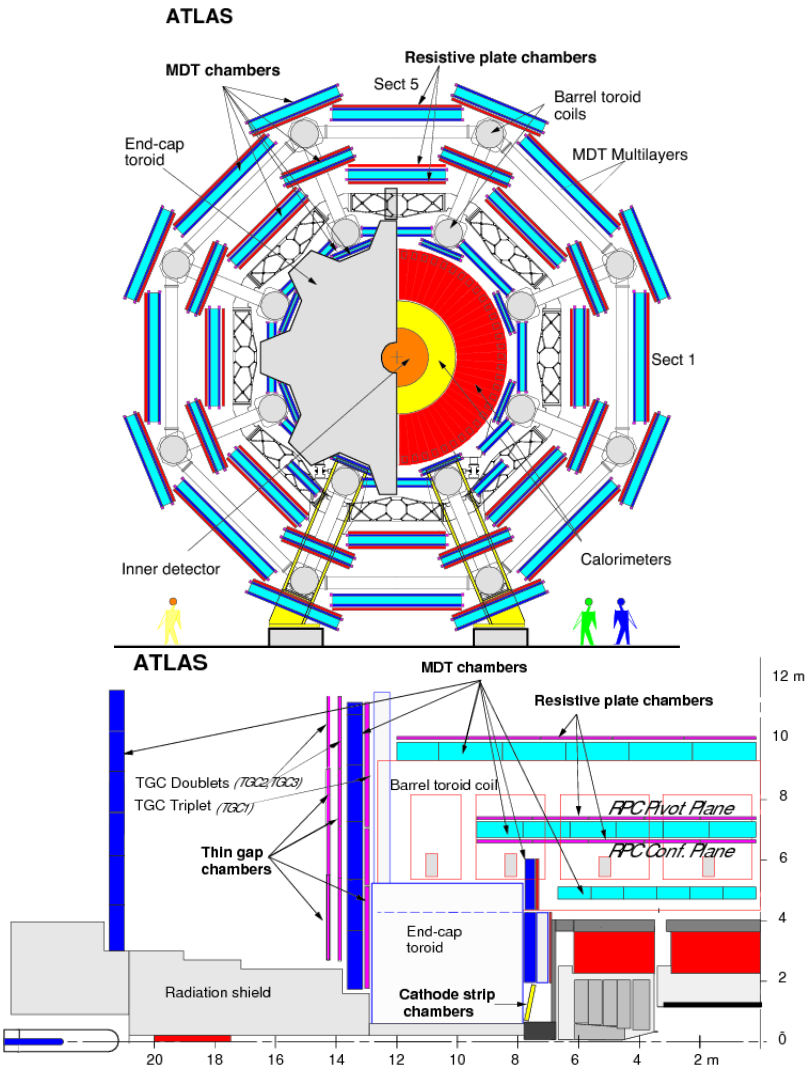

Figure 25: Schematic view of the muon spectrometer in the x-y and z-y projections, from [197].

Cathode Strip Chambers

In the forward region the rate per unit area is too high for the MDTs and Cathode Strip Chambers, with a faster response time and better resolution are used. The CSC cover the rapidity range $2.0 < |\eta| < 2.7$ in the innermost part of the end-caps. They consist of multi-wire proportional chambers with multiple closely spaced anode wires surrounded by a gas mixture of 80% Ar and 20% CO_2 with catode strips running perpendicular to the wires. This orthogonal layout allows the charge distribution to be measured in both directions normal to the beam axis. The resolution of a chamber is 40 μm in the bending plane and about 5 mm in the transverse plane.

Resistive Plate Chambers

The trigger system in the barrel consists of three concentric cylindrical layers (trigger stations) of RPC chambers around the beam axis. Each station is made of two detector layers, so that a muon going through all barrel stations will leave six hits in each of the η and ϕ coordinates. An RPC consist of two resistive parallel plates separated by a 2 mm gap, filled with a gas mixture of 94.7% $C_2H_2F_4$, 5% Iso-C_4H_{10} and 0.3% SF_6, The electric field between the plates of about 4.9 kV/mm creates electron avalanches along the ionising tracks towards the anode. The signal is read out via capacitive coupling to metallic strips, which are mounted on the outer faces of the resistive plates.

Thin Gap Chambers

In addition to the increased occupancy, the forward region suffers from radiation levels which are up to 10 times those in the central region. TGCs are used to trigger on muon tracks in the end-cap region $1.05 < |\eta| < 2.4$, as well as to provide a second measurement of the azimuthal coordinate complementing the MDT's one. They are multi-wire proportional chambers working similarly to the CSCs but with a spacing between the wire and the cathode smaller than the wire-to-wire spacing, to allow for higher granularity. Operating in a high gain mode, they are able to provide large signals with a narrow spread in time. Because of the small gap and small spacing between the wires TGC signals have a narrow spread in time. They make use of a highly quenching gas mixture of 55% CO_2 and 45% n-C_5H_{12}. TGCs are placed in two concentric rings, an inner one containing two TGC layers and an outer one containing seven. They are segmented radially and tailored to provide excellent time resolution even for very high rates. Both TGC and RPC chambers are designed to provide a signal over a time shorter than 25 ns. In this way the bunch crossing responsible for firing the trigger can be identified with an efficiency higher than 99%.

4.2.6 *Luminosity and forward detectors*

The measurement of the recorded integrated luminosity is an essential input for any cross-section measurement and affects the background estimates and the sensitivity in searches for new physics.

ATLAS has two primary detectors for the luminosity determination. LUCID, specifically designed for luminosity measurements, is a segmented gas Cherenkov detectors surrounding the beampipe at $z = \pm 17$ m. The Beam Conditions Monitor (BCM) consists of four small diamond detectors arranged symmetrically at a radial distance of 5.5 cm around the beampipe and located at $z = \pm 1.8$ m from the interaction point, that provides a beam abort signal to protect the ID from beam losses.

For a circular collider operating at a frequency f_r with n_b bunches colliding per revolution, the luminosity can be expressed as $\mathcal{L} = \mu n_b f_r / \sigma_{inel}$, with μ the average number of inelastic interactions per bunch crossing. The observed interaction rate per crossing measured during nominal data taking can then be related to the delivered luminosity. The absolute luminosity scale is obtained by measuring the horizontal and vertical beam profiles in dedicated beam separation scans, also called van der Meer scans (vdM) [206]. The luminosity calibration in 2011 yielded uncertainties of about $\pm 1.5\%$ from the vdM scans [207]. Combined with uncertainties on the extrapolation procedure, including long term stability effects, the luminosity measurement in 2011 was performed with a remarkable precision of $\pm 1.8\%$, while preliminary studies for the 2012 calibration following the same methodology as that detailed in Ref. [207] yield an uncertainty of $\pm 2.8\%$.

4.2.7 *Trigger and DAQ*

With LHC operating at its design parameters (bunch crossing rate of 40 MHz and 10^{34} cm^{-2}s^{-1}) the rate of events is expected to be 1 GHz. Such a large amount of data would be difficult to distribute and process efficiently and very expensive to be stored. Moreover the rate of production for events of interest is order of magnitudes smaller than the total rate, dominated by low-p_T inelastic and diffractive collisions.

In ATLAS a three level trigger system progressively filters out non-interesting events, making use of more detailed, and thus slower to process, information at each successive stage. A block diagram of the Trigger and DAQ systems is shown in Fig. 26.

The Level-1 (L1) trigger [208] is a hardware based trigger using fast custom electronics (ASICs and FPGAs). It makes use of partial detectors information to provide a fast decision within 2.5 μs and reduce the rate below 75 KHz, a reduction factor of 500. It considers high p_T muon segments, electromagnetic clusters, jets and τ lepton

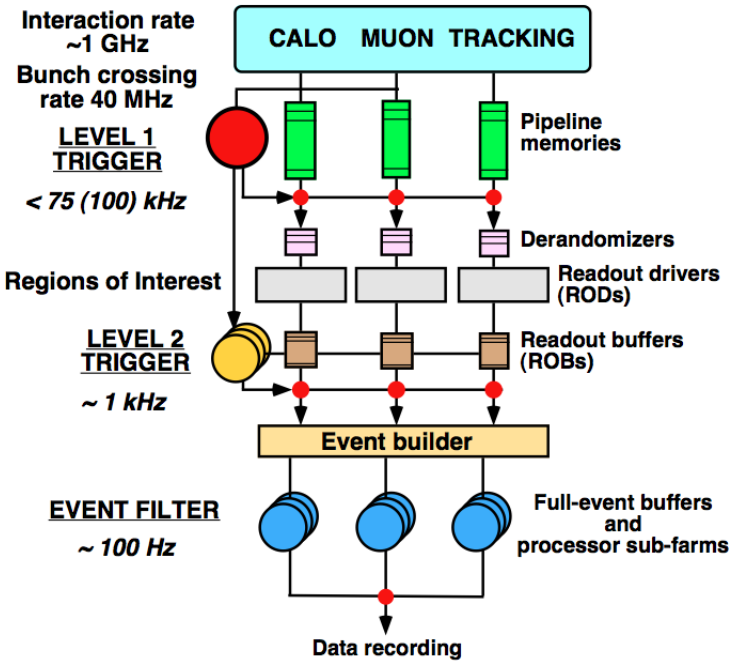

Figure 26: Block diagram of the ATLAS trigger/DAQ system [208].

candidates as well as computing an event wise jet energy sum and E_T^{miss}.

The L1 calorimeter trigger (L1Calo) considers energy deposit in *trigger towers*, regions at a reduced granularity of $\Delta\eta \times \Delta\phi = 0.1 \times 0.1$. A sliding window algorithm searches for local energy maxima across groups of trigger towers (or coarser granularity 0.2×0.2 jet elements, in the case of jets, missing energy and energy sum triggers), and tests these maxima against predefined thresholds. L1 electron and photon objects are defined as windows of 2×2 EM calorimeter trigger towers, where horizontal or vertical sums of 1×2 blocks exceed predefined thresholds, An absolute isolation requirement can also be applied by requesting the 12 towers surrounding the central core region to be less than programmable threshold.

The muon trigger (L1Muon) uses information from the TGC and RPC chambers only, and estimates the p_T of muon candidates by approximating the curvature of the muon trajectory between muon stations. Both L1Calo and L1Muon report the multiplicities of the various candidates for various thresholds to the Central Trigger Processor (CTP), which takes the final trigger decision based on logical expressions stored in look-up tables. A prescale value p can be applied separately on each trigger item to accept only a fraction of the events that could pass a given trigger selection.

While the L1 trigger decision is being formed, sub-detectors data are stored in on-detector pipeline memories. After a Level-1 accept all the data from that bunch-crossing are read-out by sub-detector

specific read-out drivers (ROD) which formats the digitized signals before sending it through optical links to read-out buffers (ROB) of the read-out system (ROS) of the data acquisition (DAQ) system.

The high-level trigger (HLT) [209], subdivided into the Level-2 (L2) and Event Filter (EF), is implemented entirely in software, and runs on off-the-shelf computers and networking technology. In contrast to the L1 trigger which has to process the events sequentially, the HLT operates asynchronously and processes many events in parallel.

The L2 has available the full resolution data, including tracking information from the Inner Detector, but to save bandwidth, it only retrieves data in the areas defined by the ROIs provided by L1. L2 makes a decision in 10ms and rejects about 95% of the events, for an output rate of 3.5 KHz. If the event is accepted the read-out system sends the whole data to the Event Building (EB) system, which merges the event fragments before the third trigger level.

At the EF leve the whole detector data is available, and the algorithms used are very similar to the ones used in the offline reconstruction. It accepts on average one out of ten events.

In total the L2 trigger uses approximately 500 computing nodes, the EF uses 1800 nodes and 100 nodes are used for event building. The total rejection factor of the trigger system is 10^7, resulting in a nominal output rate of 100 Hz[5] to be stored for subsequent analysis.

After being output from the EF events get sorted in different streams depending on the sets of trigger criteria that accepted the event. Three major streams are of interest for physics analysis: Egamma, Muons and JetTauEtmiss.

The selected events are subsequently stored on tape at the CERN computing center (Tier0) where the final reconstruction takes place. The data is also replicated to sites all over the world where they can be processed and analysed using the Worldwide LHC Computing Grid [210, 211].

5 For parts of the 2010-2012 data taking the trigger could accept events at up to 400 Hz

5 OBJECT RECONSTRUCTION AND SELECTION

This chapter describes the standard reconstruction and identification of high-level objects in ATLAS. The techniques used to estimate efficiencies and the calibration of these objects, as well as their uncertainties are also briefly reviewed. The focus is on the algorithms and selections applied to data collected during the 2012 run, as used in the next chapter.

5.1 TRACKING AND VERTEXING

The ability to detect and reconstruct trajectories of charged particles is essential for lepton identification and momentum reconstruction. Multiple track reconstruction allows to identify the vertices where either the pp interaction took place (primary vertex) or the decay of a long lived particle happened (secondary or displaced vertex). Moreover, a precise measurement of the track impact parameter allows the identification of heavy-flavour quarks inside jets.

Tracks are reconstructed within the full ID acceptance of $|\eta| < 2.5$ with a lowest momentum threshold of $p_T > 400$ MeV. A sequence of algorithms is used [212, 213]. In a first step an inside-out algorithm starts from 3-point seeds in the silicon detectors and adds hits moving away from the interaction point using a combinatorial Kalman filter[1]. Ambiguities in the track candidates are resolved, and tracks are extended into the TRT. This is the baseline algorithm and is designed for an efficient reconstruction of primary charged particles. In a second stage, a track search starts from segments reconstructed in the TRT and extends them inwards by adding silicon hits. This backtracking is mainly designed to recover secondary tracks from conversions, material interactions and long-lived particle decays. Tracks with a TRT segment but no extension into the silicon detectors are referred as TRT-standalone tracks. Besides the default track reconstruction criteria, tighter requirement can be applied to suppress the rate of fake tracks with high pile-up (*robust* selection) [212]. The track reconstruction efficiency is defined as the fraction of primary particles matched to a reconstructed track. The accuracy of the reconstruction of charged particle trajectories is limited by the combined effect of the finite resolution of the detector elements, the knowledge of the

1 A Kalman filter is an iterative algorithm that provides the optimal estimate for the system parameters based on projection from earlier measurements and current measurement

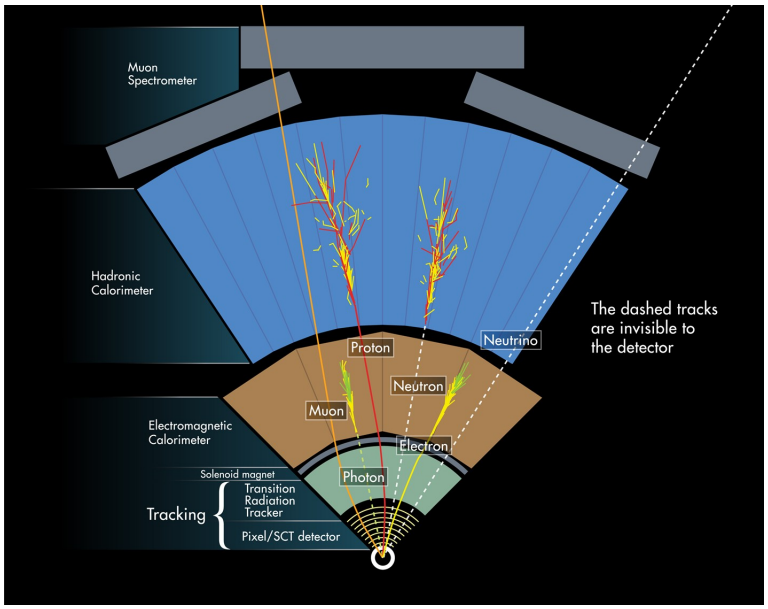

Figure 27: Schematic representation of the detector components in a plane perpendicular to the LHC beam line (transverse plane) in the barrel region. Only a small sector of the azimuthally symmetric detector is shown, starting outwards from the LHC beam vacuum pipe. Typical signatures for various particles as measured in the different detector layers are illustrated, where solid lines represent directly measurable trajectories of charged particles, and dashed lines the straight-line trajectories of neutral particles leaving no direct signals in tracking detectors.

locations of the detector elements, of the magnetic field, and of the amount of material in the detector. The reconstruction is also affected by the occupancy of detector modules, particularly in dense environments resulting from jets at high pile-up. For tracks with $p_T > 10$ GeV the efficiency, derived in a MC sample of non-diffractive events, approaches 90%.

Misalignments of the active detector elements deteriorate the resolution of the reconstructed track, while correlated geometrical distortions can lead to systematic biases on the reconstructed track parameters. The ID has been aligned using a track-based technique [214] which minimizes the track-to-hit residuals by correcting the alignment parameters. It allows the alignment of all tracking subsystems together, with the position of each individual module known to a precision better than $1\mu m$ [215].

The correct identification of the primary vertex from a hard-scattering process is crucial for physics analyses, especially at high pile-up conditions, as it allows the precise knowledge of the number of additional pile-up interactions.

Primary vertices are reconstructed using an adaptive vertex finding algorithm [216, 213]. Vertex seeds are obtained from the z-position at the beamline of the reconstructed tracks. An iterative χ^2 fit is made using the seed and nearby tracks. Tracks displaced by more than 7σ are used to seed a new vertex and the procedure is repeated until no additional vertices can be found. The beam spot position is used as a constraint. Vertices are required to contain at least two tracks.

Vertices are matched to interactions by calculating the sum of the weights of the tracks in a vertex matched to each interaction. In general, more than one vertex is found per event. The vertex with the largest sum of squared transverse momenta of the associated tracks ($\sum p_T^2$) is chosen as primary vertex of the event, while others are denoted as pile-up vertices. The increasing number of fake tracks in a high pile-up environment increases the probability to reconstruct a fake vertex. The vertex efficiency is calculated with the same track-to-particle matching used to calculate the tracking efficiency.

5.2 JETS

Hadronic jets, arising from the fragmentation of quarks and gluons, are responsible for most of the structure of collision events at the LHC. They are key ingredients of many Standard Model measurements and widely used in New Physics searches.

5.2.1 *Clustering*

The highly segmented calorimeters of the ATLAS detector enables the reconstruction of jets with high precision. The calorimeter cells are grouped to 3-dimensional clusters of topologically connected cells called topo-clusters. From topo-clusters jets can be built using any arbitrary clustering algorithm. The topo-cluster finding is optimized to noise and pile-up suppression [217, 218] and works in three steps. The first step is the identification of seeds, which are cells with energy deposits $E > 4\sigma$, where σ is a noise threshold defined as the sum in quadrature of electronic and pile-up noise. The second step is the iterative adjunction of neighboring cells with $E > 2\sigma$ to the seeds. In the third step, an extra layer of cells with $E > 0$ on the perimeter of the clustered cells are added. After topo-clusters are found, a splitting algorithm further separates the resulting clusters based on local energy maxima. Two schemes are used to calibrate topo-clusters. A calibration to the electromagnetic scale (EM topo-clusters) and local calibration weighting [219] (LCW topo-clusters). In both cases, the mass of the topo-clusters is set to zero. The EM topo-clusters are calibrated to the response from electrons. In the LCW calibration topo-clusters are classified as electromagnetic or hadronic, according to the measured energy density and the longitudinal shower depth. A weighting scheme is then used to correct for the different electron-to-pion response in the calorimeters. Dedicated corrections address effects from dead material and out-of-cluster energy [217].

5.2.2 *Jets reconstruction and calibration*

Jets are reconstructed using the Anti-k_t algorithm [56, 220] with four-momentum recombination utilising the FastJet software package [221]. The distance parameter used is $\Delta R = 0.4$, optimised to better handle high multiplicity final states. The algorithm takes as inputs topo-clusters, calibrated using the local cluster weighting (LCW). Only clusters with positive energy are considered. Jet momenta are constructed by performing a four-vector sum from these clusters, treating each as an $(E, \vec{p})$ four-vector with zero mass. Except during the E_T^{miss} computation, where the η range is not restricted, only jet candidates with $p_T > 20$ GeV and $|\eta| < 2.8$ are subsequently retained.

Further corrections are applied to bring the jet energy to the particle-level, corresponding to the energy of a jet built from the true stable particles after hadronisation, which is independent of the detector response 28. This calibration corrects for the effects of calorimeter non-compensation and inhomogeneities by using p_T- and η-dependent calibration factors based on MC corrections validated with extensive test-beam and collision-data studies [222].

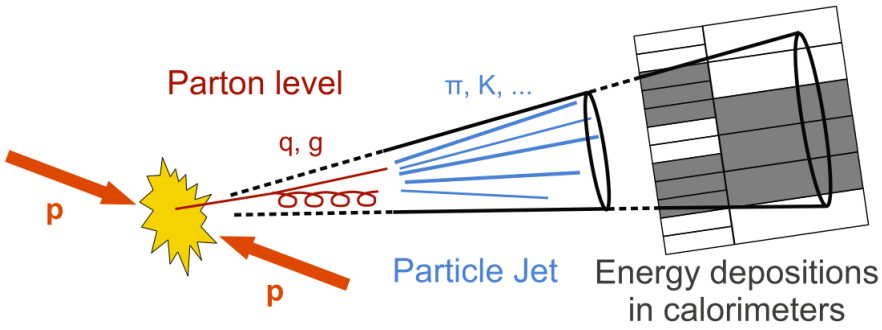

Figure 28: The production of jets in a hard scattering interaction and the different levels at which they can be defined.

One of the challenges connected with jet reconstruction at hadron colliders are simultaneous proton-proton collisions in the same or neighboring bunch crossings (pile-up). The effect of pile-up is to add energy deposits to the jets from the hard-scatter event and to create additional soft jets (pile-up jets).

The dependence of the jet response on pileup conditions is significantly reduced by implementing a correction based on the "Jet-area method" [223, 224]. In its most basic form, it makes use of two variables: the median p_T density ρ in an event and the jet catchment area A^{μ}_{jet}. The quantity $\rho \cdot A^{\mu}_{jet}$ gives an estimate of the pile-up contribution to the jet, which is subtracted from the jet four momentum. This correction is derived from MC simulations as a function of the number of reconstructed primary vertices N_{PV} and the expected average number of interactions (μ, sensitive to out-of-time pile-up) in bins of jet pseudorapidity and transverse momentum . A correction to the jet direction is then applied, to make the jet pointing back to the primary event vertex instead of the nominal center of the ATLAS detector.

The final jet energy calibration (Jet Energy Scale) is a multiplication by the average jet energy response. It corrects the jet energy by multiplying by the response ratio of MC to data $E^{LCW}_{jet}/E^{truth}_{jet}$ using isolated jets from an inclusive dijet MC sample. After applying the jet energy scale (JES), the EM jets and LCW jets are called EM+JES and LCW+JES jets, respectively. The jet pseudorapidity calibration corrects for a bias due to poorly instrumented regions of the calorimeter. Differences between data and MC simulation lead to miscalibration of jet energy which is removed by a residual in situ calibration applied to the data only.

5.2.3 *Jet energy scale and resolution uncertainties*

For many analyses the uncertainty on the Jet Energy Scale (JES) and resolution (JER) calibrations is a dominant systematic. Uncertainties on the JES and JER also have a direct impact on the determination of the missing transverse energy.

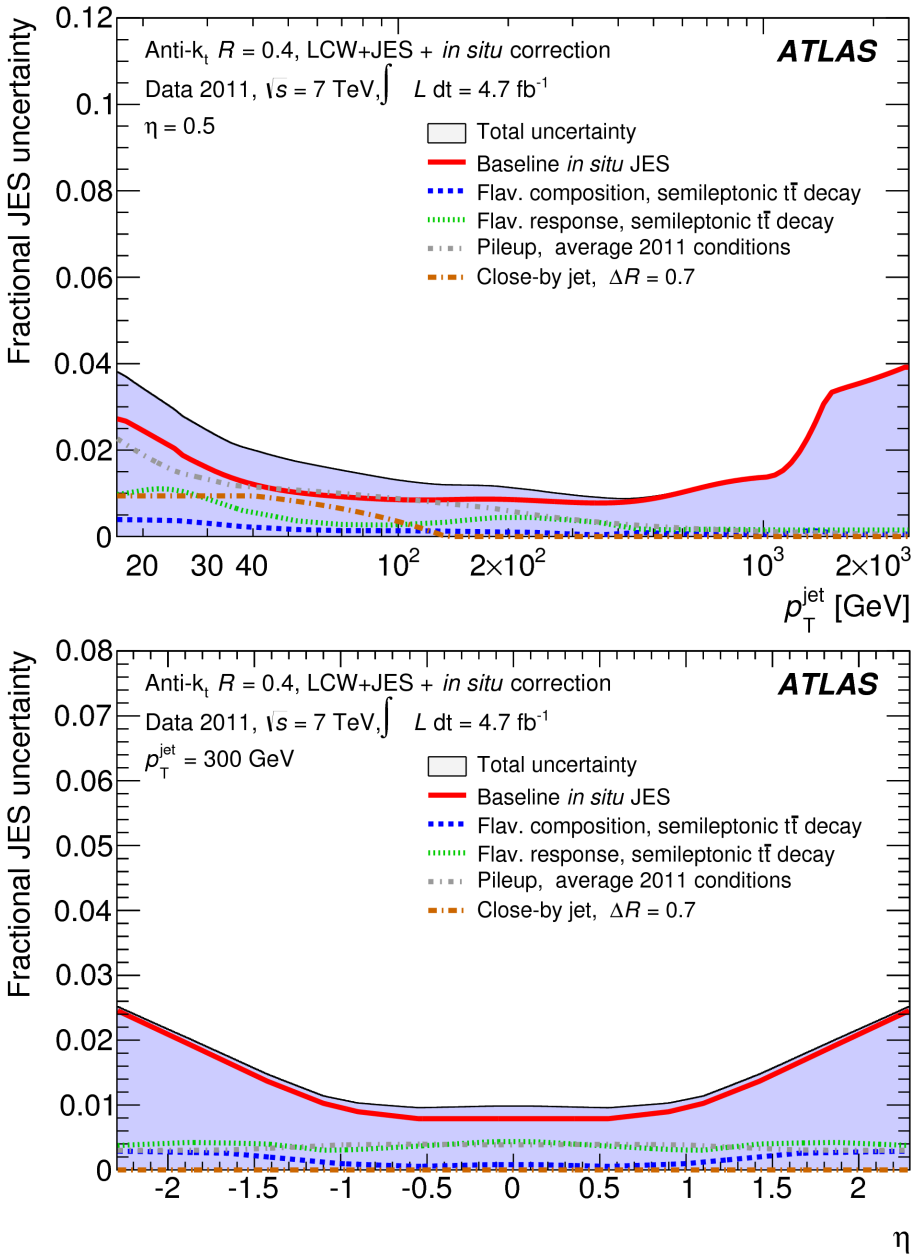

Figure 29: Fractional in situ jet energy scale systematic uncertainty as a function of the jet p_T for central jet and as function of η for jets with p_T = 300 GeV for anti-k_t jets with distance parameter of $R = 0.4$ calibrated using the LCW+JES calibration scheme. The contributions from each source of uncertainty is shown separately [222].

The uncertainty of JES has several components, such as in situ calibration uncertainties, pile-up uncertainty, flavor composition and flavor response uncertainty. In situ techniques exploit the transverse momentum balance between a jet and a well measured reference object [222]. To cover a large kinematic phase space different reference objects are used in various methods. For low jet energies the p_T balance of the jet against a Z boson or a photon is used. In order to probe jets with TeV energies multijet balance is used where the jet is balanced against one or more lower p_T jets. These uncertainties for the central region are shown in Figure 29 together with the total JES uncertainty. The JES uncertainty is found to be smaller than 4% and in the jet p_T region of 100-1000 GeV, it is less than 2%.

The jet energy resolution is measured in data by exploiting the p_T balance in events containing high-p_T jets with two in situ techniques: dijet balance and bisector method [225]. The resolutions obtained applying the in situ techniques to Monte Carlo simulation are in agreement within 10% with the resolutions determined by comparing jets at calorimeter and particle level.

5.3 b-JETS IDENTIFICATION

The identification of jets originating from the fragmentation of a B-hadron (b-tagging) is a powerful tool allowing the suppression of background processes that contain predominantly light-flavour jets. b-tagging is used in many physics analyses such as property measurements of the top quark, searches for the Higgs boson decaying to a b-quark pair ($H \to b\bar{b}$) and searches for new physics phenomena with decays to heavy flavour quarks. Several properties of b-jets are exploited in their identification. B-hadrons have a relatively long lifetime, of the order of 1.5 ps ($c\tau \sim 450$ μm). A B-hadron with $p_T = 50$ GeV will thus travel on average 3 mm in the transverse plane before decaying, leading to topologies with at least one vertex displaced from the interaction point. Because of the high b-quark mass, its decay products also tend to have higher p_T than for light jets. This causes b-jets to be wider, have higher particle multiplicities and large invariant masses. Various algorithms have been developed in ATLAS to identify b-jets [226].

- *Impact parameter taggers.* The tracks from b-hadron decay products tend to have rather large impact parameters which can be distinguished from tracks originating from the primary vertex. *IP3D* is a powerful algorithm relying on both the transverse and longitudinal impact parameters of the tracks associated with the jet. The transverse impact parameter, d_0, is the distance of closest approach of the track to the primary vertex point, in the $r - \phi$ projection. The longitudinal impact parameter, z_0, is the difference between the z coordinates of the primary vertex po-

sition and of the track at this point of closest approach in $r - \phi$. The correlation between the two input variables is taken into account using a two-dimensional log-likelihood ratio as discriminant.

- *Secondary vertex taggers.* An alternative strategy, exploited in the *SV0* and *SV1* algorithms, is the explicit reconstruction of the secondary vertex. *SV0* uses as discriminant the signed flight length significance, defined as the distance between the primary vertex and the inclusive secondary vertex divided by the measurement uncertainty. The significance is signed with respect to the jet direction, in the same way as the transverse impact parameter of tracks is. *SV1* is a similar algorithm providing higher performance due to the use of a likelihood ratio formalism. Three input variables are used: the invariant mass of all tracks used to reconstruct the vertex, the ratio of the sum of the energies of these tracks to the sum of the energies of all tracks in the jet, and the number of two-track vertices. In addition, the angle between the jet direction and the direction of the line joining the primary vertex is considered.

- *Decay chain reconstruction.* JetFitter is a decay chain reconstruction algorithm which aims at reconstructing the full hadron decay chain (from b- and c-quarks). It uses a Kalman filter to determine the trajectory defined by the primary and the b- or c-vertex, as well as their positions. The discrimination is obtained from a likelihood including track and vertex variables, as well as the flight length significances for each vertex [227].

The vertex-based algorithms exhibit much lower mistag rates than the impact-parameter-based tagger, but their efficiency for actual *b*-jets is limited by the low secondary vertex finding efficiency. Both approaches are therefore combined to define more versatile and powerful tagging algorithms. A powerful combination technique is the use of an artificial neural network, which can take advantage of complex correlations between the input variables. Two tagging algorithms are defined in this way. *IP3D*+JetFitter is a combination of the two *IP3D* and JetFitter weights. *MV1* is an artificial neural network using the results of the *IP3D*, *SV1* and *IP3D*+JetFitter algorithms as input, and provides the likelihood for a given jet to be originating from a *b*-, *c*- or light-quark. The MV1 tagger has been used *TODO* An operating point is chosen such that 70% of truth b-jets and about 1% of light-flavour or gluon jets are selected in simulated $t\bar{t}$ events [228, 229]. Charm-quark initiated jets are tagged with an efficiency of about 20%.

The performance of *b*-tagging algorithms is evaluated by measuring the efficiency to correctly identify jets originating from *b*-partons

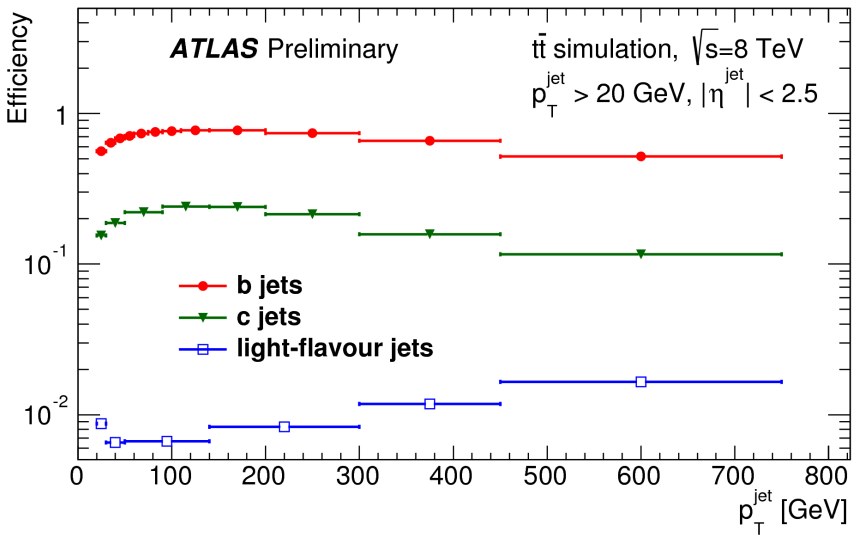

(a)

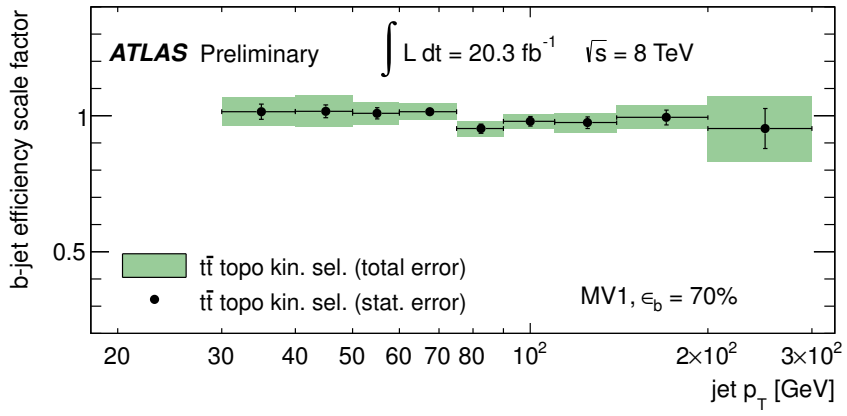

(b)

Figure 30: [Top] Efficiency of the MV1 tagger to select b, c, and light-flavour jets, as a function of jet p_T. The weight selection on the MV1 output discriminant is chosen to be 70% efficient for b jets with $p_T > 20$ GeV and $|\eta| < 2.5$, as evaluated on a sample of simulated $t\bar{t}$ events [229]. [Bottom] The b-tag efficiency data-to-simulation scale factor for the MV1 tagging algorithm at 70% efficiency on 8 TeV data, using using a tag and probe method based on kinematic selection on $t\bar{t}$ dilepton sample with two jets in the final state. The jets are reconstructed from topological clusters using the anti-k_t algorithm with a distance parameter of 0.4, applying the local calibration scheme [228].

in data as a function of the jet p_T. The efficiency in the simulation is then matched to the one in data with scale factors. The b-jet tagging efficiency is measured in a sample of jets containing muons and of $t\bar{t}$ events, which naturally contain a high fraction of b-jets, using a combination of different techniques. The efficiency for *c* and light-jets (mistag rate) is obtained from a sample of jets associated with D^* mesons and of c-hadrons produced in association with a *W* boson. The probability to misidentify light-quark and gluon jets as *b*-jets (mistag rate) has been measured on a sample of multijet events. A good agreement is found for combination of the various measurements, resulting in uncertainties for the b-tagging efficiency ranging from 2% to 4% for jets with p_T up to 200 GeV, rising to 12% for higher jets p_T.

5.4 MUONS

Muons are reconstructed using a statistical combination (STACO) algorithm, which performs a combination of the track parameters reconstructed in the muon spectrometer and in the inner detector using the corresponding covariance matrices [168].

Two different reconstruction criteria are used for the identification of muons.

- *Combined* (CB) muons consists of tracks which have been independently reconstructed in the MS and ID. This is the main type of reconstructed muons.
- *Segment-tagged* (ST) muons use a MS track to find corresponding one in the ID. ST muons are used to increase the acceptance in the cases in which the muon crossed only one layer of MS chambers, either because of its low p_T or because it falls in regions with reduced MS acceptance ($|\eta| \sim 0$ and $|\eta| \sim 1.2$).

The ID tracks used for muon reconstruction are required to have at least one pixel hit and 5 SCT hits and at most 2 active Pixel or SCT sensors transversed by the track but without hits. In the region of full TRT acceptance, $0.1 < |\eta| < 1.9$ at least 9 TRT hits are required. The number of Pixel and SCT hits is reduced by one if the track transverses a sensor module known to be inefficient according to a time dependent database.

The baseline selection requires the muons to pass the acceptance cuts $p_T > 10$ GeV and $|\eta| < 2.4$. Baseline muons are used for overlap removal with jets, photons and electrons. Further requirements are applied to select signal muons. The transverse impact parameter significance of the track, defined as $d_0/\sigma(d_0)$, calculated with respect to the primary vertex (defined in Section 5.1), is required to be less than 3 and the longitudinal impact parameter $z_0 \sin\theta$ to be less than 0.4 mm. The track-based isolation is defined as the scalar sum of

the p_T of tracks inside a cone of $\Delta R < 0.3$ around the lepton track and should be smaller than $0.12 \cdot \min(p_T, 60\ \text{GeV})$. The tracks considered in the sum must be compatible with the lepton vertex and have $p_T > 0.4$ GeV. The calorimeter-based isolation uses the transverse energy deposited in the calorimeter in a cone of radius $\Delta R < 0.3$ around the lepton, corrected for the effect of pileup, and must be less than $0.12 \cdot \min(p_T, 60\ \text{GeV})$.

The availability of two independent detectors to reconstruct the muons enables a precise determination of the muon reconstruction efficiency, as well as momentum scale and resolution parameters in the region $|\eta| < 2.5$. The muon reconstruction efficiency is measured using $Z \to \mu\mu$ and $J/\psi \to \mu\mu$ decays, using a Tag-and-Probe method [230]. A correction is applied to the simulation to account for discrepancies in the muon identification efficiency between data and MC. The measured reconstruction efficiencies for the combination of CB+ST muons is above 98% throughout the entire range with the exception of the central region of $|\eta| < 0.1$, where due to lacking instrumentation of the MS a drop to 65% is observed. The efficiencies are found to be stable as a function of the transverse momentum.

The momentum resolution and scale are additional important parameters used in the evaluation of the muon reconstruction performance. Decays of the Z, J/Ψ, and Υ resonances are used to determine the muon momentum resolution and scale and to derive a smearing correction to match the resolution in the simulation to data. The scale and momentum resolution parameters are determined in 16 different η regions of the detector using a maximum likelihood template fit to $Z \to \mu\mu$ data. The di-muon mass resolution ranges from 1.5 to 3 GeV at the Z mass in the different detector regions.

An excellent level of agreement between the corrected simulation and collision data is observed, with an agreement at permill-level through most of the detector, as shown in Fig 31.

5.5 ELECTRONS

The electron reconstruction [231] in the central region of the ATLAS detector ($|\eta| < 2.47$) starts from energy deposits (clusters) in the EM calorimeter which are then associated to reconstructed tracks of charged particles in the ID.

The EM calorimeter is segmented into towers of size $\Delta\eta \times \Delta\phi = 0.025 \times 0.025$. Inside each of these elements, the energy of all cells in all longitudinal layers is summed into the tower energy. These clusters are seeded by towers with total transverse energy above 2.5 GeV and searched for by a sliding-window algorithm [218], with a window size of 3×5 towers.

Once seed clusters have been found a matching to tracks reconstructed in the ID is performed. A loose matching is applied at this

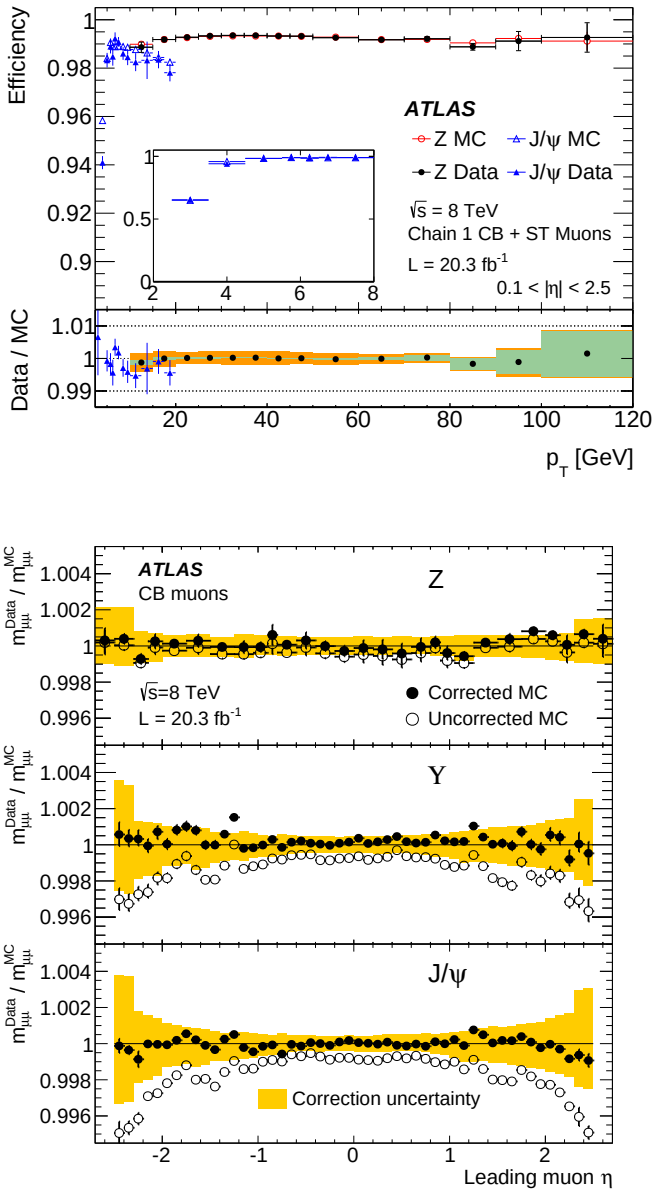

Figure 31: Measured reconstruction efficiency for CB+ST muons as a function of the muon p_T (top), for muons with $0.1 < |\eta| < 2.5$, obtained from $Z \to \mu\mu$ and $J/\Psi \to \mu\mu$ events. The green and orange areas in the bottom pad shows the statistical and total uncertainty, respectively. Ratio of the reconstructed mean mass $\langle m_{\mu\mu} \rangle$ for data and the corrected MC from J/Ψ, Υ and Z (bottom) as a function of the pseudorapidity of the leading muon [230].

stage, the distance between the track impact point and the position of the cluster must agree within $\Delta\eta < 0.05$. If more than one track is matched to the cluster, the match with the smallest ΔR distance is chosen. In order to correct for energy losses in the ID due to bremsstrahlung, the matched tracks are refitted using a Gaussian Sum Filter algorithm [232]. It yields a better estimate of the track parameters, especially in the transverse plane, by accounting for the non-linear bremsstrahlung effects.

The energy of the electron cluster is collected by enlarging its size to 3×7 in the EM barrel region and to 5×5 in the EM end-caps. The total electron energy is then computed by taking the sum of the energy deposited in the calorimeter cluster itself, the estimated energy deposited in front of the EM calorimeter, outside the cluster (lateral leakage), and beyond the LAr electromagnetic calorimeter (longitudinal leakage) [231, 233]. The correction for the material is aided by the measured presampler signal, while the other three corrections are derived from MC simulations. The four-momentum of the reconstructed electron is then computed using the cluster energy, with η and ϕ measured at the interaction vertex of the track. The absolute energy scale and the intercalibration of the different parts of the EM calorimeter are determined using pure samples of electrons from $Z \to ee$, $J/\Psi \to ee$ decays [233]. An independent cross-check of the in situ calibration is obtained from comparisons of the reconstructed energy with the momentum measured in the ID $W \to e\nu$ events.

The lineshape from $Z \to ee$ and $J/\Psi \to ee$ events is also used to determine the energy resolution and the residual difference between data and simulated event samples. Due to imperfections in the detector simulation, the energy resolution in data is about 1% larger than in the MC. This effect is corrected for with scale factors, having relative uncertainties ranging from 5% at 20 GeV to 20% at 100 GeV.

Reconstructed electrons suffer large backgrounds from different sources such as mis-identified hadrons, photon conversions, and semi-leptonic heavy-flavor decays. Additional identification criteria are applied to increase the purity of reconstructed electrons. The clusters associated with electron and photon candidates must satisfy a set of identification criteria, requiring their longitudinal and transverse profiles to be consistent with those expected for EM showers induced by such particles. Shower shape variables in both the first and second layers of the EM calorimeter and the fraction of energy deposited in the hadronic calorimeter are used in the *loose* selection with additional requirements on the associated track quality and track-cluster matching. Tightened requirements on these discriminating variables are added to the *medium* criteria together with a *loose* selection on the transverse impact parameter and on the number of hits in the TRT associated with the track, and a measured hit in the innermost layer

of the pixel detector to discriminate against photon conversions (if the transversed module is active). The *tight* selection adds a selection on the ratio of the candidate's reconstructed energy to its track momentum, E/p, stricter requirements on the discriminating variables and TRT information, and a veto on reconstructed photon conversion vertices associated with the cluster. The identification efficiencies are measured in $Z \to ee$ and $J/\Psi \to ee$ events, using a tag-and-probe technique [234, 231, 233] The ee line-shape for the calibrated data compared with the corrected simulation, and the identification efficiencies for various selection criteria measured in $Z \to ee$ decays are shown in Figure 32.

Baseline electrons are reconstructed using the *medium* identification criteria and they are further required to have $E_T = E^{clust}/\cosh(\eta)$ greater than 20 GeV and $|\eta^{clust}| < 2.47$. Signal electrons (used for the event classification) should pass the *tight* identification criteria, and are subject to additional requirements. To reject non-prompt leptons, we ask the transverse impact parameter significance of the track $d_0/\sigma(d_0)$ calculated with respect to the primary vertex to be less than 5 and the longitudinal impact parameter $z_0 \sin\theta$ to be less than 0.4mm. Signal leptons must also satisfy a cut on track and calorimeter isolation. To further suppress background from hadronic decays, an isolation requirement is applied. The calorimeter isolation transverse energy E_T^{cone} is computed by summing the transverse energy of all calorimeter cells in a cone of size ΔR around the candidate [218]. The isolation energy is corrected by subtracting the estimated contributions from the photon or electron candidate itself and from the underlying event and pile-up contributions using the technique proposed in Ref. [236] and implemented as described in Ref. [237]. A track isolation variable, p_T^{cone}, is also used for electrons. It is built by summing the transverse momenta of the tracks in a cone of size ΔR around the candidate, excluding the track associated with the candidate itself. The tracks considered in the sum must come from the reconstructed vertex with the highest sum of all associated tracks and must have at least four hits in either the pixel or SCT detector.

The track based isolation, in a cone of $\Delta R < 0.3$ around the lepton track, should be smaller than $0.18 \cdot \min(p_T, 60\ \text{GeV})$. The calorimeter-based isolation, also defined for a cone of $\Delta R < 0.3$, must be less than $0.18 \cdot \min(p_T, 60\ \text{GeV})$.

5.6 PHOTONS

Like electrons, photons interact electromagnetically, producing showers in the EM calorimeter. Being electrically neutral, they do not leave a track in the inner detector. They can however convert to an electron-positron pair in the presence of detector material.

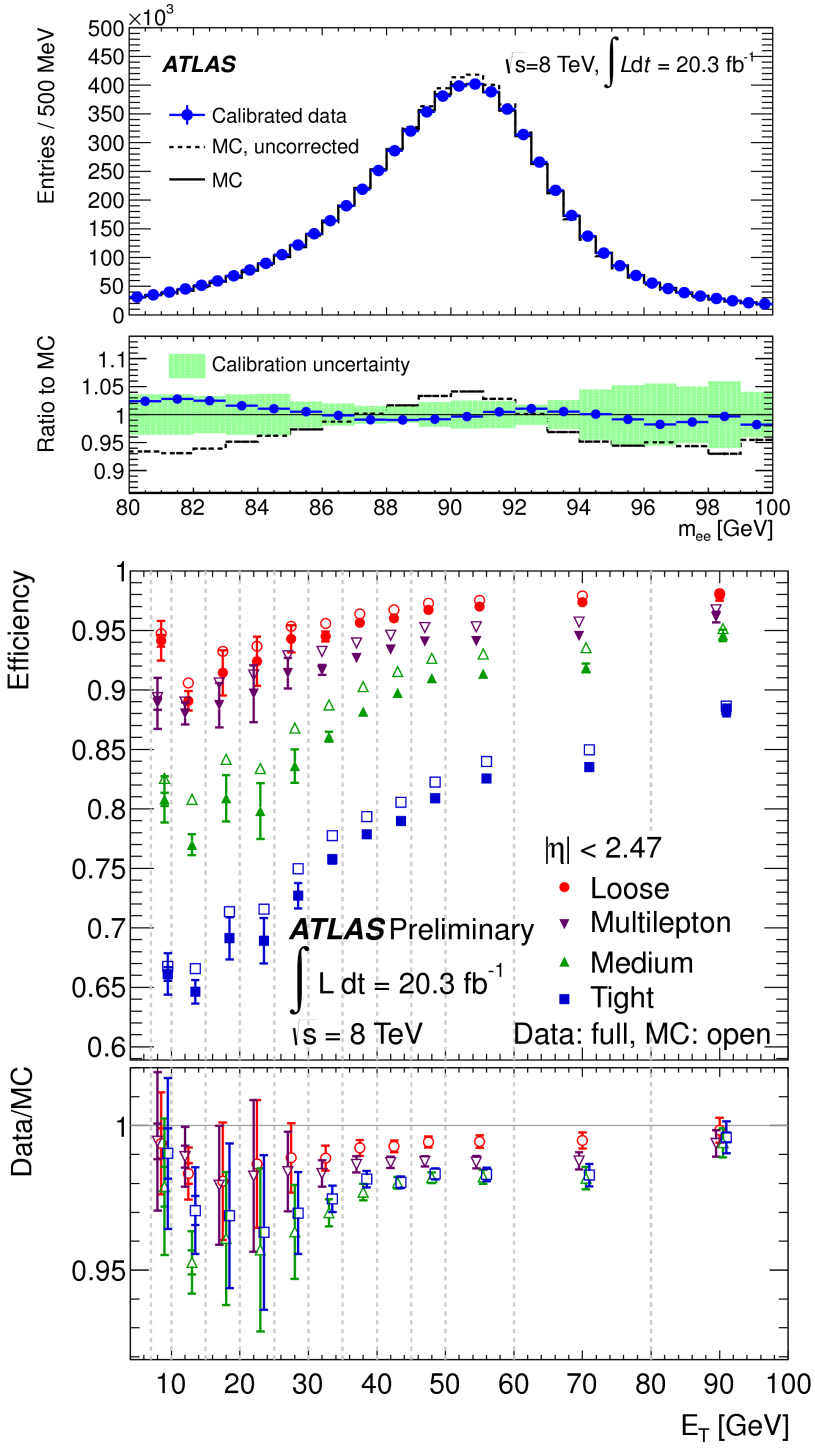

Figure 32: [Top:] Electron pair invariant mass distribution for $Z \to ee$ decays in data and improved simulation. Energy scale corrections are applied to the data. The improved simulation is shown before and after energy resolution corrections, and is normalised to the number of events in data [235]. [Bottom:] Identification efficiency in data as a function of E_T for the cut-based loose, multilepton, medium and tight selections, compared to MC expectation for electrons from $Z \to ee$ decay. The uncertainties are statistical (inner error bars) and statistical+systematic (outer error bars) [234].

Clusters without matching tracks are classified as unconverted photons [238]. Converted photons require a cluster with at least one matched track associated to a conversion vertex. If the matched track is consistent with originating from a photon conversion and if in addition a conversion vertex is reconstructed, the corresponding candidates are considered as converted photons. They are classified as single-track or double-track conversions depending on the number of assigned electron-tracks. The particular case of a conversion having only one matched track can occur if the conversion takes place late in the photon's trajectory, as it traverses the TRT; the resulting electron and positron are generally still quite close together as they exit the inner detector and the TRT is unable to resolve the two tracks separately.

The clustering algorithm for photons is almost identical to the electron algorithm. Converted photons use a window of size 3×7 cells in the barrel. Showers initiated by unconverted photons have a narrower lateral size, due to the lack of radiation, and a smaller window of 3×5 cells is used. A 5×5 cluster size is used in the end-cap for both converted and unconverted photons.

Similarly as for electrons, these lateral cluster sizes were optimised to take into account the different overall energy distributions in the barrel and endcap calorimeters while minimising the pile-up and noise contributions. The cluster energy is then determined by applying correction factors computed by a calibration scheme based on the full detector simulation [233, 235].

After reconstruction photons candidates contain a singificant contribution from misidentified jets with a large electromagnetic component, mostly from the decay of neutral particles (π^0, η). Two reference selections are defined for photon identification [239]. A *loose* selection is largely based on the analougue electron *loose* criteria, and is mostly used for triggering purposes The *tight* selection adds information from the finely segmented strip layer of the calorimeter, which provides good rejection of hadronic jets where a neutral meson carries most of the jet energy. The *tight* criteria are separately optimised for converted and unconverted photons, and depend on the reconstructed photon $|\eta|$ direction. They provide an identification efficiency above 85% for $E_T^\gamma > 40$ GeV with a background rejection factor of about 5000 [238].

Unlike electrons there is no single physics process able to produce a very clean sample of prompt photons over a large E_T^γ range. The identification efficiencies are obtained from different data-driven techniques: selecting photons from radiative decays of the Z boson, extrapolating photon properties from $Z \to ee$ decays and by estimating and subtracting the background fraction in a sample of isolated photon candidates.

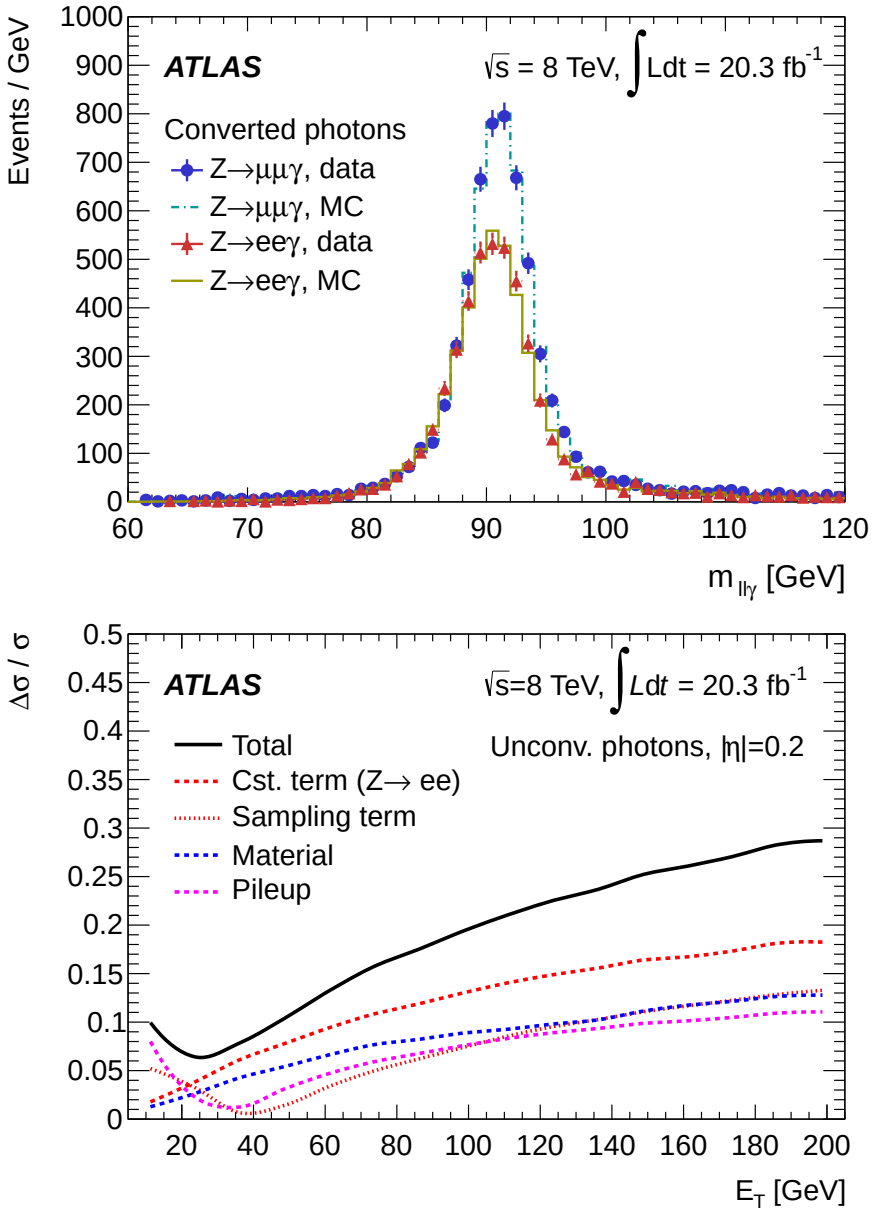

Figure 33: [Top:] Invariant mass distributions in data and simulation, for large-angle $Z \to ll\gamma$ events with converted photons in the electron and muon channels, for $\Delta R(l,\gamma) > 0.4$ and $E_T^{\gamma} > 15$ GeV. Energy corrections are applied. The MC simulation is normalised to the number of events in data. [Bottom:] Contributions of the different uncertainties to the relative resolution uncertainty as a function of E_T for unconverted photons with $|\eta| = 0.2$ [235].

Only photon candidates reconstructed in the fiducial region of the calorimeter are considered in the analysis, with the exception of the barrel-endcap transition region which suffers from a worse reconstruction efficiency. Photon candidates with a cluster containing a bad channel or overlapping with regions affected by a dead front-end board in the calorimeter are also rejected. As for electrons, the photon energy is smeared in Monte Carlo and slightly rescaled in data. The $m_{ll\gamma}$ distribution measured in a sample of radiated photons from Z decays compared to the corrected simulation, and the different contributions to the total photon energy resolution uncertainty measured in the same sample are shown in Figure 33. Signal photons are required to pass the cut-based tight photon identification, and a further selection based on a calorimetric isolation variable is applied. This observable provides further discrimination between genuine photons and fake candidates from jets. The isolation energy is defined as the sum of the transverse energy of the topo-clusters inside a cone of $\Delta R = 0.4$ around the photon, excluding a 5×7 grid of cells around the center of the cone. The isolation energy is corrected for lateral leakage in the calorimeter, causing the isolation energy to grow as function of the photon E_T, as well as for the average ambient energy (from the underlying event and pile-up) in the event. The expected soft contributions are subtracted on an event-by-event basis, the correction being based on the "jet area" method 5.2. The average contribution to the isolation from leakage are instead obtained from simulation. A requirement of an isolation energy E_T^{topo40} smaller than 4 GeV is applied to the signal photons [235].

5.7 MISSING TRANSVERSE ENERGY

Missing transverse energy is one of the most important observables at hadron colliders. It allows to discriminate leptonic decays of W bosons and top quarks from background events not containing neutrinos. It is also an important variable in searches for new weakly interacting, long-lived particles, which are predicted in many NP scenarios, including Supersymmetry. The $\vec{E}_{T^{mis}}$ is calculated from the vector sum of the energy deposits in the calorimeters and muons reconstructed in the muon spectrometer. It is typically described by its azimuthal angle and magnitude, ϕ^{miss} and E_T^{miss}. The E_T^{miss} reconstruction depends crucially on the calorimeter response. It is very sensitive to particle momentum mismeasurements, particle misidentification, detector malfunctions, particles transversing on poorly instrumented regions of the detector, cosmic-ray particles, and beam-halo particles, which may result in fake E_T^{miss}.

The ATLAS E_T^{miss} calculation [240, 241], uses reconstructed and calibrated physics objects. Calorimeter energy deposits are associated with a reconstructed and identified high-p_T parent object in a specific

order: electrons, photons, hadronically decaying tau-leptons, jets and finally muons. Deposits not associated with any such objects are also taken into account in the *soft term*.

$$E_{x(y)}^{miss} = E_{x(y)}^{miss,e} + E_{x(y)}^{miss,\gamma} + E_{x(y)}^{miss,jets} + E_{x(y)}^{miss,SoftTerm} + E_{x(y)}^{miss,\mu} \tag{71}$$

The E_T^{miss} calculation is shown in Eq. 71, where each term is calculated as the negative sum of the calibrated reconstructed objects, projected onto the x and y directions. Electrons are calibrated with the standard ATLAS electron calibration [233, 235] and photons are calibrated at the electromagnetic scale (EM). LCW+JES jets with calibrated p_T greater than 20 GeV are used in the calculation of the jet term. Because of the high granularity of the calorimeter, it is important to suppress noise contributions and to use in the E_T^{miss} calculation, in addition to the high-p_T reconstructed objects, only the calorimeter energy deposits containing a significant signal. This is achieved by calculating the E_T^{miss} soft term using only topo-clusters and tracks not associated to high-p_T objects (i.e. from unassociated topo-clusters and tracks), the topo-clusters being calibrated using the LCW technique and removing any overlap between tracks and topo-clusters. Since the analysis described here does not make use of reconstructed taus the standard ATLAS E_T^{miss} reconstruction has been modified to treat clusters associated with taus as jets. Hadronic taus are thus included either in the jet term or in the soft term, depending on the p_T of their associated jet. Contributions from muons are included in the muon term, using the muons passing the criteria described in Section 5.4 (including p_T >10 GeV) except the isolation requirement and before overlap removal. Muons reconstructed by segments which are matched to inner detector tracks extrapolated to the muon spectrometer (ST muons) are used to recover muons, typically of low p_T, which did not cross enough precision muon chambers to allow an independent momentum measurement in the muon spectrometer. To avoid double counting of energy, the parametrized muon energy loss in the calorimeters is subtracted in the E_T^{miss} calculation if the combined muon momentum is used.

Systematic uncertainties on the calibrated physics objects are evaluated independently and propagated to the E_T^{miss}. The remaining sources of uncertainties affect the soft term and arises from the MC modeling and the effects of pile-up. They are estimated using a method described in [243]. It uses the projection of the E_T^{miss} onto the Z boson transverse direction which provides a test of possible bias on the E_T^{miss} reconstruction. The data-MC ratio of this observable in $Z \to \mu\mu$ events without jets of $p_T > 20$ GeV is used as a measure of the systematic uncertainty on the soft term scale and resolution. It is found to be of the order of a few percent. The dependence of the E_T^{miss} resolution

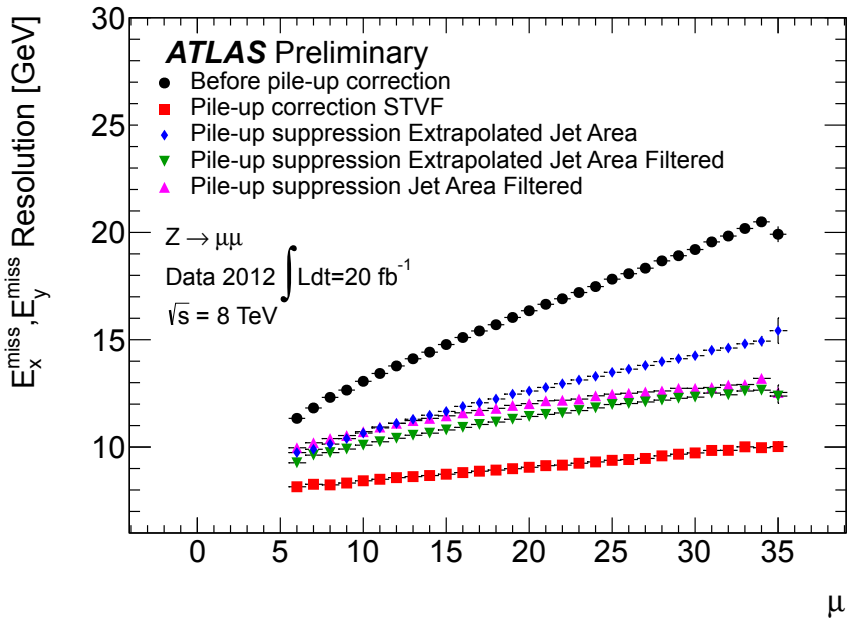

Figure 34: The dependence of the uncorrected and corrected E_T^{miss} resolution on the average number of interactions μ, measured in a large time window around the triggered events, for an inclusive $Z \to \mu\mu$ data sample [242].

on the average number of interactions in an event, obtained from an inclusive sample of $Z \to \mu\mu$ decays, is shown in Figure 34.

5.8 OVERLAP REMOVAL

After the objects reconstruction as described in the previous sections, remaining ambiguities between candidate jets with $|\eta| < 2.5$, leptons and photons are resolved using a method similar to Ref. [244]. First, any such jet candidate lying within a distance $\Delta R = 0.2$ from a baseline electron or photon is discarded. Then any lepton or photon candidate within a distance $\Delta R = 0.4$ of a jet candidate is discarded. To reduce the amount of electrons coming from the conversion of an FSR photon any baseline electron candidate within a distance of $\Delta R = 0.1$ to a muon is removed.

Part III

ANALYSIS

6

A STUDY OF THE SENSITIVITY TO THE PYTHIA8 PARTON SHOWER PARAMETERS OF $t\bar{t}$ PRODUCTION MEASUREMENTS IN pp COLLISIONS AT $\sqrt{s} = 7$ TEV WITH THE ATLAS EXPERIMENT AT THE LHC.

In this chapter various measurements of $t\bar{t}$ observables, performed by the ATLAS experiment in pp collisions at $\sqrt{s} = 7$ TeV, are used to constrain the initial- and final-state radiation parameters of the Pythia8 Monte Carlo. The tunes of the parton shower parameters to the measurements of $t\bar{t}$ production are compared to previous tunes to the Z boson transverse momentum at the LHC, and to the LEP event shapes in Z boson hadronic decays. Such a comparison provides a test of the universality of the parton shower model. The resulting tunes are applied to the NLO+PS generators MadGraph5_aMC@NLO and Powheg, and additional parameters of these generators are tuned to the $t\bar{t}$ data. For the first time in the context of Monte Carlo tuning, the correlation of the experimental uncertainties has been used to constrain the parameters of the Monte Carlo models.

6.1 MOTIVATION AND STRATEGY

The physics models employed in the Monte Carlo (MC) event generators are expected to describe simultaneously a large variety of hard scattering processes in different type of collisions [245]. Stringent tests of the universality of such models can be obtained by performing independent optimization of their parameters, henceforth referred to as *tunes*, on various hard scattering processes, on various observables, at various collider energies, or with different collider types [246]. As suggested in Ref. [247], the consistency of independent tunes supports the universality of the model, whereas deviations from this universal behavior can be associated with a breakdown of the modeling. The observed deviations between data and predictions, and the tensions between the various observables, can provide important information on the nature of the breakdown.

Measurements of $t\bar{t}$ production in hadronic collisions are sensitive to the parameters of the parton shower models. At the LHC pp collider, for the first time, $t\bar{t}$ processes can be measured with enough accuracy so as to be used for constraining the parameters of the MC models. The ATLAS experiment has performed various measurements of $t\bar{t}$ observables in pp collisions at $\sqrt{s} = 7$ TeV [248, 249, 250], some of which have been recently used in the A14 global tune

of PYTHIA8 [251]. In this study we evaluate the sensitivity of these $t\bar{t}$ measurements to the initial- (ISR) and final-state radiation (FSR) parameters of the PYTHIA8 Monte Carlo. Also, by performing independent tunes to these measurements, the resulting optimised values of the parameters can be compared against the values constrained by other observables, such as the Z boson transverse momentum as measured by ATLAS [252] and event shapes in Z boson hadronic decay as measured at LEP [253, 254, 255, 256]. The compatibility of the resulting parameters support the use of $t\bar{t}$ measurements in the context of global tunes.

The modeling of ISR and FSR in $t\bar{t}$ events is primordial to a precise measurement of the mass of the top quark, m_t. In the most precise single measurement of m_t at the Tevatron, performed with the D0 experiment [257], the uncertainty due to the modeling of ISR and FSR is constrained from the measurement of the Z/γ^* boson transverse momentum distribution [258]. This technique, which provides a significant reduction of the modeling uncertainty, assumes the universality of the parton shower model between Z boson and $t\bar{t}$ production. Whereas at the Tevatron both processes are dominated by quark-antiquark initiated production, at the LHC the $t\bar{t}$ process is dominated by gluon-gluon initiated production, and even more so the universality of ISR needs to be verified.

The NLO+PS MC event generators include next-to-leading order (NLO) corrections, in the perturbative expansion of the strong-coupling constant α_s, to the calculations of the matrix element, and supplement them with parton showers (PS). The NLO+PS predictions are less sensitive to variations of renormalisation and factorisation scales, have better accuracy in the total cross sections rates, and include effects of spin correlation. Such generators are generally preferred to PYTHIA8, which calculates the hard scattering only at leading order (LO). Also the NLO+PS generators are expected to benefit from an improved tune of the PS, and to this purpose, the PYTHIA8 tunes to the ATLAS $t\bar{t}$ measurements are applied to the NLO+PS generators POWHEG+PYTHIA8 and MadGraph5_aMC@NLO+PYTHIA8. Additional parameters of the POWHEG and MadGraph5_aMC@NLO generators, which show sensitivity to the $t\bar{t}$ measurements, are tuned to the data.

6.2 METHODOLOGY

Three ATLAS measurements of $t\bar{t}$ production at $\sqrt{s} = 7$ TeV are used to constrain the ISR and FSR parameters of the PYTHIA8 MC: differential $t\bar{t}$ cross sections as functions of jet multiplicity and jet transverse momentum [250], $t\bar{t}$ production with a veto on additional central jet activity [248], henceforth referred to as gap fraction measurements, and jet shapes in $t\bar{t}$ events [249]. The statistical correlations among

the various observables of these $t\bar{t}$ measurements were not studied, hence a set of observables is chosen, which are sufficiently statistically independent, so as to avoid any bias in the results.

The production of additional jets in $t\bar{t}$ events is sensitive to higher-order perturbative QCD effects. The present measurement is complementary to the measurement of $t\bar{t}$ production with a veto on additional jet activity [248], which is mostly sensitive to the first perturbative QCD emission. In Ref. [250] the $t\bar{t}$ production cross-section is measured differentially in jet multiplicity and in jet transverse momentum in the single-lepton channel, without explicit separation between jets related to $t\bar{t}$ decays and additional jets. These differential cross-sections are particularly sensitive to the modelling of higher-order QCD effects in Monte Carlo (MC) generators [69, 259]. The jet multiplicity is measured for several different p_T thresholds to probe the p_T-dependence of the hard emission. Especially for values larger than four, the number of jets is closely related to the number of hard emissions in QCD bremsstrahlung processes. The differential cross-section is measured separately for the five highest p_T jets. For large transverse momenta, above approximately 130 GeV, the leading jet p_T is correlated with the p_T of the $t\bar{t}$ system, as illustrated in figure 35. Therefore, measurements of the leading jet p_T provide complementary information to other existing differential production cross-section measurements of the top-quark [260]. The differential cross sections as functions of the leading-jet p_T, of the 5th leading-jet p_T, of jet multiplicity for jets with $p_T \geqslant 25$ GeV and jet multiplicity for jets with $p_T \geqslant 80$ GeV are used. The overall normalisation of these observables is sensitive to higher-order QCD corrections. In order to reduce the effect of missing higher-order QCD corrections on the minimisation of the MC parameters, the predictions of the $t\bar{t}$ + jets differential cross sections are normalised to the data, separately for each observable.

A common method to carachterize the jet activity arising from quark or gluon radiation produced in association with the $t\bar{t}$ system is to determine the fraction of events that do not contain additional jets above a given threshold. This measurement is performed in the dileptonic channel, to ensure that the additional jets can easily be distinguished from the $t\bar{t}$ decay products. The gap fraction observable is defined as $f(Q_0) = n(Q_0)/N$ where N is the number of selected $t\bar{t}$ events and $n(Q_0)$ the fraction of those events that do not contain an additional jet with $p_T > Q_0$ in a central rapidity interval $|y| < 2.1$. With the above definition the gap fraction is mostly sensitive to the leading-p_T emission accompanying the $t\bar{t}$ system. The veto criterion can however be extended to probe jet activity beyond the leading additional jet. As many of the experimental systematic uncertainties cancel in the ratio the gap fraction data are expected to constrain the modelling of quark and gluon radiation in $t\bar{t}$ events. The gap frac-

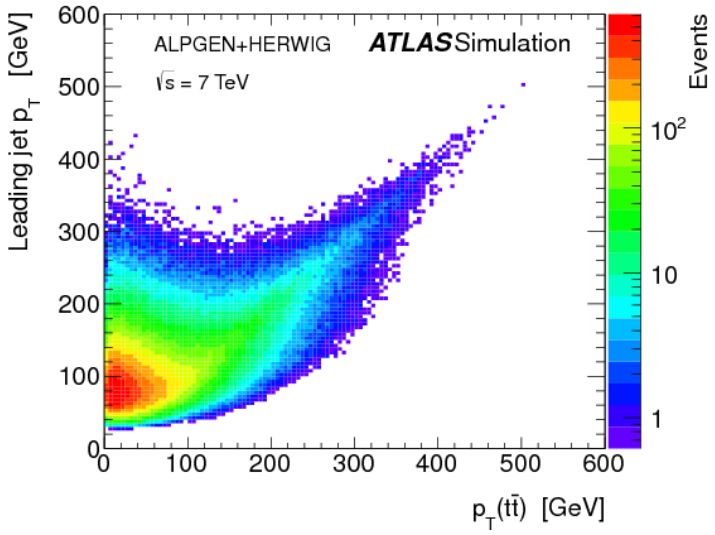

Figure 35: The relationship between the p_T of the $t\bar{t}$ system in the single-lepton channel and the p_T of the highest p_T jet in $t\bar{t}$ events generated with ALPGEN+HERWIG. The p_T of the $t\bar{t}$ system is taken at parton level and the leading jet is constructed at particle level [250].

tion has been measured in [248] for Q_0 and Q_{sum} between 25 GeV and 325 GeV and in four rapidity intervals: $|y| < 0.8$, $0.8 \leqslant |y| \leqslant 1.5$, $1.5 \leqslant |y| \leqslant 2.1$ and $|y| < 2.1$. Only the inclusive gap fraction as a function of the leading-jet p_T threshold, Q_0, is used in this study. The inclusive gap fraction as a function of the scalar transverse momentum sum of the additional jets, Q_{sum} is considered statistically correlated to the inclusive gap fraction as a function of Q_0, and is not used. The differential gap fraction measurements as a function of rapidity are also not used since the parameters of the model do not show sensitivity to the rapidity dependence of the gap fraction.

In Ref. [249], the differential and integral jet shapes as a function of the jet radius r are measured for light- and b-jets in five exclusive p_T ranges of the jet. Samples of top-quark pair events are selected in both the single-lepton and dilepton final states. The shapes of the jets initiated by bottom-quarks from the top-quark decays are compared with those of the jets originated by light-quarks from the hadronic W boson decays in the single-lepton channel. Jet shapes are sensitive to the details of the parton-to-jet fragmentation processes, such as the value of α_S used in the branchings of FSR, the fragmentation model and the underlying event. In this study only the differential jet shapes are used. They are defined as the average fraction of transverse momentum contained within an annulus of inner radius $r_a = r - \delta r/2$

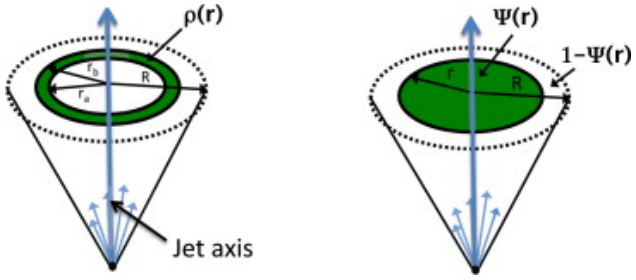

Figure 36: Definition of jet shape variables for a jet of radius R [261]. (Left:) Differential jet shape, $\rho(r)$, average fraction of transverse momentum contained within an annulus between the outer radius r_b and the inner radius r_a. (Right:) Integrated jet shape, $\psi(r)$, defined as the average fraction of transverse momentum contained within a distance r from the jet axis. $1-\psi(r)$ gives the fraction of average transverse momentum in the outer part of the jet and is often used as observable to quantify the change of the jet shape as a function of jet p_T.

and outer radius $r_b = r + \delta r/2$, where r is measured relative to the jet axis and lies in the range $\delta r/2 \leqslant r \leqslant R - \delta r/2$.

$$\rho(r) = \frac{1}{\delta r} \cdot \frac{1}{N_{jets}} \cdot \sum_{jets} \frac{p_T(r_a, r_b)}{p_T(0, R)} \tag{72}$$

R represents the maximum radius, and is set to be 0.4, the radius used in the jet reconstruction algorithm. The width of the annulus (δr) is set to 0.004 and $p_T(r_a, r_b)$ is the scalar sum of the p_T of the jet constituents with radii between r_a and r_b. Recently, another measurement of $t\bar{t}$ production in pp collisions has been performed with the ATLAS detector [262], in which differential cross sections are presented in terms of kinematic variables whose dependence on theoretical models is minimal. This measurement, which is not included in this study, is also expected to be sensitive to QCD radiation.

The Pythia8 MC version 8.201 is used throughout this study. The 4C [263] tune with the CTEQ6L1 PDF set [264], or the more recent Monash [246] tune with the NNPDF2.3 LO PDF set [265] are used as baselines for the optimisation of the parameters, henceforth referred to as *tuning*. In the Pythia8 MC event generator, the matrix elements for $t\bar{t}$ production are computed at LO, and supplemented with parton showers. The $t\bar{t}$ process receives significant corrections at NLO in α_s, and such corrections need to be accounted for when performing a tuning of the parton shower parameters to observables in the $t\bar{t}$ final state. In Ref. [259] it was shown that a modification of the parton shower emission probability with a damping factor can be used to approximate the effect of NLO corrections to the $t\bar{t}$ production. The ISR emission probability $\mathcal{P}_{ISR}$ is modified as

$$\frac{d\mathcal{P}_{ISR}}{dp_T^2} \propto \frac{1}{p_T^2} \frac{k^2 M^2}{k^2 M^2 + p_T^2} \tag{73}$$

where p_T is the transverse momentum evolution variable, as defined in Ref. [93], M is the factorisation scale, which is set to the smaller of the squared transverse masses of the two outgoing particles, and k is a fudge factor of order unity, which corresponds to the tunable parameter $p_{T,\text{damp}}^{\text{ISR}}$. The scale $k \cdot M$ corresponds to a transition from the $1/p_T^2$ to the $1/p_T^4$ behaviour in the probability of ISR emission.

Four parameters of the PYTHIA8 parton shower model are studied and tuned to the data: two ISR parameters correspond to the value of the strong-coupling constant at the mass of the Z boson for ISR, $\alpha_s^{\text{ISR}}(m_Z)$, and the fudge factor for the damping of the ISR radiation, $p_{T,\text{damp}}^{\text{ISR}}$, and two FSR parameters are the value of $\alpha_s^{\text{FSR}}(m_Z)$ and the infrared cut-off $p_{T,\text{min}}^{\text{FSR}}$. A similar fudge factor for the damping of the FSR radiation, $p_{T,\text{damp}}^{\text{FSR}}$, has been considered, but the data does not show sensitivity to this parameter. Higher-order corrections can be partially absorbed in the effective values of $\alpha_s^{\text{ISR}}(m_Z)$ and $\alpha_s^{\text{FSR}}(m_Z)$. However the structure of higher-order splitting kernels differs between ISR and FSR [266], hence the $\alpha_s^{\text{ISR}}(m_Z)$ and $\alpha_s^{\text{FSR}}(m_Z)$ parameters are allowed to assume different values in the tuning. The strategy followed in this study is to first perform independent tuning of the ISR and FSR parameters: the results of these tunes can be compared to previous tunes to test the universality of the model separately for ISR and FSR. Later, a simultaneous tune of ISR and FSR is performed, which accounts for the interplay between the ISR and FSR parameters. Whereas the values of $\alpha_s^{\text{ISR}}(m_Z)$, $\alpha_s^{\text{FSR}}(m_Z)$, and $p_{T,\text{min}}^{\text{FSR}}$ are expected to be process-independent parameters of the PYTHIA8 parton shower model, the value of $p_{T,\text{damp}}^{\text{ISR}}$ is expected to be process-specific. Moreover, the damping of the ISR emission probability should be used only when showering LO $t\bar{t}$ matrix-element calculations, and disabled by setting `SpaceShower:pTdampMatch=0` when PYTHIA8 is interfaced to NLO $t\bar{t}$ or multi-leg $t\bar{t}$+jets MC generators.

After tuning the ISR and FSR parameters to the $t\bar{t}$ data, the resulting PYTHIA8 tune is used with the NLO+PS generators POWHEG v2-r2915 [267, 78, 79, 268] and MadGraph5_aMC@NLO v2.2.2 [80]. The CT10nlo PDF set [269] is used in both POWHEG and MadGraph5_aMC@NLO. The renormalisation and factorisation scales in MadGraph5_aMC@NLO are set to the sum of the transverse masses of the top and the antitop. In POWHEG they are set at the generator default value Q, defined as $Q = \sqrt{m_t^2 + p_T^2}$, where m_t and p_T are the top quark mass and the top quark transverse momentum evaluated for the underlying Born configuration (i.e. before radiation). In the POWHEG generator, it is possible to introduce a damping factor

$$F = \frac{\texttt{hdamp}^2}{p_T^2 + \texttt{hdamp}^2} \tag{74}$$

to the singular part of the real radiation [77], where p_T is the transverse momentum of the $t\bar{t}$ system. The `hdamp` parameter is parametrised

Table 2: Parameter ranges used for the tuning of PYTHIA8, and the corresponding parameters of the 4C and Monash tunes. The '-' symbol is used in case the setting is not applicable.

Parameter	PYTHIA8 setting	Variation range	4C	Monash
$\alpha_s^{ISR}(m_Z)$	`SpaceShower:alphaSvalue`	$0.110 - 0.140$	0.137	0.1365
ISR damping	`SpaceShower:pTdampMatch`	1 (fixed)	0	0
$p_{T,damp}^{ISR}$	`SpaceShower:pTdampFudge`	$0.8 - 1.8$	-	-
$\alpha_s^{FSR}(m_Z)$	`TimeShower:alphaSvalue`	$0.110 - 0.150$	0.1383	0.1365
$p_{T,min}^{FSR}$ [GeV]	`TimeShower:pTmin`	$0.1 - 2.0$	0.4	0.5

as `hdamp` $= h \cdot m_t$, and the factor h is tuned to the $t\bar{t}$ data. Previous studies showed that values of h between one and two lead to a good description of QCD radiation in $t\bar{t}$ events [270, 271]. The starting scale of the parton shower is set to the p_T of the $t\bar{t}$ system. In the MadGraph5_aMC@NLO generator, it is possible to change the upper scale for the MC subtraction term, which corresponds to the starting scale of the parton shower [80]. The upper scale for the MC subtraction term is set as a fraction of a reference scale, which corresponds to the invariant mass of the $t\bar{t}$ system. The parameters `frac_upp` and `frac_low`, determine the minimum and maximum fractions, respectively, of the reference scale, which are used as an upper limit for the MC subtraction term. The parameters `frac_upp` and `frac_low` are set to `frac_upp` $=$ `frac_low` $= f$, the sensitivity of the $t\bar{t}$ measurements to the f parameter is studied, and the optimal value is extracted from the data. Unlike the parton shower parameters $\alpha_s^{ISR}(m_Z)$, $\alpha_s^{FSR}(m_Z)$, and $p_{T,min}^{FSR}$, the parameters `hdamp`, `frac_upp` and `frac_low` are expected to be process dependent, and the results obtained are specific to $t\bar{t}$ production. In the tuning of the `hdamp` parameter in POWHEG, and of the `frac_upp` and `frac_low` parameters in MadGraph5_aMC@NLO, the PYTHIA8 parton shower parameters are fixed to the values obtained by tuning PYTHIA8 to the $t\bar{t}$ measurements. This is based on the assumption that the effective values of $\alpha_s^{ISR}(m_Z)$ and $\alpha_s^{FSR}(m_Z)$ are not significantly affected by the inclusion of the NLO corrections to the calculations of the matrix elements of the $pp \to t\bar{t}$ process. Tables 2 and 3 show the parameters, the corresponding MC settings, and the ranges considered in the tuning for PYTHIA8 and for the NLO+PS generators, respectively.

The tuning is performed using Professor v1.4 [110] for the fit to the data, and Rivet v2.2.0 [272] for the implementation of the measurements. The method implemented in Professor permits the simultaneous tuning of several parameters by using an analytic approximation for the dependence of the physical observables on the model parame-

Table 3: Parameters ranges used for the tuning of POWHEG+PYTHIA8 and MadGraph5_aMC@NLO+PYTHIA8, and the corresponding default values.

POWHEG setting	Variation range	default
$\texttt{hdamp} = h \cdot m_t$	$0.5 \cdot m_t - 4.0 \cdot m_t$	∞
MadGraph5_aMC@NLO setting		
$\texttt{frac_low} = \texttt{frac_upp} = f$	$0.2 - 1.0$	$\texttt{frac_low} = 0.1$ $\texttt{frac_upp} = 1.0$

ters, an idea first introduced in Ref. [255]. Polynomials of third-order are used to parametrise the response of the observables to the generator parameters, the coefficients in the polynomials are obtained by fitting MC predictions generated at a set of randomly selected parameter points, called anchor points. The number of anchor points used is 50 for one-parameter tuning, 100 for two-parameters tuning, and 400 for four-parameters tuning, with $2 \cdot 10^6$ dilepton $t\bar{t}$ events and 10^7 semileptonic $t\bar{t}$ events generated at each point. The optimal values of the model parameters are obtained with a standard χ^2 minimisation of the analytic approximation to the corresponding data using MINUIT [112]. The MC statistical uncertainties are treated as uncorrelated and included in the definition of the χ^2 function. For the first time in the context of parton shower tuning in MC simulations, the correlation of the experimental uncertainties is included in the χ^2 minimisation. In presence of correlations, the χ^2 function is defined as:

$$\chi^2 = (\vec{x} - \vec{\mu})^T C^{-1} (\vec{x} - \vec{\mu}) \tag{75}$$

where $\vec{x}$ is the vector of data, $\vec{\mu}$ the interpolated MC prediction and C the covariance matrix of the data. Each source of systematic uncertainty is treated as fully correlated across the bins of each observable, and across the various observables of each of the three $t\bar{t}$ measurements. The measurement of the gap fraction has also a significant bin-to-bin statistical correlation, which is considered in the definition of the covariance matrix C. The MC statistical uncertainty of the $t\bar{t}$ +jets measurement is considered uncorrelated across bins.

6.3 SENSITIVITY STUDY

As a first step in the process of tuning the MC to the $t\bar{t}$ measurements, a study of the sensitivity of the various observables to the parameters is performed. The results of the sensitivity study can guide the selec-

tion of the observables to use for tuning the ISR and FSR parameters, respectively, and the parameters of the NLO+PS generators.

The sensitivity of each observable bin to a set of parameters p_i, is estimated from the interpolated response of the observables to the parameters, with the following formula:

$$S_i = \frac{\partial MC(\vec{p})}{|MC(p_0)| + \epsilon w_{MC}} \frac{|p_{0,i}| + \epsilon w_{p_i}}{\partial p_i} \tag{76}$$

where p_0 is the centre of the parameters range, $MC(p_0)$ is the interpolated MC prediction at p_0 and the ϵ terms, set to 1% of the parameter range are introduced to avoid the ill defined case $MC(p_0) = 0$, $\partial p_i = 0$. w_{p_i} corresponds to 80% of the original sampling range and is used to construct w_{MC}. Figure 37 shows the sensitivity of the differential $t\bar{t}$ cross sections as functions of jet multiplicity and jet transverse momentum, and of the gap fraction as a function of Q_0, to the PYTHIA8 parton shower parameters. Both measurements are mostly sensitive to the ISR parameters $\alpha_s^{ISR}(m_Z)$ and $p_{T,damp}^{ISR}$, and to less extent to the FSR parameter $\alpha_s^{FSR}(m_Z)$. Figure 38 shows the sensitivity of the light-jet shapes to the PYTHIA8 parton shower parameters. The light-jet shapes are mostly sensitive to the FSR parameter $\alpha_s^{FSR}(m_Z)$, some sensitivity is observed also to the FSR parameter $p_{T,min}^{FSR}$ and to the ISR parameter $\alpha_s^{ISR}(m_Z)$. Similar sensitivities are observed for the *b*-jet shapes.

Based on the results of the sensitivity study, the differential $t\bar{t}$ cross sections as functions of jet multiplicity and jet transverse momentum, and the gap fraction as a function of Q_0 are used to study the consistency of the ISR parameters with previous tunes to the Z boson transverse momentum, whereas the jet-shapes are used to study the consistency of the FSR parameters with previous tunes to the LEP measurements. However, the sensitivity study also shows that the ISR and FSR parameters are not completely decoupled: the observables sensitive to the ISR parameters have some sensitivity to $\alpha_s^{FSR}(m_Z)$, and the observables used to tune the FSR parameters have some sensitivity to $\alpha_s^{ISR}(m_Z)$. To account for such an interplay between ISR and FSR parameters, a simultaneous tune of ISR and FSR parameters is performed using all the measurements.

Figure 39 shows the sensitivity of the differential $t\bar{t}$ cross sections as functions of jet multiplicity and jet transverse momentum, and of the gap fraction as a function of Q_0, to the h and f parameters of POWHEG and MadGraph5_aMC@NLO. The light- and *b*-jet shapes have negligible sensitivity to the h and f parameters, hence only the $t\bar{t}$ + jets differential cross sections and the $t\bar{t}$ gap fraction measurement are used in the tuning of these parameters.

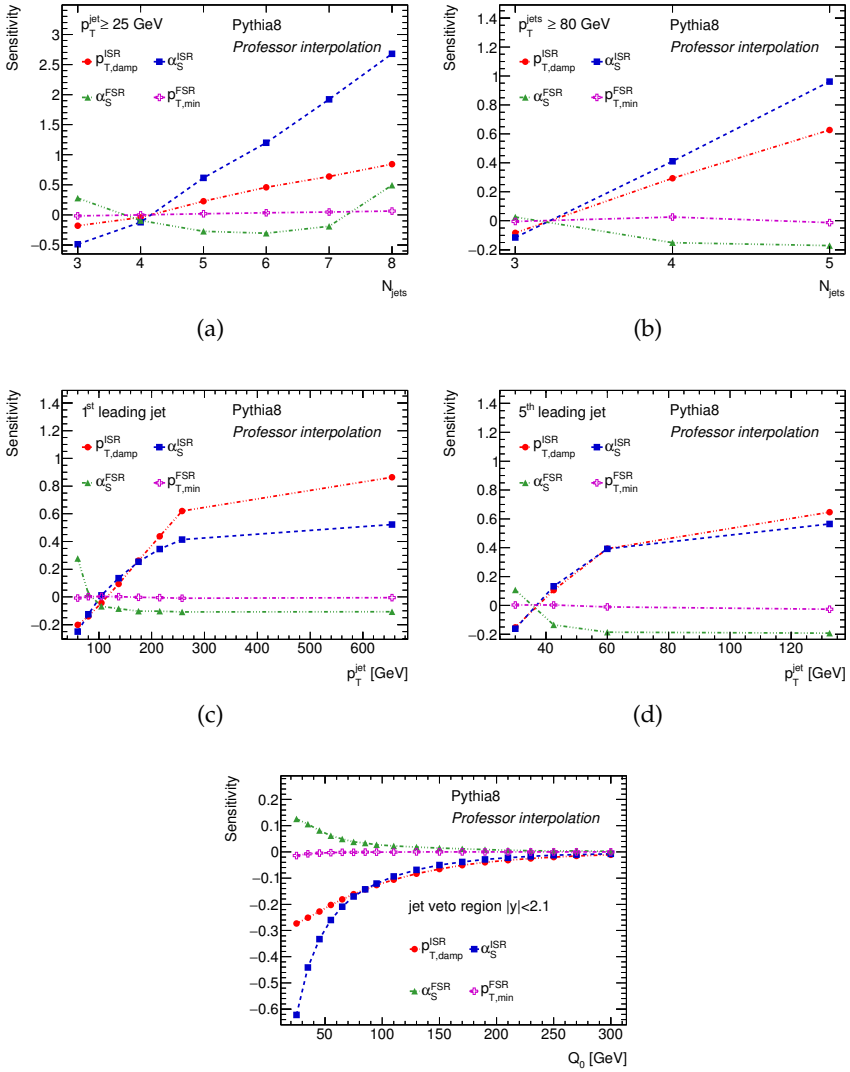

Figure 37: Sensitivity of the differential $t\bar{t}$ cross sections and $t\bar{t}$ gap fraction to the PYTHIA8 parton shower parameters $p_{T,damp}^{ISR}$ (red circles), $\alpha_s^{ISR}(m_Z)$ (blue squares), $\alpha_s^{FSR}(m_Z)$ (green triangles), and $p_{T,min}^{FSR}$ (magenta crosses). The sensitivities are shown as functions of (a) jet multiplicity for jets with $p_T{}^{jet} \geqslant 25$ GeV, (b) jet multiplicity for jets with $p_T{}^{jet} \geqslant 80$ GeV, (c) leading-jet transverse momentum, (d) 5th-leading jet transverse momentum, and (e) gap fraction as a function of Q_0.

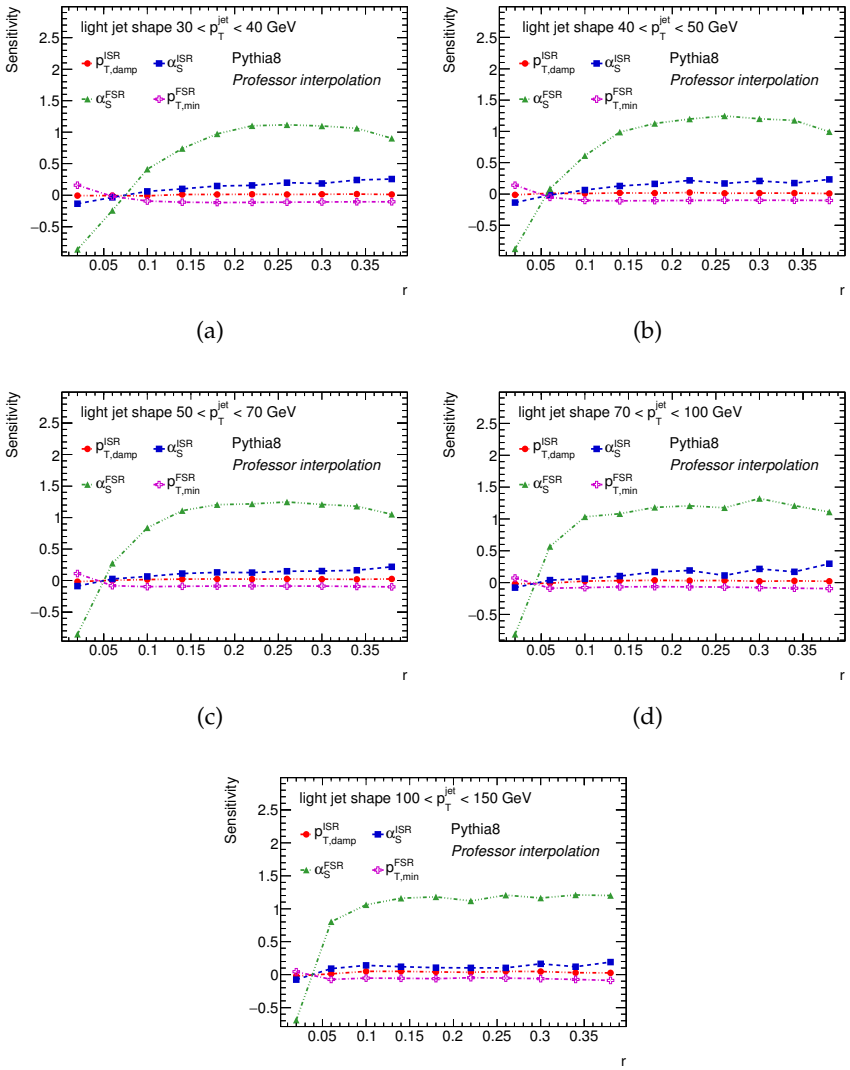

(a) (b) (c) (d) (e)

Figure 38: Sensitivity of the light-jet shapes to the PYTHIA8 parton shower parameters $p_{T,damp}^{ISR}$ (red circles), $\alpha_s^{ISR}(m_Z)$ (blue squares), $\alpha_s^{FSR}(m_Z)$ (green triangles), and $p_{T,min}^{FSR}$ (magenta crosses). The sensitivities are shown as functions of the light-jet radius r for jets with (a) $30 < p_T^{jet} < 40$ GeV, (b) $40 < p_T^{jet} < 50$ GeV, (c) $50 < p_T^{jet} < 70$ GeV, (d) $70 < p_T^{jet} < 100$ GeV, and (e) $100 < p_T^{jet} < 150$ GeV.

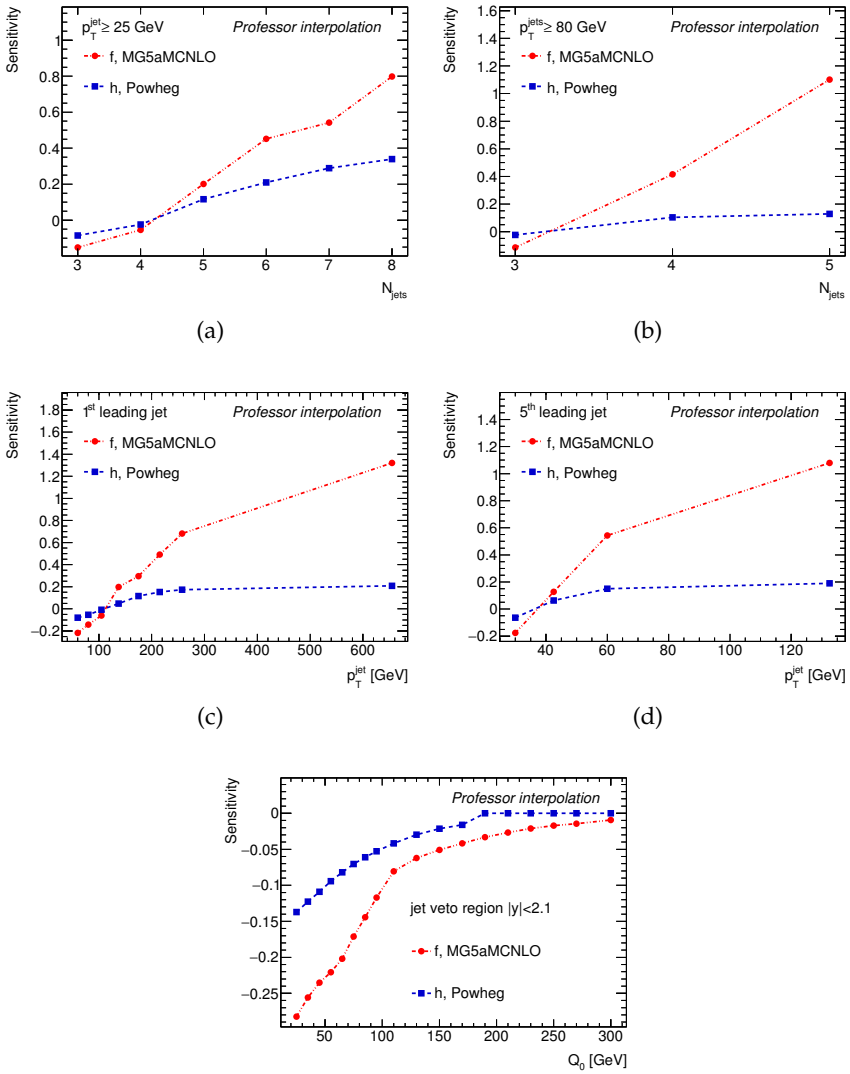

Figure 39: Sensitivity of the $t\bar{t}$ measurements to the h (red circles) and f (blue squares) parameters of POWHEG and MadGraph5_aMC@NLO, respectively. The sensitivities are shown as functions of the differential $t\bar{t}$ cross sections as functions of (a) jet multiplicity for jets with $p_T^{jet} \geqslant 25$ GeV, (b) jet multiplicity for jets with $p_T^{jet} \geqslant 80$ GeV, (c) leading-jet transverse momentum, (d) 5th-leading jet transverse momentum, and (e) gap fraction as a function of Q_0.

Table 4: Tuning results of the $\alpha_s^{ISR}(m_Z)$ and $p_{T,damp}^{ISR}$ PYTHIA8 parameters to the differential $t\bar{t}$ cross sections as functions of jet multiplicity and jet transverse momentum ($t\bar{t}$+jets), and to the gap fraction as a function of Q_0 ($t\bar{t}$ gap fraction), using the 4C tune as baseline. The '-' symbol is used in case the setting is not applicable.

Parameter	$t\bar{t}$+jets	$t\bar{t}$ gap fraction	$t\bar{t}$+jets and $t\bar{t}$ gap fraction
$\alpha_s^{ISR}(m_Z)$	0.130 ± 0.005	$0.129^{+0.012}_{-0.010}$	0.130 ± 0.005
$p_{T,damp}^{ISR}$	$1.33^{+0.11}_{-0.10}$	$1.31^{+0.21}_{-0.18}$	$1.32^{+0.10}_{-0.09}$
χ^2_{min}/dof	30/19	10/16	40/37

6.4 INITIAL-STATE RADIATION

As shown in the previous section, the differential $t\bar{t}$ cross sections as functions of jet multiplicity and jet transverse momentum, and the gap fraction as a function of Q_0, are sensitive to the ISR parameters $\alpha_s^{ISR}(m_Z)$ and $p_{T,damp}^{ISR}$. While the fudge factor for the damping of ISR, $p_{T,damp}^{ISR}$, is introduced in the specific case of the $t\bar{t}$ production to compensate for missing matrix-element corrections in the PYTHIA8 MC [263], the $\alpha_s^{ISR}(m_Z)$ parameter is expected to be universal across different processes. In particular, by comparing the value constrained in $t\bar{t}$ production, to the value preferred by the transverse momentum spectrum of Z bosons produced in pp collisions [252], the validity of the ISR parton shower model can be tested in processes dominated by different initial states: gluon-gluon for $t\bar{t}$ production and quark-antiquark for Z production. Table 4 shows the results of the tuning of the ISR parameters to the $t\bar{t}$ measurements using the 4C tune as baseline. The results are compared to the AZ tune to the Z boson transverse momentum spectrum [252], which was performed using the same 4C tune as baseline, and the same CTEQ6L1 PDF set.

Independent tuning to the differential $t\bar{t}$ cross sections as functions of jet multiplicity and jet transverse momentum, and to the gap fraction as a function of Q_0, show very similar results for the optimised parameters. The value of $\alpha_s^{ISR}(m_Z)$ obtained from the tune to both measurements is in rather good agreement with the value of the AZ tune. Figure 40 shows the comparison between the optimal values of the ISR tunes to the $t\bar{t}$ data and the AZ tune, which is constrained to the ATLAS measurement of the Z boson transverse momentum at $\sqrt{s} = 7$ TeV. The 68% confidence interval in the $\alpha_s^{ISR}(m_Z)$ and $p_{T,damp}^{ISR}$ space is obtained from the Hessian matrix of the χ^2 at the minimum.

Table 5 shows the results of the tuning of the ISR parameters to the $t\bar{t}$ measurements using the Monash tune as baseline and the NNPDF2.3 LO PDF set. The optimal values of the ISR parameters obtained using Monash as the baseline tune are slightly different to

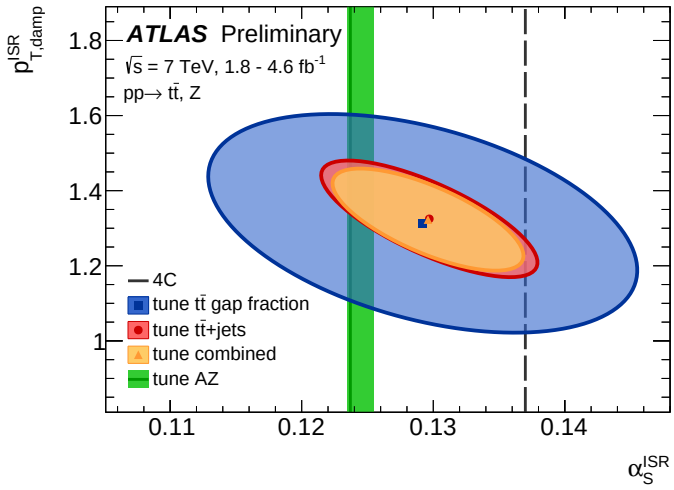

Figure 40: Optimal values of the PYTHIA8 ISR parameters $\alpha_s^{ISR}(m_Z)$ and $p_{T,damp}^{ISR}$ obtained from tunes to the $t\bar{t}$ gap fraction (blue square), $t\bar{t}$ +jets (red circle) and their combination (yellow triangle) compared to the value of $\alpha_s^{ISR}(m_Z)$ of the AZ (green line) and 4C (black dashed line) tunes. The ellipses correspond to the 68% confidence interval, and the green band shows the uncertainty on the value of $\alpha_s^{ISR}(m_Z)$ in the AZ tune.

Table 5: Tuning results of $\alpha_s^{ISR}(m_Z)$ and $p_{T,damp}^{ISR}$ PYTHIA8 parameters to the differential $t\bar{t}$ cross sections as functions of jet multiplicity and jet transverse momentum ($t\bar{t}$+jets), and to the gap fraction as a function of Q_0 ($t\bar{t}$ gap fraction), using the Monash tune as baseline. The '-' symbol is used in case the setting is not applicable.

Parameter	$t\bar{t}$+jets	$t\bar{t}$ gap fraction	$t\bar{t}$+jets and $t\bar{t}$ gap fraction (ATTBAR-ISR)	Monash
$\alpha_s^{ISR}(m_Z)$	0.124 ± 0.006	0.124 ± 0.010	$0.124^{+0.005}_{-0.006}$	0.137
$p_{T,damp}^{ISR}$	1.13 ± 0.09	$1.19^{+0.17}_{-0.15}$	1.14 ± 0.08	-
χ^2_{min}/dof	24/19	10/16	34/37	

Table 6: Tuning results of the $\alpha_s^{FSR}(m_Z)$ PYTHIA8 parameter to the differential light- and b-jet shapes in $t\bar{t}$ events, using the 4C tune as baseline.

Parameter	light-jet shapes	b-jet shapes	4C
$\alpha_s^{FSR}(m_Z)$	0.131 ± 0.001	0.126 ± 0.001	0.1383
χ^2_{min}/dof	64/49	284/49	

Table 7: Tuning results of the $\alpha_s^{FSR}(m_Z)$ PYTHIA8 parameter to the differential light- and b-jet shapes in $t\bar{t}$ events, using the Monash tune as baseline.

Parameter	light-jet shapes	b-jet shapes	Monash
$\alpha_s^{FSR}(m_Z)$	0.125 ± 0.001	0.121 ± 0.001	0.1365
χ^2_{min}/dof	71/49	219/49	

those obtained with 4C, and the value of the χ^2 is up to six points better in the case of Monash. The most relevant difference between the 4C and Monash tunes, which affects the results of the tuning of ISR, is the different PDF set, CTEQ6L1 in 4C and NNPDF2.3 LO in Monash. The tune of the ISR parameters to both the $t\bar{t}$ + jets and $t\bar{t}$ gap fraction measurements, with the Monash tune as baseline, is referred to as ATTBAR-ISR. Figure 41 shows the $t\bar{t}$ measurements compared to the PYTHIA8 predictions with the Monash and ATTBAR-ISR tunes. A very good agreement between the data and the ATTBAR-ISR tune is observed in all the distributions.

6.5 FINAL-STATE RADIATION

The light- and b-jet shapes measured in $t\bar{t}$ events are sensitive to the value of $\alpha_s^{FSR}(m_Z)$, and, to less extent, to the value of $p_{T,min}^{FSR}$. The measurements can be used to tune such FSR parameters, and the optimal values can be compared to the corresponding values tuned to the event shapes in Z boson hadronic decay as measured at LEP. In Ref. [246], values of $\alpha_s^{FSR}(m_Z)$ in the range $0.135 - 0.140$ are suggested by comparing PYTHIA8 predictions and the LEP data [253], and a Professor tune of PYTHIA8 hadronisation and FSR parameters to LEP measurements [254, 255, 256] returns 0.139 as optimal value of $\alpha_s^{FSR}(m_Z)$ [273]. Tables 6 and 7 show the results of the tuning of the FSR parameter $\alpha_s^{FSR}(m_Z)$ to the light- and b-jet shapes in $t\bar{t}$ events, using the 4C and Monash tune as baselines, respectively. The results show tension in the value of $\alpha_s^{FSR}(m_Z)$ between light- and b-jet shapes. The χ^2_{min}/dof is close to unity in the case of the light-jet shapes, whereas it is larger than 4 for the b-jet shapes, pointing to a mismodelling of the latter. Despite the better χ^2_{min}/dof of the tune of

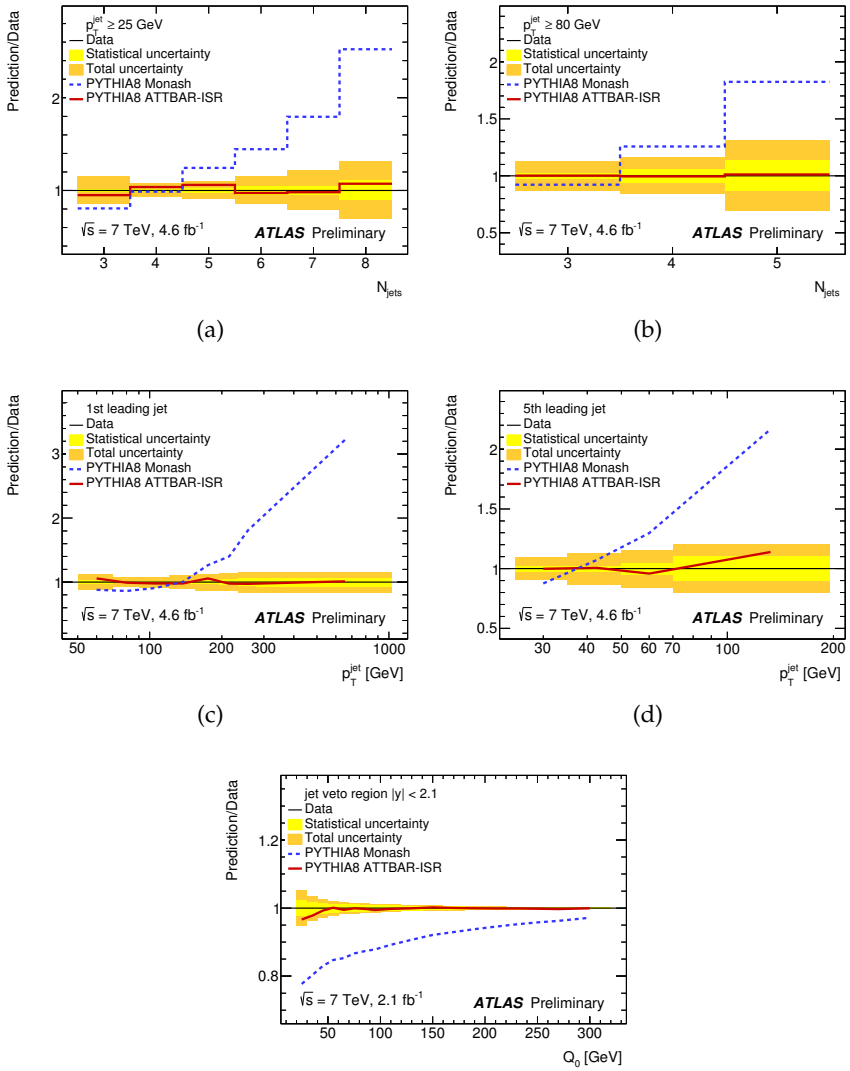

Figure 41: Predictions of PYTHIA8 with the ATTBAR-ISR (red continuous line) and Monash (blue dashed line) tunes, compared to the measured differential $t\bar{t}$ cross sections as functions of (a) jet multiplicity for jets with $p_T^{jet} \geqslant 25$ GeV, (b) jet multiplicity for jets with $p_T^{jet} \geqslant 80$ GeV, (c) leading-jet transverse momentum, (d) 5th-leading jet transverse momentum, and (e) gap fraction as a function of Q_0. The relative statistical (yellow band) and total (orange band) experimental uncertainties are shown.

Table 8: Tuning results of the $\alpha_s^{FSR}(m_Z)$ and $p_{T,min}^{FSR}$ PYTHIA8 parameters to the differential light-jet shapes in $t\bar{t}$ events, using the 4C tune as baseline.

Parameter	light-jet shapes	4C
$\alpha_s^{FSR}(m_Z)$	$0.137^{+0.003}_{-0.002}$	0.1383
$p_{T,min}^{FSR}$ [GeV]	0.88 ± 0.16	0.4
χ^2_{min}/dof	55/49	

Table 9: Tuning results of the $\alpha_s^{FSR}(m_Z)$ and $p_{T,min}^{FSR}$ PYTHIA8 parameters to the differential light-jet shapes in $t\bar{t}$ events, using the Monash tune as baseline.

Parameter	light-jet shapes (ATTBAR-FSR)	Monash
$\alpha_s^{FSR}(m_Z)$	0.135 ± 0.003	0.1365
$p_{T,min}^{FSR}$ [GeV]	$1.31^{+0.18}_{-0.20}$	0.5
χ^2_{min}/dof	57/49	

$\alpha_s^{FSR}(m_Z)$ to the light-jet shapes in $t\bar{t}$ events, the optimal values of $\alpha_s^{FSR}(m_Z) = 0.131 \pm 0.001$ and $\alpha_s^{FSR}(m_Z) = 0.125 \pm 0.001$ show some difference with respect to the values preferred by the LEP measurements of event shapes in Z boson hadronic decay.

Tables 8 and 9 show the results of the tuning of the FSR parameters $\alpha_s^{FSR}(m_Z)$ and $p_{T,min}^{FSR}$ to the light-jet shapes in $t\bar{t}$ events, using the 4C and Monash tune as baselines, respectively. The inclusion of $p_{T,min}^{FSR}$ as a free parameter in the fit does not improve the mismodelling of the *b*-jet shapes, and the corresponding tunes to the *b*-jet shapes do not converge within the sampled range of parameters.

With the addition of $p_{T,min}^{FSR}$ as a free parameter in the fit, the χ^2 of the two FSR tunes to the light-jet shapes are about ten points lower, and the resulting values of $\alpha_s^{FSR}(m_Z)$ are compatible with the values preferred by the LEP event shapes. However, the optimal value of $p_{T,min}^{FSR}$ is rather high with respect to the values used in the baseline tunes, 0.88 GeV and 1.31 GeV compared to 0.4 GeV and 0.5 GeV for the 4C and Monash tunes, respectively. Although the addition of $p_{T,min}^{FSR}$ as a free parameter restored compatibility in the value of $\alpha_s^{FSR}(m_Z)$ between the tunes to the light-jet shapes in $t\bar{t}$ events, and the tunes based on LEP event shapes, the resulting higher values of $p_{T,min}^{FSR}$ leave an undesirable gap between the FSR cut-off and the scale of hadronisation [246]. Indeed, the scale of the p_T kicks involved in string breaking of the PYTHIA8 hadronisation model (corresponding to the `StringPT:sigma` parameter) is set to $\sigma_\perp = 0.304$ GeV in the 4C tune, and $\sigma_\perp = 0.335$ GeV in the Monash tune. The result of $p_{T,min}^{FSR}$ is also incompatible with the determination of this parameter from LEP

data of Ref. [273], which is 0.41 GeV. The difference in the preferred values of $p_{T,min}^{FSR}$ suggests that there is a residual tension between the light-jet shapes in $t\bar{t}$ events and the LEP event shapes. Further studies on the impact of changing parameters of the fragmentation function, of different colour reconnection models [274], and of NLO corrections in W boson hadronic decays [275], could cast light on the nature of such a tension.

The tune of the FSR parameters to the light-jet shapes in $t\bar{t}$ events, with the Monash tune as baseline, shown in Table 9, is referred to as ATTBAR-FSR. Figure 42 shows the measurements of light-jet shapes in $t\bar{t}$ events, compared to the PYTHIA8 predictions with the Monash and ATTBAR-FSR tunes. The b-jet shapes differential distributions are compared in Fig. 43 to the PYTHIA8 predictions of the same Monash and ATTBAR-FSR tunes. The comparison shows a mismodelling of the b-jets shapes, which are predicted to be wider than observed in the data. The mismodelling is more pronounced at high jet p_T above 70 GeV and at large angle r above 0.1. The NLO corrections in top quark decays, which has been included in POWHEG [275], have an impact on the b-quark fragmentation function, and could improve the agreement between the measurements and the predictions.

6.6 SIMULTANEOUS TUNE OF ISR AND FSR

As observed in Section 6.3, the observables used for tuning the ISR parameters have some sensitivity to $\alpha_s^{FSR}(m_Z)$, and the observables used to tune the FSR parameters have some sensitivity to $\alpha_s^{ISR}(m_Z)$. To account for the interplay between ISR and FSR parameters, a simultaneous tune of ISR and FSR parameters is performed using the differential $t\bar{t}$ cross sections as functions of jet multiplicity and jet transverse momentum, the gap fraction as a function of Q_0, and the differential light-jet shapes in $t\bar{t}$ events. The differential b-jet shapes in $t\bar{t}$ events are not used, since they are not well modelled by the PYTHIA8 MC, as shown in the previous Section.

Tables 10 and 11 show the results of the tuning of the ISR and FSR parameters to the $t\bar{t}$ measurements using the 4C and Monash tunes as baselines, respectively. The results of the simultaneous tunes of ISR and FSR are in rather good agreement with the results of the independent tunes. The overall χ^2_{min}/dof is 97/85 when using the 4C tune as baseline, and 92/85 with the Monash tune as baseline. The tune of the ISR and FSR parameters to the $t\bar{t}$ data events, with the Monash tune as baseline, shown in Table 11, is referred to as ATTBAR. The PYTHIA8 predictions with the ATTBAR tune are very similar to those of the ATTBAR-ISR and ATTBAR-FSR tunes, they are shown in Figs. 47, 49, and 50.

In order to check the impact of accounting for uncertainties correlation in the χ^2 definition, a tune is performed with the same conditions

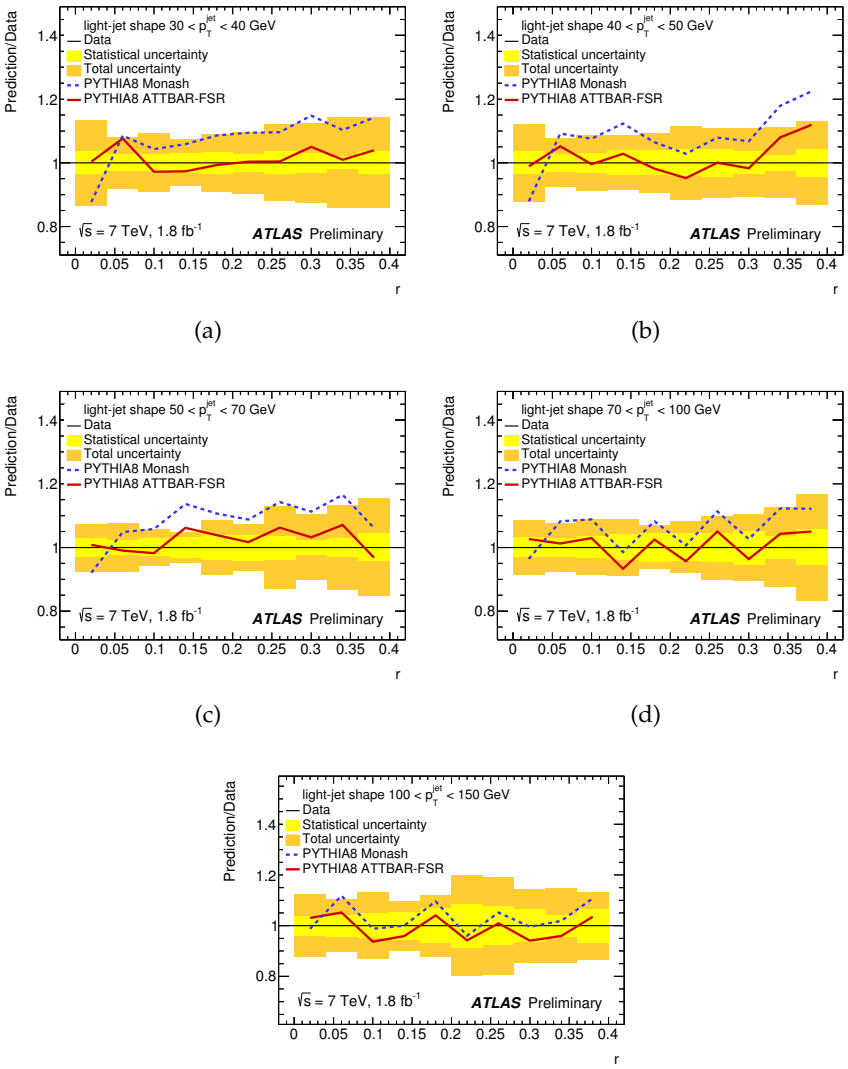

Figure 42: Predictions of PYTHIA8 with the ATTBAR-FSR (red continuous line) and Monash (blue dashed line) tunes, compared to the light-jet shapes as functions of the jet radius r for jets with (a) $30 < p_T^{jet} < 40$ GeV, (b) $40 < p_T^{jet} < 50$ GeV, (c) $50 < p_T^{jet} < 70$ GeV, (d) $70 < p_T^{jet} < 100$ GeV, and (e) $100 < p_T^{jet} < 150$ GeV. The relative statistical (yellow band) and total (orange band) experimental uncertainties are shown.

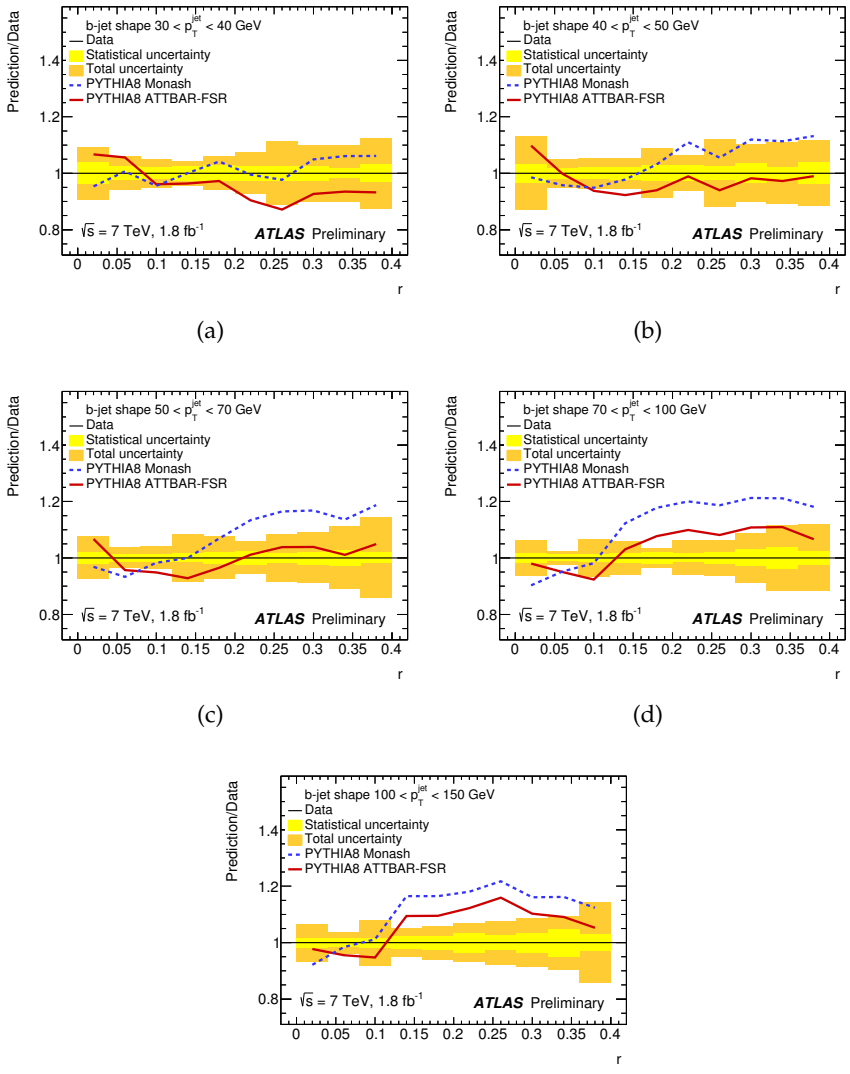

Figure 43: Predictions of PYTHIA8 with the ATTBAR-FSR (red continuous line) and Monash (blue dashed line) tunes, compared to the *b*-jet shapes as functions of the jet radius *r* for jets with (a) $30 < p_T^{jet} < 40$ GeV, (b) $40 < p_T^{jet} < 50$ GeV, (c) $50 < p_T^{jet} < 70$ GeV, (d) $70 < p_T^{jet} < 100$ GeV, and (e) $100 < p_T^{jet} < 150$ GeV. The relative statistical (yellow band) and total (orange band) experimental uncertainties are shown.

Table 10: Tuning results of the PYTHIA8 ISR and FSR parameters to the differential $t\bar{t}$ cross sections as functions of jet multiplicity and jet transverse momentum, the gap fraction as a function of Q_0, and the differential light-jet shapes in $t\bar{t}$ events, using the 4C tune as baseline. The '-' symbol is used in case the setting is not applicable.

Parameter	ATLAS $t\bar{t}$ measurements	4C
$\alpha_s^{ISR}(m_Z)$	0.127 ± 0.004	0.137
$p_{T,damp}^{ISR}$	$1.36^{+0.09}_{-0.08}$	-
$\alpha_s^{FSR}(m_Z)$	0.139 ± 0.002	0.1383
$p_{T,min}^{FSR}$ [GeV]	$0.85^{+0.16}_{-0.17}$	0.4
χ^2_{min}/dof	97/85	

Table 11: Tuning results of the PYTHIA8 ISR and FSR parameters to the differential $t\bar{t}$ cross sections as functions of jet multiplicity and jet transverse momentum, the gap fraction as a function of Q_0, and the differential light-jet shapes in $t\bar{t}$ events, using the Monash tune as baseline. The '-' symbol is used in case the setting is not applicable.

Parameter	ATLAS $t\bar{t}$ measurements (ATTBAR)	Monash
$\alpha_s^{ISR}(m_Z)$	0.121 ± 0.004	0.1365
$p_{T,damp}^{ISR}$	$1.18^{+0.08}_{-0.07}$	-
$\alpha_s^{FSR}(m_Z)$	0.137 ± 0.003	0.1365
$p_{T,min}^{FSR}$ [GeV]	1.26 ± 0.17	0.5
χ^2_{min}/dof	92/85	

Table 12: The optimal parameters and their uncertainties as determined in the ATTBAR tune and in a tune performed without uncertainties correlations.

Parameter	ATTBAR	Tune without uncertainties correlations
$\alpha_s^{ISR}(m_Z)$	0.121 ± 0.004	$0.118^{+0.007}_{-0.006}$
$p_{T,damp}^{ISR}$	$1.18^{+0.08}_{-0.07}$	$1.17^{+0.10}_{-0.09}$
$\alpha_s^{FSR}(m_Z)$	0.137 ± 0.003	$0.138^{+0.006}_{-0.005}$
$p_{T,min}^{FSR}$ [GeV]	1.26 ± 0.17	1.35 ± 0.35
χ^2_{min}/dof	92/85	13/85

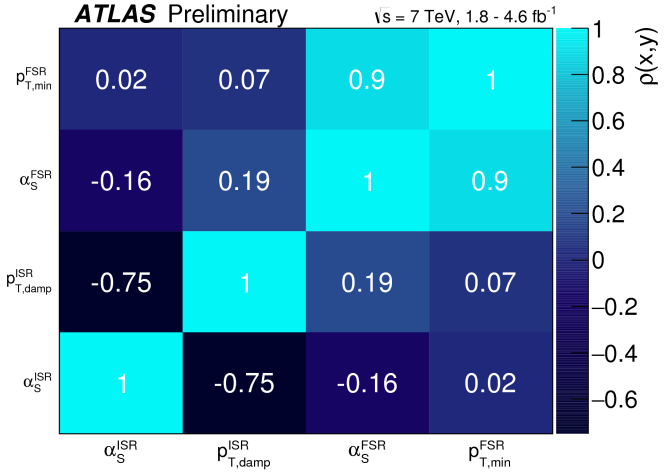

Figure 44: Parameters correlations $\rho(x, y)$ as evaluated from the Hessian matrix at χ^2_{min}, for the PYTHIA8 ATTBAR tune.

of the ATTBAR tune, but considering the total experimental uncertainties as fully uncorrelated. Table 12 shows the comparison between the ATTBAR tune, which is based on the uncertainties correlation model described in Section 6.2, and a corresponding tune without uncertainties correlations. The optimal parameters of the two tunes are in good agreement, but the uncertainties of the parameters are up to 50% lower in the ATTBAR tune. If correlations are not considered the tune yields a very small value of χ^2_{min}/dof, which is typically an indication of overestimated uncertainties. Only in ATTBAR the value of χ^2_{min}/dof is close to unity, a prerequisite to give a proper statistical meaning to the parameters values and their uncertainties. Figure 44 shows the correlations of the parton shower parameters of the ATTBAR tune, evaluated from the Hessian matrix at the minimum of the χ^2 function.

The variations of the ISR and FSR parameters induce a change in the overall energy and particle flow, which affects the underlying event activity. Measurements of the underlying event in the $t\bar{t}$ final

state could be used to tune the multi-parton-interaction (MPI) parameters, but only a measurement from CMS was performed [276], which is a preliminary result. Assuming that the MPI model can describe simultaneously both $t\bar{t}$ and Z boson production, the change in the energy and particle flow is compensated by adjusting the MPI cut-off to match the inclusive charged particle production and energy flow in Z/γ^* underlying event data measured by ATLAS at $\sqrt{s} = 7$ TeV [277]. A tune of this parameter is performed using the average density of charged particles, $< N_{chg} >$, and the scalar sum of their transverse momenta, $< \sum p_T >$, in the transverse and towards regions relative to the Z-boson direction, for $p_T^Z < 5$ GeV (see Section 2.4.4 for their definition). The MPI cut-off in ATTBAR is changed from 2.28 GeV, the value in the Monash tune, to 2.16 GeV. A compatible value of 2.17 GeV is obtained using a measurement of UE in Drell-Yan event performed by CMS [278]. The same value of the MPI cut-off is used also for the NLO+PS predictions.

6.7 TUNE OF THE MADGRAPH5_AMC@NLO GENERATOR

The simultaneous ISR and FSR PYTHIA8 tune to the $t\bar{t}$ measurements, ATTBAR, is applied to the MadGraph5_aMC@NLO generator, with the exception of the $p_{T,damp}^{ISR}$ parameter. The parameters of MadGraph5_aMC@NLO which set the upper scale of the MC subtraction term, and the starting scale of the parton shower, are tuned to the $t\bar{t}$ data. The parameters `frac_upp` and `frac_low` of MadGraph5_aMC@NLO correspond, respectively, to the maximum and minimum fractions of a reference scale, for the upper scale of the MC subtraction term, where the reference scale is set to the invariant mass of the $t\bar{t}$ system. The best agreement with the data is found by fixing `frac_upp` and `frac_low` to the same common value f, and by tuning f to the differential $t\bar{t}$ cross sections as functions of jet multiplicity and jet transverse momentum, and to the gap fraction as a function of Q_0. When interfacing MadGraph5_aMC@NLO to PYTHIA8, the FSR algorithm should employ, at least for the first emission, a *global-recoil* strategy, in which the recoil of the FSR radiation is shared between all partons in the final state. The global-recoil strategy of FSR, which is opposite to the default dipole style local-recoil strategy, is needed to avoid double counting with the MC subtraction term of the MadGraph5_aMC@NLO generator. The matrix-element corrections to ISR and FSR are disabled in PYTHIA8, so as to obtain a process-independent emission rate which matches the MadGraph5_aMC@NLO subtraction term.

The tuning of the f parameter of MadGraph5_aMC@NLO is performed in two configurations: with the recommended settings for the global recoil, and with the global recoil option disabled (local recoil). The settings for the two configurations are listed in Table 13. Tables 14

Table 13: Global-recoil and local-recoil settings of PYTHIA8 for the MadGraph5_aMC@NLO+PYTHIA8 generator. The '-' symbol is used in case the setting is not applicable.

PYTHIA8 setting	Global recoil	Local recoil
`SpaceShower:pTmaxMatch`	1	1
`SpaceShower:MEcorrections`	off	off
`TimeShower:MEcorrections`	off	off
`TimeShower:globalRecoil`	on	off
`TimeShower:globalRecoilMode`	2	-
`TimeShower:nMaxGlobalBranch`	1	-
`TimeShower:nPartonsInBorn`	2	-
`TimeShower:limitPTmaxGlobal`	on	-

Table 14: Tuning results of the MadGraph5_aMC@NLO `frac_upp` = `frac_low` = f parameter to the differential $t\bar{t}$ cross sections as functions of jet multiplicity and jet transverse momentum ($t\bar{t}$+jets), and to the gap fraction as a function of Q_0 ($t\bar{t}$ gap fraction), using the ATTBAR tune, and the global-recoil configuration.

Parameter	$t\bar{t}$+jets	$t\bar{t}$ gap fraction	$t\bar{t}$+jets and $t\bar{t}$ gap fraction
f	0.58 ± 0.03	$0.53^{+0.09}_{-0.08}$	0.57 ± 0.03
χ^2_{min}/dof	43/20	14/17	57/38

and 15 show the results of tuning the parameter f to the differential $t\bar{t}$ cross sections as functions of jet multiplicity and jet transverse momentum, and to the gap fraction as a function of Q_0, using the ATTBAR tune, for the global- and local-recoil configurations, respectively. The values of f obtained by tuning to the $t\bar{t}$ + jets measurements are consistent with the values obtained by tuning to the $t\bar{t}$ gap fraction. The values of f obtained by tuning to both measurements, are $f = 0.58 \pm 0.03$ and $f = 0.54 \pm 0.03$ for the global- and local-recoil configurations, respectively. The tune of the f parameter to the $t\bar{t}$ data, with the ATTBAR tune and the local-recoil PYTHIA8 configuration, shown in Table 15, is referred to as ATTBAR-MG5aMCNLO.

Figure 45 shows the $t\bar{t}$ measurements compared to the MadGraph5_aMC@NLO +PYTHIA8 predictions with the Monash tune and the global-recoil configuration, f-tuned predictions with the ATTBAR tune and the global-recoil configuration, and predictions with the ATTBAR-MG5aMCNLO tune.

Although the global-recoil configuration is theoretically more consistent, the χ^2_{min} of the tuning for the local-recoil configuration is up to 17 points lower, and the agreement with the data is significantly better in the gap fraction measurement, and in the 5th jet bin

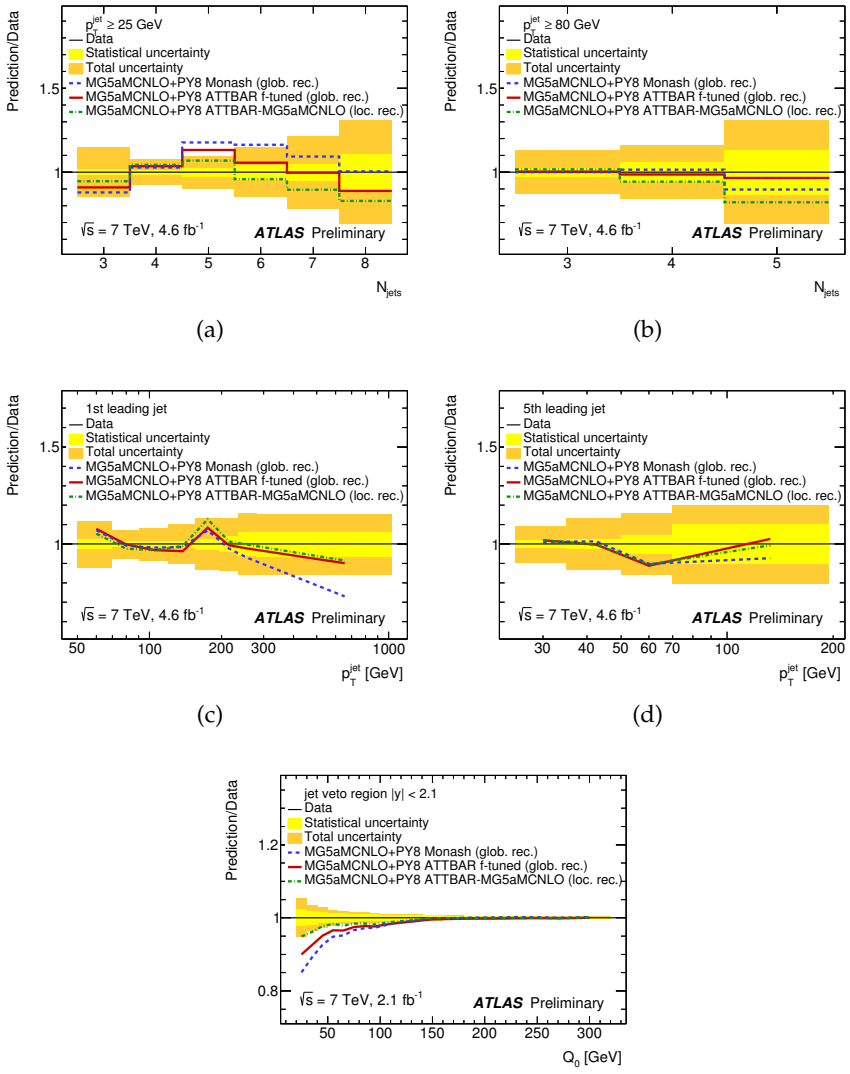

Figure 45: The MadGraph5_aMC@NLO+Pythia8 predictions with the Monash tune and the global-recoil configuration (blue dashed line), f-tuned predictions with the ATTBAR tune and the global-recoil configuration (red continuous line), and predictions with the ATTBAR-MG5aMCNLO tune (green dotted and dashed line), are compared to the measured differential $t\bar{t}$ cross sections as functions of (a) jet multiplicity for jets with $p_T^{jet} \geqslant 25$ GeV, (b) jet multiplicity for jets with $p_T^{jet} \geqslant 80$ GeV, (c) leading-jet transverse momentum, (d) 5th-leading jet transverse momentum, and (e) gap fraction as a function of Q_0. The relative statistical (yellow band) and total (orange band) experimental uncertainties are shown.

Table 15: Tuning results of the MadGraph5_aMC@NLO `frac_upp` = `frac_low` = f parameter without using the global recoil settings to the differential $t\bar{t}$ cross sections as functions of jet multiplicity and jet transverse momentum ($t\bar{t}$+jets), and to the gap fraction as a function of Q_0 ($t\bar{t}$ gap fraction), using the ATTBAR tune, and the local-recoil configuration.

Parameter	$t\bar{t}$+jets	$t\bar{t}$ gap fraction	$t\bar{t}$+jets and $t\bar{t}$ gap fraction (ATTBAR-MG5aMCNLO)
f	0.54 ± 0.03	0.50 ± 0.08	0.54 ± 0.03
χ^2_{min}/dof	29/20	11/17	40/38

Table 16: Tuning results of the `hdamp` POWHEG parameter to the differential $t\bar{t}$ cross sections as functions of jet multiplicity and jet transverse momentum ($t\bar{t}$+jets), and to the gap fraction as a function of Q_0 ($t\bar{t}$ gap fraction), using the ATTBAR tune.

Parameter	$t\bar{t}$+jets	$t\bar{t}$ gap fraction	$t\bar{t}$+jets and $t\bar{t}$ gap fraction (ATTBAR-POWHEG)
`hdamp`	$1.7^{+0.5}_{-0.3} \cdot m_t$	$2.2^{+2.9}_{-0.7} \cdot m_t$	$1.8^{+0.4}_{-0.3} \cdot m_t$
χ^2_{min}/dof	40/20	11.9/17	52.1/38

of the differential cross section as a function of jet multiplicity for jets with $p_T \geqslant 25$ GeV. The modeling of the first radiation includes fixed-order and all-order effects. For the current configuration of the MadGraph5_aMC@NLO +PYTHIA8 Monte Carlo generator it is not obvious which of these effects is responsible for the difference between the global and local recoil strategies.

6.8 TUNE OF THE POWHEG GENERATOR

The simultaneous ISR and FSR PYTHIA8 tune to the $t\bar{t}$ measurements, ATTBAR, is applied to the POWHEG generator, with the exception of the $p^{ISR}_{T,damp}$ parameter, and the `hdamp` factor of POWHEG is tuned to the $t\bar{t}$ data. The `hdamp` factor is parametrised as `hdamp` $= h \cdot m_t$, and the optimal value of h is obtained by tuning the POWHEG+PYTHIA8 prediction to the differential $t\bar{t}$ cross sections as functions of jet multiplicity and jet transverse momentum, and to the gap fraction as a function of Q_0.

Table 16 shows the results of the tuning of the h parameter to the differential $t\bar{t}$ cross sections as functions of jet multiplicity and jet transverse momentum, and to the gap fraction as a function of Q_0, using the ATTBAR tune. The value of h obtained by tuning to the $t\bar{t}$

+ jets measurements is consistent with the value obtained by tuning to the $t\bar{t}$ gap fraction, with the latter having larger uncertainty. The value of h, obtained by tuning to both measurements, is $h = 1.8^{+0.4}_{-0.3}$, which corresponds to `hdamp` $= 310^{+70}_{-50}$ GeV, and this tune is referred to as ATTBAR-POWHEG. Figure 46 shows the $t\bar{t}$ measurements compared to the POWHEG+PYTHIA8 predictions with the Monash and ATTBAR-POWHEG tunes.

6.9 SUMMARY AND CONCLUSIONS

Figures 47, 48, 49, and 50 show PYTHIA8 predictions with the ATTBAR tune, MadGraph5_aMC@NLO+PYTHIA8 predictions with the ATTBAR-MG5aMCNLO tune, and POWHEG+PYTHIA8 predictions with the ATTBAR-POWHEG tune, compared to the ATLAS $t\bar{t}$ measurements.

Independent tunes of ISR and FSR parameters of the PYTHIA8 MC to the ATLAS $t\bar{t}$ measurements, and a simultaneous tune of the ISR and FSR parameters have been performed. The latter tune, named ATTBAR, is in very good agreement with the data. The value of $\alpha_s^{ISR}(m_Z)$ tuned to the $t\bar{t}$ data is in good agreement with previous tunes to the Z boson transverse momentum distribution measured by ATLAS [252], and the value of $\alpha_s^{FSR}(m_Z)$ is in good agreement with tunes to the LEP event shapes in Z boson hadronic decays [253, 254, 255, 256]. The value of $p_{T,min}^{FSR}$ preferred by the tunes to the $t\bar{t}$ light-jet shapes is at the level of 1 GeV, which is significantly higher than the values used in the 4C and Monash tunes of about 0.5 GeV, and in disagreement with the determination of this parameter from LEP data [273]. Measurements of $t\bar{t}$ b-jet shapes are not well described by the PYTHIA8 MC, which predicts wider shapes than observed in the data. Significant disagreement with the data is observed in the region of $p_T \geqslant 70$ GeV and $r \geqslant 0.1$. Variations of the parameters considered in this study cannot account for the tension between the data and the predictions.

The ATTBAR tune is applied to the NLO+PS generators POWHEG and MadGraph5_aMC@NLO, and the sensitivity of the $t\bar{t}$ measurements to additional parameters of these generators is studied. A reasonable agreement of the POWHEG+PYTHIA8 predictions to the $t\bar{t}$ data is achieved by lowering the `hdamp` parameter, and the optimal value preferred by the data is $1.8 \cdot m_t$. The sensitivity of the $t\bar{t}$ data to the upper scale of the subtraction term, `f` $=$ `frac_low` $=$ `frac_upp`, of MadGraph5_aMC@NLO is studied. In order to match the subtraction term of MadGraph5_aMC@NLO, the PYTHIA8 FSR should be performed with a global recoil strategy. However, the MadGraph5_aMC@NLO+PYTHIA8 generator with the global recoil strategy for FSR predicts too high cross sections for $t\bar{t}$ + $\geqslant 5$ jets with $p_T \geqslant 25$ GeV, and too small gap fraction probabilities for a leading jet in the range

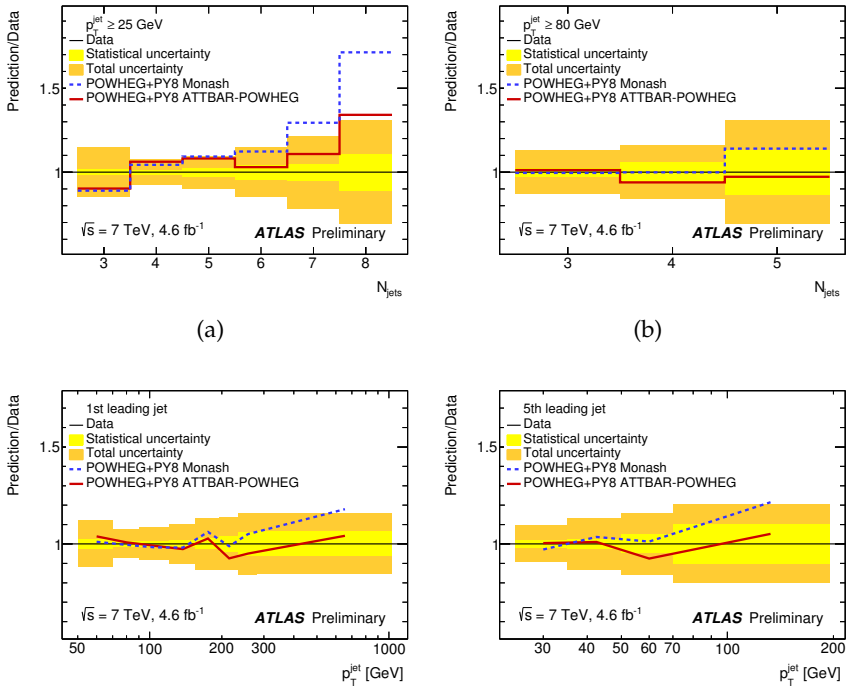

Figure 46: Predictions of POWHEG+PYTHIA8 with the ATTBAR-POWHEG (red continuous line) and Monash (blue dashed line) tunes compared to the measured differential $t\bar{t}$ cross sections as functions of (a) jet multiplicity for jets with $p_T^{jet} \geqslant 25$ GeV, (b) jet multiplicity for jets with $p_T^{jet} \geqslant 80$ GeV, (c) leading-jet transverse momentum, (d) 5th-leading jet transverse momentum, and (e) gap fraction as a function of Q_0. The relative statistical (yellow band) and total (orange band) experimental uncertainties are shown.

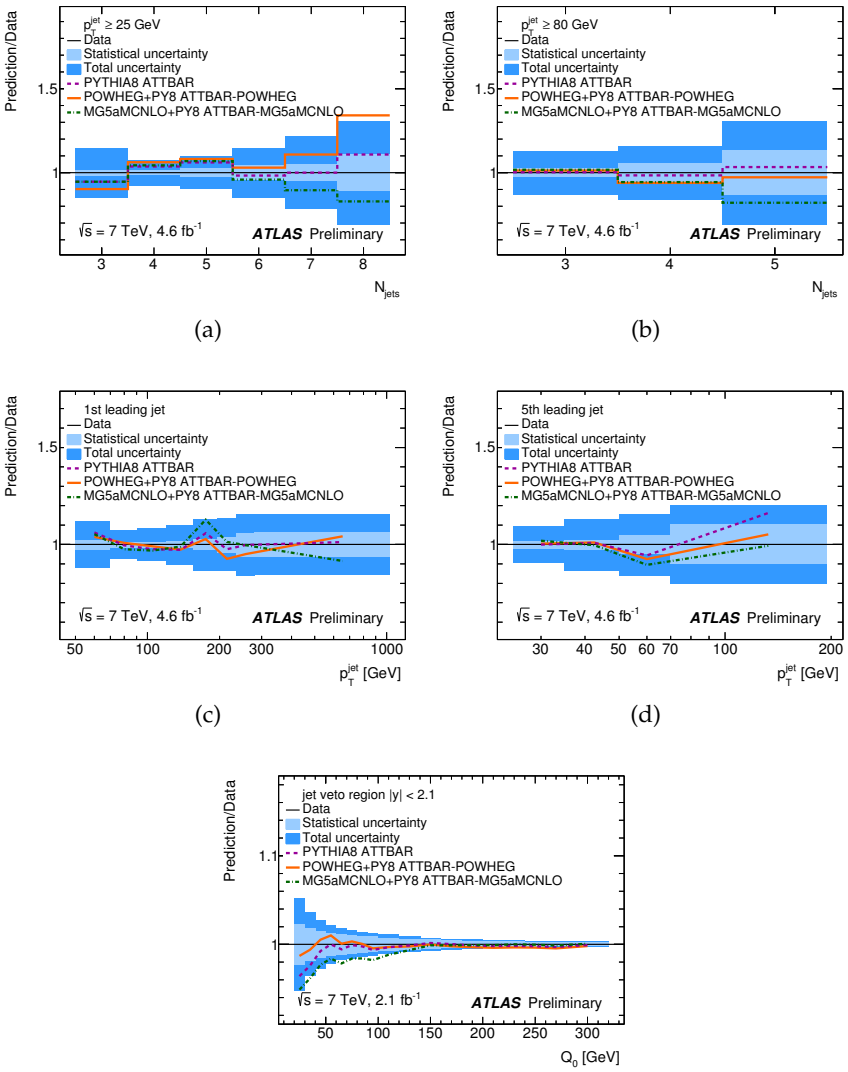

Figure 47: Predictions of PYTHIA8 (dashed magenta line), MadGraph5_aMC@NLO+PYTHIA8 (green dashed and dotted line), and POWHEG+PYTHIA8 (orange continuous line) with the ATTBAR tunes compared to the measured differential $t\bar{t}$ cross sections as functions of (a) jet multiplicity for jets with $p_T^{jet} \geqslant 25$ GeV, (b) jet multiplicity for jets with $p_T^{jet} \geqslant 80$ GeV, (c) leading-jet transverse momentum, (d) 5th-leading jet transverse momentum, and (e) gap fraction as a function of Q_0. The relative statistical (light blue band) and total (dark blue band) experimental uncertainties are shown.

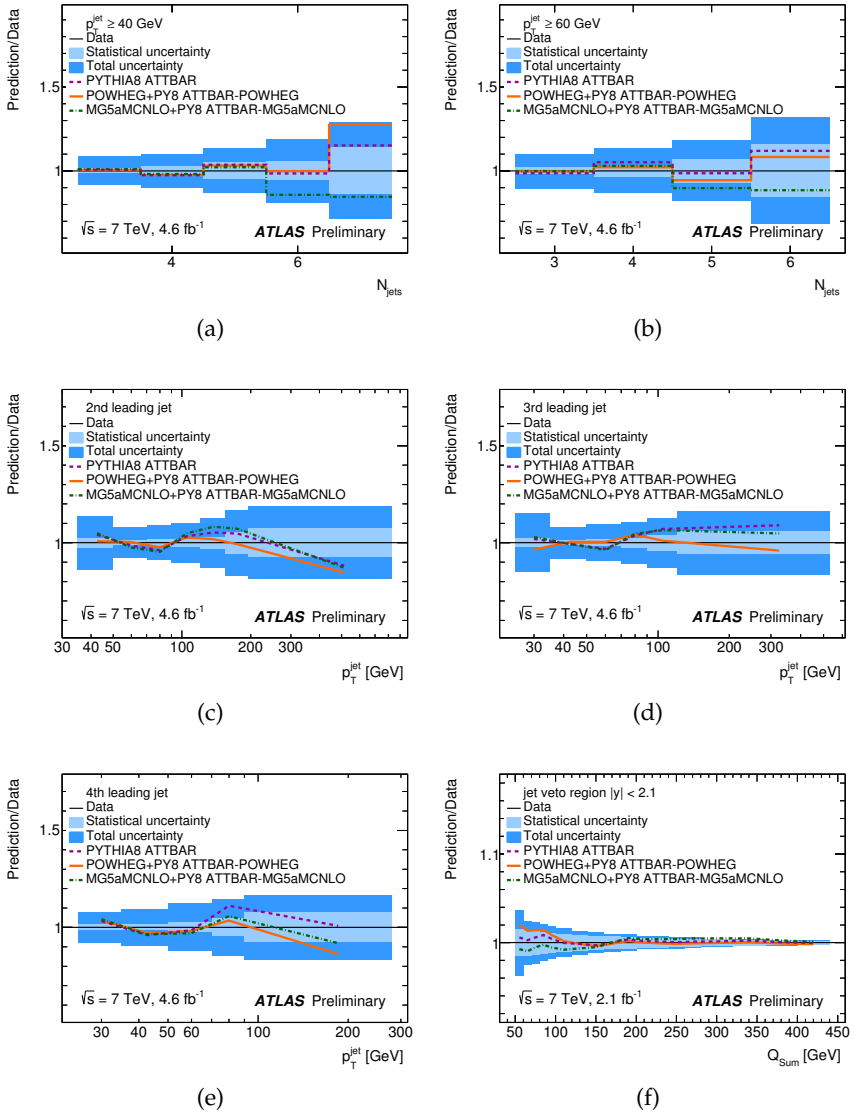

Figure 48: Predictions of PYTHIA8 (dashed magenta line), MadGraph5_aMC@NLO+PYTHIA8 (green dashed and dotted line), and POWHEG+PYTHIA8 (orange continuous line) with the ATTBAR tunes compared to the measured differential $t\bar{t}$ cross sections as functions of (a) jet multiplicity for jets with $p_T^{jet} \geqslant 40$ GeV, (b) jet multiplicity for jets with $p_T^{jet} \geqslant 60$ GeV, (c) 2nd-leading-jet transverse momentum, (d) 3rd-leading-jet transverse momentum, (d) 4th-leading jet transverse momentum, and (e) gap fraction as a function of Q_{Sum}. The relative statistical (light blue band) and total (dark blue band) experimental uncertainties are shown.

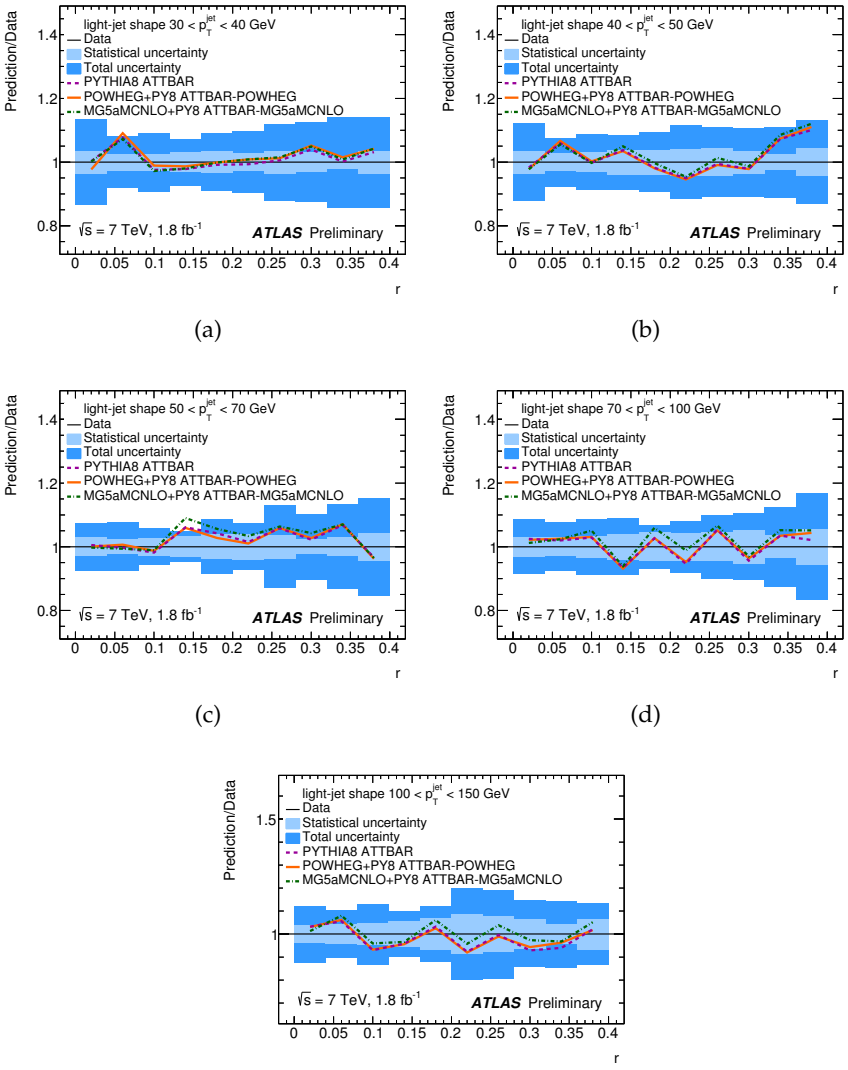

Figure 49: Predictions of PYTHIA8 (dashed magenta line), MadGraph5_aMC@NLO+PYTHIA8 (green dashed and dotted line), and POWHEG+PYTHIA8 (orange continuous line) with the ATTBAR tunes compared to the light-jet shapes as functions of the jet radius r for jets with (a) $30 < p_T^{jet} < 40$, (b) $40 < p_T^{jet} < 50$, (c) $50 < p_T^{jet} < 70$, (d) $70 < p_T^{jet} < 100$, and (e) $100 < p_T^{jet} < 150$. The relative statistical (light blue band) and total (dark blue band) experimental uncertainties are shown.

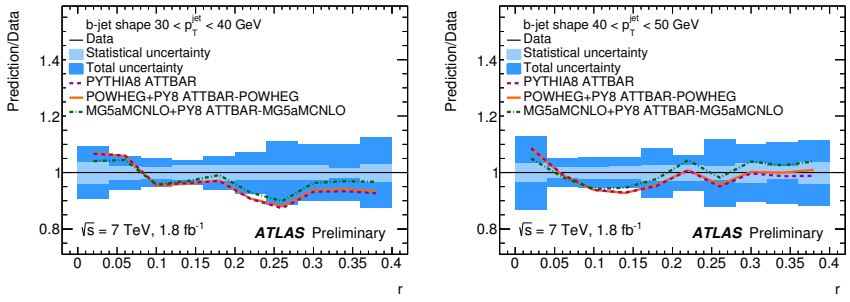

(a) (b)

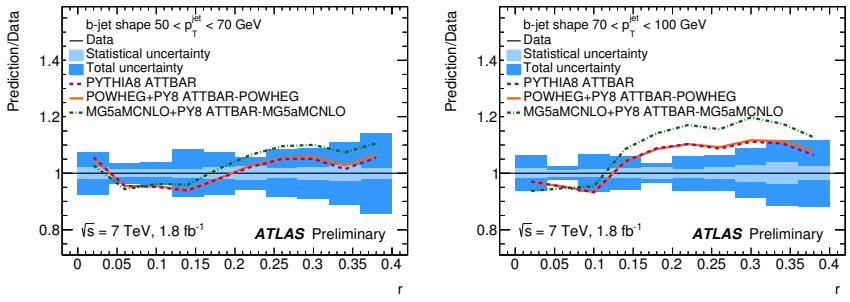

(c) (d)

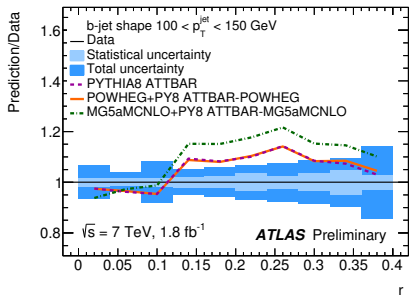

(e)

Figure 50: Predictions of PYTHIA8 (dashed magenta line), MadGraph5_aMC@NLO+PYTHIA8 (green dashed and dotted line), and POWHEG+PYTHIA8 (orange continuous line) with the ATTBAR tunes compared to the *b*-jet shapes as functions of the jet radius *r* for jets with (a) $30 < p_T^{jet} < 40$, (b) $40 < p_T^{jet} < 50$, (c) $50 < p_T^{jet} < 70$, (d) $70 < p_T^{jet} < 100$, and (e) $100 < p_T^{jet} < 150$. The relative statistical (light blue band) and total (dark blue band) experimental uncertainties are shown.

$25 \leqslant p_T \leqslant 100$ GeV, as shown in Fig. 45. Such a disagreement is not observed when using the local recoil strategy for FSR.

The use of the uncertainties correlation in the tuning procedure gives a proper statistical meaning to the parameters values and their uncertainties, and provides a significant reduction of the parameters uncertainties.

7

A GENERAL SEARCH FOR NEW PHENOMENA WITH THE ATLAS DETECTOR IN pp COLLISIONS AT $\sqrt{s} = 8\,\text{TeV}$

We report in this chapter results of a model-independent general search for new phenomena performed on the 8 TeV dataset collected by ATLAS in 2012.

7.1 SEARCHES FOR NEW PHYSICS AT COLLIDERS

Direct searches for as yet unknown particles and forces, motivated by the gauge hierarchy problem, are one of the primary objectives of the ATLAS physics program.

The traditional approach to new physics searches is that of model-based analyses. After deciding on a model of interest (e.g. a specific SUSY breaking scenario) a specific signature, or a small number of them, in which the signal contribution is enhanced is chosen. The analysis selections are further optimised using a MC simulation of the desired signal. Background estimates are then made and if no excess is observed limits on the parameters of the model can be computed. Analyses often incorporate data-driven background estimation techniques, and validate their prediction in specifically designed control regions.

The wide variety of NP scenario proposed so far, with some of them containing hundreds of parameters (such as the MSSM), makes it impossible to explore all of them with model-based searches. Moreover, the analyses optimisations are highly dependent on the assumptions made. A small variation in the parameters of the model could lead to a very different optimisation. The definition of signal and control regions is also dependent on the model considered. Care should be taken when reinterpreting the results of a search as the background estimation is dependent on the assumed signal contamination in the control regions.

Several attempts to overcome these limitations have been made. Simplified models [279], are TeV-scale effective lagrangians where only a limited number of particles and interactions are considered. They can be seen as low energy limits of more general theories where all but few particles are integrated out. Focusing on a small relevant set of degrees of freedom at a time allows the design of searches that are robust over a more complete range of masses and spectral possibilities. For example, decay chains or kinematic regions that may never occur in a particular model sub-space, but require a distinct

search design. The sensitivity to a simplified model can be presented as function of its parameters (such as masses and branching fractions), and will have applicability to any general theory giving rise to the same topology.

In signature-based searches [280, 281], a data sample with a specific signature is chosen (e.g. $\mu\mu + X$) and analysed in a model-independent way. The sample composition is studied in terms of known processes with no or very limited resort to models and usually assuming that a signal would appear as a resonance or an excess at high-p_T. The acceptances and cross-section information are then made public and can be interpreted in any model by either the collaboration itself or the theory community. The selection however does not necessarily provide the best optimization for a given signal.

7.2 MODEL INDEPENDENT GENERAL SEARCHES

While it is beneficial to be guided by a model, it remains important to be sensitive to features in the data that not anticipated by any current theory. In fact unexpected discoveries played an important role in the history of particle physics. For instance the muon, strange particles, and CP violation were not predicted in any existing model. The goal of model-independent new physics searches is to be sensitive to any deviations from known physics, whether or not they are described by one of the existing theoretical models. The only assumption, motivated by naturalness arguments, is that NP will appear in final states with high-p_T objects. General characteristics of this kind of analyses are:

- A categorization of data into exclusive final states in such a way that any signature of new physics appears predominantly in one of these categories.
- An automatic procedure to identify deviations with respect to the known Standard Model backgrounds.
- A correction accounting for the fact that the search is performed in many different variables and channels adjusting the discovery probability accordingly.

A systematic approach to the analysis of collider data is helpful in maximizing an experiment discovery potential, insuring that all the regions in the data are considered. In addition, the pattern of the observed deviations might provide useful insight on the source of the anomaly, and in determining the nature of the underlying theory that originates them (the so called "LHC inverse problem" [282]).

The increase in generality permitted by this approach carries however several limitations. Due to the large number of event classes and observables studied a detailed evaluation of all backgrounds from

data-driven techniques is unrealistic. Generic searches thus rely heavily on the MC description of backgrounds. They are also not competitive with direct searches for known signatures (e.g., a mass peak), and a negative search result is difficult to convert into a quantitative limit due to the limited confidence in a MC based background estimation and the difficulty to properly validate it in the many analysis regions. A framework to automate the testing of different hypotheses against observations using general searches data (but also results from model-based searches) has however been developed at both the Do and H1 experiments [283, 284].

7.2.1 *A history of model-independent searches*

The first attempt at a global analysis at a collider experiment has been carried out in 1998 by the L3 collaboration at LEP [285], using e^+e^- data collected at $\sqrt{s} = 183$ GeV. All final states have been considered in a single analysis and compared to the MC expectation. The distribution of several kinematic variables, such as total energy, missing transverse momentum and a number of event shapes were further inspected visually, or with simple χ^2 or Kolmogorov-Smirnov tests.

Shortly after a general search in $e\mu + X$ data was performed by the Do experiment at the Tevatron $p\bar{p}$ collider [286], for the first time using of an algorithmic approach to identify possible excesses. After partitioning the data into different final states, a multivariate algorithm, named SLEUTH, was used to determine the region of greatest excess and quantify the level to which it was compatible with the background prediction. SLEUTH takes the unbinned data as input and, using a Voronoi tessellation, divides the d-dimensional plane defined by the two to four input variables into $2^{N_{data}}$ regions. The use of an algorithm allowed a calculation of toy data and the statistical trial factor, i.e. the fact that a deviation gets statistically more likely the more phase space regions are investigated. For a subset of the regions it computes a measure of the compatibility with the background, and the fraction of pseudo-experiments in which the algorithm would find a region as incompatible as the one in data. The results of the search have been further extended in [287, 288, 289].

A disadvantage of such an approach is the large trial factor involved with working in multidimensional spaces, which degrades the search sensitivity. In 2004 the H1 collaboration at the HERA collider pursued an approach with a one dimensional search algorithm exploring the sum of transverse momenta distributions of their Run 1 dataset. This was the first analysis to perform a search in every final state accessible to the experiment [290, 291].

A global model-independent search has also been performed at the CDF experiment [292, 293]. A set of physically motivated correction factors, determined in a global fit to the data, is applied to the MC

prediction to minimize the disagreement with data. The shapes of over 15000 kinematic distributions are compared to the MC prediction, and a Kolmogorov-Smirnov test is used to evaluate the agreement. Further sensitivity is provided by two additional algorithms, similar to the one used in H1. "Bump Hunter" [294] searches invariant mass distributions for "bumps" that could indicate resonant production of new particles, while SLEUTH scans for data excesses at large summed transverse momentum.

More recently a general search following the H1 approach has been performed by the CMS collaboration, with 36 pb^{-1} of data, in events containing an electron or muon [295].

7.3 ANALYSIS STRATEGY

This analysis is the continuation of a previous ATLAS result based on 4.7 fb^{-1} of data collected at $\sqrt{s} = 7$ TeV in 2011 [1]. All event topologies involving electrons, photons, muons, jets, jets originating from *B*-hadrons (b-jets) and missing transverse momentum are investigated in a single analysis. Three kinematic distributions sensitive to contributions from NP are scanned for deviations from the SM prediction. A statistical search algorithm looks for the region of largest deviation between data and the SM, taking into account systematic uncertainties. The algorithm is used to find both excesses and deficits of data, as interference effects can produce a suppression or a "dip" in the background expectation increasing the sensitivity for some NP scenarios [296, 297, 298]. The SM prediction is mainly constructed from Monte Carlo (MC) simulation. To quantify the compatibility of the data with the SM prediction, the distribution of the *p*-values of the observed deviations is compared to an expectation obtained from pseudo-experiments that includes statistical and systematic uncertainties and their correlations between search classes. If a significant deviation is found, a dedicated analysis will be required to determine if the deviation is caused by a mismodeling of the SM prediction, or by a signal of new physics. A schematic view of the analysis workflow is shown in Figure 51.

7.4 DATA AND MC SAMPLES

7.4.1 *Data sample*

The data samples used in this analysis have been recorded by the ATLAS detector between the 4th April and 6th December 2012. Over this period the instantaneous luminosity increased from 2.74×10^{30} to 7.61×10^{33} $cm^{-2}s^{-1}$ and the peak mean number of interactions per bunch crossing increased from 5.9 to 36.53. The raw recorded data corresponds to an integrated luminosity of 21.7 fb^{-1}. Application of

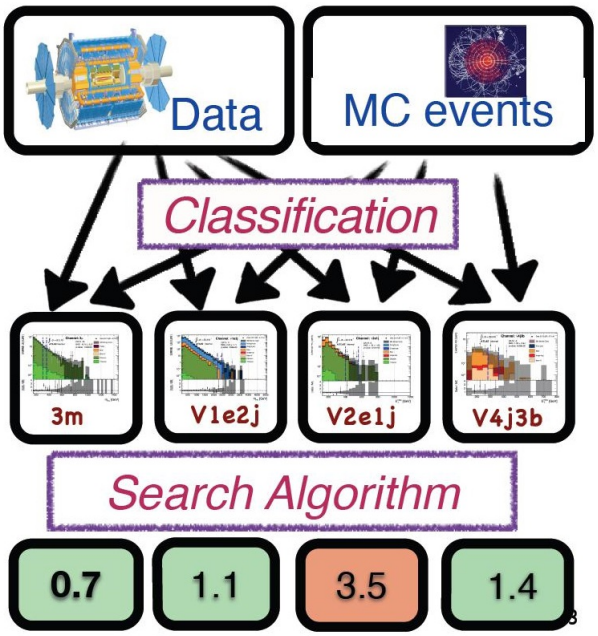

Figure 51: A schematic depiction of the workflow of the general search analysis. Data and simulated events are classified in different event classes according to the number and type of objects reconstructed. In a second step a search algorithm is used to scan distributions for deviations from the SM prediction, and flag possible anomalies.

beam, detector and data-quality requirements results in a data set with a total integrated luminosity of 20.3 fb^{-1}.

7.4.2 *Background Samples*

Monte Carlo simulated data samples are used to estimate SM backgrounds, and assess sensitivity to specific signal models. All processes producing high p_T objects with a non negligible cross section are considered for the SM estimate: inclusive jets production, $W/Z/\gamma$ production in association with jets, single top and top pair production, diboson, triboson and Higgs production. In addition samples of new physics are considered as benchmark signals. Most MC samples are produced using a GEANT4 [299] based full detector simulation [300], while the top pair, W+jets, Z+jets, γ+jets and the SUSY signal samples are passed through a fast simulation using a parameterisation of the performance of the ATLAS electromagnetic and hadronic calorimeters [301] and a GEANT4 based simulation elsewhere. Several corrections are applied to the MC to reproduce the reconstruction efficiencies of muons, electrons and photons measured in data. Additional scale factors are used to correct the b-tagging reconstruction and misidentification efficiencies.

The simulation includes the effect of multiple pp interactions and is weighted to reproduce the observed distribution of the average number of collisions per bunch crossing. Most of the MC samples used have a total integrated luminosity much larger than the one in data (typically from few 100 to few 1000 fb^{-1}). Samples of multijet production for low p_T of the jets and samples of vector boson production with a low p_T vector boson have a total luminosity only comparable to that in the data.

Every sample used in this analysis is overlaid during digitization with additional minimum bias events. Minimum bias events are generated with PYTHIA8 [302], the AM2 tune [303] and the leading-order PDF set `MSTW2008LO` [48].

- **QCD multijet**
  Simulated multijet events are generated with PYTHIA-8.165 [302], which uses $2 \to 2$ Leading-Order (LO) matrix elements (ME) with the CT10 next-to-leading-order PDFs and the ATLAS tune AU2.

- **$Z/\gamma*$ and $W+$ jet production**
  Samples of W and $Z/\gamma*$ in association with jets are simulated with the SHERPA-1.4.0 [58] MC generator with up to 5 extra partons in the matrix element. Both b- and c-quarks are treated as massive. SHERPA-1.4.0 is a complete Monte Carlo generator and thus uses its own parton shower, fragmentation and underlying event models whereas the parton density functions are taken from the next-to-leading-order PDF set CT10 [269]. The samples are normalized to the NNLO inclusive cross section calculation in [304].

- **γ+jets and $\gamma\gamma$+jets**
  Photon plus jets samples are generated with SHERPA-1.4.0 with up to 4 extra partons in the matrix element. Prompt diphoton samples are generated with ALPGEN-2.14 and PYTHIA-6.426 [305] in various ranges of the invariant diphoton mass. These samples include the processes $gg \to \gamma\gamma$ and $q\bar{q} \to \gamma\gamma$. A filter is applied to only select events where the two photons have $p_T > 35$ GeV.

- **$W/Z + \gamma/\gamma\gamma$**
  The $W\gamma$ samples are generated using ALPGEN-2.14 [306] interfaced to PYTHIA-6.426. A generator level filter requiring at least one photon with $p_T > 10$ GeV is applied. The $Z\gamma$ process is generated with SHERPA-1.4.0. The PDF set used for these samples is `CTEQ6L1` [307]. SHERPA-1.4.0 is also used to generate $W/Z + \gamma\gamma$ samples, with a leading-order matrix element. A k-factor of 1.2 is applied to the $W/Z + \gamma$ samples, while a k-factor of 2 and 3

is used for $Z + \gamma\gamma$ and $W + \gamma\gamma$, respectively, based on the NLO calculations in [308, 309].

- **Top quark pair and single top production**
  The production of top quark pairs is simulated with POWHEG [78] interfaced to PYTHIA-6.426 (with the Perugia 2011C tune) for the fragmentation and the hadronization processes. The top-quark mass is fixed to 172.5 GeV. The NLO PDF set CT10 is used. The $t\bar{t}$ cross section has been calculated at NNLO in QCD including resummation of NNLL soft gluon terms with TOP++2.0 [310, 311, 312, 313, 314, 315]. Single top samples for the Wt and s-channels are generated with POWHEG + PYTHIA-6.426 (Perugia 2011C tune) and the PDF set CT10. The single top sample for the t-channel production is generated with ACERMC-3.8 and PYTHIA-6.426 and the PDF set CT10. They are normalized to the NLL calculations in Refs. [316, 317, 318]. An additional sample generated with MADGRAPH-5.1.4.8 + PYTHIA-8.165 and the MSTW2008LO PDF is used for SM production of four top quarks.

- **Top and vector boson associated production**
  Top quark pair production also occurs with an additional electroweak boson (W, $Z/\gamma*$) or a real photon. These samples are simulated with MADGRAPH-5.1.4.8 interfaced to PYTHIA-6.426 including up to two extra partons. An additional sample is generated with MADGRAPH-5.1.4.8 + PYTHIA-8.165 and the MSTW2008LO PDF set for exclusive $t\bar{t}WW$ production. Samples for single top production in association with a leptonically decaying Z boson, generated with MADGRAPH-5.1.4.8 interfaced to PYTHIA-6.426 and the CTEQ6L1 PDF, have also been included. Samples of $t\bar{t}$ +W and $t\bar{t}$ +Z are normalized to the NLO cross section calculated in [319, 320], the others to the LO cross-section from the generator.

- **Massive diboson production**
  Diboson (WW, WZ and ZZ) events are simulated using POWHEG+ PYTHIA-6.426 and the PDF set CT10. In these samples leptonic decays are enforced. No filter is applied for WW while for WZ and ZZ a filter is applied to select events with a generator level mass of the off-shell Z larger than 4 GeV and two leptons with $p_T > 5$ GeV. Separate samples generated with SHERPA-1.4.0 are used to include the case in which a boson decays to hadrons. They are normalized to NLO inclusive cross sections obtained with MCFM [321]. Due to much larger W/Z+jets and multijet cross sections, the contribution of fully hadronic decay modes is negligible.

- **Massive triboson production**
  The triboson processes *WWW*, *ZWW* and ZZZ are generated with MadGraph-5.1.4.8 +Pythia-6.426 at LO for the case in which all bosons decay leptonically while Sherpa-1.4.0 is used for the case where one of the bosons decays into hadrons. They are normalized to the NLO inclusive calculation in Ref. [322].

- **Higgs production** SM Higgs production (with a mass of 125 GeV) is also included as a background. Samples are generated using either Pythia-8.165 with CTEQ6L1 PDF set or with Powheg+Pythia-8.165 and the CT10 PDF. The samples are normalized to the cross sections recommended by the LHC Higgs cross section working group [323].

- **Benchmark Signals**
  The production of supersymmetric particles is considered as a first benchmark signal of new physics.

  One set of signals is the pair production of top squarks (stop) $\tilde{t}$ with the decay $\tilde{t} \to t\tilde{\chi}_1^0$. Here the masses considered of the $\tilde{t}$ are 400, 500 or 600 GeV with a massless lightest neutralino that is stable.

  The second set of benchmark signals considers the pair production of gluinos which decay through a virtual stop of mass 2.5 TeV to $t\bar{t}\tilde{\chi}_1^0$ with a branching fraction of 100%. Here the mass of the neutralino is set to 100 GeV and the mass of the gluino varies from 800, 1000 to 1200 GeV. Benchmark signals are generated with Herwig++ 2.5.2 [324] and the CTEQ6L1 PDF set. Signal cross sections are calculated to next-to-leading order in the strong coupling constant, adding the resummation of soft gluon emission at next-to-leading-logarithmic accuracy (NLO+NLL) [325, 326, 327, 328, 329].

  A third set of benchmark signals is the production of a heavy Z' in the sequential SM, which assumes the same coupling to fermions as the SM Z boson [330]. The Z' masses considered are 1500, 2000 or 2500 GeV and the decays considered are to pairs of electrons or muons of opposite charge. Samples are generated with Pythia-8.165 and the MSTW2008LO PDF set.

7.5 TRIGGERS

To collect the largest data sample possible with the smallest possible bias events are selected using a logical OR of several triggers: single lepton and photon, single or multijet and E_T^{miss}. These triggers reach their maximal efficiency after applying the offline selection listed in Table 17. In order to avoid double

counting, events are taken from the different triggers according to the following priority order. Events with $E_T^{miss} > 150$ GeV are required to pass the E_T^{miss} trigger. Events failing this E_T^{miss} requirement but with a muon with $p_T > 25$ GeV are required to pass the muon trigger. Remaining events with electrons with $p_T > 25$ GeV or photons with $p_T > 40$ GeV are taken from electron and photon triggers. Events containing a jet (or b-jet) with $p_T > 500$ GeV or 5 jets (or b-jets) with $p_T > 80$ GeV are required to pass the jet and multijet triggers respectively.

The ATLAS experiment records events in different physics streams depending on the sets of trigger criteria that accepted the event. All events in the jet and missing transverse momentum (JetTauEtmiss) stream, the electron and photon (EGamma) stream and the Muon stream are considered for this analysis. As the physics streams follow an inclusive trigger selection the same event can be written to more than one stream. In order to avoid double counting of event classes, each event is taken from the stream with the loosest trigger requirement.

Following the object reconstruction described above, events are discarded if they have any jets failing quality selection criteria designed to suppress detector noise and non-collision backgrounds [217]. Events are also required to have a primary vertex reconstructed from five or more tracks with $p_T > 0.4$ GeV; the vertex with the largest $\sum p_T^2$ of the associated tracks is chosen. Non-collision backgrounds were studied in several ATLAS analyses with identical object selection criteria and these backgrounds were found to give a negligible contribution after event cleaning selections [331].

7.6 EVENTS CLASSIFICATION

After the data quality requirement, trigger, and event cleaning have been applied, the events are subdivided into exclusive classes based on the number and types of objects reconstructed in the event; electrons (e), muons (μ), photons (γ), jets (j), b-jets (b) and E_T^{miss} (ν). Hadronically decaying tau leptons have been considered as possible additional object. Their reconstruction and identification have however large uncertainties and suffer from large backgrounds from misidentified hadronic jets which are difficult to model in the simulation. Taus are thus not considered in this analysis, and their study is left for future iterations of this analysis.

This subdivision can be regarded as a classification according to the most important features of the events. The partitioning is orthogonal, with each event associated with one and only one

Trigger item	Offline requirement
Muon Stream	
EF_ mu24i_tight OR EF_mu36_tight	$p_T > 25$ GeV
EF_2mu13	$pt(\mu_1, \mu_2) > 15$ GeV
EGamma Stream	
EF_ e24vhi_ medium1 OR EF_e60_medium1	$p_T(e) > 25$ GeV
EF_2e14_medium	$p_T(e_1, e_2) > 15$ GeV
EF_g120_loose	$p_T(\gamma) > 140$ GeV
EF_g30_medium_g20_medium	$p_T(\gamma_1, \gamma_2) > 40$ GeV
JetTauEtmiss Stream	
EF_j360_a4tchad	$p_T(jet) > 500$ GeV
EF_5j55_a4tchad_L2FS	$p_T(jet_{1,\cdots,5}) > 80$ GeV
EF_xe80(T)_tclcw_loose	$E_T^{miss} > 150$ GeV

Table 17: List of the p_T cuts used for each object in order to have a fully efficient trigger.

final state. Possible final states are defined algorithmically, and are dynamically created to accommodate all events. The classification includes all possible final state configurations and object multiplicities, e.g. if a data event with 7 reconstructed muons is found it is classified in a "7-muon" event class (7μ). Similarly an event with missing transverse momentum, 2 muons, 1 photon and 4 jets is classified and considered in a corresponding event class denoted ($\nu 2\mu 1\gamma 4j$). To suppress sources of fake E_T^{miss} two additional requirements are applied on events to be classified in ν categories. The ratio of E_T^{miss} over m_{eff} (where m_{eff} is defined in each event class as the scalar sum of the p_T of the objects defining the class, including the E_T^{miss}) is required to be greater than 0.2 and the minimum azimuthal separation between the E_T^{miss} and the three leading reconstructed jets (if present) has to be greater than 0.4, otherwise the event is rejected. The p_T requirement applied on top of the trigger selection and the labels used for each object are summarized in Table 18.

object	jet	b-jet	electron	muon	photon	E_T^{miss}
label	j	b	e	μ	γ	ν
lower p_T cut [GeV]	50	50	25	25	40	150

Table 18: List of objects used for the event classification with their labels and lower p_T requirement.

7.7 BACKGROUND ESTIMATION

In this search the SM prediction for almost all processes is taken from MC simulation. Only background events with one lepton candidate originating from misidentification of hadronic jets, photon conversions or real leptons from heavy flavor decays (collectively referred to as fake leptons) are estimated using data. For categories containing more than one lepton the contribution from fake leptons is found to be small compared to the total background and taken directly from the simulation. Comparisons between data and simulation in dedicated control regions with enlarged fake-lepton contribution have shown agreement within uncertainties. Re-weighting procedures are applied to some of the MC samples to improve the modeling of the SM background. This is described in section 7.7.2

7.7.1 *Estimation of fake lepton background*

Background contributions with exactly one fake lepton are determined with a data-driven procedure referred to as the ABCD method. In an ABCD method the background rate is estimated by applying the event selections on two independent, uncorrelated variables, such that both selections enhance the signal to background ratio. This separates the phase-space into four regions: a signal dominated and three background enhanced regions. The two variables used here are the relative track isolation of the lepton and the track impact parameter significance, in which the requirements applied for signal leptons (described in Sections 5.4 and 5.5) are reverted. The expected number of background events in the signal dominated region A can be determined from the observed data events in the other three regions as $N_A = N_C \times N_B/N_D$, after removing the prompt leptons contribution predicted by the MC in regions B, C and D. The method has been tested on MC samples, and from the accuracy of the results an uncertainty of 50% is assigned to the fake lepton estimate for all event classes. The method is validated

with data at low transverse and low effective mass in 1 lepton classes with 1 jet, 3 jets, and 1 jet and 1 b-jet. By applying this data-driven procedure the analysis has reduced sensitivity to NP models predicting non-isolated leptons.

7.7.2 *Corrections to the MC prediction*

In classes containing only j and b the multijet MC samples are scaled to data with normalization factors, ranging from 0.4 to 1, derived separately in each exclusive jet multiplicity class (e.g. for the 1j2b the same normalization factor as for the 3j category is used). This ansatz is found to describe the jet multiplicity distribution also for the b-jet channels. After this scaling is applied we lose sensitivity to NP effects causing only normalization differences between data and the MC prediction in event classes containing only j and b. The simulated W/Z+jets and top pair samples are reweighed to improve the modeling in classes containing ν, by reweighing the truth-level p_T distribution of the boson or top quark pair. The W/Z+jets correction was determined in a control region requiring one lepton and high E_T^{miss} by the search for stop decays to charm and neutralinos [332]. The correction of the $t\bar{t}$ p_T distribution was determined in a search for squarks and gluinos in decays with one isolated lepton and derived in a control region requiring one lepton, high E_T^{miss}, 3 or 5 jets and one b-tagged jet [333]. These corrections lead to a lower SM prediction for classes with E_T^{miss}. The reweighing has no effect on the largest positive deviations, but decreases the number of deficits seen in data.

7.8 SYSTEMATIC UNCERTAINTIES

The systematic uncertainties have both uncorrelated components and components which are correlated between event classes and within different bins of kinematic distributions in the same event class. The correlated component is taken as a normalization uncertainty assigned coherently to all bins and event classes. The uncorrelated components vary independently among different bins and event classes. In the search algorithm, all uncertainties are treated as uncorrelated. Correlations according to the correlated uncertainty components are, however, used for the generation of the pseudo-experiments. The experimental uncertainties and the uncertainty due to the limited number of MC events are found to dominate in the majority of the event classes.

7.8.1 *Experimental Uncertainties*

The dominant detector-related systematic effects are due to the uncertainties in the jet energy scale (JES) and resolution (JER), and to the limited knowledge of the b-tagging efficiencies. The JES uncertainty estimate is based on MC studies, test-beam data and in-situ measurements (as described in Sec. 5.2).

Uncertainties on electron and muon reconstruction and identification efficiencies, as well as muon momentum scale and resolution, are not considered as they have been found negligible in all of the considered event classes. A systematic uncertainty related to the pileup modeling is determined by comparing the nominal reweighting with a shift in the weight scale of 10%. The uncertainty on the amount of collected luminosity is $\pm 2.8\%$ derived following the same methodology as [207]. Experimental uncertainties are treated as correlated and the uncertainty due to the limited number of MC events is treated as uncorrelated in the pseudo-experiment generation.

7.8.2 *Uncertainties on the background processes*

The principle of this analysis is to search for a deviation from the MC description and, if such a deviation is found, to study it with a dedicated analysis. Therefore no rigorous determination of the theoretical uncertainties was performed for the present general search. Systematic uncertainties are assigned to represent typical theoretical uncertainties of the models and generators used. The uncertainties are motivated by theoretical studies and the results of dedicated searches and measurements by the ATLAS Collaboration at high-p_T. All theory uncertainties are treated as constant over the studied parameter space. They are summarised for the SM processes considered in Table 19 and discussed below. Theoretical uncertainties are assigned per subprocess and subdivided into an uncorrelated and a correlated component. Multijet processes are modeled using MC samples for the $2 \to 2$ process only. However, as the jet multiplicity is reweighted to data, no cross-section uncertainty is applied. An uncorrelated uncertainty of 30% is assumed, based on studies described in [334], to cover any residual difference between data and the simulation. Systematic uncertainties of 10% correlated and 30% uncorrelated are applied to γ+jets and $\gamma\gamma$+jets production processes. These values are a bit larger then the uncertainties quoted in [335]. The inclusive W and Z cross-sections are known at NNLO, with an uncertainty of $\approx$5%. We assign this 5% as a correlated uncertainty, while 15% is taken as uncorre-

lated uncertainty. These uncertainties are inspired by [336]. For W/Z+heavy flavour processes a correlated uncertainty of 30% is assigned and an uncorrelated uncertainty of 10%. The uncertainty for these processes is increased to be consistent with the reweighting and uncertainties found in other ATLAS analyses, e.g. in [337]. For $t\bar{t}$ and single top, for which the inclusive cross-section is known to NNLO and NLO, respectively, a correlated uncertainty of 5% and an uncorrelated uncertainty of 20% is used. We use slightly larger uncertainties than those given in [338]. For $t\bar{t}$ production with additional vector bosons we assign a 10% correlated uncertainty and a 30% uncorrelated uncertainty. Again these numbers are slightly more conservative than those determined from pure PDF and scale variation (see e.g. [319, 320]). Diboson processes (including $W/Z + \gamma$) are known to NLO. A correlated uncertainty of 10% and an uncorrelated uncertainty of 30% are assigned for these processes. To cover possible shape uncertainties in specific phase-space regions and due to additional jet production we have quoted a more conservative uncertainty than that in [339]. For triboson production (including $W/Z + \gamma\gamma$) we consider a correlated uncertainty of 20% and 50% as an uncorrelated uncertainty. Similar numbers are found in [340]. The same conservative uncertainties are used for the single top+Z and four top production. An uncorrelated uncertainty of 20% is used for all Higgs production processes to cover systematics in specific phase-space regions, e.g. with additional jet production. The correlated uncertainty is set to 5% due to the well-known Higgs cross-sections [323].

7.9 CLASSIFICATION RESULTS

Data events are found in 573 event classes. The number of classes with an SM expectation larger than 0.1 is 697. These classes are further considered for the statistical analysis. A total of 16 event classes have an SM expectation of less than 0.1 events, but at least one data event. Two data events are found only in the $2\mu 1e5j$ event class, with a background expectation of 0.045 ± 0.028. The data and MC prediction for a subset of the 697 classes with an SM expectation greater than 0.1 is shown in Figure 52, while for the remaining event classes they are shown in Appendix **??**. Agreement between data and the SM prediction is observed for most event classes.

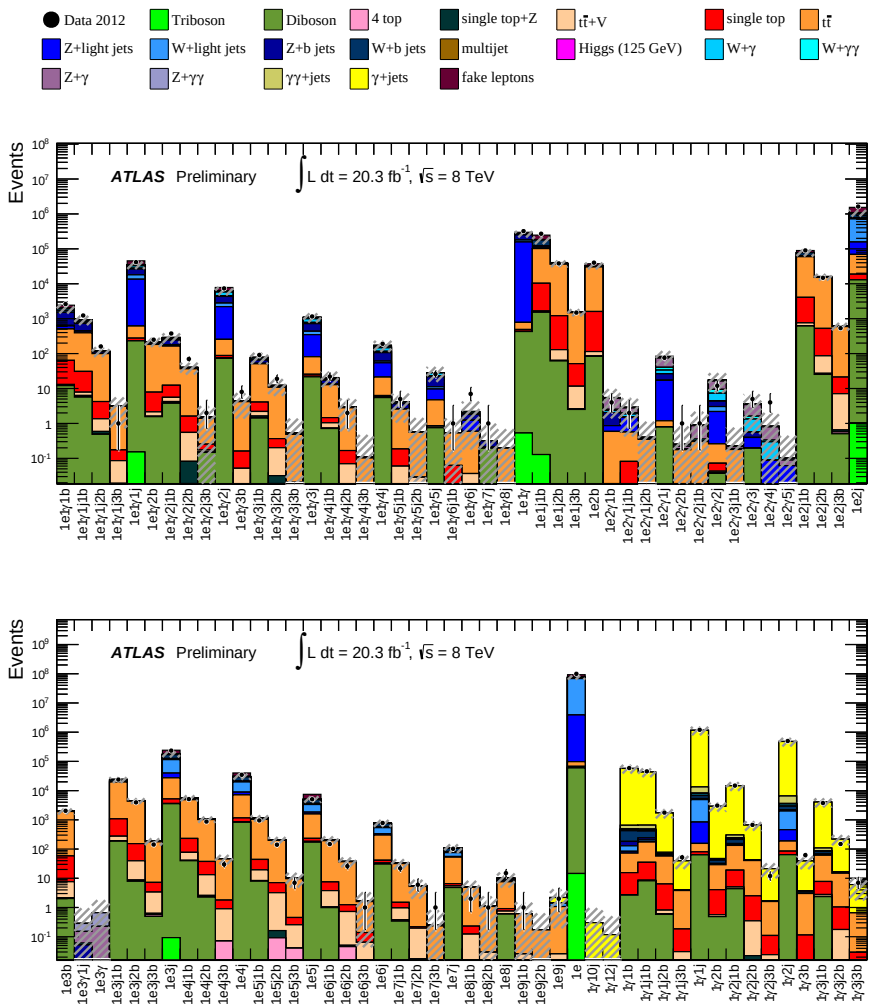

Figure 52: Number of events for event classes for which jets or E_T^{miss} triggers are used. The classes are labeled according to the abundance and type (e, μ, γ, j, b, nu) of the reconstructed objects for this event class. The data are compared to the SM background expectation as described in the text. The hatched bands indicate the total uncertainty of the SM prediction.

Systematic Uncertainties		
Background	correlated (%)	uncorrelated (%)
Multijets (normalized to data)	0	30
γ+jets and $\gamma\gamma$+jets	10	30
W/Z + light flavour production	5	15
W/Z + heavy flavour production	10	30
$t\bar{t}$ and single top	5	20
$t\bar{t}$ + vector boson	10	30
Diboson (including W/Z+γ)	10	30
Triboson	20	50
Higgs production	5	20

Table 19: Theoretical uncertainties assigned to the modeling of the background processes, subdivided into correlated and uncorrelated effects for the generation of the pseudo-experiments.

7.10 STATISTICAL INTERPRETATION

In order to quantitatively determine the level of agreement between the data and the SM expectation and to identify regions of possible deviations we use an algorithm, first developed for the H1 general search [290]. As a compromise between maximizing our sensitivity and keeping the look elsewhere effect at manageable level, it is applied only on three distributions: m_{eff} is defined as the scalar sum of transverse momenta $\sum p_T$ of all reconstructed objects including the missing energy, m_{inv} is the total invariant mass of the reconstructed objects in the event and in case the class is flagged with ν the E_T^{miss} distribution is scanned as well. These variables have been widely used in the contest of searches for new physics, being sensitive to a large class of new physics signals.

The algorithm described in the following locates the region of largest deviation, be it a deficit or an excess, in a distribution (provided in form of histogram).

The search algorithm locates the region of largest deviation in a distribution of any shape. The bin size of the scanned distributions is chosen to reflect the expected resolution of each variable

in a given class, with values ranging from 20 to 500 GeV. [1] In the scan of the m_{inv} distribution for each event class, only the region where m_{inv} is greater than the sum of the minimum p_T requirement of each contributing object is considered (e.g. 50 GeV for a 2μ class). This avoids sensitivity to the threshold regions which may not be well-modeled by the MC simulation.

The number of data events N_{obs} and the expectation N_{SM} with its total systematic uncertainty δN_{SM} is determined for each possible connected bin region of the histograms. A statistical estimator p is then used to judge which region is of most interest. This estimator is derived from the convolution of the Poisson probability density function (pdf) to account for statistical errors with a Gaussian pdf, $G(b; N_{SM}, \delta N_{SM})$ with mean N_{SM} and width δN_{SM}, to include the effect of non negligible systematic uncertainties and is defined via:

$$p = \begin{cases} A \int_0^\infty db\, G(b, N_{SM}, \delta N_{SM}) \sum_{i=N_{obs}}^{\infty} \frac{e^{-b} b^i}{i!} & N_{obs} > N_{SM} \\ A \int_0^\infty db\, G(b, N_{SM}, \delta N_{SM}) \sum_{i=0}^{i=N_{obs}} \frac{e^{-b} b^i}{i!} & N_{obs} < N_{SM} \end{cases} \tag{77}$$

The factor $A = 1/\int_0^\infty db\, G(b; N_{SM}, \delta N_{SM}) \sum_{i=0}^{\infty} \frac{e^{-b} b^i}{i!}$ ensures that the pdf is normalized to unity. If the Gaussian pdf G is replaced by a Dirac delta function $\delta(b - N_{SM})$ the estimator p results in a usual Poisson probability. The value of *p* gives an estimate of the probability for the SM expectation to fluctuate upwards or downwards with respect to the data in a given region. Here we interpret *p* as the local *p*-value of this deviation. The region of greatest deviation found by the algorithm is the region with the smallest *p*-value. Such a method is able to find narrow resonances and single outstanding events as well as signals spread over large regions of phase space in distributions of any shape. To avoid being sensitive to the effect of poor Monte Carlo statistics regions where the background prediction has a relative uncertainty of 100% are discarded by the algorithm. As a consequence, a signal that would appear as an excess in data only in event classes with poor or no Monte Carlo statistics would be missed.

1 A value of 10 GeV has been considered in the scan of the m_{eff} and m_{inv} variables for the resolution of leptons. The resolution for photons it taken as 20 GeV, while 30 GeV is used for jets and E_T^{miss}. The scan of the E_T^{miss} variable uses a constant bin size of 40 GeV for all event classes.

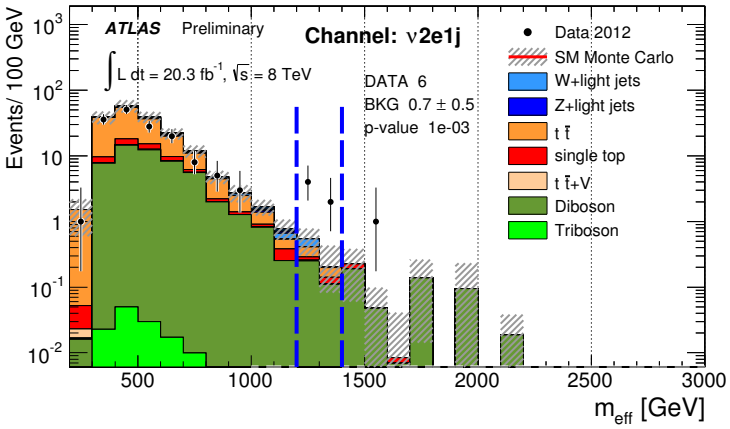

Figure 53: m_{eff} distribution for the event class with two electrons, one jet and Etmiss (ν2e1j). The dashed vertical lines indicate the region of interest which has the smallest p-value (0.0013) for this event class.

7.11 SEARCH RESULTS

To illustrate how the algorithm works, three example distributions are presented. Figure 53 shows the effective mass distribution for the event class with two electrons, one jet and E_T^{miss}; Figure 54 shows the visible invariant mass for the event class with with three muons; Figure 55 the E_T^{miss} distribution for the class containing 2 jets, 2 b-jets and E_T^{miss}. The region of greatest deviation found by the search algorithm in these distributions is indicated by vertical lines.

The probability that a statistical fluctuation occurs somewhere in the event class distributions is modelled by pseudo-experiments. In this procedure, the data are replaced by pseudo-data which are generated according to the SM expectation. We generated 2000 "pseudo ATLAS experiments", each consisting of the same event classes and distributions as considered in the data. The search algorithm is applied to each of these in the same way as for data. The p-value distributions of the "pseudo ATLAS experiment" and their statistical properties can be compared with the p-value distributions obtained from data. The effect of bin-by-bin correlations is taken into account in the generation of pseudo-experiments. The distribution of the local p-values observed in data for each event class, compared to the expectation from the SM hypothesis as obtained from the pseudo-experiments, are shown in Figures 56, 58 and 60 for the m_{eff}, m_{inv} and E_T^{miss} distributions, respectively. These figures also show for comparison the expected p-value distributions obtained when neglecting correlations in the pseudo-experiment generation. This

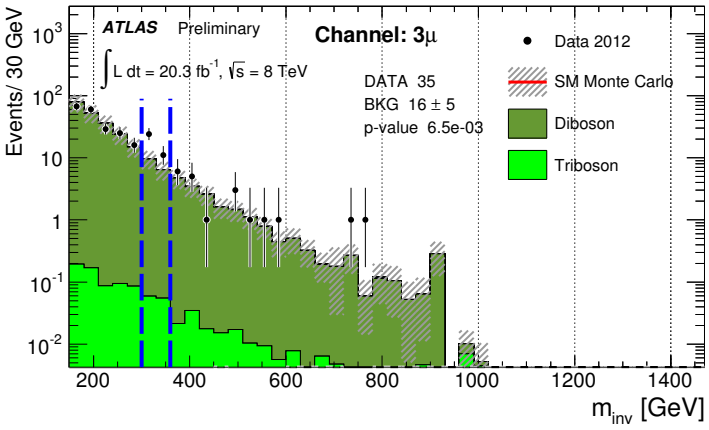

Figure 54: m_{inv} distribution for the event class with three muons (μ). The dashed vertical lines indicate the region of interest which has the smallest p-value (0.0071) for this event class.

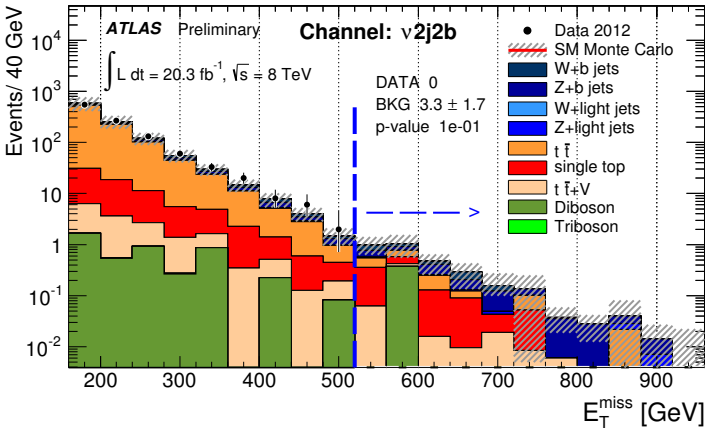

Figure 55: E_T^{miss} distribution for the event class with 2 jets, 2 b-jets and E_T^{miss} (ν2j2b). The dashed vertical line and the arrow indicate the region of interest which has the smallest p-value (0.097) for this event class.

treatment leads to smaller p-values but the probability that a single deviation occurs at very low p-values is less affected. Agreement is observed between data and the expectation from correlated systematics. In Figures 56, 59 and 61 we show the fraction of pseudo-experiments that have at least one, two, or three deviations below a given p-value (p_{min}).

No event class is found with a local p-value below 10^{-4}, corresponding roughly to a 4σ deviation. This is consistent with the expectation from pseudo-experiments. At least one class with a local p-value below 10^{-4} is expected to be found in less than 10% of the pseudo-experiments in the visible invariant mass distributions, in about 10% of the pseudo-experiments in the scan of the effective mass distributions and about 5% of the pseudo-experiments in the scan of the E_T^{miss} distributions. One event class is found in the effective mass distribution with a p-value smaller than 10^{-3}, corresponding to a probability of about 60%. The smallest p-value obtained from the scan of the E_T^{miss} distribution is 0.013. Pseudo-experiments would predict a slightly larger number of excesses indicating a possible overestimation of the systematic uncertainties. For the five largest deviations found in the scan of each variable the number of data and background events, the uncertainty on the background and the p-value in the region of interest are summarised in Table 20. The largest deviation has a local p-value of $7 \cdot 10^{-4}$ and is found in the effective mass distribution of the $1\mu 1e 1\gamma 2j$ event class, shown in Figure 62, in a region with 8 data events and a background expectation of 1.34 ± 0.63 events.

Extensive checks have been carried out to understand how the p-value distribution changes when using different MC generators for the main backgrounds and varying the size of the theoretical uncertainties up and down by a factor of two. The effect of these variations is found to be insignificant on the tail of the p-value distribution and on the largest deviations found.

7.12 SENSITIVITY TO BENCHMARK NEW PHYSICS SIGNALS

A set of pseudo-data samples were generated to assess the sensitivity of the search procedure to some specific signals of new physics. The prediction of a new physics model is added on top of the SM prediction and the sum is used to generate pseudo-data samples. To quantify our sensitivity we compute the fraction of pseudo-experiments in which at least one event class is expected to have a significance greater than a given value, both under the SM-only hypothesis and under the SM+signal hypothesis. Since this analysis searches for large deviations, the

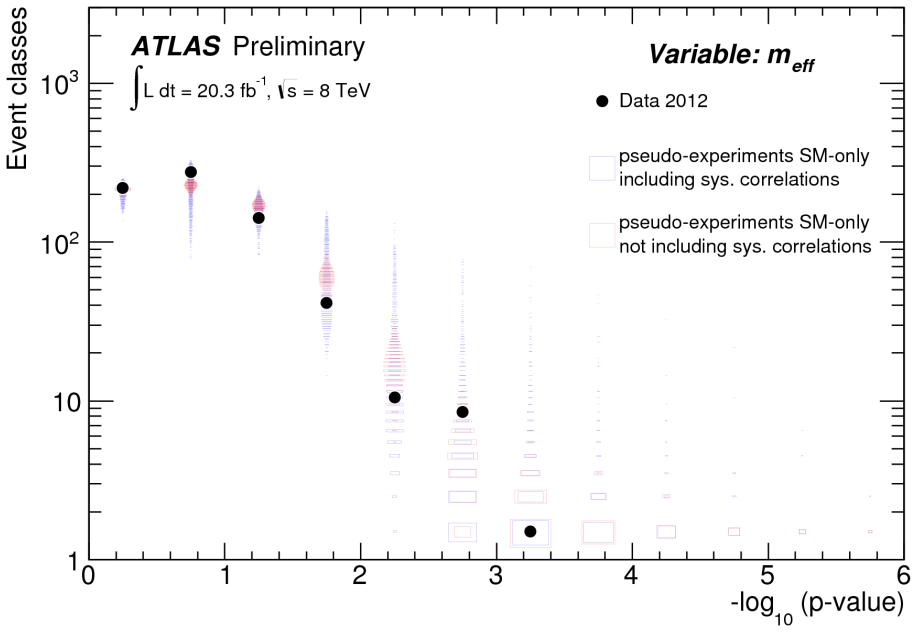

Figure 56: The observed and expected distributions for the number of event classes having a given range in $-\log_{10}(p-value)$ for the scans of the effective mass distributions. The data and mean expectation are shown together with the expected distributions obtained from the pseudo-experiments generated under the default assumptions for the correlations in the systematic uncertainties (blue) and neglecting their correlations (red).

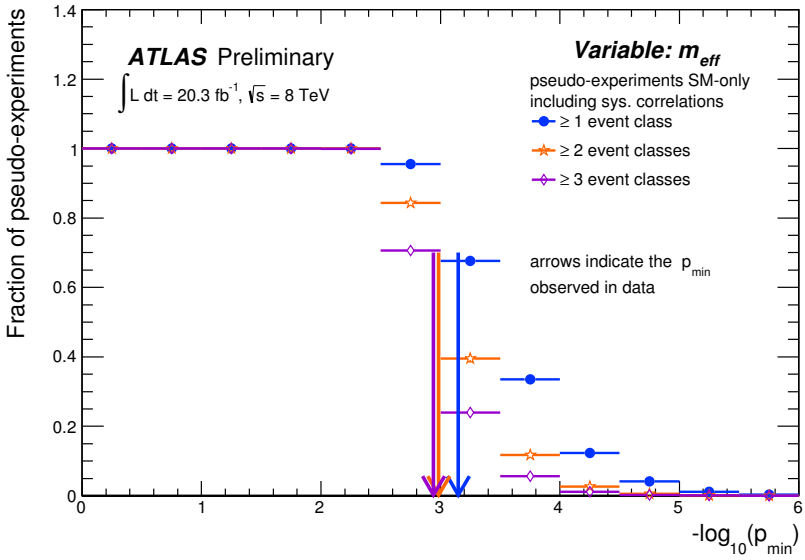

Figure 57: The fraction of pseudo-experiments which have at least one, two and three deviations with a p-value below a given threshold (p_{min}) in the scan of the effective mass distribution. The values observed in data are indicated by arrows. Pseudo-experiments are generated under the SM-only hypothesis and with the default assumption for the correlations in the systematic uncertainties.

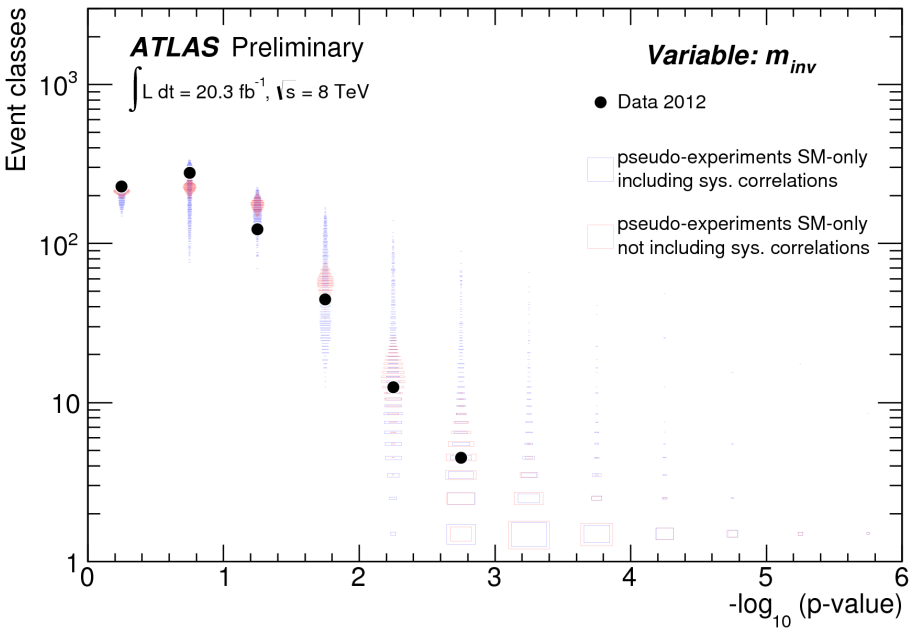

Figure 58: The observed and expected distributions for the number of event classes having a given range in $-\log_{10}(\mathrm{p-value})$ for the scans of the visible invariant mass distributions. The data and mean expectation are shown together with the expected distributions obtained from the pseudo-experiments generated under the default assumptions for the correlations in the systematic uncertainties (blue) and neglecting their correlations (red).

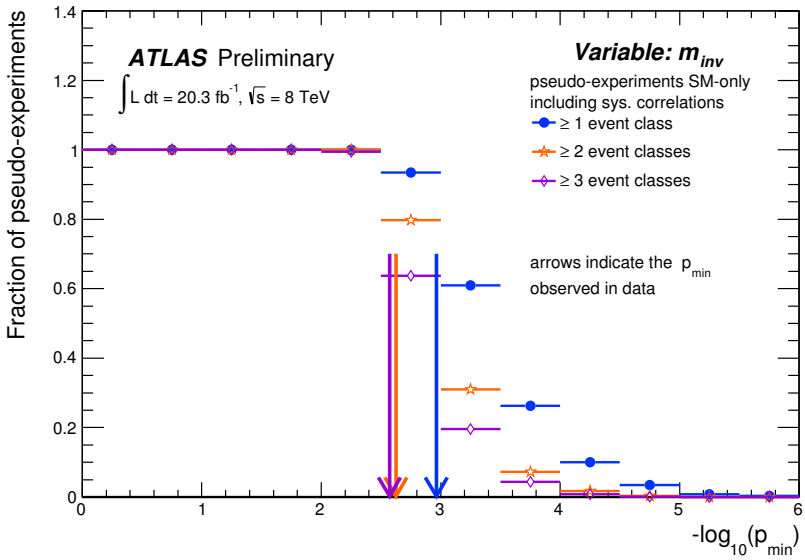

Figure 59: The fraction of pseudo-experiments which have at least one, two and three deviations with a p-value below a given threshold ($\mathrm{p_{min}}$) in the scan of the visible invariant mass distribution. The values observed in data are indicated by arrows. Pseudo-experiments are generated under the SM-only hypothesis and with the default assumption for the correlations in the systematic uncertainties.

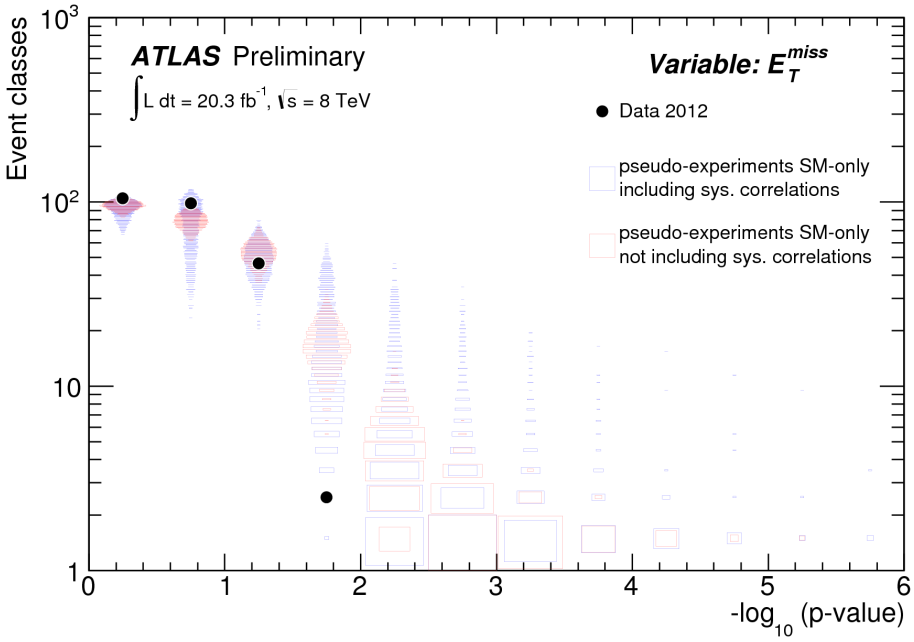

Figure 60: The observed and expected distributions for the number of event classes having a given range in $-\log_{10}(\mathrm{p-value})$ for the scans of the missing transverse energy distributions. The data and mean expectation are shown together with the expected distributions obtained from the pseudo-experiments generated under the default assumptions for the correlations in the systematic uncertainties (blue) and neglecting their correlations (red).

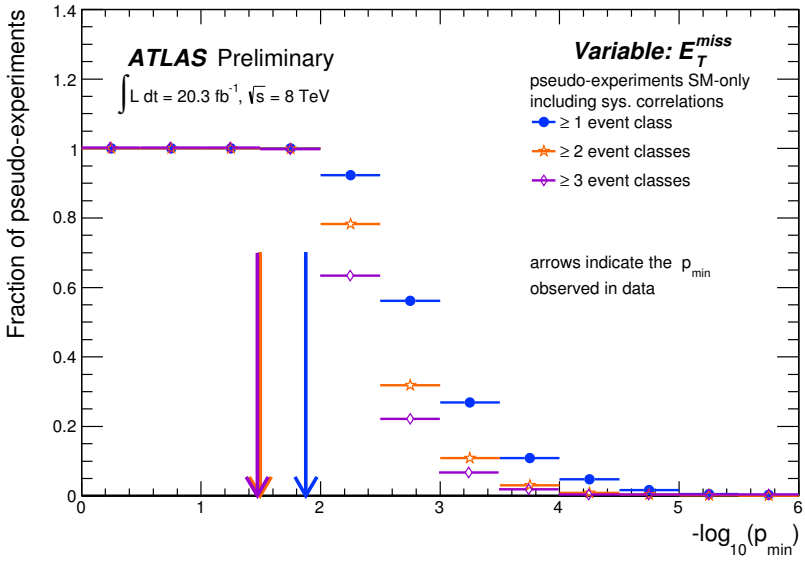

Figure 61: The fraction of pseudo-experiments which have at least one, two and three deviations with a p-value below a given threshold ($\mathrm{p_{min}}$) in the scan of the missing transverse energy distribution. The values observed in data are indicated by arrows. Pseudo-experiments are generated under the SM-only hypothesis and with the default assumption for the correlations in the systematic uncertainties.

topology	p-value	N_{Data}	$N_{MC} \pm \delta N_{MC}$
		m_{eff}	
1m1e1g2j	0.00069	8	1.4 ± 0.6
ν2e1j	0.0010	6	0.7 ± 0.5
1e2g4j	0.0011	4	0.25 ± 0.24
1e1g3j2b	0.0015	17	5.3 ± 2.0
1m2g1j	0.0018	0	8.9 ± 2.3
		m_{inv}	
1e2b	0.0011	5	0.5 ± 0.3
ν1e2j	0.0023	11	2.6 ± 1.4
ν4j3b	0.0027	7	1.3 ± 0.7
1m1e1g1b	0.0034	8	1.9 ± 0.8
1e1g2j1b	0.0052	11	2.7 ± 1.7
		E_T^{miss}	
ν2e1j	0.012	4	0.6 ± 0.5
ν2m2b	0.027	2	0.20 ± 0.19
ν4j3b	0.029	5	1.2 ± 0.8
ν1e7j	0.036	4	0.80 ± 0.78
ν1e1b	0.038	113	75 ± 19

Table 20: The five highest deviations found in the scan of the m_{eff}, m_{inv} and E_T^{miss} distributions.

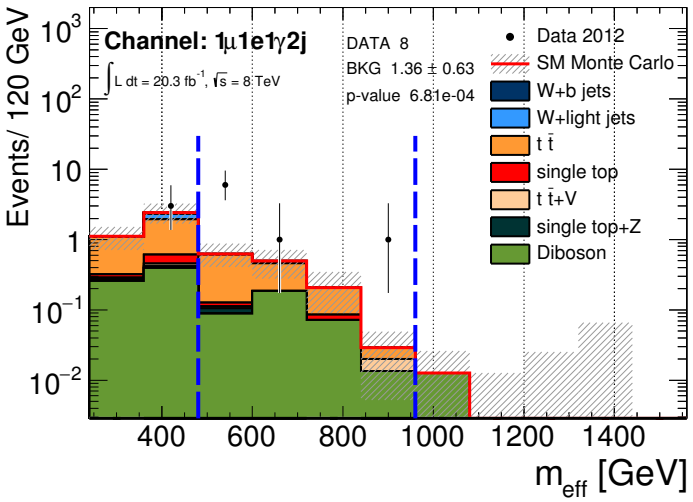

Figure 62: The m_{eff} distribution for the 1e1m1g2j event class.

sensitivity of the search needs to be compared to the discovery sensitivity and not the exclusion limits reported.

In Figure 63 (top) the effect of a signal is shown for direct stop production in the E_T^{miss} scan. No significant deviation in the p-values with respect to the SM-only hypothesis is observed, due to the relatively small stop production cross-section. In Figure 63 (middle) the effect of a signal is shown for gluino pair production in the m_{eff} scan. Pseudo-experiments for a 800 GeV gluino predict in about 95% of the cases a deviation with a p-value as low as 10^{-6}, with a probability close to zero for this to happen under the SM-only hypothesis. Due to the smaller production cross-section a gluino with a mass of 1000 GeV has a much smaller probability to yield an event class with such low p-values. Very little difference with respect to the SM expectation is visible for a gluino with a mass of 1200 GeV. The sensitivity to the Z′ signal is shown in Figure 63 (bottom). Because this signal is localized in few specific classes (i.e. $2e$, 2μ) in a narrow range of the m_{inv} distribution with low SM background the search algorithm shows marked sensitivity to it.

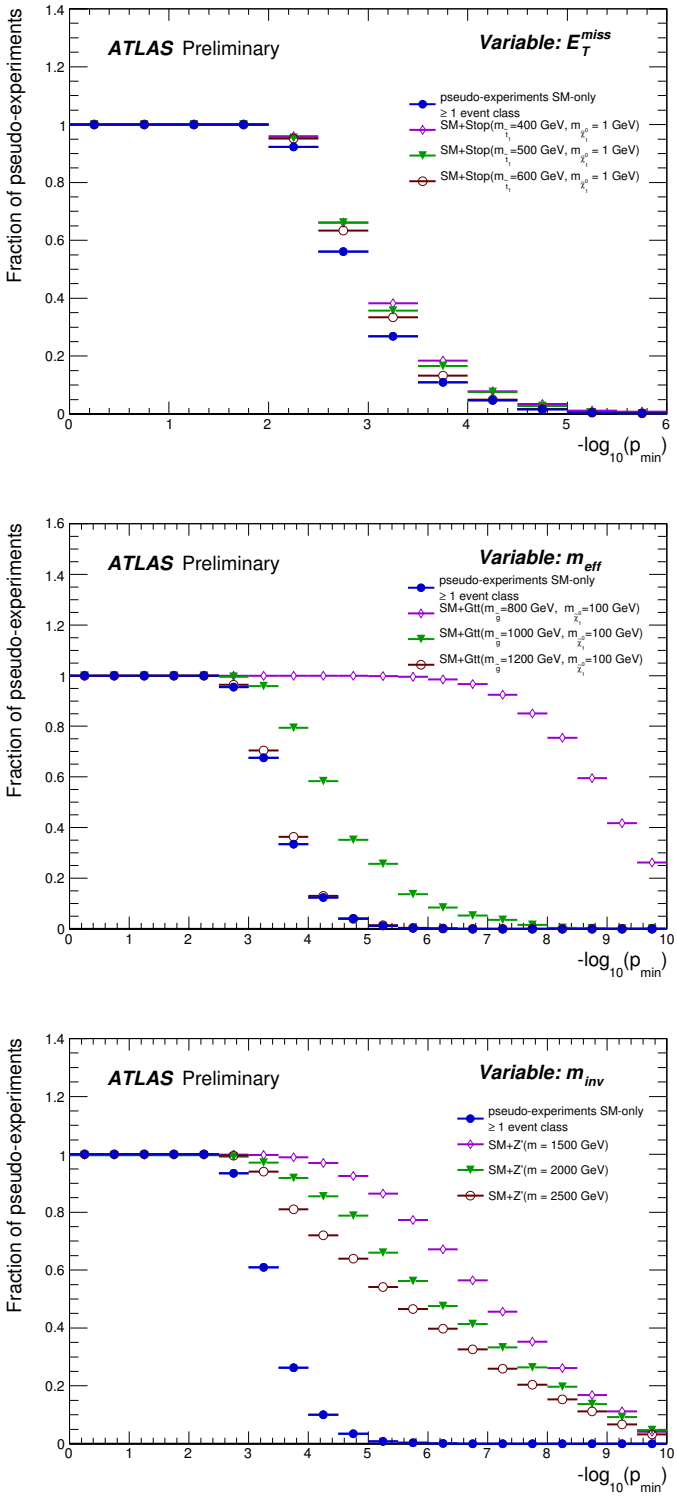

Figure 63: Sensitivity of the search method to benchmark signal models. The figure shows the expected fraction of pseudo-experiments having at least one event class with a $-\log_{10}(p-value)$ greater than the one shown on the axis for pseudo-experiments generated under the SM-only and SM+signal hypothesis. The top figure shows a model of direct stop production for the scan of the E_T^{miss} distribution. The middle figure shows the fraction of pseudo-experiments for the production of a gluino pair with various gluino masses considering the m_{eff} scans. The lower figure shows the fraction of pseudo-experiments for the production of a Z′ considering the m_{inv} scans.

CONCLUSIONS

The first run of the LHC has provided much needed data to improve our knowledge of particle physics at the TeV scale. Their analysis is providing a wealth of information, allowing us to improve our understanding of the Standard Model, as well as to put stringent constraints on models of New Physics.

As the number of top quarks available for study increased from the few tens used for discovery to the millions collected at the LHC the accuracy of the measurements of top quark properties has greatly improved, allowing precise tests of QCD predictions. In particular the modeling of extra radiation in top events has important implications for measurements of the top mass, but is also a sizeable uncertainty in other SM studies (such as Higgs production) and in searches for new physics.

In chapter 6 we have presented the ATTBAR tune of the Pythia8 parton shower ISR and FSR parameters to ATLAS measurements of $t\bar{t}$ production at 7 TeV. The Professor code, widely used in the context of Monte Carlo tuning, has been extended to include correlations in the experimental uncertainties. By adding a damping factor to the ISR emission probability the standalone Pythia8 generator is found to give a good description the extra radiation in $t\bar{t}$ events. The tuned value of $\alpha_s^{ISR}(m_Z)$ in ATTBAR is compatible with previous determinations from measurements of the Z boson transverse momentum and the value of $\alpha_s^{FSR}(m_Z)$ is in agreement with event shapes in hadronic Z decays as measured at LEP. The ATTBAR tune is then applied to the NLO+PS generators Powheg and MadGraph5_aMC@NLO, and additional parameters are tuned to data.

Several shortcomings of the models have been highlighted. The *b*-jet shapes modelling shows significant disagreement for high-p_T jets at large r. A poor description of data is also found with MadGraph5_aMC@NLO, using the recommended global recoil strategy, and further studies will be needed to understand its origin.

With the increase in the energy and luminosity of the LHC Run2, larger samples of top quarks will become available. We foresee the upcoming measurements will be able to further constraint the shower models and we advocate dedicated measurements to reduce the large uncertainties in the modeling of hadronization and color reconnection effects.

Despite being a succesfull and very predictive theory the SM fails in explaining several experimental and theoretical problems and it is believed to be only a low-energy approximation of a more complete theory valid up to very high energies.

A major fraction of the LHC physics program has been devoted to the search for new particles related to the solution of the naturalness and dark matter problems. No statistically significant hint for new physics has been found in Run 1, and for the most favoured models particle masses up to the TeV range have been excluded.

In chapter 7 we have presented results a model independent general search for new phenomena using data collected by the ATLAS detector at 8 TeV. For the first time at an LHC experiment all final states including electrons, muons, photons, jets, b-jets and missing transverse energy, for a total of 697 event classes, have been systematically studied, in what is probably the most comprehensive search for new physics performed at a collider experiment. Algorithmic techniques have been developed to identify possible discrepancies between data and the expected background, mostly obtained from MC simulation. The number and size of the observed deviations is compatible with the expectation obtained from pseudo-data. The observed agreement should be considered an important achievement for both the modeling of the physics processes and the detector simulation. The most significant disagreement found in a final state containing one electron, one muon, one photon and two jets, corresponding to a p-value of $7 \cdot 10^{-4}$, expected in about 50% of the pseudo-experiments.

After a successful run at 7 and 8 TeV the LHC will restart at a further increased energy of 13 TeV. With twice the beam energy and more then ten times the integrated luminosity a much larger parameter space will be explored; limits on NP models are expected to improve from hundreds of GeVs to TeVs and the naturalness paradigm will ultimately be put into test. In this exciting phase the general search analysis promise to be an invaluable tool for the fast and comprehensive monitoring of data in search for hints of a new theory complementing the SM up to the highest energies.

Part IV

APPENDIX

APPENDIX01

For each event class considered in the general search analysis, we report here the total number of data events observed compared to the SM background expectation. In Figure 64 and 65 are shown event classes for which an electron or photon trigger is used, Figures 66 67 and 68 show the event classes that use a muon trigger, while the event classe in Figures 69 70 and 71 use a jet or E_T^{miss} trigger. A good agreement between data and the SM prediction is observed for most of the event classes.

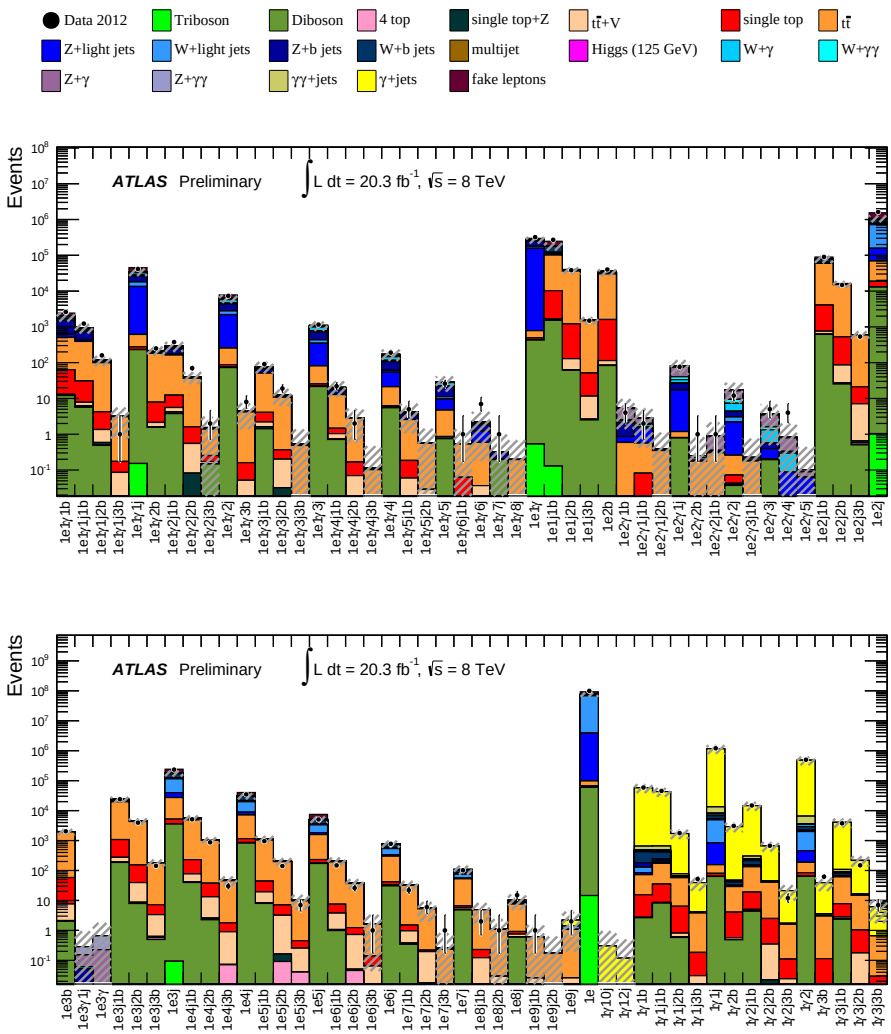

Figure 64: Number of events for event classes for which electron and photon triggers are used. The classes are labeled according to the abundance and type (e, μ, γ, j, b, ν) of the reconstructed objects for this event class. The data are compared to the SM background expectation as described in the text. The hatched bands indicate the total uncertainty of the SM prediction.

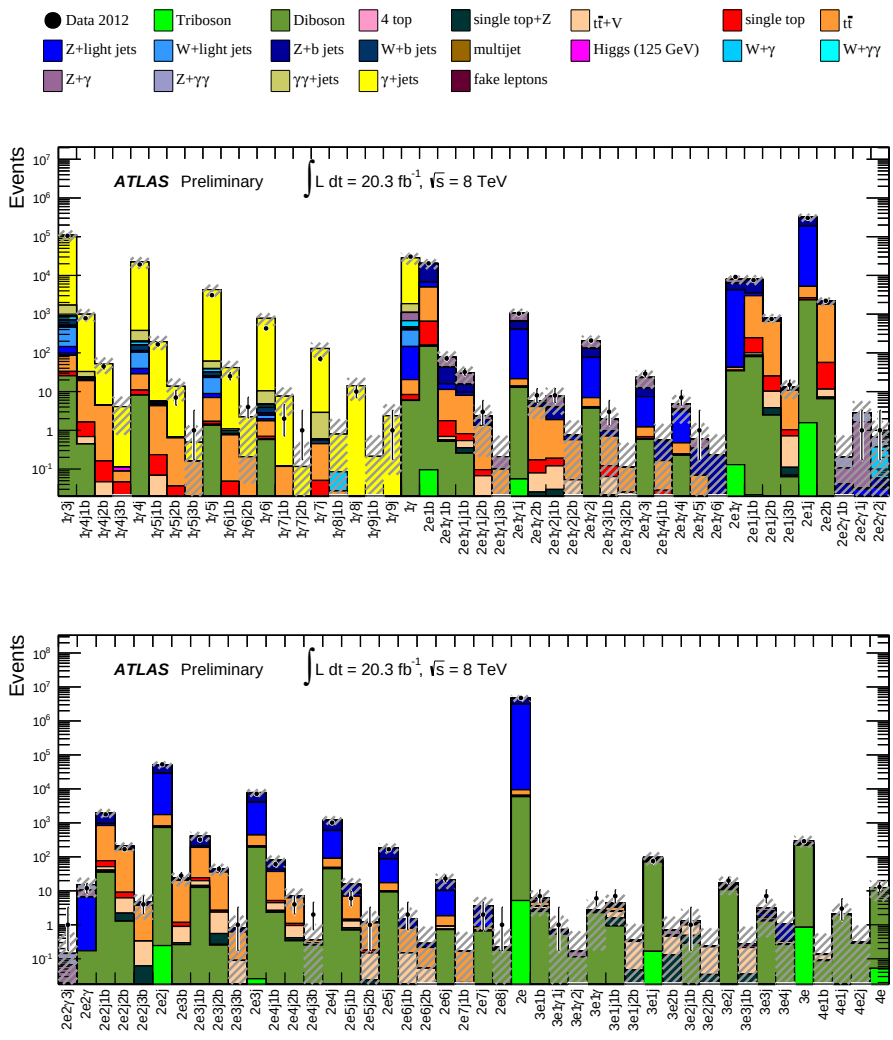

Figure 65: Number of events for event classes for which electron and photon triggers are used. The classes are labeled according to the abundance and type (e, μ, γ, j, b, ν) of the reconstructed objects for this event class. The data are compared to the SM background expectation as described in the text. The hatched bands indicate the total uncertainty of the SM prediction.

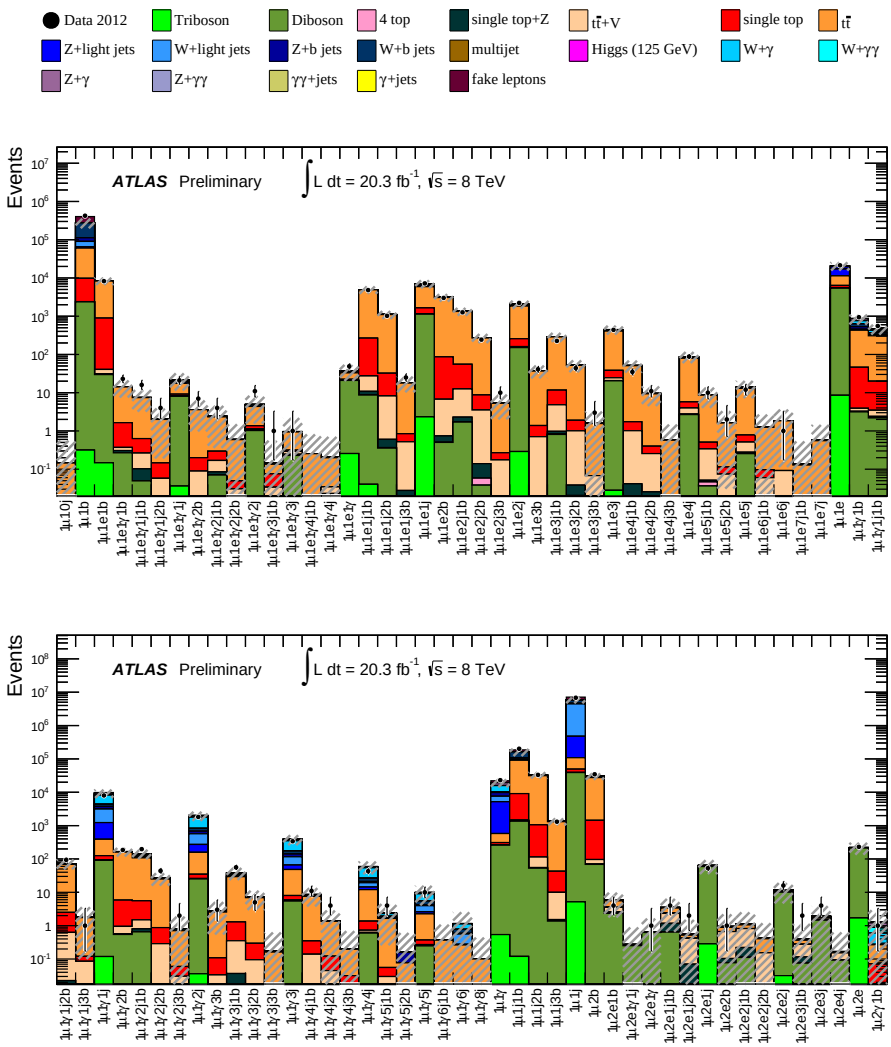

Figure 66: Number of events for event classes for which muon triggers are used. The classes are labeled according to the abundance and type (e, μ, γ, j, b, ν) of the reconstructed objects for this event class. The data are compared to the SM background expectation as described in the text. The hatched bands indicate the total uncertainty of the SM prediction.

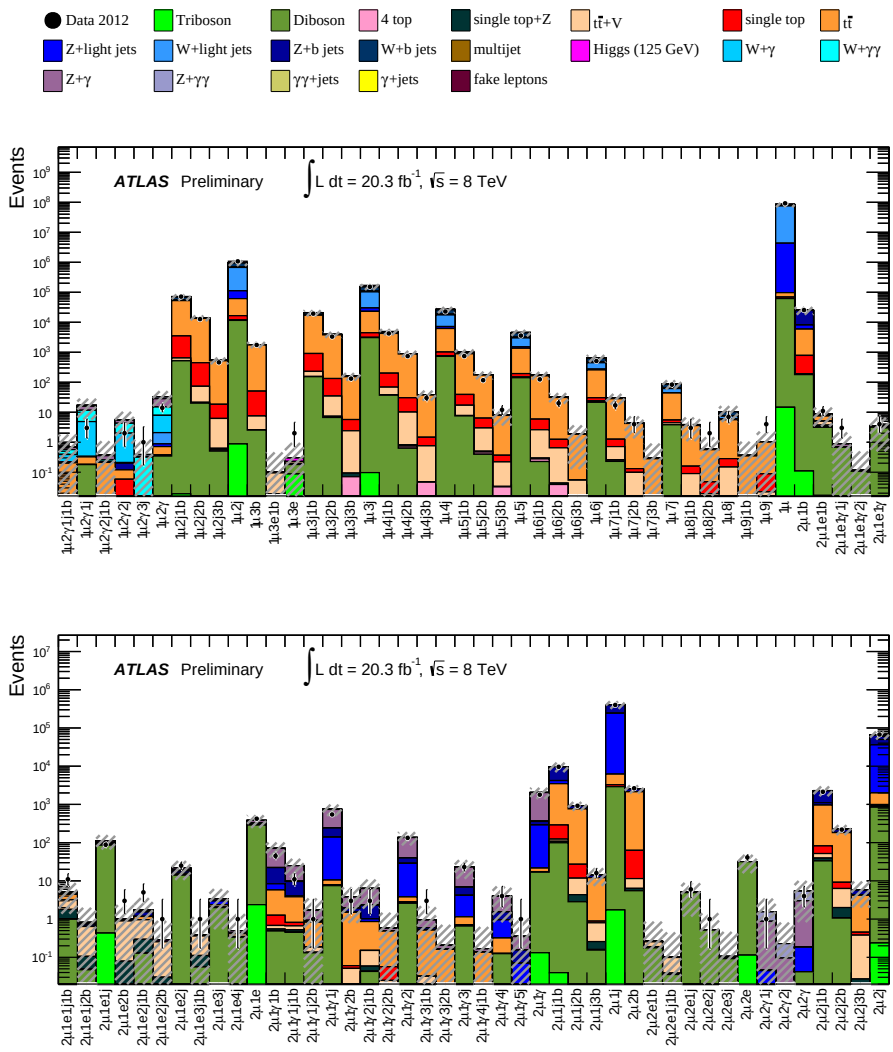

Figure 67: Number of events for event classes for which muon triggers are used. The classes are labeled according to the abundance and type (e, μ, γ, j, b, ν) of the reconstructed objects for this event class. The data are compared to the SM background expectation as described in the text. The hatched bands indicate the total uncertainty of the SM prediction.

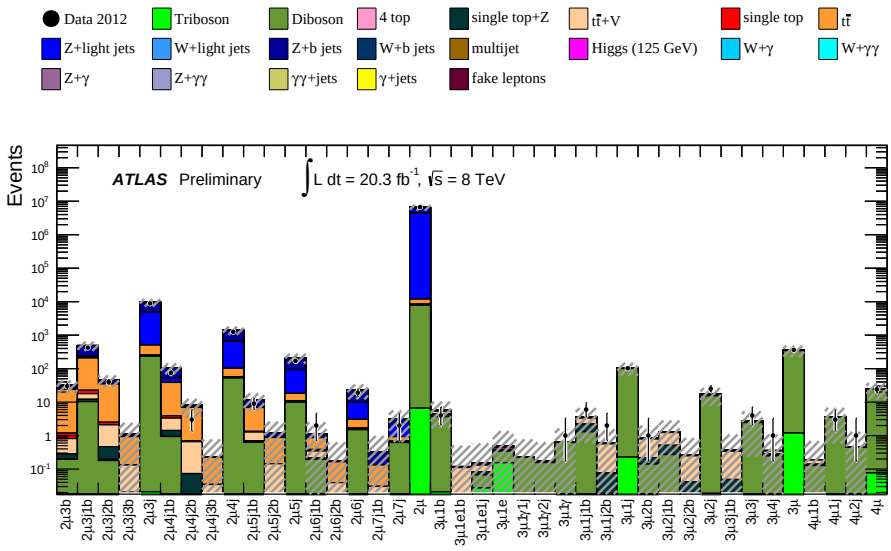

Figure 68: Number of events for event classes for which muon triggers are used. The classes are labeled according to the abundance and type (e, μ, γ, j, b, ν) of the reconstructed objects for this event class. The data are compared to the SM background expectation as described in the text. The hatched bands indicate the total uncertainty of the SM prediction.

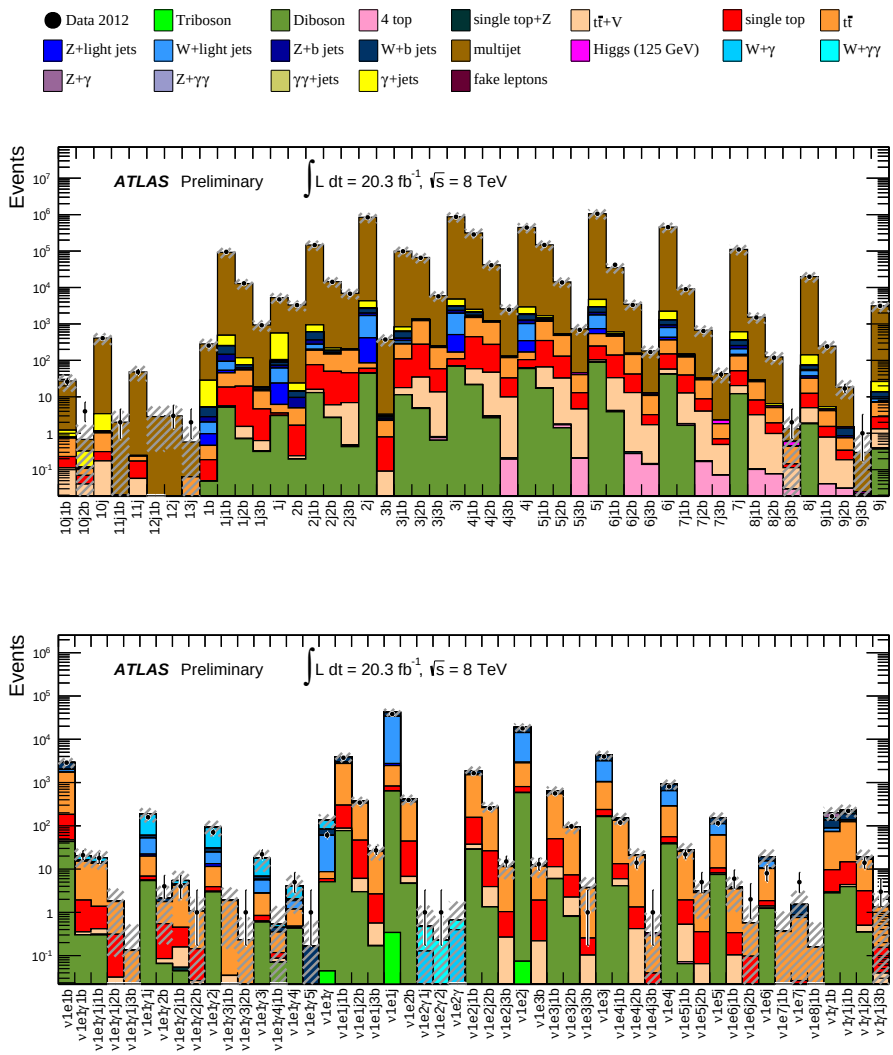

Figure 69: Number of events for event classes for which jets or E_T^{miss} triggers are used. The classes are labeled according to the abundance and type (e, μ, γ, j, b, ν) of the reconstructed objects for this event class. The data are compared to the SM background expectation as described in the text. The hatched bands indicate the total uncertainty of the SM prediction.

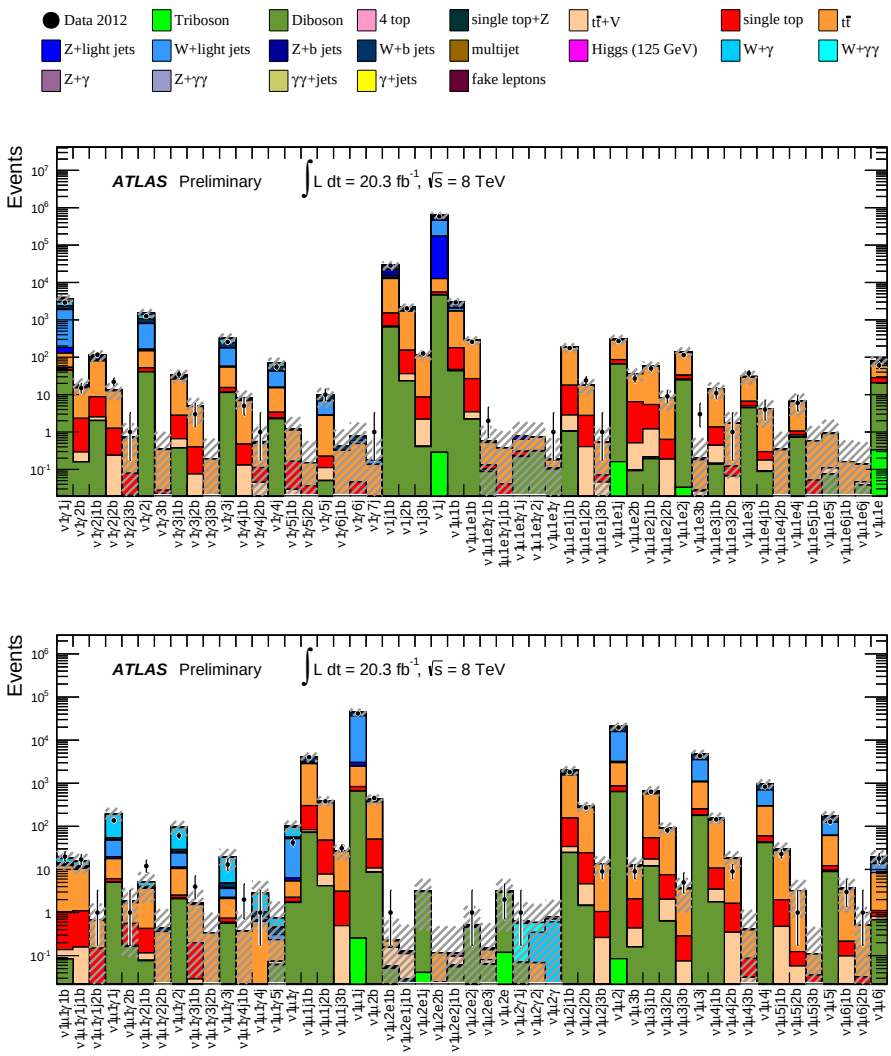

Figure 70: Number of events for event classes for which jets or E_T^{miss} triggers are used. The classes are labeled according to the abundance and type (e, μ, γ, j, b, ν) of the reconstructed objects for this event class. The data are compared to the SM background expectation as described in the text. The hatched bands indicate the total uncertainty of the SM prediction.

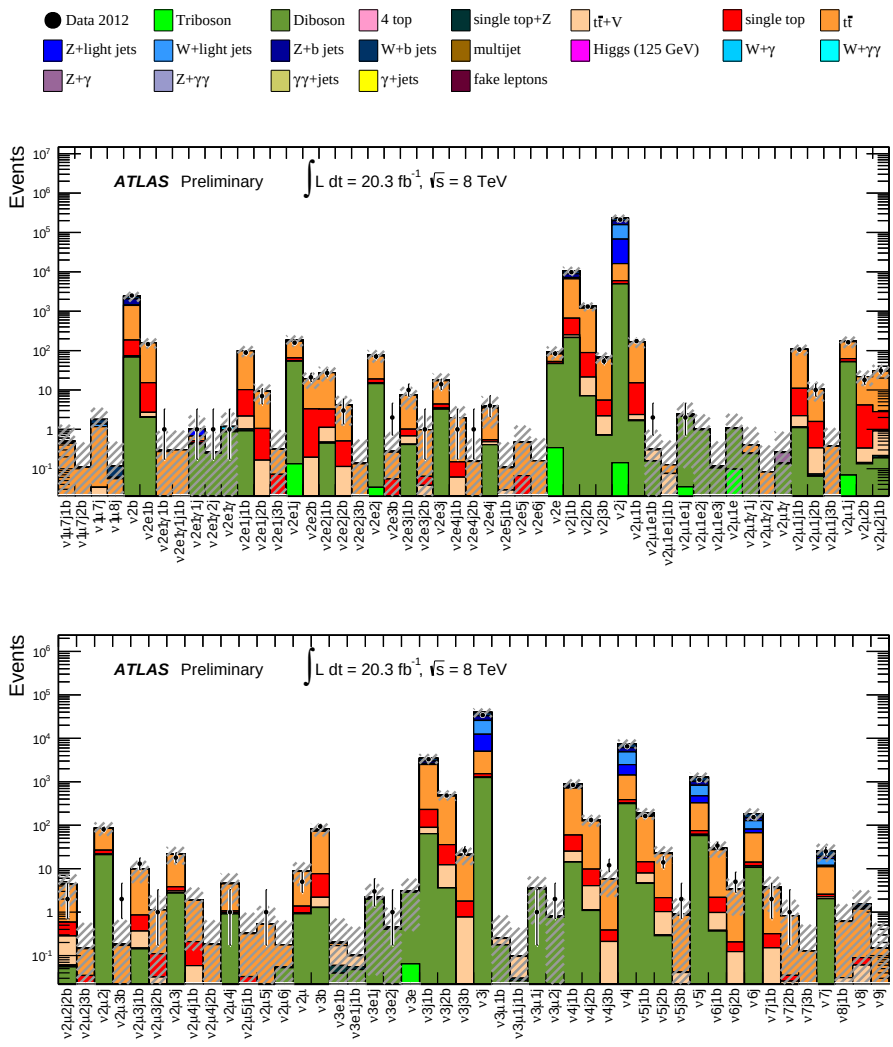

Figure 71: Number of events for event classes for which jets or E_T^{miss} triggers are used. The classes are labeled according to the abundance and type (e, μ, γ, j, b, ν) of the reconstructed objects for this event class. The data are compared to the SM background expectation as described in the text. The hatched bands indicate the total uncertainty of the SM prediction.

APPENDIX02

Table 21 summarises the settings of the ATTBAR tunes for the Pythia8, MadGraph5_aMC@NLO+Pythia8, and Powheg+Pythia8 generators.

Table 21: Options and parameters settings of the ATTBAR, ATTBAR-MG5aMCNLO and ATTBAR-POWHEG tunes of PYTHIA8, MADGRAPH5_aMC@NLO+PYTHIA8, and POWHEG+PYTHIA8. All the other parameters and model switches correspond to the settings of the base tune (Monash) for PYTHIA8, and to the default values for MadGraph5_aMC@NLO and POWHEG. The '-' symbol is used in case the setting is not applicable.

PYTHIA8 settings	ATTBAR	ATTBAR-MG5aMCNLO	ATTBAR-POWHEG
SpaceShower:alphaSvalue	0.121	0.121	0.121
SpaceShower:pTdampMatch	1	0	0
SpaceShower:pTdampFudge	1.18	-	-
TimeShower:alphaSvalue	0.137	0.137	0.137
TimeShower:pTmin	1.26	1.26	1.26
MultipartonInteractions:pT0Ref	2.16	2.16	2.16
TimeShower:globalRecoil	-	off	-
SpaceShower:pTmaxMatch	0	1	2
SpaceShower:MEcorrections	on	off	on
TimeShower:MEcorrections	on	off	on
POWHEG:veto	-	-	1
POWHEG:vetoCount	-	-	3
POWHEG:pThard	-	-	0
POWHEG:pTemt	-	-	0
POWHEG:emitted	-	-	0
POWHEG:pTdef	-	-	2
POWHEG:MPIveto	-	-	0
MADGRAPH5_aMC@NLO settings			
frac_upp	-	0.54	-
frac_low	-	0.54	-
scaleMCdelta	-	0	-
POWHEG settings			
hdamp	-	-	$1.8 \cdot m_t$

BIBLIOGRAPHY

[1] ATLAS Collaboration, *A general search for new phenomena with the ATLAS detector in pp collisions at* $\sqrt{s} = 7$ *TeV*, ATLAS-CONF-2012-107.

[2] ATLAS Collaboration, *A general search for new phenomena with the ATLAS detector in pp collisions at* $\sqrt{s} = 8$ *TeV*, ATLAS-CONF-2014-006.

[3] ATLAS Collaboration, G. Aad et al., *Search for squarks and gluinos with the ATLAS detector in final states with jets and missing transverse momentum using* $\sqrt{s} = 8$ *TeV proton–proton collision data*, JHEP **1409** (2014) 176, arXiv:1405.7875 [hep-ex].

[4] ATLAS Collaboration, G. Aad et al., *Search for direct pair production of the top squark in all-hadronic final states in proton-proton collisions at* $\sqrt{s} = 8$ *TeV with the ATLAS detector*, JHEP **1409** (2014) 015, arXiv:1406.1122 [hep-ex].

[5] ATLAS Collaboration, *A study of the sensitivity to the Pythia8 parton shower parameters of* $t\bar{t}$ *production measurements in* pp *collisions at* $\sqrt{s} = 7$ *TeV with the ATLAS experiment at the LHC*,. ATLAS-PHYS-PUB-2015-007.

[6] C. N. Yang and R. L. Mills, *Conservation of Isotopic Spin and Isotopic Gauge Invariance*, Phys. Rev. **96** (1954) 191–195. http://link.aps.org/doi/10.1103/PhysRev.96.191.

[7] Y. Nambu and G. Jona-Lasinio, *Dynamical Model of Elementary Particles Based on an Analogy with Superconductivity. I*, Phys. Rev. **122** (1961) 345–358. http://link.aps.org/doi/10.1103/PhysRev.122.345.

[8] Y. Nambu and G. Jona-Lasinio, *Dynamical Model of Elementary Particles Based on an Analogy with Superconductivity. II*, Phys. Rev. **124** (1961) 246–254. http://link.aps.org/doi/10.1103/PhysRev.124.246.

[9] J. Goldstone, *Field Theories with Superconductor Solutions*, Nuovo Cim. **19** (1961) 154–164.

[10] S. Glashow, *Partial Symmetries of Weak Interactions*, Nucl.Phys. **22** (1961) 579–588.

[11] P. W. Higgs, *Broken Symmetries and the Masses of Gauge Bosons*, Phys. Rev. Lett. **13** (1964) 508–509. http://link.aps.org/doi/10.1103/PhysRevLett.13.508.

[12] G. S. Guralnik, C. R. Hagen, and T. W. B. Kibble, *Global Conservation Laws and Massless Particles*, Phys. Rev. Lett. **13** (1964) 585–587. http://link.aps.org/doi/10.1103/PhysRevLett.13.585.

[13] F. Englert and R. Brout, *Broken Symmetry and the Mass of Gauge Vector Mesons*, Phys. Rev. Lett. **13** (1964) 321–323. http://link.aps.org/doi/10.1103/PhysRevLett.13.321.

[14] S. Weinberg, *A Model of Leptons*, Phys.Rev.Lett. **19** (1967) 1264–1266.

[15] A. Salam, *Weak and electromagnetic interactions*,. Proc. of the 8th Nobel Symposium on 'Elementary particle theory, relativistic groups and analyticity', Stockholm, Sweden, 1968, edited by N. Svartholm, p.367-377.

[16] G. 't Hooft and M. J. G. Veltman, *Regularization and renormalization of gauge fields*, Nucl. Phys. **B44** (1972) 189–213.

[17] Gargamelle Neutrino Collaboration Collaboration, F. Hasert et al., *Observation of Neutrino Like Interactions Without Muon Or Electron in the Gargamelle Neutrino Experiment*, Phys.Lett. **B46** (1973) 138–140.

[18] UA1 Collaboration Collaboration, G. Arnison et al., *Experimental Observation of Isolated Large Transverse Energy Electrons with Associated Missing Energy at s**(1/2) = 540-GeV*, Phys.Lett. **B122** (1983) 103–116.

[19] UA1 Collaboration Collaboration, G. Arnison et al., *Experimental Observation of Lepton Pairs of Invariant Mass Around 95-GeV/c**2 at the CERN SPS Collider*, Phys.Lett. **B126** (1983) 398–410.

[20] https://en.wikipedia.org/wiki/Standard_Model#/media/\File:Standard_Model_of_Elementary_Particles.svg. Accessed: 2015-06-30.

[21] ATLAS Collaboration, G. Aad et al., *Observation of a new particle in the search for the Standard Model Higgs boson with the ATLAS detector at the LHC*, Phys.Lett. **B716** (2012) 1–29, arXiv:1207.7214 [hep-ex].

[22] CMS Collaboration Collaboration, S. Chatrchyan et al., *Observation of a new boson at a mass of 125 GeV with the*

CMS experiment at the LHC, Phys.Lett. **B716** (2012) 30–61, arXiv:1207.7235 [hep-ex].

[23] ATLAS, CMS Collaboration, G. Aad et al., *Combined Measurement of the Higgs Boson Mass in* pp *Collisions at* $\sqrt{s} = 7$ *and 8 TeV with the ATLAS and CMS Experiments*, Phys.Rev.Lett. **114** (2015) 191803, arXiv:1503.07589 [hep-ex].

[24] ATLAS Collaboration, *Measurements of the Higgs boson production and decay rates and coupling strengths using pp collision data at* $\sqrt{s} = 7$ *and 8 TeV in the ATLAS experiment*, ATLAS-CONF-2015-007 (2015).

[25] M. Baak, M. Goebel, J. Haller, A. Hoecker, D. Kennedy, et al., *The Electroweak Fit of the Standard Model after the Discovery of a New Boson at the LHC*, Eur.Phys.J. **C72** (2012) 2205, arXiv:1209.2716 [hep-ph].

[26] Gfitter Group Collaboration, M. Baak et al., *The global electroweak fit at NNLO and prospects for the LHC and ILC*, Eur.Phys.J. **C74** (2014) 3046, arXiv:1407.3792 [hep-ph].

[27] N. Cabibbo, *Unitary Symmetry and Leptonic Decays*, Phys.Rev.Lett. **10** (1963) 531–533.

[28] M. Kobayashi and T. Maskawa, *CP Violation in the Renormalizable Theory of Weak Interaction*, Prog.Theor.Phys. **49** (1973) 652–657.

[29] S. Weinberg, *Non-Abelian Gauge Theories of the Strong Interactions*, Phys. Rev. Lett. **31** (1973) 494–497. http://link.aps.org/doi/10.1103/PhysRevLett.31.494.

[30] H. Fritzsch, M. Gell-Mann, and H. Leutwyler, *Advantages of the color octet gluon picture*, Physics Letters B **47** no. 4, (1973) 365 – 368. http://www.sciencedirect.com/science/article/pii/0370269373906254.

[31] R. Crewther, P. Di Vecchia, G. Veneziano, and E. Witten, *Chiral Estimate of the Electric Dipole Moment of the Neutron in Quantum Chromodynamics*, Phys.Lett. **B88** (1979) 123.

[32] C. A. Baker et al., *Improved Experimental Limit on the Electric Dipole Moment of the Neutron*, Phys. Rev. Lett. **97** (2006) 131801. http://link.aps.org/doi/10.1103/PhysRevLett.97.131801.

[33] R. D. Peccei and H. R. Quinn, CP *Conservation in presence of Pseudoparticles*, Phys. Rev. Lett. **38** (1977) 1440–1443. http://link.aps.org/doi/10.1103/PhysRevLett.38.1440.

[34] S. Weinberg, *A New Light Boson?*, Phys.Rev.Lett. **40** (1978) 223–226.

[35] F. Wilczek, *Problem of Strong p and t Invariance in the Presence of Instantons*, Phys.Rev.Lett. **40** (1978) 279–282.

[36] Particle Data Group Collaboration, K. Olive et al., *Review of Particle Physics*, Chin.Phys. **C38** (2014) 090001.

[37] D. J. Gross and F. Wilczek, *Ultraviolet Behavior of Non-Abelian Gauge Theories*, Phys. Rev. Lett. **30** (1973) 1343–1346. http://link.aps.org/doi/10.1103/PhysRevLett.30.1343.

[38] H. D. Politzer, *Reliable Perturbative Results for Strong Interactions?*, Phys. Rev. Lett. **30** (1973) 1346–1349. http://link.aps.org/doi/10.1103/PhysRevLett.30.1346.

[39] E. D. Bloom, D. Coward, H. DeStaebler, J. Drees, G. Miller, et al., *High-Energy Inelastic e p Scattering at 6-Degrees and 10-Degrees*, Phys.Rev.Lett. **23** (1969) 930–934.

[40] M. Breidenbach, J. I. Friedman, H. W. Kendall, E. D. Bloom, D. Coward, et al., *Observed Behavior of Highly Inelastic electron-Proton Scattering*, Phys.Rev.Lett. **23** (1969) 935–939.

[41] T. Kinoshita, *Mass singularities of Feynman amplitudes*, J.Math.Phys. **3** (1962) 650–677.

[42] T. Lee and M. Nauenberg, *Degenerate Systems and Mass Singularities*, Phys.Rev. **133** (1964) B1549–B1562.

[43] J. Gao, M. Guzzi, J. Huston, H.-L. Lai, Z. Li, et al., *CT10 next-to-next-to-leading order global analysis of QCD*, Phys.Rev. **D89** no. 3, (2014) 033009, arXiv:1302.6246 [hep-ph].

[44] G. Altarelli and G. Parisi, *Asymptotic Freedom in Parton Language*, Nucl.Phys. **B126** (1977) 298.

[45] Y. L. Dokshitzer, *Calculation of the Structure Functions for Deep Inelastic Scattering and e+ e- Annihilation by Perturbation Theory in Quantum Chromodynamics.*, Sov.Phys.JETP **46** (1977) 641–653.

[46] V. Gribov and L. Lipatov, *Deep inelastic e p scattering in perturbation theory*, Sov.J.Nucl.Phys. **15** (1972) 438–450.

[47] S. Forte and G. Watt, *Progress in the Determination of the Partonic Structure of the Proton*, Ann.Rev.Nucl.Part.Sci. **63** (2013) 291–328, arXiv:1301.6754 [hep-ph].

[48] A. Martin, W. Stirling, R. Thorne, and G. Watt, *Parton distributions for the LHC*, Eur.Phys.J. **C63** (2009) 189–285, arXiv:0901.0002 [hep-ph].

[49] NNPDF Collaboration, R. D. Ball et al., *Parton distributions for the LHC Run II*, JHEP **1504** (2015) 040, arXiv:1410.8849 [hep-ph].

[50] H1, ZEUS Collaboration, F. Aaron et al., *Combined Measurement and QCD Analysis of the Inclusive* $e^{\pm}p$ *Scattering Cross Sections at HERA*, JHEP **1001** (2010) 109, arXiv:0911.0884 [hep-ex].

[51] S. Alekhin, J. Blumlein, S. Klein, and S. Moch, *Variable-Flavor-Number Scheme in Analysis of Heavy-Quark Electro-Production Data*, arXiv:0908.3128 [hep-ph].

[52] P. Jimenez-Delgado and E. Reya, *Variable flavor number parton distributions and weak gauge and Higgs boson production at hadron colliders at next-to-next-to-leading order of QCD*, Phys. Rev. D **80** (2009) 114011. http://link.aps.org/doi/10.1103/PhysRevD.80.114011.

[53] P. Jimenez-Delgado and E. Reya, *Dynamical next-to-next-to-leading order parton distributions*, Phys. Rev. D **79** (2009) 074023. http://link.aps.org/doi/10.1103/PhysRevD.79.074023.

[54] G. P. Salam, *Towards Jetography*, Eur.Phys.J. **C67** (2010) 637–686, arXiv:0906.1833 [hep-ph].

[55] G. F. Sterman and S. Weinberg, *Jets from Quantum Chromodynamics*, Phys.Rev.Lett. **39** (1977) 1436.

[56] M. Cacciari, G. P. Salam, and G. Soyez, *The anti-k_t jet clustering algorithm*, JHEP **04** (2008) 063, arXiv:0802.1189 [hep-ph].

[57] A. Buckley, J. Butterworth, S. Gieseke, D. Grellscheid, S. Hoche, et al., *General-purpose event generators for LHC physics*, Phys.Rept. **504** (2011) 145–233, arXiv:1101.2599 [hep-ph].

[58] T. Gleisberg, S. Hoeche, F. Krauss, M. Schonherr, S. Schumann, et al., *Event generation with SHERPA 1.1*, JHEP **0902** (2009) 007, arXiv:0811.4622 [hep-ph].

[59] S. Catani and M. Seymour, *A General algorithm for calculating jet cross-sections in NLO QCD*, Nucl.Phys. **B485** (1997) 291–419, arXiv:hep-ph/9605323 [hep-ph].

[60] S. Catani, S. Dittmaier, M. H. Seymour, and Z. Trocsanyi, *The Dipole formalism for next-to-leading order QCD calculations with massive partons*, Nucl.Phys. **B627** (2002) 189–265, arXiv:hep-ph/0201036 [hep-ph].

[61] S. Frixione, Z. Kunszt, and A. Signer, *Three jet cross-sections to next-to-leading order*, Nucl.Phys. **B467** (1996) 399–442, arXiv:hep-ph/9512328 [hep-ph].

[62] D. A. Kosower, *Antenna factorization of gauge theory amplitudes*, Phys.Rev. **D57** (1998) 5410–5416, arXiv:hep-ph/9710213 [hep-ph].

[63] V. Sudakov, *Vertex parts at very high-energies in quantum electrodynamics*, Sov.Phys.JETP **3** (1956) 65–71.

[64] T. Sjöstrand, *A Model for Initial State Parton Showers*, Phys.Lett. **B157** (1985) 321.

[65] T. D. Gottschalk, *Backwards Evolved Initial State Parton Showers*, Nucl.Phys. **B277** (1986) 700.

[66] S. Hoeche, F. Krauss, S. Schumann, and F. Siegert, *QCD matrix elements and truncated showers*, JHEP **0905** (2009) 053, arXiv:0903.1219 [hep-ph].

[67] J. Alwall, S. Hoche, F. Krauss, N. Lavesson, L. Lonnblad, et al., *Comparative study of various algorithms for the merging of parton showers and matrix elements in hadronic collisions*, Eur.Phys.J. **C53** (2008) 473–500, arXiv:0706.2569 [hep-ph].

[68] M. L. Mangano, M. Moretti, and R. Pittau, *Multijet matrix elements and shower evolution in hadronic collisions:* $Wb\bar{b}$ + n *jets as a case study*, Nucl.Phys. **B632** (2002) 343–362, arXiv:hep-ph/0108069 [hep-ph].

[69] M. L. Mangano, M. Moretti, F. Piccinini, and M. Treccani, *Matching matrix elements and shower evolution for top-quark production in hadronic collisions*, JHEP **0701** (2007) 013, arXiv:hep-ph/0611129 [hep-ph].

[70] S. Catani, F. Krauss, R. Kuhn, and B. Webber, *QCD matrix elements + parton showers*, JHEP **0111** (2001) 063, arXiv:hep-ph/0109231 [hep-ph].

[71] F. Krauss, *Matrix elements and parton showers in hadronic interactions*, JHEP **0208** (2002) 015, arXiv:hep-ph/0205283 [hep-ph].

[72] L. Lönnblad, *Correcting the color dipole cascade model with fixed order matrix elements*, JHEP **0205** (2002) 046, arXiv:hep-ph/0112284 [hep-ph].

[73] L. Lönnblad and S. Prestel, *Matching Tree-Level Matrix Elements with Interleaved Showers*, JHEP **1203** (2012) 019, arXiv:1109.4829 [hep-ph].

[74] P. Nason and B. Webber, *Next-to-Leading-Order Event Generators*, Ann.Rev.Nucl.Part.Sci. **62** (2012) 187–213, arXiv:1202.1251 [hep-ph].

[75] S. Hoeche, F. Krauss, M. Schonherr, and F. Siegert, *A critical appraisal of NLO+PS matching methods*, JHEP **1209** (2012) 049, arXiv:1111.1220 [hep-ph].

[76] S. Frixione and B. R. Webber, *Matching NLO QCD computations and parton shower simulations*, JHEP **06** (2002) 029, arXiv:hep-ph/0204244.

[77] S. Alioli, P. Nason, C. Oleari, and E. Re, *NLO Higgs boson production via gluon fusion matched with shower in POWHEG*, JHEP **0904** (2009) 002, arXiv:0812.0578 [hep-ph].

[78] S. Alioli, P. Nason, C. Oleari, and E. Re, *A general framework for implementing NLO calculations in shower Monte Carlo programs: the POWHEG BOX*, JHEP **1006** (2010) 043, arXiv:1002.2581 [hep-ph].

[79] S. Frixione, P. Nason, and C. Oleari, *Matching NLO QCD computations with parton shower simulations: the POWHEG method*, JHEP **0711** (2007) 070, arXiv:0709.2092 [hep-ph].

[80] J. Alwall, R. Frederix, S. Frixione, V. Hirschi, F. Maltoni, et al., *The automated computation of tree-level and next-to-leading order differential cross sections, and their matching to parton shower simulations*, JHEP **1407** (2014) 079, arXiv:1405.0301 [hep-ph].

[81] K. Hamilton and P. Nason, *Improving NLO-parton shower matched simulations with higher order matrix elements*, JHEP **1006** (2010) 039, arXiv:1004.1764 [hep-ph].

[82] S. Hoche, F. Krauss, M. Schonherr, and F. Siegert, *NLO matrix elements and truncated showers*, JHEP **1108** (2011) 123, arXiv:1009.1127 [hep-ph].

[83] S. Hoeche, F. Krauss, M. Schonherr, and F. Siegert, *QCD matrix elements + parton showers: The NLO case*, JHEP **1304** (2013) 027, arXiv:1207.5030 [hep-ph].

[84] L. LÃ¶nnblad and S. Prestel, *Merging Multi-leg NLO Matrix Elements with Parton Showers*, JHEP **1303** (2013) 166, arXiv:1211.7278 [hep-ph].

[85] S. Hoeche, F. Krauss, P. Maierhoefer, S. Pozzorini, M. Schonherr, et al., *Next-to-leading order QCD predictions for top-quark pair production with up to two jets merged with a parton shower*, arXiv:1402.6293 [hep-ph].

[86] R. Field, *The underlying event in hadronic collisions*, Ann.Rev.Nucl.Part.Sci. **62** (2012) 453–483.

[87] CDF Collaboration, T. Affolder et al., *Charged jet evolution and the underlying event in $p\bar{p}$ collisions at 1.8 TeV*, Phys.Rev. **D65** (2002) 092002.

[88] CDF Collaboration, R. Field and R. C. Group, *PYTHIA tune A, HERWIG, and JIMMY in Run 2 at CDF*, arXiv:hep-ph/0510198 [hep-ph].

[89] T. Sjöstrand and M. van Zijl, *A Multiple Interaction Model for the Event Structure in Hadron Collisions*, Phys.Rev. **D36** (1987) 2019.

[90] R. Corke, *Multiple Interactions in Pythia 8*, arXiv:0901.2852 [hep-ph].

[91] T. Sjöstrand, *Colour reconnection and its effects on precise measurements at the LHC*, arXiv:1310.8073 [hep-ph].

[92] P. Z. Skands and D. Wicke, *Non-perturbative QCD effects and the top mass at the Tevatron*, Eur.Phys.J. **C52** (2007) 133–140, arXiv:hep-ph/0703081 [HEP-PH].

[93] T. Sjöstrand and P. Z. Skands, *Transverse-momentum-ordered showers and interleaved multiple interactions*, Eur. Phys. J. C **39** (2005) 129–154, arXiv:hep-ph/0408302 [hep-ph].

[94] S. Gieseke, C. Rohr, and A. Siodmok, *Colour reconnections in Herwig++*, Eur.Phys.J. **C72** (2012) 2225, arXiv:1206.0041 [hep-ph].

[95] X. Artru and G. Mennessier, *String model and multiproduction*, Nucl.Phys. **B70** (1974) 93–115.

[96] D. Amati and G. Veneziano, *Preconfinement as a Property of Perturbative QCD*, Phys.Lett. **B83** (1979) 87.

[97] A. Bassetto, M. Ciafaloni, and G. Marchesini, *Color Singlet Distributions and Mass Damping in Perturbative QCD*, Phys.Lett. **B83** (1979) 207.

[98] B. Webber, *A QCD Model for Jet Fragmentation Including Soft Gluon Interference*, Nucl.Phys. **B238** (1984) 492.

[99] J.-C. Winter, F. Krauss, and G. Soff, *A Modified cluster hadronization model*, Eur.Phys.J. **C36** (2004) 381–395, arXiv:hep-ph/0311085 [hep-ph].

[100] G. Bali and K. Schilling, *Static quark - anti-quark potential: Scaling behavior and finite size effects in SU(3) lattice gauge theory*, Phys.Rev. **D46** (1992) 2636–2646.

[101] B. Andersson, G. Gustafson, G. Ingelman, and T. Sjöstrand, *Parton Fragmentation and String Dynamics*, Phys.Rept. **97** (1983) 31–145.

[102] B. Andersson, *The Lund Model*. Cambridge Monographs on Particle Physics, Nuclear Physics and Cosmology (Book 7). Cambridge University Press, 1998.

[103] B. Andersson, G. Gustafson, and B. Soderberg, *A General Model for Jet Fragmentation*, Z.Phys. **C20** (1983) 317.

[104] M. Bowler, *e+ e- Production of Heavy Quarks in the String Model*, Z.Phys. **C11** (1981) 169.

[105] B. Andersson, G. Gustafson, and T. Sjöstrand, *Baryon Production in Jet Fragmentation and Υ Decay*, Phys.Scripta **32** (1985) 574.

[106] T. Sjöstrand, *Jet Fragmentation of Nearby Partons*, Nucl.Phys. **B248** (1984) 469.

[107] D. Lange, *The EvtGen particle decay simulation package*, Nucl.Instrum.Meth. **A462** (2001) 152–155.

[108] S. Jadach, Z. Was, R. Decker, and J. H. Kuhn, *The tau decay library TAUOLA: Version 2.4*, Comput.Phys.Commun. **76** (1993) 361–380.

[109] Z. Was, *TAUOLA for simulation of tau decay and production: perspectives for precision low energy and LHC applications*, Nucl.Phys.Proc.Suppl. **218** (2011) 249–255, arXiv:1101.1652 [hep-ph].

[110] A. Buckley, H. Hoeth, H. Lacker, H. Schulz, and J. E. von Seggern, *Systematic event generator tuning for the LHC*, Eur.Phys.J. **C65** (2010) 331–357, arXiv:0907.2973 [hep-ph].

[111] A. Bacchetta, H. Jung, A. Knutsson, K. Kutak, and F. Samson-Himmelstjerna, *A method for tuning parameters of Monte Carlo generators and a its application to the determination of the unintegrated gluon density*, Eur.Phys.J. **C70** (2010) 503–511, arXiv:1001.4675 [hep-ph].

[112] F. James and M. Roos, *Minuit: A System for Function Minimization and Analysis of the Parameter Errors and Correlations*, Comput. Phys. Commun. **10** (1975) 343–367.

[113] A. Borriello and P. Salucci, *The Dark matter distribution in disk galaxies*, Mon.Not.Roy.Astron.Soc. **323** (2001) 285, arXiv:astro-ph/0001082 [astro-ph].

[114] F. Zwicky, *Die Rotverschiebung von extragalaktischen Nebeln*, Helv.Phys.Acta **6** (1933) 110–127.

[115] H. Dahle, *A compilation of weak gravitational lensing studies of clusters of galaxies*, arXiv:astro-ph/0701598 [astro-ph].

[116] D. Clowe, M. Bradac, A. H. Gonzalez, M. Markevitch, S. W. Randall, et al., *A direct empirical proof of the existence of dark matter*, Astrophys.J. **648** (2006) L109–L113, arXiv:astro-ph/0608407 [astro-ph].

[117] WMAP Collaboration Collaboration, D. Spergel et al., *Wilkinson Microwave Anisotropy Probe (WMAP) three year results: implications for cosmology*, Astrophys.J.Suppl. **170** (2007) 377, arXiv:astro-ph/0603449 [astro-ph].

[118] Planck Collaboration Collaboration, P. Ade et al., *Planck 2013 results. XVI. Cosmological parameters*, Astron.Astrophys. (2014), arXiv:1303.5076 [astro-ph.CO].

[119] K. A. Olive, G. Steigman, and T. P. Walker, *Primordial nucleosynthesis: Theory and observations*, Phys.Rept. **333** (2000) 389–407, arXiv:astro-ph/9905320 [astro-ph].

[120] SDSS Collaboration Collaboration, M. Tegmark et al., *The 3-D power spectrum of galaxies from the SDSS*, Astrophys.J. **606** (2004) 702–740, arXiv:astro-ph/0310725 [astro-ph].

[121] J. L. Feng, *Dark Matter Candidates from Particle Physics and Methods of Detection*, Annual Review of Astronomy and Astrophysics **48** no. 1, (2010) 495–545, http://dx.doi.org/10.1146/annurev-astro-082708-101659. http://dx.doi.org/10.1146/annurev-astro-082708-101659.

[122] G. Bertone, D. Hooper, and J. Silk, *Particle dark matter: Evidence, candidates and constraints*, Phys.Rept. **405** (2005) 279–390, arXiv:hep-ph/0404175 [hep-ph].

[123] R. J. Scherrer and M. S. Turner, *On the Relic, Cosmic Abundance of Stable Weakly Interacting Massive Particles*, Phys.Rev. **D33** (1986) 1585.

[124] H. Georgi and S. L. Glashow, *Unity of All Elementary-Particle Forces*, Phys. Rev. Lett. **32** (1974) 438–441. http://link.aps.org/doi/10.1103/PhysRevLett.32.438.

[125] P. Langacker, *Grand Unified Theories and Proton Decay*, Phys.Rept. **72** (1981) 185.

[126] J. C. Pati and A. Salam, *Lepton Number as the Fourth Color*, Phys.Rev. **D10** (1974) 275–289.

[127] A. Buras, J. R. Ellis, M. Gaillard, and D. V. Nanopoulos, *Aspects of the Grand Unification of Strong, Weak and Electromagnetic Interactions*, Nucl.Phys. **B135** (1978) 66–92.

[128] R. Mohapatra, *Supersymmetric grand unification*, arXiv:hep-ph/9801235 [hep-ph].

[129] S. Coleman and J. Mandula, *All Possible Symmetries of the S Matrix*, Phys. Rev. **159** (1967) 1251–1256. http://link.aps.org/doi/10.1103/PhysRev.159.1251.

[130] H. Miyazawa, *Baryon Number Changing Currents*, Prog. Theor. Phys. **36 (6)** (1966) 1266–1276.

[131] J. Gervais and B. Sakita, *Field theory interpretation of supergauges in dual models*, Nucl. Phys. **B34** (1971) 632–639.

[132] Y. Golfand and E. Likhtman, *Extension of the Algebra of Poincare Group Generators and Violation of p Invariance*, JETP Lett. **13** (1971) 323–326.

[133] D. Volkov and V. Akulov, *Is the Neutrino a Goldstone Particle?*, Phys. Lett. **B46** (1973) 109–110.

[134] J. Wess and B. Zumino, *A Lagrangian Model Invariant Under Supergauge Transformations*, Phys. Lett. **B49** (1974) 52.

[135] J. Wess and B. Zumino, *Supergauge Transformations in Four-Dimensions*, Nucl. Phys. **B70** (1974) 39–50.

[136] R. Haag, J. T. Łopuszański, and M. Sohnius, *All possible generators of supersymmetries of the S-matrix*, Nuclear Physics B **88** (1975) 257–274.

[137] S. Dimopoulos and H. Georgi, *Softly Broken Supersymmetry and SU(5)*, Nucl. Phys. **B193** (1981) 150.

[138] (The Super-Kamiokande Collaboration) Collaboration, Y. Hayato et al., *Search for proton decay through* $p \to \overline{\nu}\nu K^+$ *in a large water Cherenkov detector*, Phys. Rev. Lett. **83** (1999) 1529–1533. http://link.aps.org/doi/10.1103/PhysRevLett.83.1529.

[139] R. Barbieri, S. Ferrara, and C. A. Savoy, *Gauge Models with Spontaneously Broken Local Supersymmetry*, Phys.Lett. **B119** (1982) 343.

[140] M. Dine and A. E. Nelson, *Dynamical supersymmetry breaking at low-energies*, Phys.Rev. **D48** (1993) 1277–1287, arXiv:hep-ph/9303230 [hep-ph].

[141] M. Dine, A. E. Nelson, Y. Nir, and Y. Shirman, *New tools for low-energy dynamical supersymmetry breaking*, Phys.Rev. **D53** (1996) 2658–2669, arXiv:hep-ph/9507378 [hep-ph].

[142] P. Binetruy and E. Dudas, *Gaugino condensation and the anomalous U(1)*, Phys.Lett. **B389** (1996) 503–509, arXiv:hep-th/9607172 [hep-th].

[143] G. Dvali and A. Pomarol, *Anomalous U(1) as a mediator of supersymmetry breaking*, Phys.Rev.Lett. **77** (1996) 3728–3731, arXiv:hep-ph/9607383 [hep-ph].

[144] L. Girardello and M. T. Grisaru, *Soft Breaking of Supersymmetry*, Nucl.Phys. **B194** (1982) 65.

[145] S. P. Martin, *A Supersymmetry primer*, Adv.Ser.Direct.High Energy Phys. **21** (2010) 1–153, arXiv:hep-ph/9709356 [hep-ph].

[146] G. L. Kane, C. F. Kolda, L. Roszkowski, and J. D. Wells, *Study of constrained minimal supersymmetry*, Phys.Rev. **D49** (1994) 6173–6210, arXiv:hep-ph/9312272 [hep-ph].

[147] A. Djouadi, J.-L. Kneur, and G. Moultaka, *SuSpect: A Fortran code for the supersymmetric and Higgs particle spectrum in the MSSM*, Comput.Phys.Commun. **176** (2007) 426–455, arXiv:hep-ph/0211331 [hep-ph].

[148] C. F. Berger, J. S. Gainer, J. L. Hewett, and T. G. Rizzo, *Supersymmetry Without Prejudice*, JHEP **0902** (2009) 023, arXiv:0812.0980 [hep-ph].

[149] N. Craig, *The State of Supersymmetry after Run I of the LHC*, arXiv:1309.0528 [hep-ph].

[150] G. Nordstrom, *Über die Möglichkeit, das elektromagnetische Feld und Gravitationsfeld zu vereinigen*, Phys.Z. **15** (1914) 504–506, arXiv:physics/0702221 [physics.gen-ph].

[151] T. Kaluza, *Zum Unitätsproblem in der Physik*, Sitzungsber.Preuss.Akad.Wiss.Berlin (Math.Phys.) **1921** (1921) 966–972.

[152] O. Klein, *Quantentheorie und fünfdimensionale Relativitätstheorie*, Z.Phys. **37** (1926) 895–906.

[153] N. Arkani-Hamed, S. Dimopoulos, and G. Dvali, *The Hierarchy problem and new dimensions at a millimeter*, Phys.Lett. **B429** (1998) 263–272, arXiv:hep-ph/9803315 [hep-ph].

[154] E. Adelberger, J. Gundlach, B. Heckel, S. Hoedl, and S. Schlamminger, *Torsion balance experiments: A low-energy frontier of particle physics*, Prog.Part.Nucl.Phys. **62** (2009) 102–134.

[155] T. Appelquist, H.-C. Cheng, and B. A. Dobrescu, *Bounds on universal extra dimensions*, Phys.Rev. **D64** (2001) 035002, arXiv:hep-ph/0012100 [hep-ph].

[156] L. Randall and R. Sundrum, *A Large mass hierarchy from a small extra dimension*, Phys.Rev.Lett. **83** (1999) 3370–3373, arXiv:hep-ph/9905221 [hep-ph].

[157] L. Susskind, *Dynamics of spontaneous symmetry breaking in the Weinberg-Salam theory*, Phys. Rev. D **20** (1979) 2619–2625. http://link.aps.org/doi/10.1103/PhysRevD.20.2619.

[158] S. Weinberg, *Implications of dynamical symmetry breaking*, Phys. Rev. D **13** (1976) 974–996. http://link.aps.org/doi/10.1103/PhysRevD.13.974.

[159] S. Weinberg, *Implications of dynamical symmetry breaking: An addendum*, Phys. Rev. D **19** (1979) 1277–1280. http://link.aps.org/doi/10.1103/PhysRevD.19.1277.

[160] E. Farhi and L. Susskind, *Technicolor*, Phys.Rept. **74** (1981) 277.

[161] C. T. Hill and E. H. Simmons, *Strong dynamics and electroweak symmetry breaking*, Phys.Rept. **381** (2003) 235–402, arXiv:hep-ph/0203079 [hep-ph].

[162] D. B. Kaplan, H. Georgi, and S. Dimopoulos, *Composite Higgs Scalars*, Phys.Lett. **B136** (1984) 187.

[163] H. Georgi and D. B. Kaplan, *Composite Higgs and Custodial SU(2)*, Phys.Lett. **B145** (1984) 216.

[164] N. Arkani-Hamed, A. G. Cohen, and H. Georgi, *Electroweak symmetry breaking from dimensional deconstruction*, Phys.Lett. **B513** (2001) 232–240, arXiv:hep-ph/0105239 [hep-ph].

[165] O. S. Brüning, P. Collier, P. Lebrun, S. Myers, R. Ostojic, J. Poole, and P. Proudlock, *LHC Design Report*. CERN, Geneva, 2004. https://cds.cern.ch/record/782076.

[166] L. Evans and P. Bryant, *LHC Machine*, JINST **3** (2008) S08001.

[167] *LEP design report*. CERN, Geneva, 1984. https://cds.cern.ch/record/102083?

[168] ATLAS Collaboration, *The ATLAS Experiment at the CERN Large Hadron Collider*, JINST **3** (2008) S08003.

[169] CMS Collaboration Collaboration, S. Chatrchyan et al., *The CMS experiment at the CERN LHC*, JINST **3** (2008) S08004.

[170] LHCb Collaboration Collaboration, J. Alves, A. Augusto et al., *The LHCb Detector at the LHC*, JINST **3** (2008) S08005.

[171] ALICE Collaboration Collaboration, K. Aamodt et al., *The ALICE experiment at the CERN LHC*, JINST **3** (2008) S08002.

[172] TOTEM Collaboration Collaboration, G. Anelli et al., *The TOTEM experiment at the CERN Large Hadron Collider*, JINST **3** (2008) S08007.

[173] MoEDAL Collaboration Collaboration, J. Pinfold et al., *Technical Design Report of the MoEDAL Experiment*,.

[174] LHCf Collaboration Collaboration, O. Adriani et al., *The LHCf detector at the CERN Large Hadron Collider*, JINST **3** (2008) S08006.

[175] M. Bajko et al., *Report of the Task Force on the Incident of 19th September 2008 at the LHC*, Mar, 2009. https://cdsweb.cern.ch/record/1168025/.

[176] ATLAS Collaboration Collaboration, *ATLAS detector and physics performance: Technical Design Report, 1*. Technical Design Report ATLAS. CERN, Geneva, 1999. https://cdsweb.cern.ch/record/391176.

[177] ATLAS Collaboration Collaboration, *ATLAS detector and physics performance: Technical Design Report, 2*. Technical Design Report ATLAS. CERN, Geneva, 1999. https://cdsweb.cern.ch/record/391177.

[178] ATLAS Collaboration Collaboration, *ATLAS inner detector: Technical Design Report, 1*. Technical Design Report ATLAS. CERN, Geneva, 1997. https://cdsweb.cern.ch/record/331063.

[179] ATLAS Collaboration Collaboration, S. Haywood, L. Rossi, R. Nickerson, and A. Romaniouk, *ATLAS inner detector: Technical Design Report, 2*. Technical Design Report ATLAS. CERN, Geneva, 1997. https://cdsweb.cern.ch/record/331064.

[180] ATLAS Collaboration Collaboration, N. Wermes and G. Hallewel, *ATLAS pixel detector: Technical Design Report*. Technical Design Report ATLAS. CERN, Geneva, 1998. https://cdsweb.cern.ch/record/381263.

[181] G. Aad, M. Ackers, F. Alberti, M. Aleppo, G. Alimonti, et al., *ATLAS pixel detector electronics and sensors*, JINST **3** (2008) P07007.

[182] A. Abdesselam, T. Akimoto, P. Allport, J. Alonso, B. Anderson, et al., *The barrel modules of the ATLAS semiconductor tracker*, Nucl.Instrum.Meth. **A568** (2006) 642–671.

[183] ATLAS Collaboration Collaboration, A. Abdesselam et al., *The ATLAS semiconductor tracker end-cap module*, Nucl.Instrum.Meth. **A575** (2007) 353–389.

[184] A. Ahmad, Z. Albrechtskirchinger, P. Allport, J. Alonso, L. Andricek, et al., *The Silicon microstrip sensors of the ATLAS semiconductor tracker*, Nucl.Instrum.Meth. **A578** (2007) 98–118.

[185] ATLAS TRT Collaboration Collaboration, E. Abat et al., *The ATLAS TRT barrel detector*, JINST **3** (2008) P02014.

[186] E. Abat, E. Arik, M. Arik, N. Becerici, O. Dogan, et al., *The ATLAS TRT end-cap detectors*, JINST **3** (2008) P10003.

[187] ATLAS TRT Collaboration Collaboration, E. Abat et al., *The ATLAS Transition Radiation Tracker (TRT) proportional drift tube: Design and performance*, JINST **3** (2008) P02013.

[188] ATLAS Collaboration Collaboration, *ATLAS central solenoid: Technical Design Report*. Technical Design Report ATLAS. CERN, Geneva, 1997. https://cdsweb.cern.ch/record/331067.

[189] ATLAS Collaboration Collaboration, *ATLAS calorimeter performance: Technical Design Report*. Technical Design Report ATLAS. CERN, Geneva, 1996. https://cdsweb.cern.ch/record/331059.

[190] ATLAS Collaboration Collaboration, *ATLAS liquid-argon calorimeter: Technical Design Report*. Technical Design Report ATLAS. CERN, Geneva, 1996. https://cdsweb.cern.ch/record/331061.

[191] ATLAS Collaboration Collaboration, *ATLAS tile calorimeter: Technical Design Report*. Technical Design Report ATLAS. CERN, Geneva, 1996. https://cdsweb.cern.ch/record/331062.

[192] ATLAS Collaboration Collaboration, *ATLAS muon spectrometer: Technical Design Report*. Technical Design Report ATLAS. CERN, Geneva, 1997. https://cdsweb.cern.ch/record/331068.

[193] ATLAS Collaboration Collaboration, J. P. Badiou, J. Beltramelli, J. M. Baze, and J. Belorgey, *ATLAS barrel toroid: Technical Design Report*. Technical Design Report ATLAS. CERN, Geneva, 1997. https://cdsweb.cern.ch/record/331065.

[194] ATLAS Collaboration Collaboration, *ATLAS end-cap toroids: Technical Design Report*. Technical Design Report ATLAS. CERN, Geneva, 1997. https://cdsweb.cern.ch/record/331066.

[195] ATLAS Collaboration Collaboration, *ATLAS magnet system: Technical Design Report, 1*. Technical Design Report ATLAS. CERN, Geneva, 1997. https://cdsweb.cern.ch/record/338080.

[196] ATLAS Collaboration, G. Aad et al., *Readiness of the ATLAS Liquid Argon Calorimeter for LHC Collisions*, Eur.Phys.J. **C70** (2010) 723–753, arXiv:0912.2642 [physics.ins-det].

[197] ATLAS Collaboration, G. Aad et al., *Commissioning of the ATLAS Muon Spectrometer with Cosmic Rays*, Eur.Phys.J. **C70** (2010) 875–916, arXiv:1006.4384 [physics.ins-det].

[198] ATLAS Electromagnetic Barrel Liquid Argon Calorimeter Group Collaboration, B. Aubert et al., *Construction, assembly and tests of the ATLAS electromagnetic barrel calorimeter*, Nucl.Instrum.Meth. **A558** (2006) 388–418.

[199] ATLAS Collaboration, M. Aleksa et al., *Construction, assembly and tests of the ATLAS electromagnetic end-cap calorimeters*, JINST **3** (2008) P06002.

[200] ATLAS Collaboration, G. Aad et al., *Drift Time Measurement in the ATLAS Liquid Argon Electromagnetic Calorimeter using Cosmic Muons*, Eur.Phys.J. **C70** (2010) 755–785, arXiv:1002.4189 [physics.ins-det].

[201] G. Aielli, A. Aloisio, M. Alviggi, V. Aprodu, V. Bocci, et al., *The RPC first level muon trigger in the barrel of the ATLAS experiment*, Nucl.Phys.Proc.Suppl. **158** (2006) 11–15.

[202] S. Majewski, G. Charpak, A. Breskin, and G. Mikenberg, *A THIN MULTIWIRE CHAMBER OPERATING IN THE HIGH MULTIPLICATION MODE*, Nucl.Instrum.Meth. **217** (1983) 265–271.

[203] ATLAS Collaboration Collaboration, *ATLAS Muon Spectrometer Thin Gap Chambers Construction Manual*. Technical Design Report ATLAS. CERN, Geneva, 1998. ATLAS-TGC-001-98.

[204] F. Bauer, U. Bratzler, H. Dietl, H. Kroha, T. Lagouri, et al., *Construction and test of MDT chambers for the ATLAS muon spectrometer*, Nucl.Instrum.Meth. **A461** (2001) 17–20.

[205] T. Argyropoulos, K. A. Assamagan, B. H. Benedict, V. Chernyatin, E. Cheu, et al., *Cathode strip chambers in ATLAS: Installation, commissioning and in situ performance*, IEEE Trans.Nucl.Sci. **56** (2009) 1568–1574.

[206] S. van der Meer, *Calibration of the effective beam height in the ISR*, Tech. Rep. CERN-ISR-PO-68-31. ISR-PO-68-31, CERN, Geneva, 1968.

[207] ATLAS Collaboration, *Improved luminosity determination in pp collisions at $\sqrt{s} = 7$ TeV using the ATLAS detector at the LHC*, Eur.Phys.J. **C73** (2013) 2518, arXiv:1302.4393 [hep-ex].

[208] ATLAS Collaboration Collaboration, *ATLAS level-1 trigger: Technical Design Report*. Technical Design Report ATLAS. CERN, Geneva, 1998. https://cdsweb.cern.ch/record/381429.

[209] ATLAS Collaboration Collaboration, P. Jenni, M. Nessi, M. Nordberg, and K. Smith, *ATLAS high-level trigger, data-acquisition and controls: Technical Design Report*. Technical Design Report ATLAS. CERN, Geneva, 2003.

[210] C. Eck et al., *LHC computing Grid: Technical Design Report. Version 1.06 (20 Jun 2005)*. Technical Design Report LCG. CERN, Geneva, 2005.

[211] I. Bird et al., *Update of the Computing Models of the WLCG and the LHC Experiments*, Tech. Rep. CERN-LHCC-2014-014. LCG-TDR-002, CERN, Geneva, Apr, 2014.

[212] T. Cornelissen, M. Elsing, S. Fleischmann, W. Liebig, E. Moyse, and A. Salzburger, *Concepts, Design and Implementation of the ATLAS New Tracking (NEWT)*, ATLAS-SOFT-PUB-2007-007 no. ATL-SOFT-PUB-2007-007, (2007).

[213] ATLAS Collaboration Collaboration, *Performance of the ATLAS Inner Detector Track and Vertex Reconstruction in the High Pile-Up LHC Environment*, ATLAS-CONF-2012-042 no. ATLAS-CONF-2012-042, (2012).

[214] ATLAS Collaboration, *Alignment Performance of the ATLAS Inner Detector Tracking System in 7 TeV proton-proton collisions at the LHC*, ATLAS-CONF-2010-067.

[215] ATLAS Collaboration, *Alignment of the ATLAS Inner Detector and its Performance in 2012*, ATLAS-CONF-2014-047.

[216] ATLAS Collaboration Collaboration, *Performance of primary vertex reconstruction in proton-proton collisions at $\sqrt{s}$ =7 TeV in the ATLAS experiment*, ATLAS-CONF-2010-069 no. ATLAS-CONF-2010-069, (2010).

[217] ATLAS Collaboration, *Jet energy measurement with the ATLAS detector in proton-proton collisions at $\sqrt{s} = 7$ TeV*, Eur.Phys.J. **C73** (2013) 2304, arXiv:1112.6426 [hep-ex].

[218] W. Lampl et al., *Calorimeter Clustering Algorithms: Description and Performance*, ATL-LARG-PUB-2008-002.

[219] ATLAS Collaboration, *Local hadronic calibration*, ATLAS-LARG-PUB-2009-001-2 (2009).

[220] M. Cacciari and G. P. Salam, *Dispelling the* N^3 *myth for the* k_t *jet-finder*, Phys. Lett. **B641** (2006) 57–61, arXiv:hep-ph/0512210.

[221] G. S. M. Cacciari, G. P. Salam. http://fastjet.fr/.

[222] ATLAS Collaboration, G. Aad et al., *Jet energy measurement and its systematic uncertainty in proton-proton collisions at* $\sqrt{s} = 7$ *TeV with the ATLAS detector*, Eur.Phys.J. **C75** no. 1, (2015) 17, arXiv:1406.0076 [hep-ex].

[223] M. Cacciari and G. P. Salam, *Pileup subtraction using jet areas*, Phys.Lett. **B659** (2008) 119–126, arXiv:0707.1378 [hep-ph].

[224] ATLAS Collaboration, *Pile-up subtraction and suppression for jets in ATLAS*, ATLAS-CONF-2013-083.

[225] ATLAS Collaboration, G. Aad et al., *Jet energy resolution in proton-proton collisions at* $\sqrt{s} = 7$ *TeV recorded in 2010 with the ATLAS detector*, Eur.Phys.J. **C73** no. 3, (2013) 2306, arXiv:1210.6210 [hep-ex].

[226] ATLAS Collaboration, *Commissioning of the ATLAS high-performance b-tagging algorithms in the 7 TeV collision data*, ATLAS-CONF-2011-102.

[227] G. Piacquadio and C. Weiser, *A new inclusive secondary vertex algorithm for b-jet tagging in ATLAS*, J.Phys.Conf.Ser. **119** (2008) 032032.

[228] ATLAS Collaboration, *Calibration of* b*-tagging using dileptonic top pair events in a combinatorial likelihood approach with the ATLAS experiment*, Tech. Rep. ATLAS-CONF-2014-004, CERN, Geneva, Feb, 2014.

[229] ATLAS Collaboration, *Calibration of the performance of* b*-tagging for* c *and light-flavour jets in the 2012 ATLAS data*, Tech. Rep. ATLAS-CONF-2014-046, CERN, Geneva, Jul, 2014.

[230] ATLAS Collaboration, G. Aad et al., *Measurement of the muon reconstruction performance of the ATLAS detector using 2011 and 2012 LHC proton-proton collision data*, Eur.Phys.J. **C74** no. 11, (2014) 3130, arXiv:1407.3935 [hep-ex].

[231] ATLAS Collaboration, G. Aad et al., *Electron reconstruction and identification efficiency measurements with*

the ATLAS detector using the 2011 LHC proton-proton collision data, Eur.Phys.J. **C74** no. 7, (2014) 2941, arXiv:1404.2240 [hep-ex].

[232] ATLAS Collaboration, *Improved electron reconstruction in ATLAS using the Gaussian Sum Filter-based model for bremsstrahlung*, ATLAS-CONF-2012-047.

[233] ATLAS Collaboration, *Electron performance measurements with the ATLAS detector using the 2010 LHC proton-proton collision data*, Eur.Phys.J. **C72** (2012) 1909, arXiv:1110.3174 [hep-ex].

[234] *Electron efficiency measurements with the ATLAS detector using the 2012 LHC proton-proton collision data*, Jun, 2014. ATLAS-CONF-2014-032.

[235] ATLAS Collaboration, G. Aad et al., *Electron and photon energy calibration with the ATLAS detector using LHC Run 1 data*, Eur.Phys.J. **C74** no. 10, (2014) 3071, arXiv:1407.5063 [hep-ex].

[236] M. Cacciari, G. P. Salam, and S. Sapeta, *On the characterisation of the underlying event*, JHEP **1004** (2010) 065, arXiv:0912.4926 [hep-ph].

[237] ATLAS Collaboration, G. Aad et al., *Measurement of the inclusive isolated prompt photon cross section in* pp *collisions at* $\sqrt{s} = 7$ *TeV with the ATLAS detector*, Phys.Rev. **D83** (2011) 052005, arXiv:1012.4389 [hep-ex].

[238] ATLAS Collaboration, *Expected photon performance in the ATLAS experiment*, Apr, 2011. ATL-PHYS-PUB-2011-007.

[239] ATLAS Collaboration, *Measurements of the photon identification efficiency with the ATLAS detector using 4.9* fb^{-1} *of pp collision data collected in 2011*, ATLAS-CONF-2012-123.

[240] *Performance of Missing Transverse Momentum Reconstruction in ATLAS studied in Proton-Proton Collisions recorded in 2012 at 8 TeV*, Tech. Rep. ATLAS-CONF-2013-082, CERN, Geneva, Aug, 2013.

[241] ATLAS Collaboration, *Performance of Missing Transverse Momentum Reconstruction in Proton-Proton Collisions at 7 TeV with ATLAS*, Eur.Phys.J. **C72** (2012) 1844, arXiv:1108.5602 [hep-ex].

[242] ATLAS Collaboration, *Pile-up Suppression in Missing Transverse Momentum Reconstruction in the ATLAS*

Experiment in Proton-Proton Collisions at sqrts = 8 TeV, ATL-CONF-2014-019.

[243] ATLAS Collaboration, *Performance of Missing Transverse Momentum Reconstruction in ATLAS with 2011 Proton-Proton Collisions at $\sqrt{s} = 7$ TeV*, ATLAS-CONF-2012-101.

[244] ATLAS Collaboration, "Expected performance of the atlas experiment - detector, trigger and physics." CERN-OPEN-2008-020, 2009.

[245] J. M. Katzy, *QCD Monte-Carlo model tunes for the LHC*, Prog.Part.Nucl.Phys. **73** (2013) 141–187.

[246] P. Skands, S. Carrazza, and J. Rojo, *Tuning PYTHIA 8.1: the Monash 2013 Tune*, European Physical Journal **74** (2014) 3024, arXiv:1404.5630 [hep-ph].

[247] H. Schulz and P. Skands, *Energy Scaling of Minimum-Bias Tunes*, Eur.Phys.J. **C71** (2011) 1644, arXiv:1103.3649 [hep-ph].

[248] ATLAS Collaboration, G. Aad et al., *Measurement of $t\bar{t}$ production with a veto on additional central jet activity in pp collisions at sqrt(s) = 7 TeV using the ATLAS detector*, Eur.Phys.J. **C72** (2012) 2043, arXiv:1203.5015 [hep-ex].

[249] ATLAS Collaboration, G. Aad et al., *Measurement of jet shapes in top-quark pair events at $\sqrt{s} = 7$ TeV using the ATLAS detector*, Eur.Phys.J. **C73** (2013) 2676, arXiv:1307.5749 [hep-ex].

[250] ATLAS Collaboration Collaboration, G. Aad et al., *Measurement of the $t\bar{t}$ production cross-section as a function of jet multiplicity and jet transverse momentum in 7 TeV proton-proton collisions with the ATLAS detector*, JHEP **1501** (2015) 020, arXiv:1407.0891 [hep-ex].

[251] ATLAS Collaboration, *ATLAS Run 1 Pythia8 tunes*, Nov, 2014. ATL-PHYS-PUB-2014-021.

[252] ATLAS Collaboration, G. Aad et al., *Measurement of the Z/γ^* boson transverse momentum distribution in pp collisions at $\sqrt{s} = 7$ TeV with the ATLAS detector*, JHEP **1409** (2014) 145, arXiv:1406.3660 [hep-ex].

[253] L3 Collaboration, P. Achard et al., *Studies of hadronic event structure in e^+e^- annihilation from 30-GeV to 209-GeV with the L3 detector*, Phys. Rept. **399** (2004) 71–174, arXiv:hep-ex/0406049 [hep-ex].

[254] ALEPH Collaboration, R. Barate et al., *Studies of quantum chromodynamics with the ALEPH detector*, Phys.Rept. **294** (1998) 1–165.

[255] DELPHI Collaboration, P. Abreu et al., *Tuning and test of fragmentation models based on identified particles and precision event shape data*, Z.Phys. **C73** (1996) 11–60.

[256] JADE, OPAL Collaboration, P. Pfeifenschneider et al., *QCD analyses and determinations of alpha(s) in e+ e- annihilation at energies between 35-GeV and 189-GeV*, Eur.Phys.J. **C17** (2000) 19–51, arXiv:hep-ex/0001055 [hep-ex].

[257] Do Collaboration, V. M. Abazov et al., *Precision measurement of the top-quark mass in lepton+jets final states*, Phys. Rev. Lett. **113** (2014) 032002, arXiv:1405.1756 [hep-ex].

[258] Do Collaboration, V. M. Abazov et al., *Precise study of the Z/γ^* boson transverse momentum distribution in $p\bar{p}$ collisions using a novel technique*, Phys. Rev. Lett. **106** (2011) 122001, arXiv:1010.0262 [hep-ex].

[259] R. Corke and T. Sjöstrand, *Improved Parton Showers at Large Transverse Momenta*, Eur.Phys.J. **C69** (2010) 1–18, arXiv:1003.2384 [hep-ph].

[260] ATLAS Collaboration Collaboration, G. Aad et al., *Measurements of top quark pair relative differential cross-sections with ATLAS in pp collisions at $\sqrt{s} = 7$ TeV*, Eur.Phys.J. **C73** no. 1, (2013) 2261, arXiv:1207.5644 [hep-ex].

[261] CMS Collaboration Collaboration, S. Chatrchyan et al., *Shape, Transverse Size, and Charged Hadron Multiplicity of Jets in pp Collisions at 7 TeV*, JHEP **1206** (2012) 160, arXiv:1204.3170 [hep-ex].

[262] ATLAS Collaboration, *Differential top-antitop cross-section measurements as a function of observables constructed from final-state particles using pp collisions at $\sqrt{s} = 7$ TeV in the ATLAS detector*, arXiv:1502.05923 [hep-ex].

[263] R. Corke and T. Sjöstrand, *Interleaved Parton Showers and Tuning Prospects*, JHEP **1103** (2011) 032, arXiv:1011.1759 [hep-ph].

[264] J. Pumplin, D. Stump, J. Huston, H. Lai, P. M. Nadolsky, et al., *New generation of parton distributions with*

uncertainties from global QCD analysis, JHEP **0207** (2002) 012, arXiv:hep-ph/0201195 [hep-ph].

[265] R. D. Ball, V. Bertone, S. Carrazza, C. S. Deans, L. Del Debbio, et al., *Parton distributions with LHC data*, Nucl.Phys. **B867** (2013) 244–289, arXiv:1207.1303 [hep-ph].

[266] T. Sjöstrand, S. Ask, J. R. Christiansen, R. Corke, N. Desai, et al., *An Introduction to PYTHIA 8.2*, arXiv:1410.3012 [hep-ph].

[267] P. Nason, *A New method for combining NLO QCD with shower Monte Carlo algorithms*, JHEP **0411** (2004) 040, arXiv:hep-ph/0409146 [hep-ph].

[268] S. Frixione, P. Nason, and G. Ridolfi, *A Positive-weight next-to-leading-order Monte Carlo for heavy flavour hadroproduction*, JHEP **0709** (2007) 126, arXiv:0707.3088 [hep-ph].

[269] H.-L. Lai et al., *New parton distributions for collider physics*, Phys. Rev. **D82** (2010) 074024, arXiv:1007.2241 [hep-ph].

[270] ATLAS Collaboration, *Comparison of Monte Carlo generator predictions for gap fraction and jet multiplicity observables in top-antitop events*, ATL-PHYS-PUB-2014-005.

[271] ATLAS Collaboration, *Comparison of Monte Carlo generator predictions to ATLAS measurements of top pair production at 7 TeV*, ATL-PHYS-PUB-2015-002.

[272] A. Buckley, J. Butterworth, L. Lönnblad, D. Grellscheid, H. Hoeth, et al., *Rivet user manual*, Comput.Phys.Commun. **184** (2013) 2803–2819, arXiv:1003.0694 [hep-ph].

[273] N. Fischer, S. Gieseke, S. Plätzer, and P. Skands, *Revisiting radiation patterns in e^+e^- collisions*, Eur.Phys.J. **C74** no. 4, (2014) 2831, arXiv:1402.3186 [hep-ph].

[274] S. Argyropoulos and T. Sjöstrand, *Effects of color reconnection on $t\bar{t}$ final states at the LHC*, JHEP **1411** (2014) 043, arXiv:1407.6653 [hep-ph].

[275] J. M. Campbell, R. K. Ellis, P. Nason, and E. Re, *Top-pair production and decay at NLO matched with parton showers*, arXiv:1412.1828 [hep-ph].

[276] CMS Collaboration, *Study of the underlying event, b-quark fragmentation and hadronization properties in tbart events*, Sep, 2013. CMS-PAS-TOP-13-007.

[277] ATLAS Collaboration, G. Aad et al., *Measurement of distributions sensitive to the underlying event in inclusive Z-boson production in* pp *collisions at* $\sqrt{s} = 7$ *TeV with the ATLAS detector*, Eur.Phys.J. **C74** no. 12, (2014) 3195, arXiv:1409.3433 [hep-ex].

[278] CMS Collaboration, S. Chatrchyan et al., *Measurement of the underlying event in the Drell-Yan process in proton-proton collisions at* $\sqrt{s} = 7$ *TeV*, Eur.Phys.J. **C72** (2012) 2080, arXiv:1204.1411 [hep-ex].

[279] LHC New Physics Working Group Collaboration, D. Alves et al., *Simplified Models for LHC New Physics Searches*, J.Phys. **G39** (2012) 105005, arXiv:1105.2838 [hep-ph].

[280] CDF Collaboration, T. Aaltonen et al., *Search for Anomalous Production of Events with Two Photons and Additional Energetic Objects at CDF*, Phys.Rev. **D82** (2010) 052005, arXiv:0910.5170 [hep-ex].

[281] ATLAS Collaboration, G. Aad et al., *Search for new phenomena in events with three or more charged leptons in* pp *collisions at* $\sqrt{s} = 8$ *TeV with the ATLAS detector*, arXiv:1411.2921 [hep-ex].

[282] N. Arkani-Hamed, G. L. Kane, J. Thaler, and L.-T. Wang, *Supersymmetry and the LHC inverse problem*, JHEP **0608** (2006) 070, arXiv:hep-ph/0512190 [hep-ph].

[283] Do Collaboration, V. Abazov et al., *Search for new physics using QUAERO: A General interface to Do event data*, Phys.Rev.Lett. **87** (2001) 231801, arXiv:hep-ex/0106039 [hep-ex].

[284] S. Caron and B. Knuteson, *QUAERO and H1: An Interface to high-p(T) HERA event data*, Eur.Phys.J. **C53** (2008) 167–175, arXiv:hep-ph/0612201 [hep-ph].

[285] L3 Collaboration, *A global comparison between L3 data and Standard Model Monte Carlo - a first attempt*, L3-note-2305 (1998).

[286] Do Collaboration Collaboration, B. Abbott et al., *Search for new physics in* eμX *data at DØ using SLEUTH: A quasi model independent search strategy for new physics*, Phys.Rev. **D62** (2000) 092004, arXiv:hep-ex/0006011 [hep-ex].

[287] Do Collaboration Collaboration, B. Abbott et al., *A quasi-model-independent search for new high p_T physics at DØ*, Phys.Rev.Lett. **86** (2001) 3712–3717, arXiv:hep-ex/0011071 [hep-ex].

[288] Do Collaboration Collaboration, V. Abazov et al., *A Quasi model independent search for new physics at large transverse momentum*, Phys.Rev. **D64** (2001) 012004, arXiv:hep-ex/0011067 [hep-ex].

[289] Do Collaboration Collaboration, V. M. Abazov et al., *Model independent search for new phenomena in $p\bar{p}$ collisions at $\sqrt{s} = 1.96$ TeV*, Phys.Rev. **D85** (2012) 092015, arXiv:1108.5362 [hep-ex].

[290] H1 Collaboration, A. Aktas et al., *A general search for new phenomena in ep scattering at HERA*, Phys.Lett. **B602** (2004) 14–30, arXiv:hep-ex/0408044 [hep-ex].

[291] H1 Collaboration, F. Aaron et al., *A General Search for New Phenomena at HERA*, Phys.Lett. **B674** (2009) 257–268, arXiv:0901.0507 [hep-ex].

[292] CDF Collaboration, T. Aaltonen, et al., *Model-independent and quasi-model-independent search for new physics at CDF*, Phys. Rev. D **78** (2008) 012002, arXiv:0712.1311 [hep-ex].

[293] CDF Collaboration, T. Aaltonen et al., *Global Search for New Physics with 2.0 fb^{-1} at CDF*, Phys.Rev. **D79** (2009) 011101, arXiv:0809.3781 [hep-ex].

[294] G. Choudalakis, *On hypothesis testing, trials factor, hypertests and the BumpHunter*, arXiv:1101.0390 [physics.data-an].

[295] CMS Collaboration, *Model Unspecific Search for New Physics in pp Collisions at sqrt(s) = 7 TeV*, CMS-PAS-EXO-10-021.

[296] T. G. Rizzo, *Indirect Searches for Z-prime-like Resonances at the LHC*, JHEP **0908** (2009) 082, arXiv:0904.2534 [hep-ph].

[297] G. Bella, E. Etzion, N. Hod, Y. Oz, Y. Silver, et al., *A Search for heavy Kaluza-Klein electroweak gauge bosons at the LHC*, JHEP **1009** (2010) 025, arXiv:1004.2432 [hep-ex].

[298] Y. Bai and W.-Y. Keung, *Dips at Colliders*, arXiv:1407.6355 [hep-ph].

[299] GEANT4 Collaboration, S. Agostinelli et al., *GEANT4: A simulation toolkit*, Nucl. Instrum. Meth. **A506** (2003) 250–303.

[300] ATLAS Collaboration, *The ATLAS Simulation Infrastructure*, Eur. Phys. J. **C70** (2010) 823–874, arXiv:1005.4568 [physics.ins-det].

[301] ATLAS Collaboration, *The simulation principle and performance of the ATLAS fast calorimeter simulation FastCaloSim*, ATL-PHYS-PUB-2010-013.

[302] T. Sjöstrand, S. Mrenna, and P. Z. Skands, *A Brief Introduction to PYTHIA 8.1*, Comput. Phys. Commun. **178** (2008) 852–867, arXiv:0710.3820.

[303] ATLAS Collaboration, *Further ATLAS tunes of PYTHIA 6 and Pythia 8*, ATL-PHYS-PUB-2011-014.

[304] K. Melnikov and F. Petriello, *Electroweak gauge boson production at hadron colliders through O(alpha(s)**2)*, Phys. Rev. **D74** (2006) 114017, arXiv:hep-ph/0609070.

[305] T. Sjöstrand, S. Mrenna, and P. Z. Skands, *PYTHIA 6.4 Physics and Manual*, JHEP **0605** (2006) 026, arXiv:hep-ph/0603175.

[306] M. L. Mangano et al., *ALPGEN, a generator for hard multiparton processes in hadronic collisions*, JHEP **07** (2003) 001, arXiv:hep-ph/0206293.

[307] P. M. Nadolsky et al., *Implications of CTEQ global analysis for collider observables*, Phys. Rev. **D78** (2008) 013004, arXiv:0802.0007 [hep-ph].

[308] G. Bozzi, F. Campanario, M. Rauch, and D. Zeppenfeld, *$Z\gamma\gamma$ production with leptonic decays and triple photon production at NLO QCD*, Phys.Rev. **D84** (2011) 074028, arXiv:1107.3149 [hep-ph].

[309] G. Bozzi, F. Campanario, M. Rauch, and D. Zeppenfeld, *$W^{+-}\gamma\gamma$ production with leptonic decays at NLO QCD*, Phys.Rev. **D83** (2011) 114035, arXiv:1103.4613 [hep-ph].

[310] M. Cacciari, M. Czakon, M. Mangano, A. Mitov, and P. Nason, *Top-pair production at hadron colliders with next-to-next-to-leading logarithmic soft-gluon resummation*, Phys.Lett. **B710** (2012) 612–622, arXiv:1111.5869 [hep-ph].

[311] P. Baernreuther, M. Czakon, and A. Mitov, *Percent Level Precision Physics at the Tevatron: First Genuine NNLO QCD Corrections to* $q\bar{q} \to t\bar{t} + X$, Phys.Rev.Lett. **109** (2012) 132001, arXiv:1204.5201 [hep-ph].

[312] M. Czakon and A. Mitov, *NNLO corrections to top pair production at hadron colliders: the quark-gluon reaction*, JHEP **1301** (2013) 080, arXiv:1210.6832 [hep-ph].

[313] M. Czakon and A. Mitov, *NNLO corrections to top-pair production at hadron colliders: the all-fermionic scattering channels*, JHEP **1212** (2012) 054, arXiv:1207.0236 [hep-ph].

[314] M. Czakon, P. Fiedler, and A. Mitov, *The total top quark pair production cross-section at hadron colliders through* $O(\alpha_s^4)$, Phys.Rev.Lett. **110** (2013) 252004, arXiv:1303.6254 [hep-ph].

[315] M. Czakon and A. Mitov, *Top++: A Program for the Calculation of the Top-Pair Cross-Section at Hadron Colliders*, arXiv:1112.5675 [hep-ph].

[316] N. Kidonakis, *Next-to-next-to-leading-order collinear and soft gluon corrections for t-channel single top quark production*, Phys.Rev. **D83** (2011) 091503, arXiv:1103.2792 [hep-ph].

[317] N. Kidonakis, *Two-loop soft anomalous dimensions for single top quark associated production with a W- or H-*, Phys.Rev. **D82** (2010) 054018, arXiv:1005.4451 [hep-ph].

[318] N. Kidonakis, *NNLL resummation for s-channel single top quark production*, Phys.Rev. **D81** (2010) 054028, arXiv:1001.5034 [hep-ph].

[319] J. M. Campbell and R. K. Ellis, $t\bar{t}W$ *production and decay at NLO*, JHEP **1207** (2012) 052, arXiv:1204.5678 [hep-ph].

[320] M. Garzelli, A. Kardos, C. Papadopoulos, and Z. Trocsanyi, $t\,\bar{t}\,W^{+-}$ *and* $t\,\bar{t}\,Z$ *Hadroproduction at NLO accuracy in QCD with Parton Shower and Hadronization effects*, JHEP **1211** (2012) 056, arXiv:1208.2665 [hep-ph].

[321] J. M. Campbell, R. K. Ellis, and C. Williams, *Vector boson pair production at the LHC*, JHEP **1107** (2011) 018, arXiv:1105.0020 [hep-ph].

[322] F. Campanario, V. Hankele, C. Oleari, S. Prestel, and D. Zeppenfeld, *QCD corrections to charged triple vector boson production with leptonic decay*, Phys.Rev. **D78** (2008) 094012, arXiv:0809.0790 [hep-ph].

[323] HTTPS://TWIKI.CERN.CH/TWIKI/BIN/VIEW/\LHCPhysics/CERNYELLOWREPORTPAGEAT8TEV. Accessed: 2010-09-30.

[324] M. Bahr et al., *Herwig++ Physics and Manual*, Eur. Phys. J. **C58** (2008) 639–707, arXiv:0803.0883 [hep-ph].

[325] W. Beenakker, R. Hopker, M. Spira, and P. M. Zerwas, *Squark and gluino production at hadron colliders*, Nucl. Phys. **B492** (1997) 51–103, arXiv:hep-ph/9610490.

[326] A. Kulesza and L. Motyka, *Threshold resummation for squark-antisquark and gluino-pair production at the LHC*, Phys.Rev.Lett. **102** (2009) 111802, arXiv:0807.2405 [hep-ph].

[327] A. Kulesza and L. Motyka, *Soft gluon resummation for the production of gluino-gluino and squark-antisquark pairs at the LHC*, Phys.Rev. **D80** (2009) 095004, arXiv:0905.4749 [hep-ph].

[328] W. Beenakker, S. Brensing, M. Kramer, A. Kulesza, E. Laenen, et al., *Soft-gluon resummation for squark and gluino hadroproduction*, JHEP **0912** (2009) 041, arXiv:0909.4418 [hep-ph].

[329] W. Beenakker, S. Brensing, M. Kramer, A. Kulesza, E. Laenen, et al., *Squark and gluino hadroproduction*, Int.J.Mod.Phys. **A26** (2011) 2637–2664, arXiv:1105.1110 [hep-ph].

[330] P. Langacker, *The Physics of Heavy Z′ Gauge Bosons*, Rev.Mod.Phys. **81** (2009) 1199–1228, arXiv:0801.1345 [hep-ph].

[331] ATLAS Collaboration, *Search for squarks and gluinos with the ATLAS detector in final states with jets and missing transverse momentum and* 20.3fb^{-1} *of* $\sqrt{s}$ *= 8 TeV proton-proton collisions*, ATLAS-CONF-2013-047.

[332] ATLAS Collaboration, *Search for pair produced top squarks decaying into a charm quark and the lightest neutralinos with* 20.3fb^{-1} *of pp collisions at* $\sqrt{s} = 8$ *TeV with the ATLAS detector at the LHC*, ATLAS-CONF-2013-068.

[333] ATLAS Collaboration, *Search for squarks and gluinos in events with isolated leptons, jets and missing transverse momentum at* $\sqrt{s} = 8$ *TeV with the ATLAS detector at the LHC*, ATLAS-CONF-2013-062.

[334] ATLAS Collaboration, *Measurement of multi-jet cross sections in proton-proton collisions at a 7 TeV center-of-mass*

energy, Eur.Phys.J. **C71** (2011) 1763, arXiv:1107.2092 [hep-ex].

[335] ATLAS Collaboration, *Measurement of the production cross section of an isolated photon associated with jets in proton-proton collisions at $\sqrt{s}$ = 7 TeV with the ATLAS detector*, Phys.Rev. **D85** (2012) 092014, arXiv:1203.3161 [hep-ex].

[336] ATLAS Collaboration, *Measurement of the production cross section for Z/gamma* in association with jets in pp collisions at $\sqrt{s}$= 7 TeV TeV with the ATLAS detector*, Phys.Rev. **D85** (2012) 032009, arXiv:1111.2690 [hep-ex].

[337] ATLAS Collaboration, G. Aad et al., *Search for squarks and gluinos in events with isolated leptons, jets and missing transverse momentum at $\sqrt{s} = 8$ TeV with the ATLAS detector*, arXiv:1501.03555 [hep-ex].

[338] S. Moch and P. Uwer, *Theoretical status and prospects for top-quark pair production at hadron colliders*, Phys.Rev. **D78** (2008) 034003, arXiv:0804.1476 [hep-ph].

[339] ATLAS Collaboration, G. Aad et al., *Measurement of the WW cross section in $\sqrt{s} = 7$ TeV pp collisions with the ATLAS detector and limits on anomalous gauge couplings*, Phys.Lett. **B712** (2012) 289–308, arXiv:1203.6232 [hep-ex].

[340] ATLAS Collaboration, *Search for associated production of the Higgs boson in the $WH \to WWW^{(*)} \to l\nu l\nu l\nu$ and $ZH \to ZWW^{(*)} \to lll\nu l\nu$ channels with the ATLAS detector at the LHC*, ATLAS-CONF-2013-075.

COLOPHON

This document was typeset using the typographical look-and-feel `classicthesis` developed by André Miede. The style was inspired by Robert Bringhurst's seminal book on typography "*The Elements of Typographic Style*". `classicthesis` is available for both LaTeX and LyX:

http://code.google.com/p/classicthesis/

Happy users of `classicthesis` usually send a real postcard to the author, a collection of postcards received so far is featured here:

http://postcards.miede.de/

Final Version as of December 24, 2015 (`classicthesis` version 0.1).

DECLARATION

Put your declaration here.

Freiburg, June, 2015

Simone Amoroso